FCRD Technical Integration Office (TIO)
DOCUMENT NUMBER REQUEST
TRANSMITTAL SHEET

1. Document Information

Document Title/Description:	Natural System Evaluation and Tool Development – FY11 Progress Report	Revision:	N/A
Assigned Document Number:	FCRD-USED-2011-000223	Effective Start Date:	N/A
Document Author/Creator:	Yifeng Wang, et.al	**OR**	
Document Owner:	Yifeng Wang	Date Range:	
Originating Organization:	Sandia National Laboratories (SNL)	From:	To:

Milestone   ☐ M1   ☒ M2   ☐ M3   ☐ M4   ☐ Not a Milestone

Milestone Number::   M21UF034004

Work Package WBS Number: WP# FTSN11UF0340 / WBS # 1.02.08.03

Controlled Unclassified Information (CUI) Type   ☒ None   ☐ OUO   ☐ AT   ☐ Other

FCRD	SYSTEM:		Year:	
	☐ FUEL	Fuels		
	☐ INTL	International		
	☐ MDSM	Modeling and Simulation		
	☐ MPACT	Materials Protection, Accounting, and Control for Transmutation		
	☐ NEAMS	Nuclear Energy Advanced Modeling and Simulation		
	☐ REAC	Reactor Campaign		
	☐ SAFE	Safeguards Campaign		
	☐ SEPA	Separations		
	☐ SYSA	System Analysis		
	☐ SYSE	System Engineering		
	☐ TIO	Technical Integration Office		
	☒ USED	Used Fuel Disposition		
	☐ WAST	Waste Campaign		
	☐			

2. Records Management Requirements

Category: ☒ General Record   ☐ QA Record   ☐ Controlled Doc   ☐ Controlled QA Doc

Keywords: Natural System, Evaluation, Tool Development, FY11, Progress Report

Medium: ☐ Hard Copy   ☐ CD/Disk (each CD/Disk must have an attached index)   ☒ Electronic:

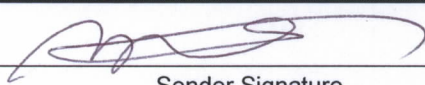Total Number of Pages (including transmittal sheet): 291

IF QA Record

QA Classification: ☐ Lifetime   ☒ Non-Permanent

Uniform Filing Code:	*Disposition Authority:*	*Retention Period:*

Special Instructions:

3. Signatures

SENDER:	YIFENG WANG		7/19/201
	Print/Type Sender Name	Sender Signature	Date
QA RECORD VALIDATOR:			
	Print/Type Authenticator Name	Authenticator Signature	Date
ACCEPTANCE/RECEIPT:			
	Print/Type Receiver Name	Receiver Signature	Date

Submit to: **Connie.Bates@inl.gov** or **fcrddms@inl.gov**

Appendix E
FCT Document Cover Sheet

Name/Title of Deliverable/Milestone	Natural System Evaluation and Tool Development – FY11 Progress Report (M21UF034004)
Work Package Title and Number	FTSN1UF0340 Generic Natural System Evaluation
Work Package WBS Number	FTSN1UF0340
Responsible Work Package Manager	Yifeng Wang
	(Name/Signature)

Date Submitted   7/15/2011

Quality Rigor Level for Deliverable/Milestone	☒ QRL-3	☐ QRL-2	☐ QRL-1 ☐ Nuclear Data	☐ N/A*

This deliverable was prepared in accordance with   Sandia National Laboratories

(Participant/National Laboratory Name)

QA program which meets the requirements of
     ☒ DOE Order 414.1   ☐ NQA-1-2000

This Deliverable was subjected to:

☒ Technical Review   ☐ Peer Review

Technical Review (TR)   **Peer Review (PR)**

Review Documentation Provided   **Review Documentation Provided**

☐ Signed TR Report or,   ☐ Signed PR Report or,
☐ Signed TR Concurrence Sheet or,   ☐ Signed PR Concurrence Sheet or,
☒ Signature of TR Reviewer(s) below   ☐ Signature of PR Reviewer(s) below

Name and Signature of Reviewers

Malcolm Siegel   _Malcolm Siegel_

_____   _____

_____   _____

*Note: In some cases there may be a milestone where an item is being fabricated, maintenance is being performed on a facility, or a document is being issued through a formal document control process where it specifically calls out a formal review of the document. In these cases, documentation (e.g., inspection report, maintenance request, work planning package documentation or the documented review of the issued document through the document control process) of the completion of the activity along with the Document Cover Sheet is sufficient to demonstrate achieving the milestone. QRL for such milestones may be also be marked N/A in the work package provided the work package clearly specifies the requirement to use the Document Cover Sheet and provide supporting documentation.

Natural System Evaluation and Tool Development – FY11 Progress Report

Fuel Cycle Research & Development

Executive Summary

The U.S. Department of Energy Office of Nuclear Energy, Office of Fuel Cycle Technology has established the Used Fuel Disposition Campaign (UFDC) to conduct the research and development (R&D) activities related to storage, transportation and disposal of used nuclear fuel and high level nuclear waste. The Mission of the UFDC is

> *To identify alternatives and conduct scientific research and technology development to enable storage, transportation and disposal of used nuclear fuel and wastes generated by existing and future nuclear fuel cycles.*

The work package of natural system evaluation and tool development directly supports the following UFDC objectives:

1. Develop a fundamental understanding of disposal system performance in a range of environments for potential wastes that could arise from future nuclear fuel cycle alternatives through theory, simulation, testing, and experimentation.
2. Develop a computational modeling capability for the performance of storage and disposal options for a range of fuel cycle alternatives, evolving from generic models to more robust models of performance assessment.

The work scope for FY11 includes four major tasks: (1) development of a detailed R&D plan for natural system evaluation and tool development; (2) in-depth analsis of key attributes and new concepts identified in the R&D plan; (3) preliminary demonstration of new modeling and experimental tools; and (4) conceptual design of a databse for natural system evaluation. The work was performed in the collaboration among five national laboratories:

INL: Work on the fuel reprocessing side to support the concept development of the direct disposal of ER salt waste.

LANL: Evluate existing capabilities for modeling fluid flow and transport in fractured media. Evaluate chemical heterogenetity on radionuclide transport in natural systems.

LBNL: Continue in-depth analysis and capability demonstration for simulating thermal-hydrological-mechanical-chemical (THMC) couplings in the near field of a generic clay repository.

LLNL**:** Continue the reversibility and kinetic study of radionuclide sorption on mineral phases and demonstrate experimental capabilities.

SNL: Continue a feasibility study on the direct disposal of electrorefining waste in a salt repository and coordinate all activities related to natural system evaluation and tool development. Perform literature review on radionuclide interaction with clay minerals and formations.

The major accomplishments are summarized as follows:

*   Based on international experience, discrete fracture network simulation is likely to play an important role in any future investigation of a hard-rock site for a nuclear waste repository, either alone or as part of a hybrid continuum/DFN computational strategy. Initial scoping investigations suggest that LaGriT, FEHM, and the unstructured grid particle tracking method could be used in combination to build a prototype simulation capability. In order to model more complex systems with large numbers of fractures, automated workflows need to be developed that interfaces software that generate fracture network realizations, either stochastic or deterministic, with automated mesh generation tools.

- Spatial heterogeneity in K_d has a significant effect on radionuclide breakthough in a natural system. The appropriate treatment of K_d in a performance assessment context depends on the spatial correlation length relative to the length of the transport path. If the correlation length is short relative to the length of the transport path, then the effective upscaled K_d approximates the mean K_d. In this situation, a constant K_d equal to the mean K_d gives good results. Conversely, if the correlation length is long compared to the travel distance, then K_d is essentially an uncertain parameter. Substituting parametric uncertainty for spatial variability could lead to significant overestimation of peak of the mean radionuclide discharge into the biosphere.

- A comprehensive review was conducted on radionuclide interactions with clay minerals and clay formations. The review considers how chemical reactions couple with the geomechanical compaction under conditions relevant to nuclear waste disposal. From a geochemical perspective, the degree of compaction ranges from the single clay particle or dilute suspensions up to heavily compacted clay columns. This range of systems allows for a broad range of chemical variability based on the degree of particle-particle interaction even though the chemistry of the solid phase may be consistent throughout. The review discusses the interfacial chemistry in physically restrictive environments and its implications radionuclide sorption to clays. A comprehensive list of K_d values and diffusion coeficients of radionuclides and heavy metals in various clay formations is complied.

- Research has been performed on the behavior of aqueous Pu(IV) and intrinsic Pu(IV) nano-colloids in the presence of goethite at 25 and 80°C and over a range of concentrations from undersaturated to oversaturated with respect to PuO_2(am, hyd). The strong affinity of aqueous Pu(IV) for the goethite surface is explained by the epitaxial growth of bcc Pu_4O_7 nano-colloids on goethite. The behavior is affected minimally by temperature. This strong affinity cannot be achieved when intrinsic Pu(IV) nano-colloids are reacted with goethite over 103 days. The results indicate that the fate of Pu is dependent on its initial form and its subsequent stability under changing geochemical conditions. Both intrinsic colloids and those sorbed to goethite have the potential to be transported with groundwater. This work has been extended to examine the behavior of aqueous Pu(IV) and intrinsic Pu(IV) nano-colloids and interaction with clay mineral montmorillonite.

- Geomechanical modeling of the DRZ requires the consideration of the effects of fractures on the constitutive relationship between stress and strain. A new constitutive relationship, relating stress and strain for fractured porous rock, that accounts for the different geomechanical behavior of fractures and the general rock mass was developed in FY10. The new constitutive relationship has been extended here to address anisotropic stress conditions. Furthermore, the model development has also been advanced to describe the functional dependence of porosity and bulk compressibility on stress. Several comparisons with laboratory data on the mechanical response of clay, shale, and other rock types have shown that the nonlinearity introduced by the new constitutive model is needed to reflect the observed behavior.

- Experimental work on saturated and unsaturated flow through clay shows significant deviations from the traditional Darcy's law relationship between flux and the hydraulic gradient. A new constitutive relationship for unsaturated flow through clay, based on a non-Newtonian flow process, was developed. This leads to a nonlinear relationship between flux and the hydraulic gradient, and a new relationship between hydraulic conductivity and pore size. These results were used to develop a revised relationship between capillary pressure and relative permeability. The new constitutive relationships are fundamentally different from traditional relationships for saturated and unsaturated flow in porous media. Comparisons with data show that the new constitutive relationships are consistent with experimental observations of unsaturated flow through a compacted sand-bentonite mixture.

- The TOUGH-FLAC thermal-hydrological-mechanical code was updated to include the new stress-strain constitutive model. The code was used to model rock-mass deformation and pore

pressure around an underground excavation, using published hydromechanical parameters and boundary conditions determined for the Opalinus Clay, Switzerland. A Gouy-Chapman diffuse-double layer model for geochemically induced swelling and shrinkage was implemented in the TOUGHREACT thermal-hydrological-chemical code. The model simulation shows that geochemical conditions, such as ion concentration and exchangeable cation compositon, can affect clay swelling.

- To further test the concept of direct disposal of ER salt in a salt repository, experimental techniques were developed for characterizing microstructure of ER salt and testing the stability of ER salt in a repository environment. A process for making surrogate ER salts of various compositions was developed. The surrogate salts have been characterized for their microstructures with XRF and SEM. The microstructural analysis reveals that phase separation appears to occur in the ER salt – a good indicator for microphase encapsulation of radionuclide by a salt matrix. Iodine tends to bond cesium in the salt. Dissolution experiments for fine surrogate ER salt particles have been performed, which showed that the contacted solution quickly reached the solubility of salt. Removing LiCl from the salt may not reduce its solubility limit or dissolution rate. A technique for making surrogate ER salt pellets was developed using room temperature mechanical pressing. The pellets with various ratios of NaI to NaCl were made for studying the efficacy of radionuclide encapsulation by salt. A preliminary test indicates that the obtained pellets seem to remain structurally intact during the dissolution experiment with WIPP brines. Due to its effectiveness, the developed pressing technique can potentially be used for densification of ER salt if needed.

- International collaboration has been considered to be essential for many research topics. Potential areas and approaches for such collaboration were identified.

All the FY11 activites will be continued in FY12. The FY12 will be expanded to include the following three research topics, which have been identified to be in high priority in the R&D plan:

- **Topic S2:** Disposal concept development for natural systems. The work will define a generic set of key parameters (e.g., lithology, water chemistry) for natural system studies.
- **Topic S3:** Disposal system modeling. The work will develop a comprehensive subsystem model for natural system performance evaluation. This subsystem model will be used for integration and prioritization of relevant natural system evaluation activities.
- **Topic S4:** Development of a centralized technical database for natural system evaluation.

Table of Contents

List of Figures

List of Tables

Chapter 1: Natural System Evaluation and Tool Development: Scope and Approach

1.1   Objectives

The U.S. Department of Energy Office of Nuclear Energy, Office of Fuel Cycle Technology has established the Used Fuel Disposition Campaign (UFDC) to conduct the research and development (R&D) activities related to storage, transportation and disposal of used nuclear fuel and high level nuclear waste. The Mission of the UFDC is

> *To identify alternatives and conduct scientific research and technology development to enable storage, transportation and disposal of used nuclear fuel and wastes generated by existing and future nuclear fuel cycles*.

The work package of natural system evaluation and tool development directly supports the following UFDC objectives:

- Develop a fundamental understanding of disposal system performance in a range of environments for potential wastes that could arise from future nuclear fuel cycle alternatives through theory, simulation, testing, and experimentation.
- Develop a computational modeling capability for the performance of storage and disposal options for a range of fuel cycle alternatives, evolving from generic models to more robust models of performance assessment.

The natural system is an integral part of a geologic nuclear waste repository. Spatially, it extends from a so-called disturbed rock zone (DRZ), created by mechanical, thermal and chemical perturbations due to underground excavation or waste emplacement, to the surrounding geologic media, and continues all the way to a specified repository boundary. The natural system evaluation and tool development work package supports all four stages of geologic repository development: site screening, site selection, site characterization, and site suitability study.   The information collected in this work package will play a pivotal role in site screening and site selection.

From the well-accepted multiple barrier concept for waste repository safety, each barrier is supposed to be utilized for its safety function independently to the optimal extent. In this sense the natural barrier needs to be evaluated and necessary research conducted to ensure its optimal safety function. From repository-design point-of- view, an appropriate balance must be maintained between the natural system and the engineered barrier system (EBS) in the contribution to the total system performance. In practice, there is a risk to placing too much reliance on the engineered barrier while not fully taking credit for the natural system. Such practice often results in an overly conservative, very expensive EBS design. Thus, as one of its main objectives, the natural system evaluation and tool development package will ensure that sufficient research will be conducted to fully exploit the credit that can be taken for the natural system barrier.

The UFDC is currently evaluating the viability of mined repositories in various geologic media (i.e., salt, clay, granite) as well as deep borehole disposal in crystalline rocks. Given the generic nature of this work, the R&D activities formulated in this planning document will focus on general tool development, generic

data collection, and enhanced understanding of geologic media and processes involved in waste disposal through integrated modeling, laboratory and field work. Models and methods for improved understanding can be developed without site-specific data from an actual site considered for disposal in the U.S. Data from representative geologic environments (salt, clay/argillites/shale, and crystalline rock) obtained through international collaboration and literature search can potentially be used for the generic R&D, to ensure that the models and methods work for the desired purpose. The tools to be developed will include (1) numerical models and modeling tools, (2) experimental techniques and field-testing capabilities that can be used for validating the models, and (3) technical data that are needed to support simulations.

In FY11, we developed a comprehensive R&D plan for natural system evaluation and tool development (Wang, 2011). This plan has laid out major R&D activities and approaches for the next five years. The plan serves as guidance for the effective integration of the related activities and for the close coordination with other UFDC work packages. Note that the UFD R&D is a mission oriented program. The activities related to the natural system evaluation and tool development need to directly support future site screening, site selection, site characterization and site suitability study. The R&D plan will ensure that all related work will be conducted towards this goal.

1.2   Research Scope

Based on *Used Fuel Disposition Campaign Disposal Research and Development Roadmap* (Nutt, 2011), a R&D plan for Natural System Evluation and Tool Development was developed (Wang, 2011). The plan identifies 27 key R&D topics. These topics are divided into 2 levels: the system level and the process level.

System level R&D topics:

Topic #S1
Title: Evaluation of potential impacts of disposal options on fuel cycles
Description: The DOE is now reconsidering its nuclear waste disposal policy and re-evaluating alternative options to the current once-through open fuel cycle. This policy shift creates a unique opportunity for exploring new concepts and ideas that can potentially lead to the development of transformational technologies for an efficient and clean nuclear fuel cycle. The choice of waste disposal environments may potentially impact the development of upstream processes of the fuel cycle. Such impacts have not been fully explored and evaluated. This research topic will focus on new concept development. Specific activities will include:
- Comparative study of different disposal environments
- Identification and evaluation of potential impacts of different disposal environments on waste separation and waste form development.

Topic #S2
Title: Disposal concept development – Natural system
Description: As explicitly identified in the UFDC R&D roadmap (DOE, 2011), there is a need for developing a range of generic disposal system design concepts. This research topic will support the overall UFDC effort on the development of disposal system design concepts by cataloging possible combinations and geometries of both host rock and far-field media (e.g., mineral and chemical compositions, physical dimensions, hydrologic properties). The task will define a generic set of key parameters (e.g., water chemistry) for other UFDC activities. Specific activities will include:
- Literature review

- Concept development

Topic #S3
Title: Disposal system modeling – Natural system
Description: Disposal system modeling is crucial for the whole life cycle of repository development. Such modeling tools will be essential for management decisions on project priority and resource allocation. This research will serve two purposes: (1) supporting the development of the Generic Disposal System Environment (GDSE) models as well as the development of higher-fidelity performance assessment models, and (2) developing a comprehensive subsystem model for natural system performance evaluation. The subsystem model will include (1) detailed thermal-hydrologic-mechanical-chemical process models (with appropriate levels of fidelity) for flow field and radionuclide transport calculations and (2) probabilistic performance assessment capabilities. This subsystem model will be used for integration and prioritization of relevant natural system evaluation activities. Specific activities will include:

- Selection of flow and radionuclide transport codes
- Improvements to the selected codes
- Wrapping the selected process codes with a Monte-Carlo simulation tool
- Performing Monte-Carlo simulations for the evaluation of natural systems.

Topic #S4
Title: Development of a centralized technical database for natural system evaluation
Description: Given the quantity of data already accumulated through various repository programs and also the data to be collected from the UFDC R&D activities, it is essential for future repository development to archive and categorize these data in an appropriate manner so that they can be easily accessible to UFDC participants and has appropriate quality assurance enforced. This task will focus on the database development for natural system evaluations. The data to be collected will include thermodynamic data for radionuclide speciation and sorption, groundwater chemistry, hydraulic and mechanical property data, mineralogical and compositional data of representative host and far-field media, spatial distributions of potential host formations, etc. To support site screening and selection, there is a need to develop tools for spatial data analysis and visualization (e.g., a geographic information system). Specific activities will include:

- Collection of user requirements
- Database design
- Data collection and database population
- Maintenance of database.

Topic #S5
Title: Evaluation of state-of-the-art of site characterization techniques
Description: Site characterization techniques evolved and improved both in the U.S. and other nations as geologic repository programs progress. Advances both in the disposal science and other geotechnical fields (e.g., oil and gas industry, mineral mining, geothermal exploration, and carbon sequestration) may lead to improved site characterization techniques that could be applied to future site characterization efforts. This activity will evaluate and identify potential field survey techniques that may prove useful for site characterization. The effort will be equally divided into four areas: geophysical techniques, geochemical techniques, hydrological testing techniques, and rock mechanics techniques. Specific activities will include:

- Literature review
- Gap analysis
- Recommendations for future technique development

Topic #S6
Title: Development and demonstration of geophysical techniques for site characterization
Description: Existing non-invasive geophysical techniques are adequate for characterizing large-scale subsurface features and physical properties, but continued advances could help achieve high-resolution images of time-varying properties and structural changes that may be important during the site selection or characterization stages. For example, high-resolution seismic imaging of subsurface faults under development for oil and gas exploration purposes could advance to the point where sub-meter sized features can be more easily resolved and high-angle (near vertical) reflectors can be directly imaged. Similarly, advances in seismic imaging could allow the direct detection of fluids and their migration through fractures. Laboratory experiments and waveform modeling approaches could be pursued to develop and test new seismic methods for fluid monitoring. Strategies may be needed to integrate multiple geophysical techniques to optimize information gathering in host-rock and geologic environments. This task will focus on the development of new geophysical techniques that can provide unprecedented high spatial resolutions. Specific activities will be formulated based on the results from Topic #S5.

Topic #S7
Title: Identification of the needs for using Underground Research Laboratories (URLs)
Description: Underground research laboratories (URLs) could be used to conduct experiments designed to address non-site-specific issues. Experimental activities conducted in URLs (and operations-related surface facilities) could potentially help improve public confidence through demonstrating fundamental understanding of disposal and operational concepts. If the U.S. foregoes repository siting for an extended period of time, studies in a domestic URL could help maintain repository development expertise. However, there may be reasons (e.g., cost) not to develop URLs in the U.S. unless they are in geologic media where one does not currently exist elsewhere. Domestic R&D needs could potentially be met by gaining access to URLs in other countries working in relevant geologic media through collaborative studies and experiments. This research topic will identify potential areas in which the UFDC can benefit the most from international collaboration on the URL research. Specific activities will include:
- Identification of the needs for URLs
- Formulating URL development strategy, especially the international collaboration approaches.

Topic #S8
Title: Natural analogue studies
Description: Natural analogues such as uranium deposits preserve information about physical and chemical processes that may be relevant to nuclear waste isolation in a geologic repository. This information could be useful for repository performance assessment model validation and confidence building. Natural analogues are also needed to identify potential effects of geologic processes that may be relevant to waste disposal. Identification of such processes is critical for site screening. Current hydrogeologic modeling practices tend to assume that the system will be static other than changes induced by the repository itself. This is an assumption that needs to be investigated and analogues are the best way for testing this assumption. In a study of analogues for argillaceous rock, a variety of geologic processes have been found that can significantly affect flow and transport pathways through otherwise very low permeability materials. Specific activities will include:
- Literature review
- Systematic evaluation of the uses of natural analogue data for repository development
- Data compliation and synthesis

Topic #S9
Title: Testing and modeling to support evaluation of direct salt disposal option for electrorefiner salt

Description: To properly evaluate the direct disposal option for electrorefiner (ER) salt, the stability of the ER salt needs to be well understood with respect to conditions it will likely be exposed to in a salt repository. In addition, if treatment methods applied to the salt can make it more stable for disposal, that approach also needs to be explored and characterized. This does not include adding material to form a new phase (waste form). Rather it involves thermal treatments that can lead to new phases forming from existing material and possible segregation of the salt based on composition.

This project is proposed to include the following phases.

- Establishing baseline
- Treatment technology and benefits
- Salt characterization (compositions, microstructures, and leaching rates)
- Source term model development
- Implications to waste transportation.

The first three phases are aimed at delivering all of the information needed to complete the fourth and fifth phases.

Process-level R&D topics:

Topic #P1

Title: Development of discrete fracture network (DFN) model

Description: There is a need to develop improved modeling tools to represent fractures or fracture sets as discrete features. Experience in Sweden and Finland suggests that DFN models offer advantages over continuum models for sparsely fractured media such as fractured crystalline basement rock, especially when fracture networks or network statistics are well characterized. There is also a need for DFN studies for argillaceous host rock in the disturbed rock zone (DRZ). DFN modeling capability would provide an alternative to continuum codes and would also be invaluable for numerically determining effective parameters for use in existing continuum codes. This task will develop a DFN code for modeling multiple-scale, three-dimensional fracture networks. The specific activities will include:

- Review of state of the art of DFN model development
- DFN code development
- Code verification and validation
- Code demonstration

Topic #P2

Title: Parameter estimation and uncertainty quantification of field testing

Description: Parameters used in the assessment of groundwater flow and radionuclide transport in saturated media are determined from a wide range of laboratory and field-scale testing. Laboratory measurements are generally conducted under controlled conditions and the uncertainty for parameters from these experiments related to instrumental errors is relatively small. In contrast, field testing such as hydraulic testing in fractured media and tracer testing in the subsurface is analyzed with imperfect knowledge of the hydrogeological system at depth. Consequently, there are often issues of nonuniqueness and significant uncertainties in the parameter values derived from this testing. In the past these uncertainties typically have been evaluated using simple statistical analyses or professional judgment for propagation to total system performance assessments. This task will assess the use of advanced methods in parameter estimation and uncertainty analysis in the interpretation of field testing in saturated media. The task will also address the issues related to flow localization and the associated diffusion into immobile water. Specific activities will include:

- Literature review of state of the art in hydrologic parameter estimation
- Formulation of new techniques (e.g. new optimization techniques)

- Demonstration of new techniques.

Topic #P3
Title: Development of a new theory for preferential flow in unsaturated porous media
Description: Groundwater recharge associated with the unsaturated zone is an important factor for characterizing any repository site and for evaluating its performance. Because thermal effects, multiphase-flows (similar to unsaturated flow) may also occur near the drift in the host formation of a given repository. Preferential flow is a common flow mechanism in the unsaturated zone and has been described as one of the most frustrating processes in terms of hampering accurate predictions of flow and transport in the unsaturated zone, as a result of its complexity. This work attempts to apply an optimal principle (that water flow resistance is minimized for the entire flow domain) to steady-state unsaturated flow processes as the optimality principles have been successfully used in other areas. Specific activities will include:

- Formulation of new preferential flow model
- Comparison of model results with laboratory measurements of fingering flow (available in the literature) and the existing models.

Topic #P4
Title: Investigation of water movement and transport in low permeability media (clay formations)
Description: Low permeability geologic formations such as clay formations are considered as effective media for waste isolation. Understanding water movement in such media is crucial for the performance assessment of a waste isolation system. It was recently discovered that water advection and chemical diffusion in low-permeability media may not follow traditional linear laws such as Darcy's law and Fick's law. This task will systematically study water flow regimes and their transport behaviors in clay formations as a function of clay formation texture and pore geometry. New methodologies will be developed for modeling these non-traditional flow and transport behaviors. Specific activities will include:

- Selection and characterization of clay samples
- Experimental testing of flow regimes in clay samples
- Experimental testing of diffusion regimes in clay samples
- Development of modeling capabilities
- Prediction of water movement and chemical species diffusion in clay formations

Topic #P5
Title: Investigation of water movement and transport in low permeability media (salt formations)
Description: Low permeability geologic formations such as salt beds are considered as effective media for waste isolation. Understanding of water movement in such media is crucial for the performance assessment of a waste isolation system. Significant gaps exist in predicting moisture movement along salt grain boundaries under stress and temperature gradient. This task will establish constitutive relationships for moisture movement in the near-field of a salt repository through laboratory analysis, field testing and modeling. Specific activities will include:

- Experimental testing of water movement in consolidated salt
- Experimental testing of chemical species diffusion in salt
- Development of modeling capabilities
- Prediction of water movement and chemical species diffusion in salt formations.

Topic #P6
Title: Investigation of water movement and transport in deep borehole disposal environments

Description: In the deep borehole disposal concept, high level nuclear waste will be emplaced in the depth interval of 3 to 4 km below the surface, based on the premise that water movement at that depth would be minimal. Characterization of water flow in such environments is a technical challenge. This task will first collect relevant information of deep ground water movement and formulate a strategy for developing field characterization strategies for deep borehole disposal. The information to be collected will include those obtained from continental drilling programs. The task will then focus on the development of novel techniques for characterizing deep ground water movement (e.g., using isotopic signatures). Specific activities will include:

- Literature review on water movement in deep subsurface environments
- Development of novel techniques for deep ground water movement
- Extending the existing groundwater flow models to deep subsurface environments.

Topic #P7

Title: Novel in-situ techniques for groundwater chemistry characterization

Description: An understanding of the repository far-field geochemical system is critical to understanding repository performance. Geochemical conditions and the characteristics and composition of the ground water in the repository far field govern the mobility and solubility of radioactive elements. In addition, the chemistry of water flowing from the far field into the near-field environment is an important control on the near-field chemical environment, which, in turn, affects engineered barrier degradation rates. There is a need for developing chemical sampling techniques to characterize initial fluid composition in shale and salt. This activity will explore and develop novel techniques for characterizing groundwater chemistry. The emphasis will be given to the techniques that can provide fast, accurate, in-situ and high spatial resolution measurements (e.g., in boreholes) with minimum human perturbations. The techniques that can characterize flow localization and the associated chemical heterogeneity is particularly of interest. Specific activities will include:

- Literature review
- Development of high resolution in-situ characterization techniques
- Field demonstration of new techniques

Topic #P8

Title: Reactive transport modeling of groundwater chemistry evolution and radionuclide transport

Description: This task will aim at improving the existing reactive transport modeling tools for simulating groundwater chemistry evolution and radionuclide migration along the flow path from the DRZ, to the far field and ultimately to the boundary of a repository. Radionuclide transport modeling remains a computationally challenging task. Except for the extreme situation of diffusion-dominated conditions, transport models are more sensitive than flow models to numerical grid effects and small-scale heterogeneity. Relatively fine grids are needed to avoid numerical dispersion when traditional finite-difference or finite-element methods are employed. Multiple radionuclides linked through decay chains need to be considered, and the simulation time steps are thus limited by the most mobile (least retarded) radioelement. In addition, transport modeling to assess geosphere performance typically requires parametric uncertainty to be addressed, which places a premium on fast execution time of modeling codes. This task will focus on the following improvements to the existing reactive transport modeling capability:

- Incorporation of interfacial reactions (e.g., surface complexation), microbially-mediated reactions, colloid-facilitated transport, and radionuclide decay and ingrowth
- Improved representation of spatial heterogeneity of chemical and transport properties
- Coupling of radionuclide transport with evolving water chemistry along a transport pathway (e.g. alkaline plumes)

- Robustness of numerical algorithms for coupling chemical reactions with solute transport
- Explicit consideration of structural complexity of the media in the solute transport (e.g.the fracture-matrix system in DRZ or the micro, macro-pores system for host clay rock)

Topic #P9
Title: Evaluation of the effects of spatial heterogeneity on radionuclide transport
Description: Some key parameters that control radionuclide transport in natural system generally vary spatially. Existing repository performance assessments try to capture this variability with model input parameter uncertainty, which inevitably lead to a significant overestimate of total radionuclide release. This task will develop modeling capabilities to capture the effects of the spatial heterogeneity (e.g., K_d values) on radionuclide transport in natural systems. The work will include two parts: the modeling capabilities for realistic representation of spatial heterogeneity and the experimental technique for quantification of this heterogeneity. The work will significantly reduce both the predicted total radionuclide release from a repository and the associated uncertainty through improved performance prediction of the natural barrier system. Specific activities will include:
- Representation of spatial heterogeneity in reactive transport models
- Development of characterization techniques for quantification of spatial heterogeneity
- Model validation and demonstration.

Topic #P10
Title: Better understanding of radionuclide interaction with geomedia
Description: As they move through the natural system, radionuclides released from the engineered barrier will experience a complex set of physical and chemical interactions with the geologic media. Existing models generally assume that radionuclide retention in the natural system could be described with a linear, equilibrium K_d approach. The reality may be much more complex. This task will develop key experimental techniques and modeling tools in the following areas:
- Thermodynamics and kinetics of radionuclide sorption onto or desorption from representative mineral substrates (e.g. different clay minerals)
- Radionuclide behaviors in high rock/water ratio environments, especially in nanopores and interlayers
- Coupling of redox reactions with radionuclide sorption
- Complexation of radionuclides with natural organic matter
- Radionuclide sorption in the presence of competing species, high ionic strength media, or at elevated temperatures
- Extrapolation from simple system measurements to complex systems
- Radionuclide transport in low permeability media (e.g., membrane effect of clay formation).

Topic #P11
Title: New perspective of colloid-facilitated radionuclide transport
Description: Colloid facilitated transport (CFT) may have been overestimated in previous performance assessments because many aspects of CFT are not well constrained, thus making pessimistic bounding assumptions necessary. CFT is also an important issue for confidence building of a performance assessment model. Important uncertain processes and parameters associated with CFT include: desorption processes and rates, colloid immobilization processes and associated parameters, the degree to which colloids behave as heterogeneous populations in the subsurface, the role of chemical and flow transients in mobilizing and immobilizing colloids, and colloid generation processes. This task will focus on two key aspects of the CFT: (1) colloid particle formation and transport in porous geologic media and (2) radionuclide partitioning among pore water, colloid particles, and stationary substrates. In recent

years, much progress has been made in nanoscience and nanotechnology. Such progress allows re-examining CFT in a new perspective, for example, understanding the size dependence of particle surface chemistry and radionuclide sorption capability. This work will involve laboratory measurements, model development, and field testing. Novel in-situ colloid characterization techniques will be explored. Specific activities will include:

- Literature review
- Better understanding colloid-radionuclide-stationary mineral phase interactions
- Development of novel in-situ techniques for characterizing CFT
- Development of modeling capabilities for simulating CFT.

Topic #P12

Title: Upscaling of key hydrological and geochemical parameters

Description: It is known that some key parameters (e.g., dispersion coefficient, matrix diffusion coefficient) controlling radionuclide transport in geologic media are scale-dependent. Capture of this scale dependence is crucial for predicting radionuclide transport in a geologic repository environment. This task will systematically evaluate the existing techniques for upscaling key hydrologic and geochemical parameters, identify the gaps in upscaling, and develop new methodologies for bridging the identified gaps. The parameters of interest include matrix diffusion coefficients, sorption coefficient, chemical reaction kinetics, etc. The laboratory and field experiments of various scales will be explored for conceptual model development and validation. Specific will activities include:

- Literature review on hydrological and geochemical upscaling
- Data collection and multiple scale testing
- Model development for hydrological and geochemical upscaling.

Topic #P13

Title: Evaluation of biological processes

Description: Transport of dissolved radionuclides in the host rock and other geologic units is affected by microbial activity in the host rock and other geologic units (non-host-rock). The effects of biological processes include the formation of complexants, the formation of microbial colloids, the biodegradation of organic compounds, and the bioaccumulation of radionuclides. Similar to purely inorganic complexants, there is a potential for enhanced transport of radionuclides associated with organic complexants. There are fundamental gaps in the methods of characterizing biological processes and their effects on the repository system, and fundamental gaps in available data. This activity will develop better techniques for quantifying microbial activity in a subsurface environment and improve the existing methodology for evaluating microbial impacts on water chemistry and radionuclide transport. Specific activities will include:

- Literature review
- Development of new techniques for characterization of microbial activity in subsurface environments
- Upgrading the existing biogeochemical modeling capability for evaluating microbial activity and its impact on radionuclide transport.

Topic #P14

Title: Technical basis for thermal loading limits

Description: The repository thermal loading limits are of concern for thermal-mechanical effects on the host rocks and the other geologic units of the geosphere. Thermal expansion, tensile and compressive stresses, and altered properties of fractures, faults, and the rock matrix are possible. There can also be thermal-chemical alteration of the host rocks and the other geologic units, including, mineral

precipitation, dissolution, alteration of minerals with attendant volume changes, and altered properties of fractures, faults, the rock matrix, and the formation of near-field chemically altered zones (rind). This task will systematically examine the technical basis for the thermal limits of various disposal media (i.e., the maximum wall temperature allowed). Specific activities will include:
- Literature review
- Examination of technical basis for thermal limits of various disposal media, including certain thermal-hydrologic-mechanical-chemical calculations.

Topic #P15

Title: Modeling of disturbed rock zone (DRZ) evolution (clay repository)

Description: There is a need for improved understanding and representation of the evolution of disturbed rock zone characteristics as a result of thermal-mechanical-hydrological-chemical changes in clay environments, including the coupled evolution of near-field host rock and any backfill/buffer materials that would be used in the design of the repository. This task will address the following specific issues associated with the DRZ:
- Improved methods for representing the complex coupling of processes (physical, chemical, thermal, mechanical), including the coupling of the engineered and natural systems
- Improved methods for representing near- and far-field interface chemistry (perturbation & transient phenomena, repository operation, thermal effect)
- Quantifying gas generation and representing potential impacts (gas displacement and leakage)
- Evaluating the effects of excavation and ventilation-induced fracturing in clay/shale environments
- Better understanding of fracture initiation and healing (re-compaction as a function of environment)
- Improved understanding of heterogeneity and anisotropic properties in the DRZ and their impacts
- Evaluating the potential for the development of fast transport pathways that could bypass the natural or engineered system and associated impacts
- Development of model tools for capturing these processes/issues mentioned above.

Topic #P16

Title: Modeling of DRZ evolution (salt repository)

Description: Evolution of the DRZ in salt is very sensitive to the stress state and exhibits steep transient deformation behavior that evolves into steady-state deformation. This behavior can be understood in terms of plastic dislocation mechanisms in salt crystals. Hence, creep closure of underground openings in salt at ambient temperature can be understood at a mechanistic level. Based on studies at WIPP, the nature of the DRZ can be adequately described for engineering and analysis purposes in terms of stress invariants, which is conducive to finite element calculations. Long-term behavior including healing can be assessed by tracking the stress state within the structural calculation. For the long-term disposal of high level wastes, a better understanding of rock salt creeping and fracture sealing around the DRZ at elevated temperatures and in the presence of moisture is required. This work will develop the needed tools for testing and simulating salt repository room closure, salt creeping and fracture healing in the presence of moisture at elevated temperatures. Specific activities will include:
- Literature review
- Laboratory and field testing on salt creeping and fracture healing
- Model simulation and data integration.

Topic #P17

Title: Modeling of DRZ evolution (deep borehole disposal)

Description: For deep borehole disposal, simulation of multi-borehole arrays should be undertaken for a system consisting of 10 to 100 individual boreholes. Such investigations could evaluate the potential for communication between boreholes, thermal or hydrologic interactions, and large-scale responses to

borehole arrays. Performance assessments are needed to establish a better sense of the potential performance variability that might be expected in multiple implementations of borehole disposal fields. This activity will simulate the coupled thermal-hydrological-mechanical-chemical processes around a single borehole and multiple boreholes as well. Specific activities will include:

- Literature and data collection
- Thermal-hydrological-mechanical-chemical calculations.

Topic #P18

Title: In-situ testing of DRZ development

Description: In situ testing could prove quite valuable for proof-of-principle testing. A field test provides an opportunity to observe anticipated phenomenology, validate modeling capabilities, and fine tune design options. This task will focus on full-scale heating testing for the DRZ evolution in both salt and clay repositories. In-situ testing will confirm the predictive ability of repository models and provides a range of expected parameters and rock mass response. Full-scale heater tests will determine:

- Extent and properties of the disturbed zone
- Fracture healing characteristics
- Changes in permeability and porosity
- Thermomechanical response of compacted backfill
- Water migration and influx rates (where applicable)
- Moisture behavior (e.g., partial vapor pressure)
- Compositional changes; all for heated conditions representative of repository conditions.

1.3 Approaches

System point of view: Reconsideration of nuclear policy and waste disposal options provides a unique opportunity for evaluating the potential impacts of the choice of waste disposal option on the overall fuel cycle. A good example for this is the concept of direct disposal of electrorefiner salt in a salt repository (Wang et al., 2011). Preliminary study has shown that this concept can potentially simplify waste separation and waste form development. Therefore, the natural system evaluation should be consciously coordinated with UFDC and FCT activities to maximize its impact on the overall fuel cycle development. Close coordination of natural system evaluation with other UFDC work packages is essential for the success of this work.

Tools & multiple applications: The tools and capabilities to be developed for natural system evaluation include four integral components: technical data, modeling tools, laboratory techniques, and field observation techniques. An appropriate balance among the four components must be carefully determined in terms of allocation of resources. Given the generic nature of this research, all research topics focus on general tool development and non-site specific data collection. For model development, it should be noted that multiple fidelity models may be needed for different applications, ranging from support of simple decision-making to an ultimate comprehensive license application. The tools to be developed should be able to meet this need.

Data management & quality assurance (QA): During last few decades, a large quantity of technical data has been accumulated through various repository programs or other programs. It is important to ensure that each natural system evaluation activity to fully leverage the existing data. The development of a centralized technical database is a key component for knowledge management.

To ensure that key technical data collected in this work package are usable or recoverable for various future applications, it is imperative that each research activity formulated above must enforce an appropriate level of quality assurance (QA). For example, materials and solutions (e.g., clays) used for testing at different laboratories should be standardized for testing result comparisons.

International collaboration: International collaboration is essential for success of many of the research research topics identified.   Actual international collaboration will be carried out in individual research topic areas, and the funding levels may need to adjust as needed.

1.4   Mapping of FY11 Activties to the R&D Research Topics

The work scope for FY11 includes four major tasks: (1) development of a detailed R&D plan for natural system evaluation and tool development; (2) in-depth analsis of key attributes and new concepts identified in the R&D plan; (3) preliminary demonstration of new modeling and experimental tools; and (4) Conceptual design of a databse for natural system evaluation.   The work was performed in the collaboration among Idaho National Laboratory (INL), Los Alamos National Laboratory (LANL), Lawrence Berkeley National Laboratory (LBNL), Lawrence Livermore national Laboratory (LLNL) and Sandia National Laboratories (SNL):

INL: Work on the fuel reprocessing side to support the concept development of the direct disposal of ER salt waste.

LANL: Evaluate existing capabilities for modeling fluid flow and transport in fractured media. Evaluate chemical heterogenetity on radionuclide transport in natural systems.

LBNL: Continue in-depth analysis and capability demonstration for simulating thermal-hydrological-chemical-mechanical (THCM) couplings in the near field of a generic clay repository.

LLNL**:** Continue the reversibility and kinetic study of radionuclide sorption on mineral phases and demonstrate experimental capabilities.

SNL: Continue a feasibility study on the direct disposal of electrorefining waste in a salt repository and coordinate all activities related to natural system evaluation and tool development. Perform literature review on radionuclide interaction with clay minerals and formations.

A summary of the work plan and the mapping of on-going activities are provided in Table 1-1.

Table 1.1 Summary of Research Topics for Natural System Evaluation & Tool Development

R&D topic	Decision point supported					Nature of R&D
	Overall fuel cycle	Site screening	Site Selection	Site characterization	Site suitability	
S1: Evaluation of potential impacts of disposal options on fuel cycles	X	X				Concept development
S2: Disposal concept development – Natural system	X	X	X	X	X	Concept development
S3: Disposal system modeling – Natural system	X	X	X	X	X	Modeling (developing integration & decision tools); data collection; process understanding
S4: Development of a centralized technical database for natural system evaluation	X	X	X	X	X	Data collection & archive (knowledge management)
S5: Evaluation of state of the art of site characterization techniques			X	X	X	Review
S6: Development and demonstration of geophysical techniques for site characterization			X	X	X	Field technique development & demonstration
S7: Identification of the needs for using Underground Research Laboratories (URLs)			X	X	X	Review
S8: Natural analog studies		X	X	X	X (Confidence building)	Data collection
S9: Testing and modeling to support evaluation of direct salt disposal option for electrorefiner salt	X	X	X	X	X	Laboratory testing, data collection, modeling
P1: Development of discrete fracture network (DFN) model			X	X	X	Modeling; data collection; field testing
P2: Parameter			X	X	X (Reducing	Modeling, field testing

estimation and uncertainty quantification of field testing				(Reducing uncertainty)	uncertainty)	
P3: Development of a new theory for preferential flow in unsaturated porous media		X	X	X	Modeling; data collection
P4: Investigation of water movement and transport in low permeability media (clay formations)		X	X	X	Modeling, lab experiments
P5: Investigation of water movement and transport in low permeability media (salt formations)		X	X	X	Modeling, lab & field testing
P6: Investigation of water and transport movement in deep borehole disposal environments	X	X	X	X	Modeling, data collection, field technique development
P7: Novel in-situ techniques for groundwater chemistry characterization		X	X	X	Technique development; process understanding
P8: Reactive transport modeling of groundwater chemistry evolution and radionuclide transport		X	X (Reducing uncertainty)	X (Reducing uncertainty)	Modeling, data collection; process understanding
P9: Evaluation of the effects of spatial heterogeneity on radionuclide transport		X	X (Reducing uncertainty & total dose)	X (Reducing uncertainty & total dose)	Modeling, characterization technique development; process understanding
P10: Better understanding radionuclide interaction with geomedia	X	X	X (Reducing uncertainty & total dose)	X (Reducing uncertainty & total dose)	Lab experiments, modeling, process understanding
P11: New perspective of colloid-facilitated radionuclide transport	X	X	X (Confidence building)	X (Confidence building)	Modeling, lab experiments, field testing, process understanding

P12: Upscaling of key hydrological and geochemical parameters				X	X	Modeling, lab & field testing, process understanding
P13: Evaluation of biological processes			X	X	X	Technique development, modeling, process understanding
P14: Technical basis for thermal loading	X	X	X	X	X	Modeling, data collection, process understanding
P15: Modeling of disturbed rock zone (DRZ) evolution (clay repository)			X	X	X	Modeling, data collection, process understanding
P16: Modeling of DRZ evolution (salt repository)			X	X	X	Modeling, data collection, process understanding
P17: Modeling of DRZ evolution (deep borehole disposal)			X	X	X	Modeling, data collection, process understanding
P18: In-situ testing of DRZ development			X	X	X	Field testing, data collection

Shaded rows indicate R&D topics that have been partly addressed by FY11 activities.

1.5 Organization of This Document

The major results of FY11 work are summarized in each chapter of this report:

- Chapter 1 defines the work scope for FY11 and the overall natural system evaluation and tool development. (Contributor: SNL – Yifeng Wang)

- Chapter 2 summarizes the status of the initial stages of the DFN software development process related to requirements definition, algorithm design and prototyping (Research Topic P1). (Contributors: LANL - Scott Painter, Carl Gable and George Zyvoloski)

- Chapter 3 is focused on understanding consequences of treating spatially variable K_d as spatially constant (Research Topic P4). (Contributors: LANL - Scott Painter, Shaoping Chu, Zhenxue Dai, and Zhiming Lu)

- Chapter 4 provides a comprehensive review on radionuclide interactions with clay minerals and formations, with emphasis on the transitions of interfacial behavior from a dilute system to a highly compacted system (Topics P2 and P10). (Contributors: SNL- Andy Miller and Yifeng Wang)

- Chapter 5 is focused on the evaluation of the sorption behavior of Pu at elevated temperatures in the presence of relevant minerals and over a range of concentrations that span environmental conditions in the near-field and far-field Research Topics 10 and 11). (Contributors: LLNL - Mavrik Zavarin, Pihong Zhao, Zurong Dai, Susan A. Carroll and Annie B. Kersting)

- Chapter 6 is focused on the development of constitutive relationships for elastic deformation of clay rock, a thermal-hydrologic-mechanical (THM) modeling study and a Thermal-Hydrologic-Chemical (THC) modeling study (Research Topics P4, P8, P15, and P18). (Contributors: LBNL - Hui-Hai Liu, Lianchong Li, Liange Zheng, James Houseworth, and Jonny Rutqvist)

- Chapter 7 documents the experimental technique development for testing the concept of direct disposal electrorefining salt in a salt repository (Research Topics S1 and S9). (Contributors: INL - Michael Simpson; University of Idaho - Michael Shaltry; SNL – Hernesto Tellez, Andy Miller and Yifeng Wang)

- Chapter 8 is focused on idenfiying potential areas for international collaboration. International collaboration has been considered to be essential for many research topics. (Contributor: LBNL – Jens Birkholzer)

- Chapter 9 summarizes the major results of the FY11 work and provides the perspective for FY12. (Contributor: SNL – Yifeng Wang)

1.6   References

Nutt M. (2011) *Used Fuel Disposition Campaign Disposal Research and Development Roadmap,* (FCR&D-USED-2011-000065 REV0), U.S. DOE Used Fuel Disposition Campaign.

Wang Y. (2011) *Research & Development Plan for Used Fuel Disposition Campaign (UFDC) Natural Systems Evaluation and Tool Development*, U.S. DOE Used Fuel Disposition Campaign, May 25, 2011.

Chapter 2: Flow and Transport in Fractured Media –Development of Discrete Fracture Network Models

2.1   Introduction

Relatively impermeable hard rocks such as fractured granite and fractured welded tuffs have been considered previously as potential repository host media. Fractures are ubiquitous in such media and provide the primary migration pathways for radionuclides. Experience has shown that flow and transport in fractured rock is rarely described adequately by uniform or mildy nonuniform isotropic continuum representations (Neuman , 2005) and a range of alternatives to the classical continuum representation have been developed. These alternative approaches may be grouped into three general classes: discrete fracture network representations, complex continuum representations, and hybrid representations.

Discrete fracture network (DFN) models depict the rock mass as an interconnected network of explicitly represented fractures. In the reductionist tradition, the approach implicitly assumes that detailed statistical descriptions of small observable features will, once combined in numerical simulations, lead to understanding of the system as a whole. Networks of fractures are first stochastically generated using a stochastic model derived from site data. A computational mesh is placed on each fracture plane usually ensuring that the mesh on each of a pair of intersecting fractures matches along the intersection. Groundwater flow equations are then solved using this computational mesh. The final step is then to simulate radionuclide transport using the computed flow field, usually by particle tracking. Most large-scale applications do not explicitly mesh the matrix volumes between adjacent fractures. Instead the effects of diffusion into the unrepresented matrix volume are represented (modeled) in the transport step (e.g. Painter et al., 2008). Although DFN simulations have mostly been used in theoretical studies, feasibility of detailed site-specific applications has also been clearly demonstrated (e.g. Cvetkovic et al., 2004, Svensk Kärnbränslehantering , 2011).

Complex continua representations generalize a simple effective continuum representation to account for various flow and transport phenomena. Dual continuum models (Barenblatt et al., 1960; Warren and Root, 1963) represent fractured porous rock as two overlapping and interacting continua. In its most general form (e.g. Duguid and Lee, 1977), known as the dual permeability model, flow and transport takes place in both the fracture and matrix continua while accounting for fluid and solute migration between the two continua in response to pressure and concentration differences. Commonly, flow in the matrix system is neglected relative to flow in the fracture system. In this case, the matrix acts as a non-conductive reservoir for fluid and/or solute storage and the fracture system provides the fluid migration pathways. In this variant, usually referred to as the dual porosity model, fluid and solute flux are proportional to the pressure and concentration differences between the two continua at a given location and time. The dual continuum class of models has also been generalized (Pruess and Narasimhan, 1985; Zyvoloski et al., 2008) to better represent gradients internal to the matrix blocks. In this approach, multiple continua are used to represent matrix processes. Flow between spatially adjacent matrix cells may be included or not represented, depending on the variant.

Regardless of how the matrix/fracture interactions are represented, multiple continuum models originally conceptualized the fracture flow system as having a representative elementary volume (REV) that establishes a spatial scale above which the flow properties become approximately independent of scale. For natural fracture patterns, which often have a broad distribution of fracture lengths, the existence of a classical REV scale may be questionable. Neuman proposed a stochastic continuum approach that does

not require an REV (Neuman, 1987, 2005). In his approach, an effective permeability tensor and other required flow/transport properties are assigned to each grid block in a conventional continuum conceptualization. However, the properties vary from grid cell to grid cell according to a stochastic model. Moreover, the stochastic model is dependent on the size of the grid block. Thus, a different stochastic model is required if the spatial discretization is changed. Parameterization of a stochastic continuum model, which generally requires inverse modeling of multiple pressure interference and solute tracer tests, has been demonstrated at the Apache Leap field site (e.g. Neuman, 2005). The stochastic continuum model may be combined with any of the dual or multiple continuum ideas to represent fracture/matrix interactions.

Hybrid methods adopt a reductionist view similar to DFN models but also use continuum representations for practical computational reasons (e.g. to reduce the overall size of the computational mesh). Hybrid methods fall into two subclasses: nested and upscaled. In nested models, explicit DFN models are used along transport pathways or in other regions where high spatial resolution is required and continuum representations are used in regions that are of less interest. This approach allows for a DFN representation of transport in and near expected transport pathways while still modeling a sufficiently large region to honor natural hydraulic boundary conditions. In upscaled models, explicit DFN representations are constructed and stochastically generated. However, the flow problem is not solved on the full DFN. Instead, the DFN is used to establish, grid block by grid block, equivalent permeability tensors for use in a continuum model. Jackson (2000), Svensson (2001) and Bodros et al. (2007) provide examples of upscaling algorithms for the permeability tensors. Experience with upscaled models for flow has generally been good, but the approach is questionable for transport. Extensions that attempt to recover the transport effects of subgrid velocity variability through stochastic simulation have emerged (Painter et al. 2005) but have not been fully explored.

Experience suggests that it should be possible to model a sufficiently well-characterized site in a variety of ways and that combinations of methods may allow for the most efficient use of available information. Extensive studies by the Swedish Nuclear Fuel and Waste Management Company in support a safety case for a proposed spent fuel repository (Svensk Kärnbränslehantering, 2011) has clearly demonstrated practical utility of hybrid approaches to flow and transport modeling. Given this experience it is likely that DFN and DFN/continuum hybrids will play an important role in future assessments of fractured hard rock sites. However, modern and non-proprietary modeling tools for supporting such assessments and for addressing key unresolved scientific issues are lacking.

This chapter begins to address Topic P1 of the R&D Plan for UFDC Natural Systems Evaluation and Tool Development – Development of Discrete Fracture Models (Wang, 2011; Chapter 1). The longer-term objective is to develop discrete fracture network (DFN) flow and transport modeling capability, which was identified as a capability gap. This chapter summarizes the status of the initial stages of the DFN software development process related to requirements definition, algorithm design and prototyping.

2.2   State of the Art

In order to represent a fractured media for computation of fluid flow and mass transport there are four main steps. First the fractures must be described and characterized quantitatively. This might be explicit descriptions of the shape and orientation of each fracture or it might be statistical and be expressed in terms of distributions. Second, if explicit representations of fractures are required for calculations a computational mesh representation of the fractures must be created that is both representative of the fracture system and compatible with the flow and mass transport numerical model. Third is the calculation of fluid flow that might be done on the explicit fracture network mesh or on some upscaled

equivalent continuum representation. The fourth step is the calculation of radionuclide mass transport using the calculated flow field. In the remainder of this section we focus on the second step, the creation of an explicitly meshed representation of fracture networks.

The last ten years has seen an increase in a number of papers that describe specific implementations of methods to mesh 3D fracture networks. The problem of representing and mesh fracture networks in 2D is not trivial; however, both in terms of computational cost and computational infrastructure, this is a solved problem. Mesh representation in three dimensions still presents difficulties. In the work of Karimi-Fard et al. (2006) constrained Delaunay meshing is employed in 2D using the software Triangle (Shewchuk, 1996) and in 3D TetGen (Si, 2004). In this application a 3D fracture network is constructed with planar fractures but flow is computed on an upscaled continuum. Erhel et al. (2009) develop a method to mesh large stochastically generated fracture networks by prudent modification of the fractures so that undesirable and pathological geometric configurations do not occur. Similarly, a series of recent papers (Mustapha et al., 2009, Mustapha, 2010, Mustapha et al., 2010) outlines methods to mesh fracture networks in 3D with intersecting triangulations. These papers take the approach of modifying the fracture network geometry to create fracture representations that are more easily turned into discrete mesh representations. However, the result is non-planar triangulations, which introduces some difficulties when applying the mesh to some flow and mass transport discretizations.

There are a number of software packages available for characterization, meshing and computations. Some of these are listed and briefly described below.

FracMan, www.fracturedreservoirs.com. Fracture network characterization and generation from observations or statistical representations; meshing of fracture networks and upscaling DFN flow properties to equivalent porous medium parameters. The associated MAFIC module has some flow and transport capabilities, but according to the company website, it is generally applicable only to relatively small networks.
DFNModeler, Geological Survey of Alabama. Fracture network characterization and representation of interpretation of compartmentalization of coal bed methane formations.
MShale www.mfrac.com. Orthogonal fracture network generation. Designed for computing stress strain for coal bed methane formations.
Petral, Schumberger, Fracture characterization and representation. Upscaled representation of matrix can be represented in Eclipse reservoir simulation package.
Rockflow, http://www.rockflow.de. Simulation of Flow, Mass and Heat Transfer and Deformation in Fractured Porous Rock.
CONNECTFLOW (Joyce et al 2011)**,** Serco Assurance, connectflow.com. Three-dimensional DFN generation and flow/transport modeling; hybrid DFN/continuum modeling with nested and upscaled models. Flow and transport in large networks has been demonstrated. Transport is treated approximately.
HydroGeoSphere/FRAC3DVS www.hydrogeosphere.org. Flow and transport including discretized matrix for three-dimensional networks fractures. Limited to orthogonal fractures.

At present there does not appear to be a non-proprietary DFN flow and transport modeling tool with sufficient capabilities to support the research needs of the Used Fuel Disposition Campaign. In addition, at present, there does not appear to be a general-purpose mesh generation tool that will generate triangulations of intersecting planar fracture networks such that the resulting triangulations are conforming Delaunay triangulations. Conforming Delaunay triangulations are necessary for accurate flow/transport solutions in commonly used control volume flow codes.

2.3   Technical Approach

The longer-term objective of this study is to develop modern discrete fracture network (DFN) flow and transport modeling tools. A 6-step approach is being used:

1. Review of existing approaches, algorithms, and computer codes.
2. Identification of key algorithmic issues.
3. Development of prototype tools using existing flow, transport and mesh generation software.
4. Test/refinement of algorithms using the prototypes.
5. Development of code requirements and design specifications.
6. Code implementation and testing.

Preliminary results of step 1 are summarized in Sections 2.1 and 2.2 of this report. Status of steps 2 and 3 is summarized in the following section.

2.4   Technical Results

2.4.1   Key algorithmic issues

Three algorithmic considerations related to DFN flow and transport simulations are identified: meshing, solving for flow, and modeling radionuclide transport.

Meshing considerations. Mesh generation for DFN flow and transport simulations involves constructing a quality mesh on each fracture surface that also meets two constraints: (1) the mesh on each fracture must conform to intersections with other fractures, and (2) the meshes for each of two intersecting fraction must coincide along the intersection. The second constraint may be relaxed if mortar methods (e.g. Ewing et al., 2000, Arbogast et al., 2000, Pichot et al., 2010) are used to solve for flow and transport. Mortar methods are not addressed here.

Figure 2-1a shows a simple example of two intersecting fractures. Nodes are shown as blue dots; the triangulation of the nodes is shown with blue lines. If a finite element method is used to solve for flow, the triangles are the basic computational unit (element); each is contained within a single fracture. If a control volume method is used for the flow, the basic computational unit is the control volume. If a node is not on a fracture intersection, the associated control volume is a polygon. For nodes that lie on fracture intersections, the associated control volume lies in the planes of both fractures. The control volume for the central node in Figure 2-1a is shown in Figure 2-1b.

Regardless of whether the mesh is generated for use in a control volume of finite element calculation, the major meshing issues are associated with pathological cases that lead to small and or high aspect ratio cells/elements. Some examples are shown in Figure 2-2. Note that these are associated with "triple intersections" wherein a fracture intersection is intersected by a third fracture and with near misses to triple intersections.

Solving for flow. Numerical methods for solving for flow within the DFN must be able to accommodate the fully unstructured grid, which is locally two-dimensional within each fracture. Three methods are identified: conventional finite elements, mixed hybrid finite elements, and control volumes.

Early 3-D DFN research codes and most existing commercial codes use the finite element method to solve for flow within the fracture network. The finite element method is able to accommodate fully unstructured grids without difficulty, but is not locally mass conserving. Lack of local mass conservation is an issue for radionuclide transport simulations because it can lead to nonphysical mass accumulation. If a particle tracking method is used for the radionuclide transport simulation, for example, lack of local mass conservation can cause particles representing packets of radionuclide mass to become stuck in the computational mesh. If enough particles become stuck a misleading representation of geosphere performance would result. Local postprocessing of the finite-element flow solution using the approach of Cordes and Kinzelbach (1992) or similar method can improve the local mass conservation dramatically. This method is difficult to implement especially at fracture intersections.

Applied to groundwater flow, the mixed-hybrid finite-element method (Mose et al., 1994) simultaneously approximates the hydraulic head and groundwater velocity. The number of unknowns is doubled, but the approximation to the groundwater velocity is obtained as a continuous field, thus avoiding velocity discontinuities that plague transport calculations.

The finite element method and the mixed-hybrid finite-element method are convenient for saturated flow but are not ideal for unsaturated or multiphase flow. Control volume methods are traditionally used for these situations. Applied to flow, the control volume method solves conservation equations for water mass on each computational cell. Applied to radionuclide transport, the control volume method solves conservation equations for radionuclide mass on each computational cell, thus avoiding any issues with local mass conservation. The computer codes FEHM (Zyvoloski, 1997) and TOUGH2 (Pruess et al., 1999) are based on the control volume method.

Modeling radionuclide transport. Although the finite element, mixed-hybrid finite-element, or control volume method can be used to solve the advection dispersion equation to represent radionuclide transport, particle tracking on the computed groundwater velocity field is the more common approach to representing radionuclide transport in DFN modeling. Particle tracking does not produce numerical dispersion and can accommodate complex dispersivity tensors. In addition, computational strategies that include the effects of matrix diffusion and sorption by postprocessing the results of particle tracking simulations without matrix diffusion are among the most efficient and practical methods available for representing the transport effects of matrix diffusion.

Particle tracking requires the flow velocity and dispersion tensor at all points in the simulation domain. Velocity (and by extension dispersion tensors) is explicitly available in a mixed- hybrid finite- element solution to flow; particle tracking is relatively straightforward in this case. Particle tracking using flow solutions obtained on unstructured control volume grids is more problematic. Specifically, the control volume flow solution does not provide the continuous velocity field. Instead, it provides a set of scalar quantities that are approximations to the normal component of the darcy flux integrated over each face of each control volume (in two-dimension, each control "volume" is a polygon and each "face" is one line segment on the perimeter of the polygon). If particle tracking is to be used on an unstructured control volume, it is necessary to reconstruct a continuous velocity field from these scalar quantities. There is no unique solution to this reconstruction problem and, as far as we are aware, no general method in the literature.

A new method for particle tracking using flow solutions obtained on unstructured control volume grids has been developed (Painter et al., 2011) and is currently being tested for use in DFN transport

simulations. The method works on a subset of finite volume methods where each fracture has been partitioned into control volumes (polygons) formed by perpendicular bisectors between adjacent nodes in an underlying triangulation of cell centers. Specifically, a nodal network triangulated into a triangular element mesh is presumed to be available. A control volume V_i is constructed around each node i in the triangulation (Figure 2-2) such that V_i is bounded by the set of perpendicular bisectors between node i and each of its neighbors. Note that this approach makes no assumption about the shape of the finite volume cell. It is further assumed that a control-volume method with 2-point flux approximation has been used to solve for groundwater head. Specifically, the conservation equation is written for a control volume V_i as

$$S_i |V_i| \frac{\partial h_i}{\partial t} = \sum_{j \in N(i)} Q_{ij} \qquad (2-1)$$

where S_i, h_i and $|V_i|$ are the specific storage [L^{-1}], head [L] and volume [L^3] in cell i, respectively. Here $N(i)$ is the list of neighbors adjacent to cell i, $Q_{ij} \equiv \int_{V_i \cap V_j} \mathbf{q} \cdot \mathbf{n}_{ij}\, ds$ is volumetric flow rate [L^3/T] through the face connecting cells i and j, and $\mathbf{n}_{ij}$ is the unit normal on the same face.

Our interest is in the velocity vector $\mathbf{v} = \mathbf{q}/\phi$ in the entire domain. However, the flow solution only provides the Q_{ij}, the normal components of $\mathbf{q}$ at each cell face. The approach proposed and tested here has two steps. In the first step, the Q_{ij} for each cell are used to construct an approximate representative value of $\mathbf{q}$ for that cell (denoted $\mathbf{q}_i$, for cell i). Second, the $\mathbf{q}_i$ are then associated with the nodes and the original triangulation (dashed lines in Figure 2-2) is then used to interpolate to any point in the computational domain.

The first step is to reconstruct cell-centered velocities. To this end, $\mathbf{q}$ is (temporarily) approximated as being constant in each cell. The volumetric flow rate across the face common to cells i and j then becomes $Q_{ij} = \mathbf{q}_i \cdot \mathbf{A}_{ij}$ where $\mathbf{A}_{ij} \equiv A_{ij}\mathbf{n}_{ij}$ is the vector area for the face. An analogous equation can be written for each face on the cell, thus producing the linear system for each cell i

$$\mathbf{G}_i \mathbf{q}_i = \boldsymbol{\gamma}_i \qquad (2-2)$$

Here $\mathbf{G}_i$ is a $n_i \times d$ matrix, $\mathbf{q}_i$ is $d \times 1$, and γ_i is $n_i \times 1$, n_i is number of neighbors for cell i, and d is dimensionality of the space. Each row of the $\mathbf{G}_i$ matrix is the vector area for one face. The columns vector γ_i is the volumetric flow rate across the faces, as calculated by the control volume flow code. The column vector $\mathbf{q}_i$, the Darcy flux for the cell, is the unknown.

In two dimensions, a control volume has a minimum of 3 sides and in many applications involving an unstructured grid will have more. Similarly, a control volume in 3-D has 4 or more sides. Thus, equation 2-2 is an $n_i \times d$ system with $n_i > d$; i.e. it is an overdetermined system. Following standard techniques, a least-squares estimate $\hat{\mathbf{q}}_i$ can be constructed for the Darcy velocity $\mathbf{q}_i$

$$\hat{\mathbf{q}}_i = \left(\mathbf{G}^\mathrm{T}\mathbf{G}\right)^{-1}\mathbf{G}^\mathrm{T}\boldsymbol{\gamma} \qquad (2-3)$$

where the subscript i on $\mathbf{G}$ and γ has been suppressed for readability. An estimate of the velocity for the cell is then obtained as $\hat{\mathbf{v}}_i = \dfrac{\hat{\mathbf{q}}_i}{\phi}$ where ϕ is porosity in the cell.

For the types of grids considered here, nodes are specified on the domain boundaries (see Figure 2-2). For nodes on Dirichlet boundaries, Equation 2-3 can be applied as for interior nodes. For nodes on Neumann type boundaries, the specified flux constraint must be included, which leads to a linearly constrained linear least squares problem for the boundary flux vector $\hat{\mathbf{q}}_i^b$ in the i-th cell:

$$\hat{\mathbf{q}}_i^b = \underset{\mathbf{q}_i}{\mathrm{argmin}}\|\mathbf{G}\mathbf{q}_i - \boldsymbol{\gamma}\| \quad \text{subject to } \mathbf{B}\mathbf{q}_i = \boldsymbol{\beta} \tag{2-4}$$

where $\mathbf{B}$ is a $n_i^b \times d$ matrix, and β is $n_i^b \times 1$; $n_i^b < d$ is the number of boundary faces for the cell in question. The matrix $\mathbf{B}$ and the column vector β are analogous to $\mathbf{G}$ and γ but are written for the subset of faces for the cell in question that lie on the boundary. Explicit solutions are available (e.g. Amemiya, 1985):

$$\hat{\mathbf{q}}_i^b = \hat{\mathbf{q}}_i - \left(\mathbf{G}^{\mathrm{T}}\mathbf{G}\right)^{-1}\mathbf{B}\left(\mathbf{B}^{\mathrm{T}}\left(\mathbf{G}^{\mathrm{T}}\mathbf{G}\right)^{-1}\mathbf{B}\right)^{-1}\left(\mathbf{B}\hat{\mathbf{q}}_i - \boldsymbol{\beta}\right) \tag{2-5}$$

with Equation (5) for $\hat{\mathbf{q}}_i$. In the event that $n_i^b = d$ (i.e. for nodes at the corners of the domain) the boundary conditions alone determine the nodal velocities.

Two tests of the new particle tracking procedure are shown in Figures 2-3 and 2-4. Figure 2-3 shows the reconstructed nodal velocities on a rectangular fracture discretized into an unstructured control volume grid. The uniform left-to-right flow is reproduced with very small error by the reconstruction procedure. Particle trajectories without dispersion (streamlines) on a fracture intersected by an injection and a withdrawal well are shown in Figure 2-4. In this example, fluid is injected in the upper-right corner and withdrawn in the lower-left corner. The streamlines are symmetric about the diagonal and have the familiar shape of the quarter five-spot problem (corner to corner flow). Note also that two of the trajectories start near the no-flow boundaries but remain in the computational region at all times.

2.4.1   Prototype Development

A prototyping capability that combines the LANL-developed codes LaGriT (Los Alamos Grid Toolbox, 2011), FEHM (Zyvoloski, 2007) and Walkabout (Painter et al., 2011) is under development.

Rather than attempt the most general capability from the beginning, a practical approach that uses constraints on the fracture network geometry to eliminate the difficult pathological cases is being used. This approach will result in the near term in an initial capability for addressing some important scientific questions as well as a test bed for exercising all aspects of the DFN modeling process (generation, meshing, flow, transport). Some meshing examples that illustrate the status of the prototyping effort are shown in Figures 2-6 through 2-10. These examples focus on fracture networks without matrix material filling the volume between fractures. The approach is to generate intersecting surface triangulations that are compatible with the intended flow and transport modeling software, FEHM (FEHM, 2011). The simplification is imposed that each fracture be planar. An additional constraint is that the triangulation created on the surface of each planar fracture will be a Delaunay triangulation (Delaunay 1934, de Berg *et al*. 2008). This ensures that the associated Voronoi (Okabe, 1992) polygons that are utilized in the FEHM discretization are valid.

A test of the capability of the FEHM code to solve for flow on a mesh composed of 2-D control volumes and control volumes like that in Figure 2-2b is shown in Figure 2-11. In this test, water was injected in the upper left corner and removed from the lower right corner. The color contours represent pressure.

2.5   Conclusions, Status and Path Forward

Based on international experience, discrete fracture network simulation is likely to play an important role in any future investigation of a hard-rock site for a nuclear waste repository, either alone or as part of a hybrid continuum/DFN computational strategy. Initial scoping investigations shown here suggest that LaGriT, FEHM, and the unstructured grid particle tracking method described here could be used in combination to build a prototype simulation capability. In order to model more complex systems with large numbers of fractures, automated workflows need to be developed that interfaces software that generate fracture network realizations, either stochastic or deterministic, with automated mesh generation tools. Since most of the difficulties that arise in meshing a large network of fractures have to do with handling special and pathological cases of intersections that occur at or near grazing angles or intersections that result in extremely short lines of intersections, we are working to implement a practical approach that constrains the fracture network representation to eliminate pathological cases. This will be done so that *a priori* angle and distance constraints can be set. These parameters will then determine the practical length scale of the problem. If the length scale is small, than features with small length scale can be represented but the cost will be to have small computational cells and increased computational costs. The underpinnings for this approach are presented in Murphy *et al.* (2001).
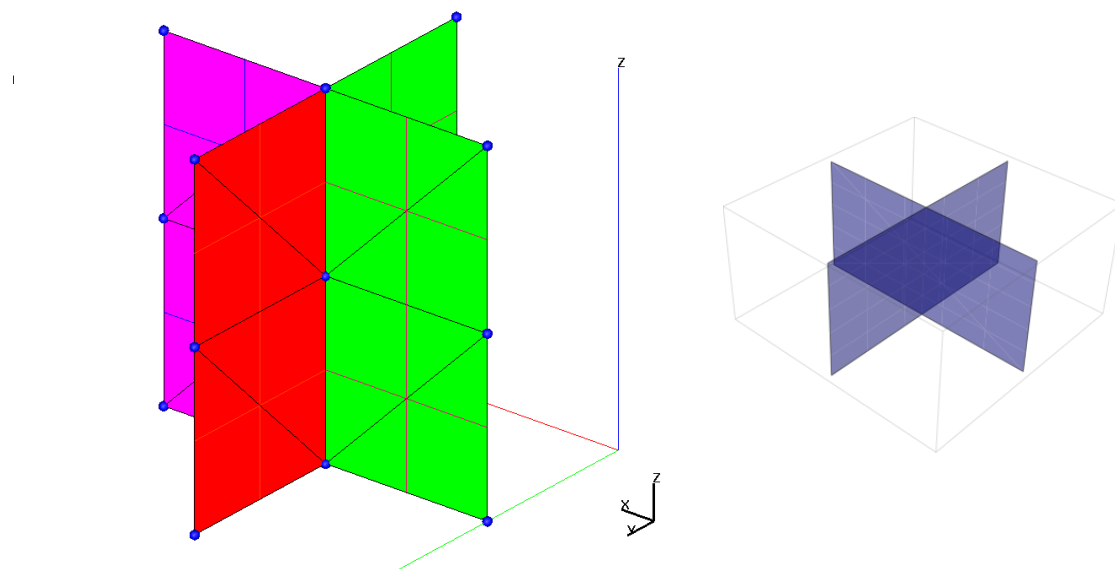
Figure 2 1. Simple example of two orthogonal intersecting planar fracture surfaces. The fracture surfaces are represented by triangles (left image). The control volume for the central node is shown on the right.
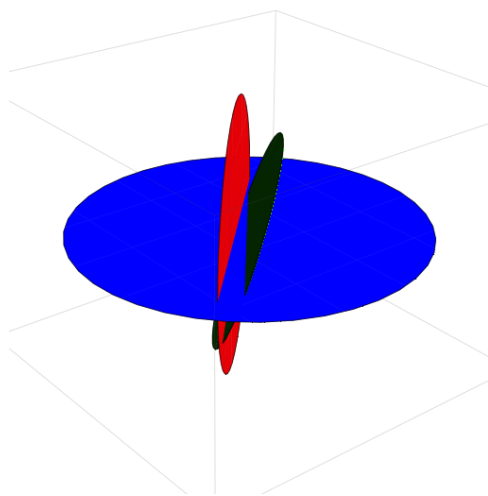
Figure 2-2. Example configuration that causes problems in meshing DFN models for flow and transport calculations. To resolve the space on the blue fracture between the black and red fractures would require very small computational elements, which causes problems with flow and transport codes. Rather than develop robust algorithms to mesh such configurations, an approach is under development that constrains the DFN based on geologic considerations to avoid these problematic configurations.
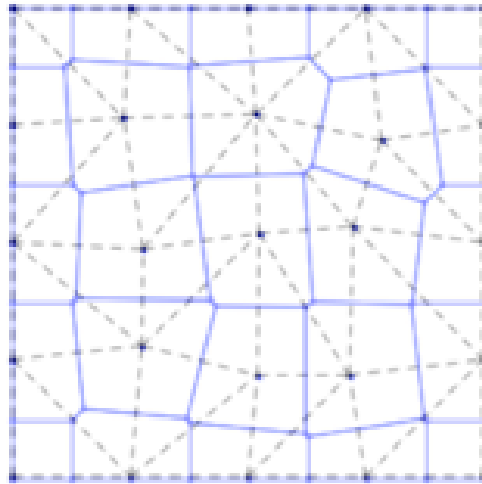
Figure 2-3. Example triangulation and associated control volumes for a 25-node mesh on a fracture. The triangulation is shown with dashed lines. The control-volume elements are shown as solid blue lines.
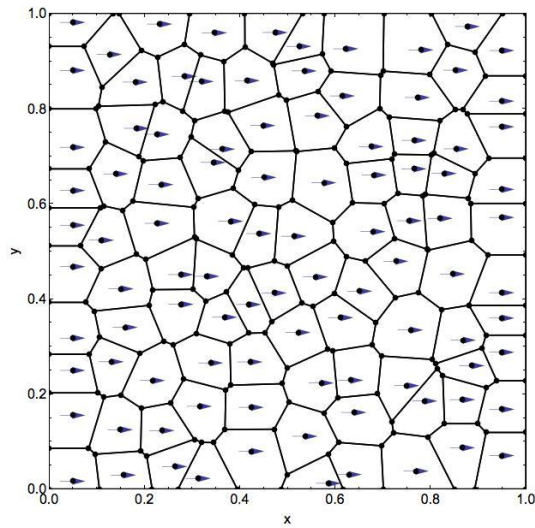
Figure 2-4. Reconstructed velocity from a control-volume flow solution on a fractured plane discretized by an unstructured control volume grid. Constant head conditions are imposed on the left and right boundaries. The top and bottom boundaries are no-flow. Flow vectors are shown centered at the node points.
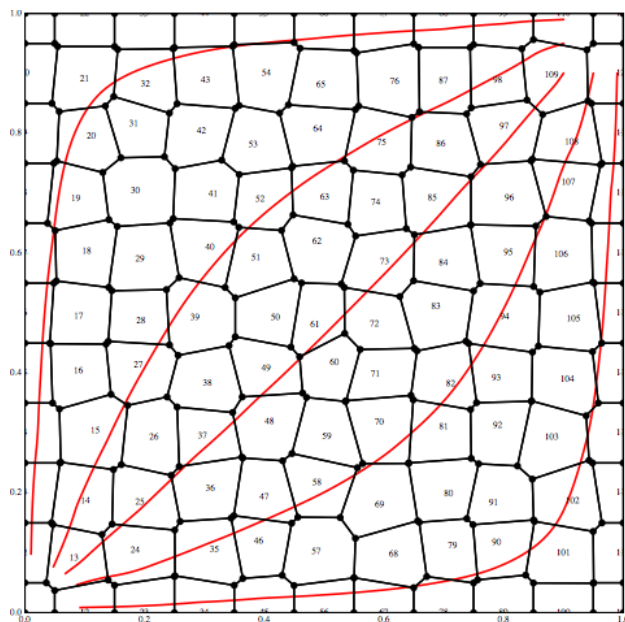
Figure 2-5. Calculated particle trajectories on a fracture plane using a fully unstructured grid. Such capability is needed for DFN simulation capabilities based on control volume grids, but has not been addressed previously.
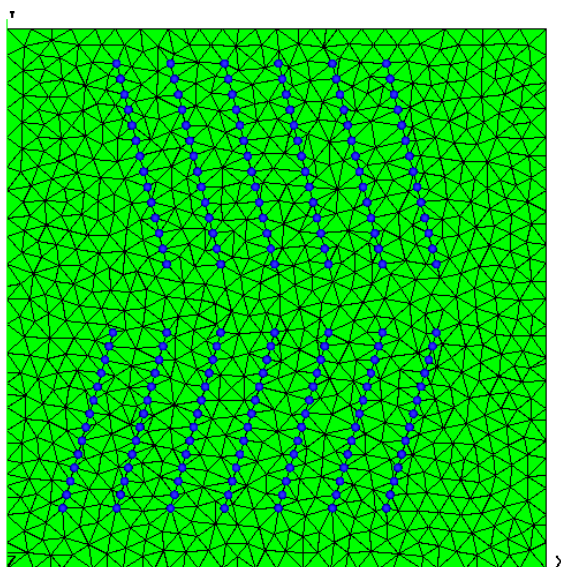
Figure 2-6. A LaGrit generated Delaunay triangle mesh on a fracture plane. This mesh conforms to line segments representing intersections with other fractures. As noted in the text, this capability to conform to internal line segments is a key capability in mesh generation for DFNs.
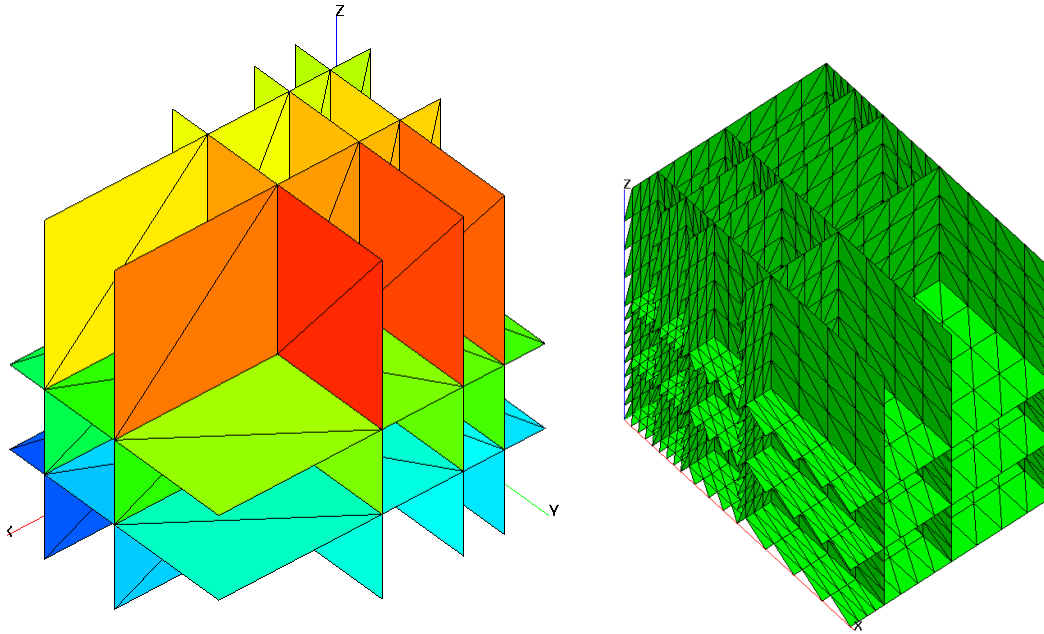
Figure 2-7. On the left is a low-resolution representation of an orthogonal set of fracture planes. On the right, the mesh resolution is finer with multiple triangles discretizing the surface between fracture intersections.
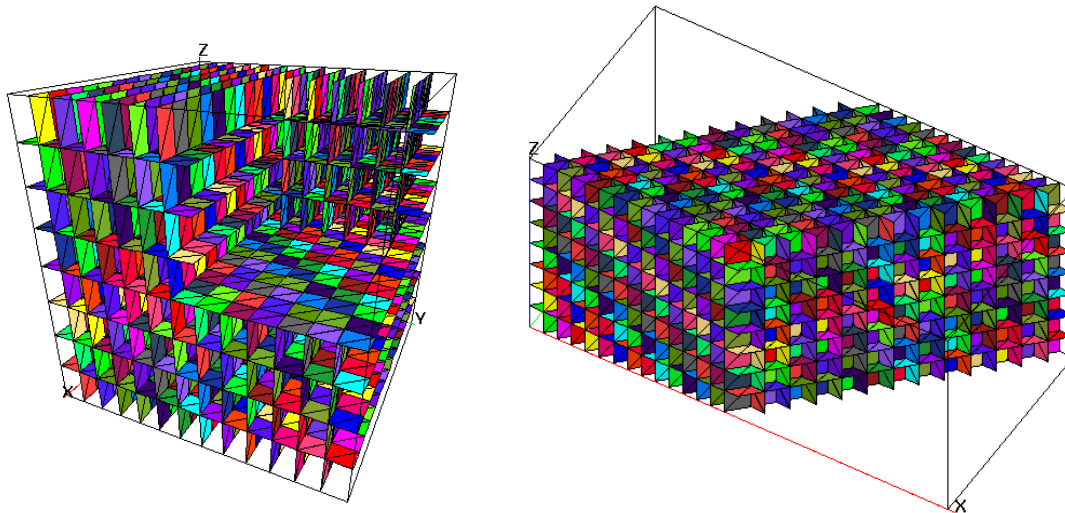
Figure 2-8. On the left is an orthogonal fracture network represented by intersecting triangular meshes. On the right is a similar mesh but instead of being orthogonal, the fractures intersect at 45 degrees.
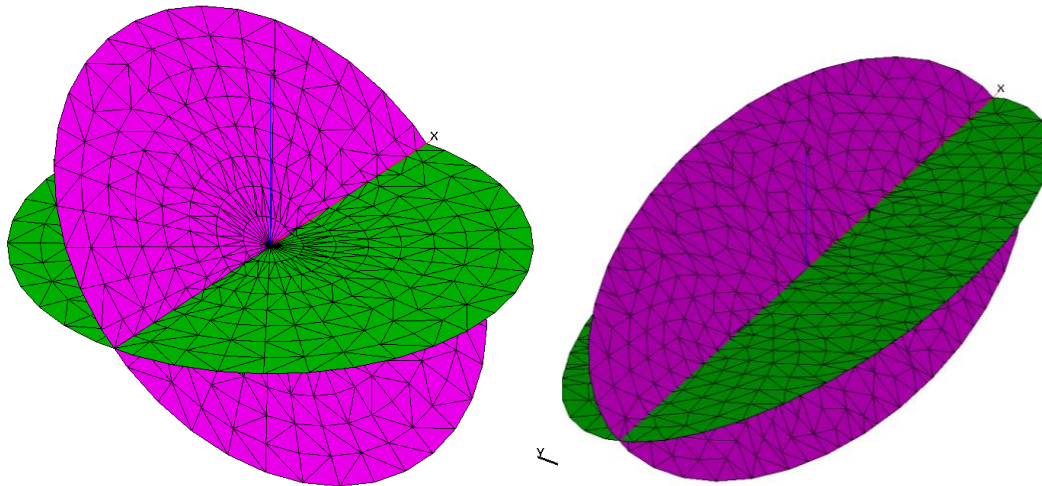
Figure 2-9. Circular and elliptical fracture planes intersecting at 45 degrees. Note that the cells of each triangulation conform along the line of intersection.
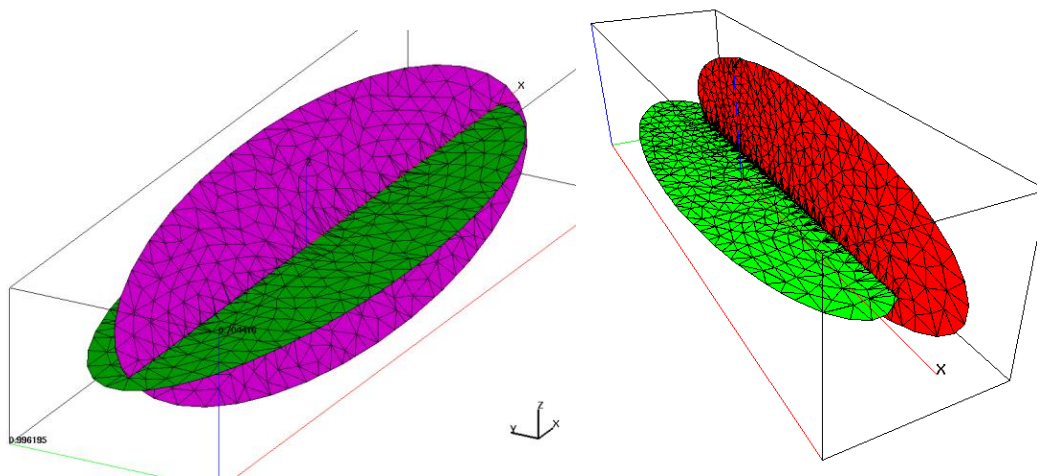
Figure 2-10. Intersecting elliptical fractures in which the line of intersection is interior to the fracture on one end and intersects the fracture edge on the other end.
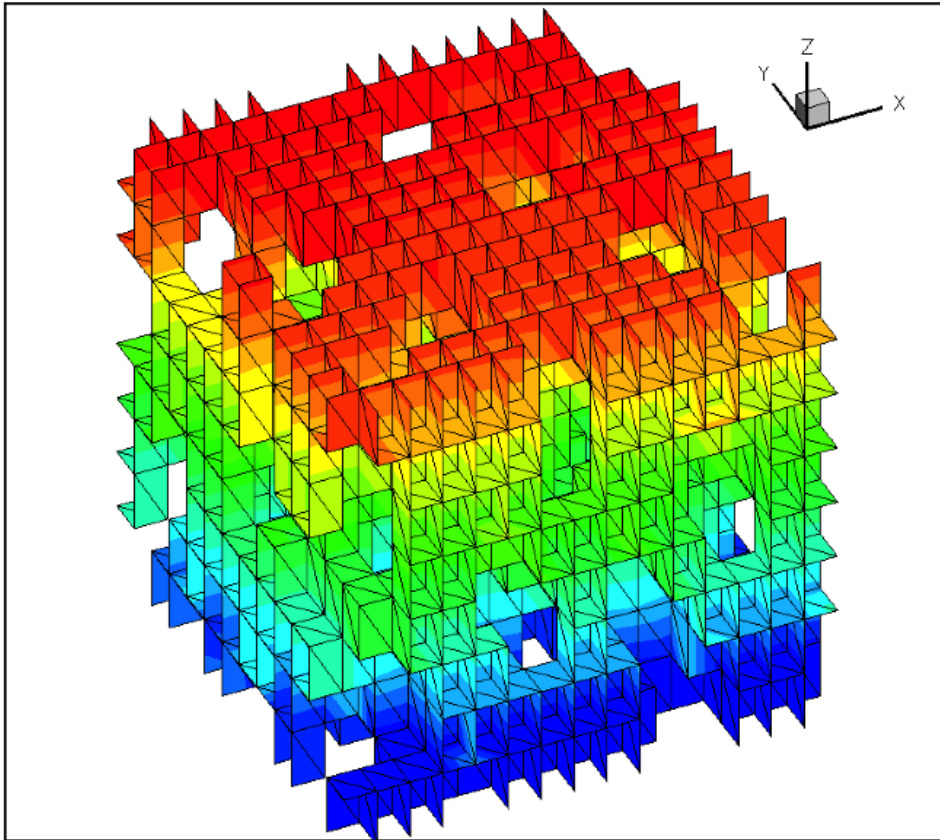
Figure 2-11. Pressure field generated by FEHM using a complex DFN grid generated by LaGrit.

2.6 References

Amemiya T. (1985). Advanced Econometrics. Harvard University Press.

Arbogast T., Cowsar L. C., Wheeler M. F., Yotov I. (2000) Mixed finite element methods on non-matching multiblock grids, SIAM Journal Numerical Analysis 37(4), 1295-1315.

Barrenblat, G.I., Zheltov Y.P., Kochina I.N. (1960) Basic concepts in the theory of seepage of homogeneous liquids in fissured rocks. Journal of Applied Mathematics of Mechanics (English Translation) 24, 1286–1303.

Botros F. E., Hassan A. E., Reeves D. M., and Pohll G. (2008) On mapping fracture networks onto continuum, Water Resources Research 44, W08435, doi:10.1029/2007WR006092.

Cordes C. and Kinzelbach W., (1992) Continuous groundwater velocity field and path lines in linear, bilinear, and trilinear finite elements, Water Resources Research 28(11), 2903-2911.

Cvetkovic V., Painter S., Outters N., and Selroos J.-O. (2004) Stochastic simulation of radionuclide migration in discretely fractured rock near Aspo hard rock laboratory, Water Resources Research 40, W02404, doi:10.1029/2003WR002655.

de Berg M., Cheong O., van Kreveld M., Overmars M. (2008). Computational Geometry: Algorithms and Applications. Springer-Verlag. ISBN 978-3-540-77973-5.

Delaunay B. (1934) Sur la sphère vide, Izvestia Akademii Nauk SSSR, Otdelenie Matematicheskikh i Estestvennykh Nauk, 7:793–800.

Deguid J.O. and Lee P. C. Y. (1977) Flow in fractured porous rock, Water Resources Research 13, 558–566.

Erhel J., de Dreuzy J.R., Poirriez B. (2009) Flow simulation in three-dimensional discrete fracture networks, SIAM Journal on Scientific Computing 31(4), 2688-2705.

Ewing R., Lazarov R., Lin T., and Lin Y. (2000) The mortar finite volume element methods and domain decomposition. East-West Journal of Numerical Mathematics 8, 93–110.

Joyce S., Simpson T., Hartley L., Applegate D., Hoek J., Jackson P., Swan D., Marsic N., Follin S. (2010) Groundwater flow modelling of periods with temperate climate conditions – Forsmark. SKB R-09-20, Svensk Kärnbränslehantering AB.

Karimi-Fard M., Gong B., Durlofsky L. J. (2006) Generation of coarse-scale continuum flow models from detailed fracture characterizations. Water Resources Research 42 (10) W10423.

Los Alamos Grid Toolbox, LaGriT (2011) Los Alamos National Laboratory, <http://lagrit.lanl.gov>.

Mosé R., Siegel P., Ackerer P., and Chavent G. (1994) Application of the mixed hybrid finite element approximation in a groundwater flow model: Luxury or necessity? Water Resources Research 30(11), 3001–3012, doi:10.1029/94WR01786.

Murphy M., Mount D. M., Gable C. W. (2001) A point-placement strategy for conforming delaunay tetrahedralization, International Journal of Computational Geometry and Applications 11, 669-682.

Mustapha H., Dimitrakopoulos R. (2009) Discretizing two-dimensional complex fractured fields for incompressible two-phase flow, International Journal for Numerical Methods in Fluids 65 (7), 764-780.

Mustapha H., (2010) G23FM: a tool for meshing complex geological media, Computational Geosciences 15 (3) 385-397, DOI: 10.1007/s10596-010-9210-6.

Mustapha H., Dimitrakopoulos R., Graf T., Firoozabadi A. (2010) Discretizing Complex Fractured Media for Flow and Transport Simulations, American Institute of Physics Conference Proceedings 1281, 1566-1570.

Neuman, S. P. (1987) Stochastic continuum representation of fractured rock permeability as an alternative to the REV and discrete fracture concepts. In Farmer I.W., Daemen J. J. K., Desai C.S., Glass C.E. Neuman S. P. (eds) Rock Mechanics, Proceedings of the 28th US Symposium, Tucson, Arizona. AA Balkema, Rotterdam.

Neuman, S. P. (2005) Trends, prospects and challenges in quantifying flow and transport through fractured rocks, Hydrogeology Journal 13, 124–147.

Okabe A., Boots B., Sugihara K., Chiu S. N. (1992) Spatial Tessellations: Concepts and Applications of Voronoi Diagrams, John Wiley & Sons.

Painter S. and Cvetkovic V. (2005) Upscaling discrete fracture network simulations: An alternative to continuum transport models, Water Resources Research 41, W02002, doi:10.1029/2004WR003682.

Painter S., Cvetkovic V., Mancillas J., and Pensado O. (2008) Time domain particle tracking methods for simulating transport with retention and first-order transformation, Water Resources Research 44, W01406, doi:10.1029/2007WR005944.

Painter S., Gable C., and Kelkar S. (2011) Pathline tracing on fully unstructured control volume grids, In review 2011.

Pichot G., Erhel, J., de Dreuzy, J. R. (2010) A mixed hybrid Mortar method for solving flow in discrete fracture networks. Applicable Analysis: An International Journal 89 (10), 1629–1643.

Pruess K. and Narasimhan T.N. (1985) A practical method to modeling fluid and heat flow in fractured porous media. Society Petroleum Engineers Journal 25(1), 14–26.

Pruess K., Oldenburg C., and Moridis G. (1999) TOUGH2 Users Guide, Version 2.0, LBNL-43134, Lawrence Berkeley National Laboratory, Berkeley CA.

Svensk Kärnbränslehantering AB (2011) Long-term safety for the final repository for spent nuclear fuel at Forsmark, SKB TR-11-01, Svensk Kärnbränslehantering AB

Shewchuk J. R., Triangle: Engineering a 2D Quality Mesh Generator and Delaunay Triangulator, First Workshop on Applied Computational Geometry (Philadelphia, PA), 124-133, ACM, May 1996, <www.cs.cmu.edu/~quake/triangle.html>.

Si H., TetGen: A quality tetrahedral mesh generator and three-dimensional Delaunay triangulator, software <http://tetgen.berlios.de/files/tetgen-manual.pdf>.

Svensson U. (2001), A continuum representation of fracture networks: Part I. Method and basic test cases, Journal of Hydrology 250, 170–186.

Warren J.E. and Root P.J. (1963) The behavior of naturally fractured reservoirs. Society of Petroleums Engineers Journal 3, 245–255.

Wang Y. (2011) *Research & Development Plan for Used Fuel Disposition Campaign (UFDC) Natural Systems Evaluation and Tool Development*, U.S. DOE Used Fuel Disposition Campaign, May 25, 2011.

Zyvoloski G. A. (2007) FEHM: A control volume finite element code for simulating subsurface multi-phase multi-fluid heat and mass transfer. Los Alamos Unclassified Report LA-UR-07-3359.

Zyvoloski G. A, Robinson B. A, Viswanathan H. S. (2008) Generalized dual porosity: A numerical method for representing spatially variable sub-grid scale processes, Advances in Water Resources 31 (3) 535–544, DOI: 10.1016/j.advwatres.2007.11.006

Chapter 3: Radionuclide Transport in Heterogeneous Media – Effects of Spatial Variability in Sorption Coefficients

3.1   Introduction

The physical properties of a repository geosphere that control the movement of water and the migration of dissolved or colloidal radionuclides are usually heterogeneous by nature and typically exhibit spatial fluctuations over a large range of spatial scales. At largest scales, division of the geosphere transport pathways into hydrostratigraphic units (for example repository host rock and non-host rock in the transport pathway) is almost always explicit and deterministic in performance assessment modeling. However, sorption properties of geologic material typically exhibit spatial variability even within individual hydrogeologic units. As a result, the equilibrium distribution coefficient K_d [m^3/kg] tends to also vary spatially.

Painter et al. (2001) and Zavarin et al. (2004) provided examples of actinide K_d variability in the single-porosity and fractured media, respectively. Painter et al. (2001) analyzed variability in neptunium sorption properties of the alluvial aquifer near Yucca Mountain, Nevada. They used a database of measured groundwater chemistries and a calibrated diffuse-layer surface complexation model (Turner and Pabalan, 1999) that relates groundwater chemistry to K_A, where K_A is surface-area normalized equilibrium distribution coefficent ($K_A = K_d/A$ and A is specific surface area [m^2/kg]). They found that horizontal spatial correlation in K_A was well described by an exponentially decaying model with characteristic spatial scale of 400 m (Figure 3-1). The fitted spatial covariance model was assumed isotropic (omnidirectional) in the horizontal plane because data limitations prevented testing for anisotropic spatial correlations. Using an estimate for specific surface area, they developed a random space function (RSF) model for neptunium K_d with geometric mean of 0.015 m^3/kg, log-variance of 0.82 and exponentially decaying spatial correlation with characteristic scale length (range) of 400 m. At the Nevada Test site, Zavarin et al. (2004) studied the heterogeneity of radionuclide sorption coefficients in volcanic rocks with different mineral facies. The covariance of uranium sorption coefficients, computed theoretically using surface complexation reaction equations, measured mineral contents, and assumed site exposure in vertical boreholes at that site fits an exponential function well (Figure 3-2) (Stoller-Navarro Joint Venture, 2009).
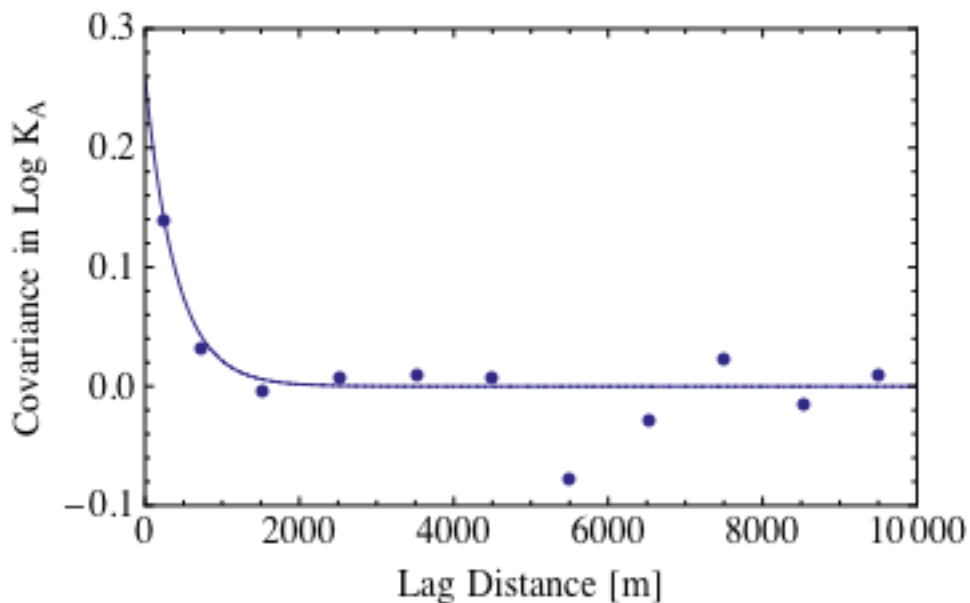
Figure 3-1. Spatial covariance in the horizontal direction for pentavalent neptunium Np(V) in the alluvial aquifer near Yucca Mountain Nevada (replotted from Painter et al. 2001). Here $K_A = K_d/A$ where K_d is equilibrium distribution coefficient $[m^3/kg]$ and A is specific surface area $[m^2/m^3]$. The curve is a fitted exponential model with range of 400 m.
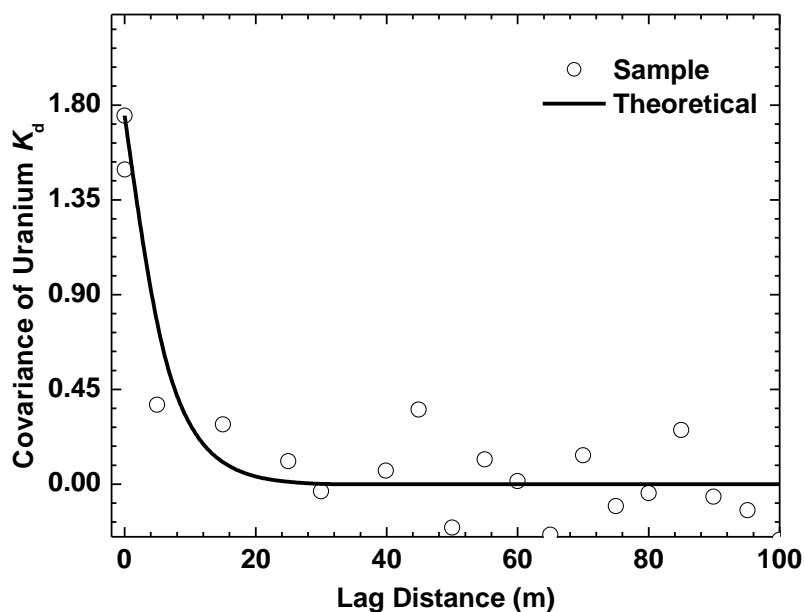
Figure 3-2. Covariance of uranium sorption coefficient (K_d) fits an exponential function well in the vertical direction at the Nevada Test site (modified from Stoller-Navarro Joint Venture, 2009).

Spatial variability within each rock type, such as that shown in Figures 3-1 and 3-2, is rarely treated explicitly in performance assessment modeling. Instead K_d is typically treated as spatially constant but uncertain. That is, K_d is sampled from an uncertainty distribution and then treated as spatially constant within each realization. Depending on how the uncertainty distribution is established, this procedure has the potential to overestimate uncertainty and overestimate early breakthrough of radionuclides. In particular, if the K_d uncertainty distribution is based on spatially distributed measurements (the usual case) and has not been adjusted for other sources of uncertainty, sampling spatially constant K_d's from that distribution and substituting parametric uncertainty for spatially variability have potential to produce a pessimistic picture of the geosphere barrier (e.g. Painter et al., 2001).

Painter et al. (2001) investigated the consequences of substituting parametric uncertainty for spatial K_d variability in the context of neptunium transport in the alluvial aquifer near Yucca Mountain, Nevada. They used a Lagrangian framework and a two-site mobile/immobile model for radionuclide retention. In this model, access to sorption sites is kinetically limited and characterized by a single rate constant α. The product of α and the mean groundwater travel time $\langle \tau \rangle$ is a dimensionless Damköhler-like number that quantifies the importance of kinetic limitations, with $\alpha\langle \tau \rangle \gg 1$ implying near-equilibrium sorption conditions and $\alpha\langle \tau \rangle \ll 1$ implying strong kinetic controls. Their key findings on K_d variability are: (1) treating K_d as deterministic and spatially uniform incurs only a small error in the expected discharge, (2) treating K_d as uncertain but spatially uniform (parametric uncertainty) may produce a larger error in the breakthrough curve, especially at early times, but the effect on the peak expected dose is modest, (3) in general, condensed metrics of performance for the geologic barrier (i.e. peak expected dose) are less sensitive than the time-dependent breakthrough to heterogeneity, and (4) breakthrough is more sensitive to heterogeneity when sorption is kinetically controlled (as opposed to equilibrium).

The results of Painter et al. (2001) suggest that heterogeneity in K_d is of minor importance as compared to physical (permeability) heterogeneity. However, their analyses focused on a particular site, and it is not clear how general the conclusions are. In particular, the Painter et al. study focused on one particular metric of interest (the peak of the expected dose), was for a site with relatively modest K_d variability (log-variance of 0.82), made use of simplifying assumptions (no dispersion, first-order analytical results), and did not address variability in sorption characteristics of fractured media.

This chapter addresses Topic P4 of the R&D Plan for the UFDC Natural Systems Evaluation and Tool Development – Evaluation of the effects of spatial heterogeneity on radionuclide transport (Wang, 2011; Chapter 1). The focus is on understanding consequences of treating spatially variable K_d as spatially constant. There are four objectives: (1) to review current methods and approaches for assessing the transport effects of spatial variability in K_d, (2) to extend the previous assessment by Painter et al. (2001) to heterogeneous single-porosity media with higher levels of K_d variability including longitudinal and transverse dispersion, (3) to make a preliminary assessment of the effect of variability in matrix sorption coefficients in fractured media, and (4) to recommend additional research and development that will lead to more realistic representations of K_d spatial variability in future performance assessments.

3.2   Previous Results on Transport Effects of Spatial Variability in Sorption Coefficient

The spatial variations of the reactive transport parameters (such as sorption coefficient) in porous and fractured media have been studied at variable scales from column experiments to field tracer tests (e.g. Robin et al. 1991; Allen-King et al. 1998, 2006; Painter et al. 2001; Zavarin et al. 2004; Stoller-Navarro Joint Venture, 2009). The statistical and stochastic characterizations (upscaling or downscaling) of

transport parameters provide a theoretical and practical link between controlled experimental results at the laboratory/bench scales to multi-kilometer field scales at which contaminant remediation and risk assessment are actually conducted.

Upscaling is a process of replacing a heterogeneous domain by a homogeneous one that reproduces the equivalent response with the same boundary conditions imposed (Rubin, 2003). Therefore, upscaling is also an extrapolating process that transfers parameter values from small scale to large scale and can be viewed as a process of averaging heterogeneity at a smaller scale. It has received intense attention from hydrogeologists. The objective of upscaling is to retrieve effective or equivalent parameters (Cushman et al., 2002) by different means of averaging from the scale at which parameters are collected (e.g. in boreholes in field or from core samples in lab) to the scale at which transport parameters are used in numerical modeling. There are various upscaling methods (see the review article by Cushman et al., 2002 and reference therein), including volume averaging (Whitaker, 1967; Slattery, 1967), homogenization (Hornung, 1997), renormalization (King, 1989; Noetinger, 1994), fractals (Neuman, 1990; Molz et al., 2004), ensemble averaging (Dykaar and Kitanidis, 1992), Eulerian perturbation (Dagan,1989), spectral integral approach (Gelhar and Axness, 1983; Rajaram, 1997), Lagrangian approach (Rajaram, 1997; Painter and Cvetkovic, 2005), fast Fourier transform and Green's function method (Huang and Hu, 2000,2001), continuous time random walk (Noetinger and Estebenet, 2000; Berkowitz et al., 2006), effective medium theory (Sanchez-Vila et al., 1996; Renard and de Marsily, 1997; Fokker, 2001; Sanchez-Vila et al., 2006) and indicator geostatistics-based approach (Dai et al., 2007a, 2007b).

A significant challenge in upscaling reactive transport parameters is to develop scale-appropriate conceptual and statistical models to represent physical and chemical heterogeneities that impact solute migration estimates. Characterization of transport parameters (such as sorption coefficients) for porous media has been studied for decades, and various upscaling methods have been developed (Cushman et al., 2002 and references therein). Characterization of transport parameters for fractured porous media presents particular challenges due to the medium complexity and high heterogeneity (e.g. Neumann, 2005). In fractured-rock systems, the mass transfer coefficient that quantifies mass transfer between fracture and matrix is one of the most important transport parameters because it links both physical heterogeneity (reflected in permeability and tortuosity) and chemical heterogeneity (in sorption coefficient). In practice, it is not uncommon that values of tortuosity and sorption coefficient measured from column experiments are used directly, without upscaling, for field-scale reactive transport modeling. However, without using scale-justified effective parameters, field-scale modeling may lead to inaccurate simulation of physical and chemical processes.

3.2.1. Upscaling sorption coefficients in single-porosity media

The studies of effective transport parameters in physically and chemically heterogeneous porous media have attracted much attention in the past two decades (Dagan, 1989; Rubin, 2003). Numerous investigations show that the effective transport parameters are spatially and/or temporally scale-dependent in both porous media, such as retardation factor (Bellin et al., 1993; Rajaram, 1997; and Fernàndez-Garcia et al., 2005), diffusion coefficient (Dai et al., 2007b; Liu et al., 2007a), sorption coefficient (Liu et al., 2008; Dai et al., 2009) and macrodispersivity (Neuman, 1990; Gelhar, 1992; Dai et al., 2004). The scale dependence of the effective transport parameters is understood to originate from heterogeneities of geological formations and be of a great significance in contaminant transport theory and remediation practice due to necessities of upscaling transport parameters across scales from column experiments to field-scale modeling. For contaminant transport of a reactive solute with linear equilibrium adsorption, spatial variability of sorption coefficients (K_d) of the solute has significant effects on the effective (upscaled) retardation factors (R) (Robin et al., 1991; Bellin et al., 1993; Burr et al., 1994). So far, most of the measurements of sorption coefficients are gained in smaller, experimental column scales, while

contaminant remediation and risk assessment are actually conduct at larger, field scales. Therefore, to gain effective transport parameters for field-scale modeling, it is necessary to transfer knowledge obtained at a smaller column scale to a larger field scale through upscaling, which is one of the most important processes for field-scale transport modeling.

Detailed characterization of spatial distributions of K_d (or retardation factor R) for reactive solutes has disclosed large heterogeneities and stimulates studies of upscaling R using stochastic theory. Using a Lagrangian approach, Rajaram (1997) derived analytical expressions for time and scale dependence by assuming various spatial correlations between K_d and hydrological conductivity K. His research reveals that retardation factor in unimodal porous media changes with scale and approximates its arithmetic mean when the temporal and spatial scales become sufficient large. Fernàndez-Garcia et al. (2005) further confirmed the conclusions of Rajaram (1997) by numerical experiments. More studies on the scaling of R in unimodal porous media have been conducted by Tompson (1993), Bellin et al. (1993), Cvetkovic and Dagan (1994), Chao et al. (2000), Painter et al. (2001), Andersson et al. (2004), and Samper and Yang (2006).

3.2.2   Upscaling sorption coefficients in fractured formations

The retardation of a solute relative to the fracture flow velocity is due to diffusion out of fractures and sorption onto matrix minerals. These processes are affected by various factors, including fracture aperture, fracture volume fraction, matrix porosity and tortuosity, and type and surface area of matrix minerals.

Scaling effects of transport parameters in fractured rocks including the effect of matrix diffusion/sorption have been studied by several authors (e.g., Huang and Hu, 2001; Hu et al., 2002; Cvetkovic et al., 2004, 2007; Painter and Cvetkovic, 2005; Frampton and Cvetkovic, 2007; Reimus et al., 2007; Dai et al. 2009). For example, Dai et al. (2009) analyzed the situation where matrix K_d along the fracture is a random space function and derived expressions for effective retardation factor and matrix K_d. The effective parameters provide a way to include the effect of smaller scale variability of K_d in performance assessment or process models performed on a larger scale without explicit representation of matrix K_d variability. An example using this result is shown in Figure 3-5. Note that small value of integral scale corresponds to an uncorrelated white noise process for the K_d variability and the large integral scale corresponds to treating K_d as parametric uncertainty. For comparison the geometric mean of the sorption coefficient in this example is 3.95 cm^3/g. Ignoring spatial variability and treating K_d as deterministic (constant and without uncertainty) would underestimate K_d by 11% to 21%, depending on the true integral scale. Conversely, treating K_d as an uncertain parameter would overestimate the K_d by a factor of 0 to 12%, depending on the integral scale.
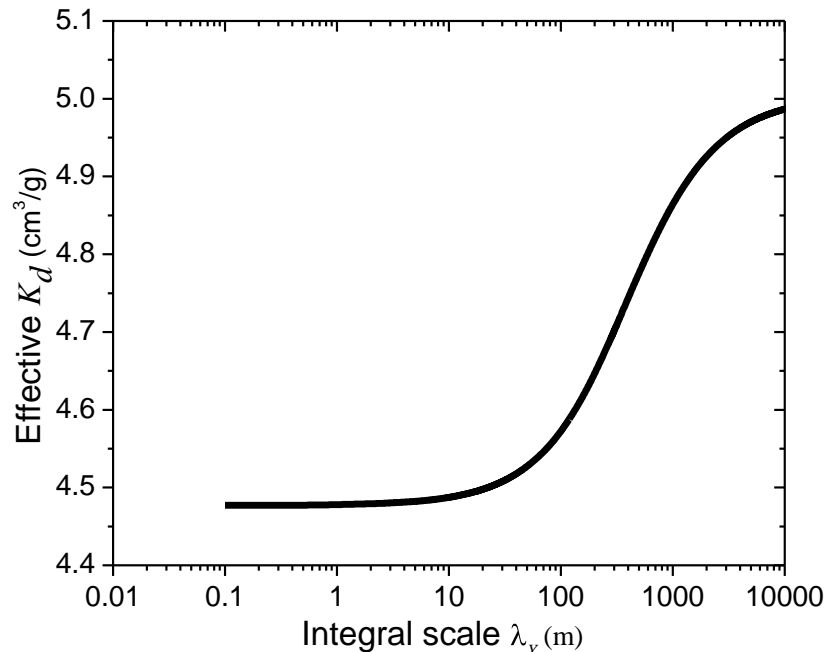
Figure 3-3. Effective sorption coefficient K_d increases with correlation length of indicator variable and decreases with the ratio of domain size to correlation length $L = 1000$ m. For comparison, the geometric mean of the sorption coefficient is about 3.25. Modified from Dai et al (2009).

3.2.3 Hierarchical multimodal reactive mineral facies-based representation of heterogeneity (Deng et al. 2010)

The upscaling approaches described in Sections 3.2.1 and 3.2.2 focused on unimodal distributions of sorption properties, typically represented as a random space function with a single correlation length. However, geologic formations are typically more complicated than a single-scale random space function (e.g. Painter and Paterson, 2004). For sedimentary formations, sedimentary facies-based characterizations are firmly established as a means to represent multimodal hydraulic conductivity distribution (Ritz et al., 2004; Dai et al., 2004) as well as sorption heterogeneity (Allen-King et al., 1998).

Because different reactive minerals have different sorption capacities, spatial variability of the reactive minerals significantly affects the sorption process and thus contaminant transport. From small to large scales, the reactive minerals constitute reactive mineral assemblages, which in turn form reactive mineral facies. As an analogue to sedimentary facies with hierarchical architecture (Scheibe and Freyberg, 1995; Dai et al., 2004), a hierarchical structure of mineral facies has been proposed to represent spatial distributions of reactive mineral facies and to upscale the matrix sorption coefficient in both single-porosity (Deng, in review) and fractured media (Deng et al. 2010).

Figure 3-4 illustrates the multiscale conceptual model based on a simplified synthesis of uranium transport in altered fractured volcanic rocks (Stoller-Navarro Joint Venture, 2009; Deng et al., 2010). The distributions of reactive mineral facies are characterized in a three-tiered hierarchy with a population of

sorption coefficients at each hierarchical level. This hierarchy is an organized framework of sorption reactions between reactive minerals and dissolved uranium in water. However, the conceptual model and methods proposed by Deng et al. (2010) are not limited to the particular organization used for sorption reaction and can be extended to be suitable to different reactions, chemical species and geologic media.

Reactive minerals at the microform scale (10^{-6} to 10^{-2} m) refer to any minerals that are sensitive to one or a group of specified geochemical reactions. As shown in Figure 3-4A, the reactive minerals represent the lowest level of the hierarchical structure, equivalent to the scale of mineral grains in a rock thin section. Minerals with large surface areas usually have relatively large sorption coefficients (Stumm and Morgan, 1995). For a given type of reactive mineral, the variation in sorption coefficients is dependent not only on grain size and shape, but also on texture, crystal structure, variability of chemical composition of the minerals and fluctuation in physical and chemical conditions under which the sorption reaction takes place (Stumm and Morgan, 1995). Since pure reactive mineral separates are obtained from synthesis or separation process, their sorption coefficients can be measured in tubes under controlled physiochemical conditions after the reactive mineral size and surface area are determined.

In practice, reactive mineral assemblages (RMAs) are often used instead of pure minerals in column experiments. A reactive mineral assemblage at the mesoform scale (10^{-2} to 10^{1} m) is an association of coexisting non-reactive and reactive minerals for one or a group of specified geochemical reactions. The mesoform scale ranges from a hand specimen or experimental column to a small rock outcrop (Figure 3-4B). Due to different statistical distributions of the sorption coefficients among different reactive minerals (Figure 3-3A), the different RMA may have different statistical distributions of sorption coefficients. If the distributions of sorption coefficients for the different reactive minerals are widely separated, the RMA composed of the reactive minerals will have a multimodal statistical distribution for the sorption coefficients (Figure 3-4B). If a RMA consists of only one kind of reactive mineral or several kinds of reactive minerals with similar mean sorption coefficients, its sorption coefficient will have a single mode (close to the mean of the reactive minerals).

Figure 3-4C displays the reactive mineral facies at the macroform scale (10^{1} to 10^{3} m), the top hierarchical level. The macroform scale is equivalent to the field scale, at which the field reactive transport modeling and risk assessment are actually conducted. A reactive mineral facies is a body of rock that is characterized by a few reactive and non-reactive mineral assemblages for one or a group of specified geochemical reactions.

This conceptual model of the hierarchical structure of the reactive mineral facies provides the basis for upscaling the sorption coefficient from lab column-scale distributions of reactive minerals to the field scale (Deng et al. 2010). For example, explicit expressions for tortuosity and sorption coefficient of heterogeneous matrix materials along a fracture migration pathway are provided by Deng et al. (2010).
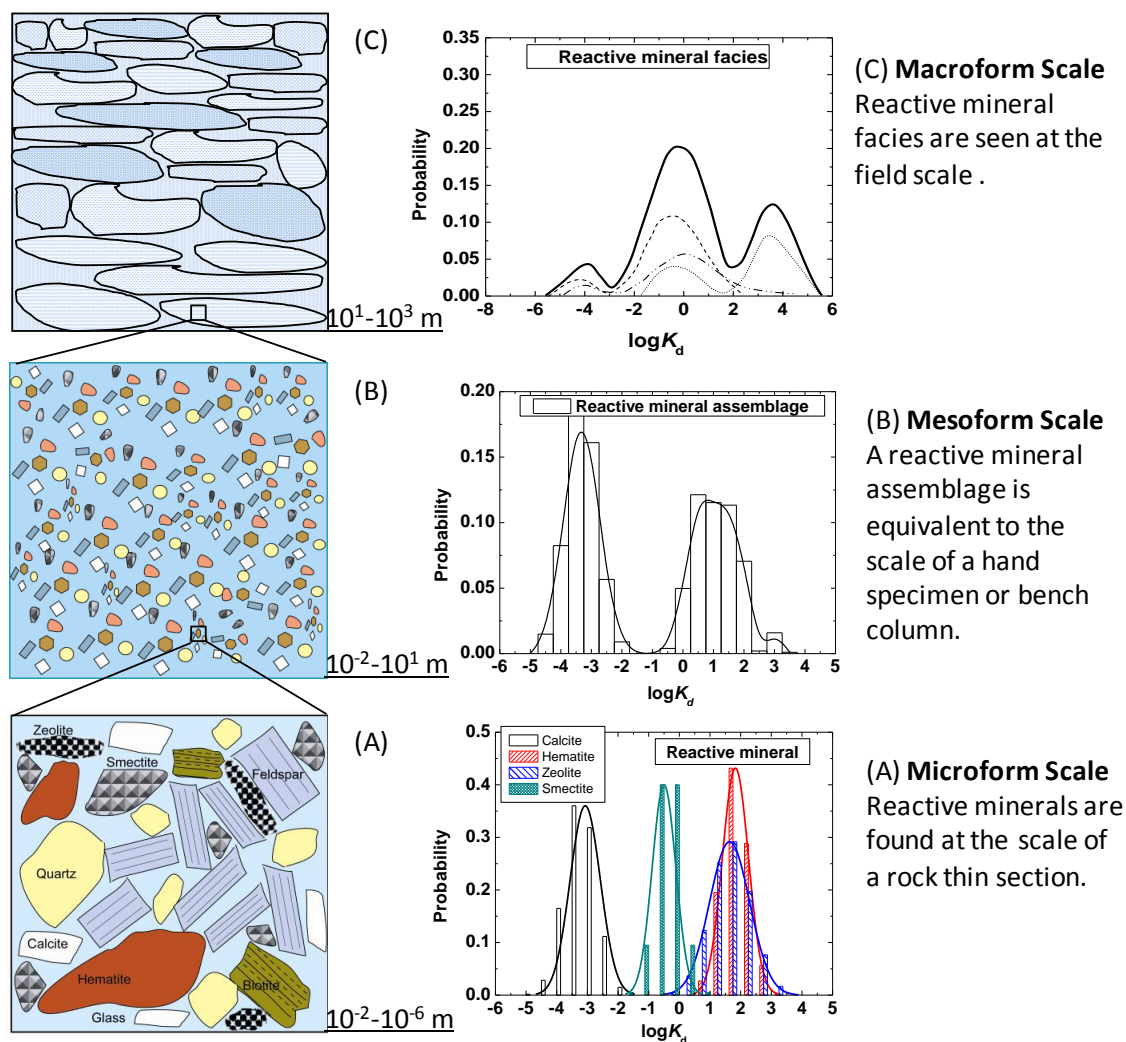
Figure 3-4. Hierarchical structure of reactive mineral facies. The distributions of uranium matrix sorption coefficients for reactive minerals are abstracted from Zavarin et al. (2004), Stoller-Navarro Joint Venture (2009 and Deng et al., 2010)

3.3 Consequences of Representing Spatial Variability as Parametric Uncertainty: Technical Approach

Although a great deal of research has been done on transport effects of spatial variability in sorption coefficient, the vast majority of that work has been focused on the theoretical aspects of the upscaling problem. Research explicitly addressing the consequences of treating a spatially variably K_d as an uncertainty parameter in the waste disposal context is lacking, with the one exception being the work of Painter et al (2001). Two Monte Carlo studies are undertaken here to address this. The first study looks at transport in porous media with higher levels of variability than addressed by Painter et al. (2001). The second study addresses the effect of matrix variability on expected transport.

3.3.1   Single-porosity media

A series of model simulations were performed to study the effect of heterogeneities in sorption coefficient (K_d) distribution on transport. Simulations were performed on a three-dimensional grid in which flow is aligned with the *x*-axis with a pressure gradient of 1.8835×10^1 Pa/m. The grid dimensions are 20 km (x direction) by 10 km (y direction) in the horizontal directions and 500 m thick (z direction). In each simulation, 10000 particles are released at the inlet 500 m from domain boundary within a patch of the y-z plane, and the breakthrough curves at a downstream location (a y-z plane 19 km from the release plane) were recorded. The dimensions of the patch are 9600 m in the *y*-direction and 500 m in the vertical direction. Particle-tracking model runs were carried out with longitudinal dispersivity of 100 m.

The K_d distributions are based on Np data for Argillic Tuff Confining Unit (ATCU) from Yucca Flat in the Nevada Test Site (Appendix I, Stoller-Navarro Joint Venture, 2007). The dataset shows that K_d of Np follows a log-normal distribution with a mean value of 3.937 ml/g, and log-variance of 2.16. Decay is neglected in this set of simulations. The grid size are set as 100 m in x and y directions and 5 m in z direction. The simulations were performed for different K_d horizontal correlation length scenarios (2000m, 1000m, 500m and no correlation) and the vertical correlation scale was fixed at 50m for all simulations; 51 realizations were used for each set of parameters.

Figures 3-5 to 3-8 show geostatistically generated realizations of K_d distributions for four assumed K_d horizontal correlation lengths, using a sequential Gaussian random field generator *sgsim* from GSLIB (Deutsch and Journel, 1992). Figure 3-5 is for a correlation length of 2000m, Figure 3-6 is for correlation length of 1000m, Figure 3-7 is for a correlation length of 500m, and Figure 3-8 is for the case of a random field without correlation. The K_d field is random distributed (white noise) in Figure 3-8.
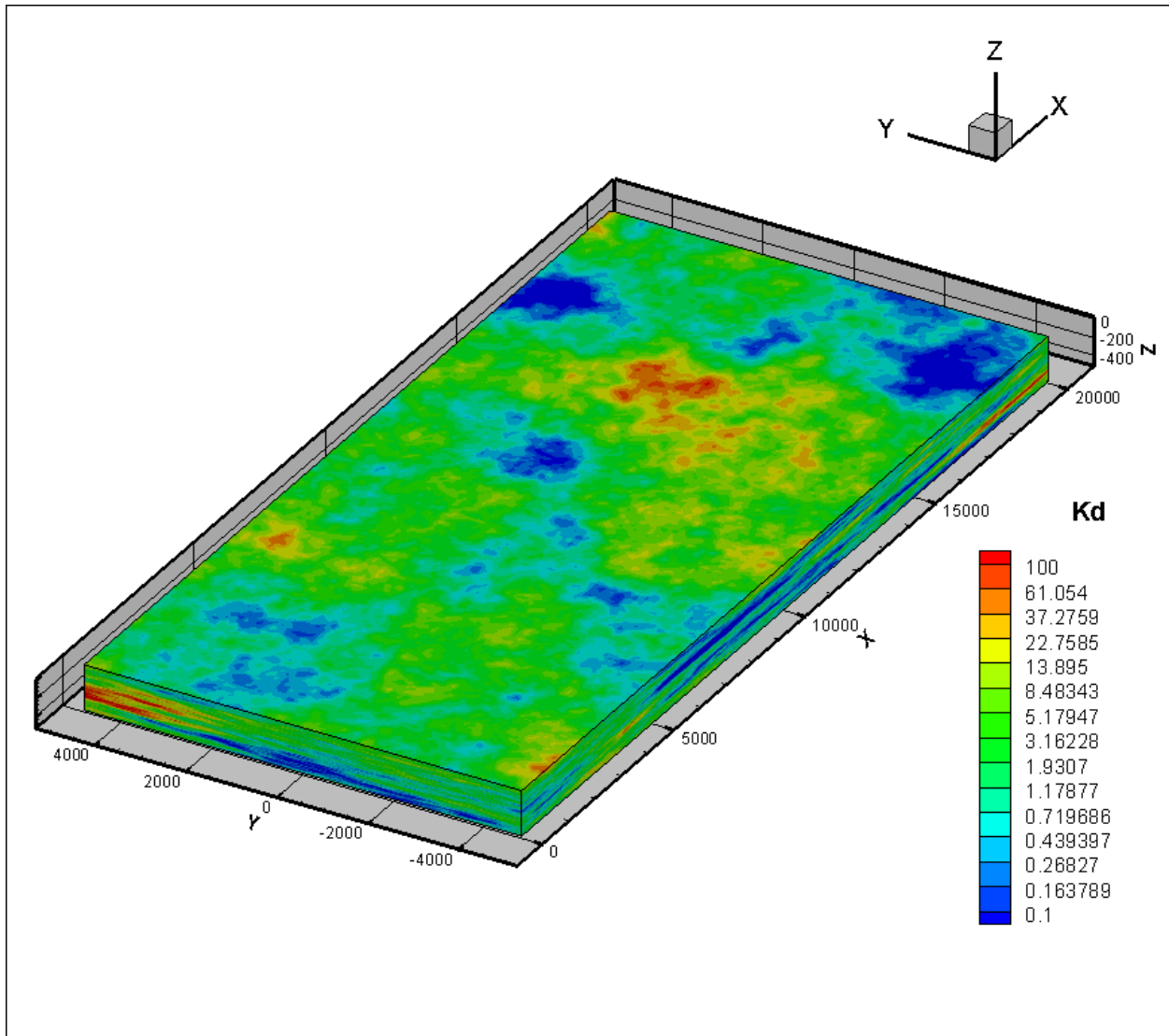
Figure 3-5. Example plot of heterogeneous K_d distribution with correlation length of (2000m $\times$ 2000m $\times$ 50m).
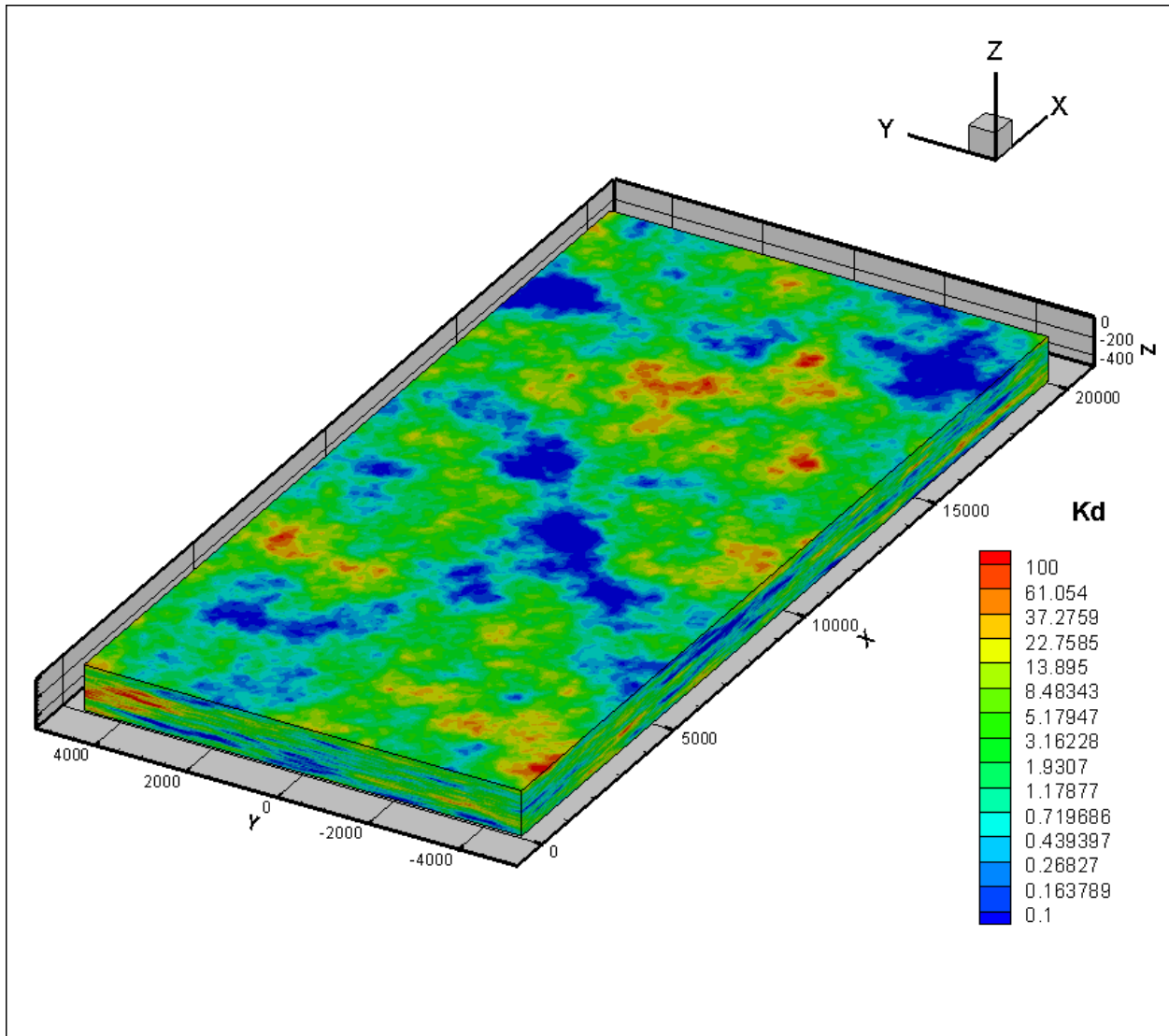
Figure 3-6. Example plot of heterogeneous K_d distribution with correlation length of (1000m × 1000m × 50m).
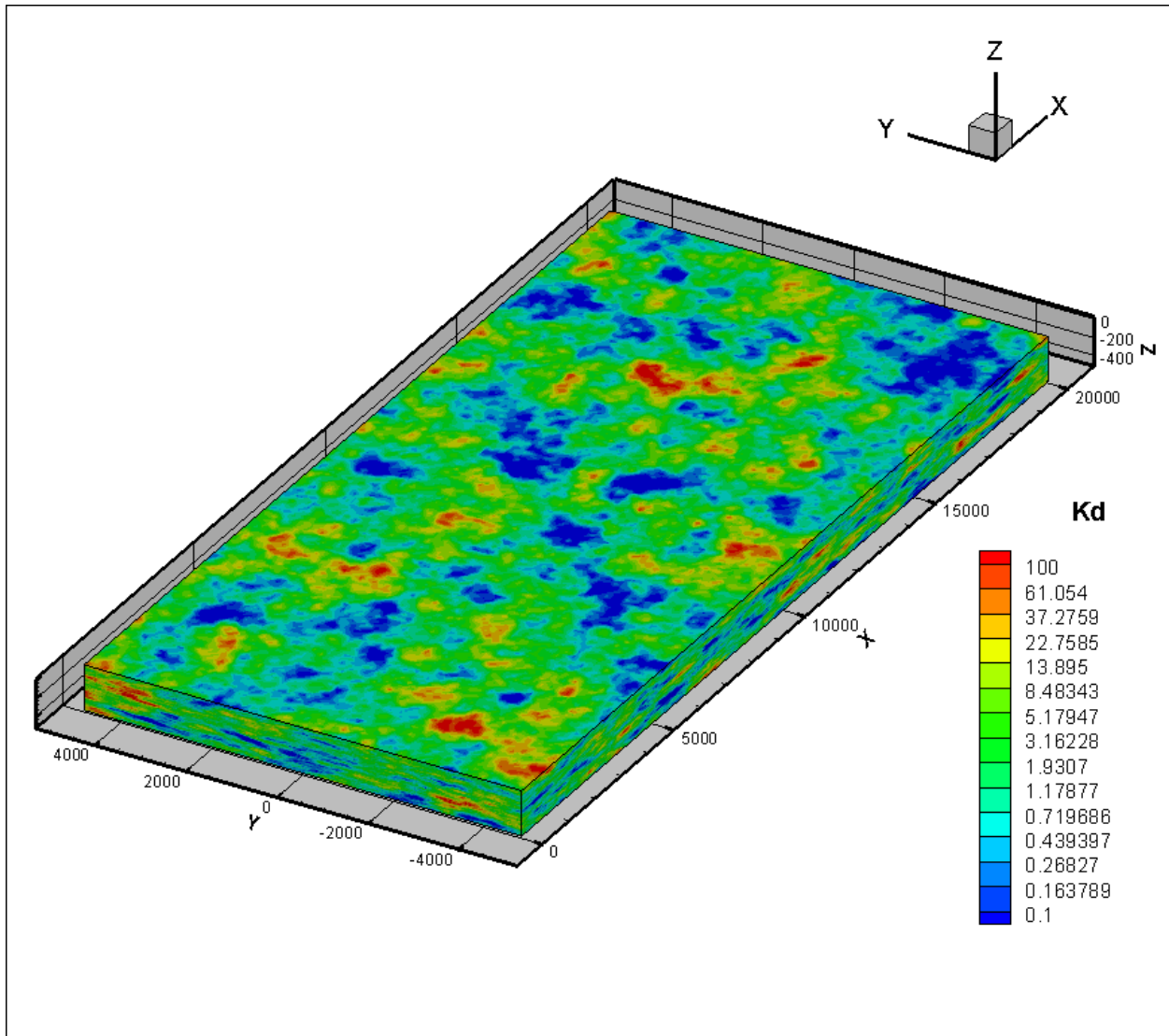
Figure 3-7. Example plot of heterogeneous K_d distribution with correlation length of (500m $\times$ 500m $\times$ 50m).
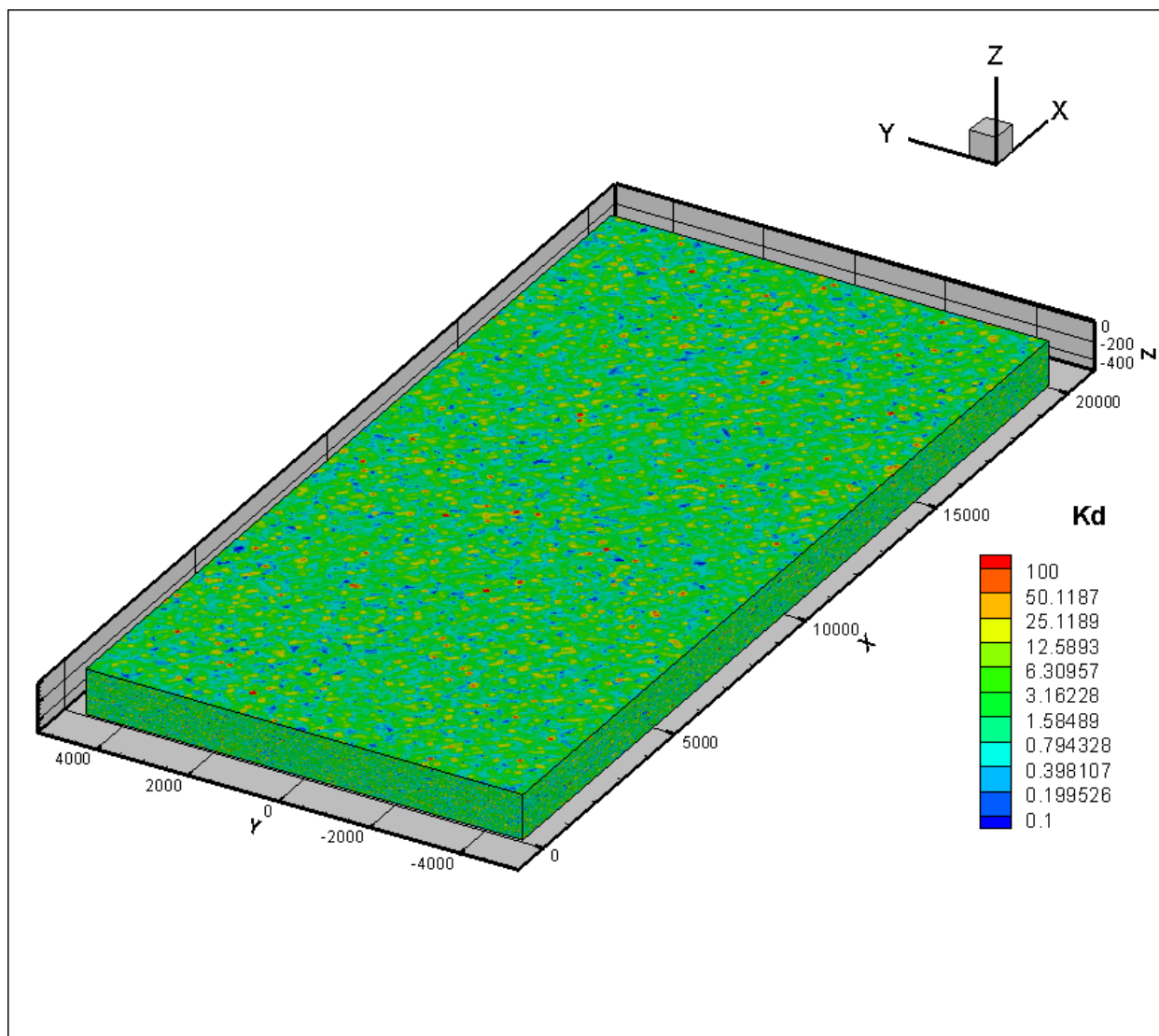
Figure 3-8. Example plot of heterogeneous K_d distribution without correlation.

3.3.2 Fractured rock

In fractured but otherwise low permeability rock, diffusion into the matrix and sorption onto matrix minerals are the primary processes that delay downstream movement of radionuclides. The retention properties of the matrix may vary both perpendicular and parallel to the fracture (Figure 3-9).
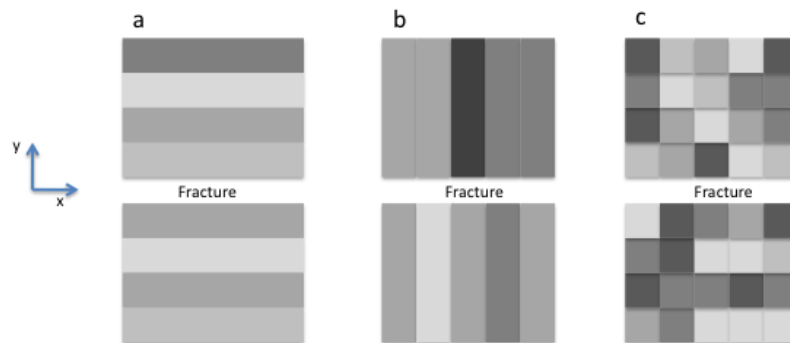
Figure 3-9. Three types of matrix variability. The K_d variability shown in (a) – with distance from the fracture – is analyzed here. Variability along the fracture (b) was analyzed previously (Deng et al. 2010).

Dai et al. (2009) and Deng et al. (2010) have analyzed the type of variability shown in Figure 3-9b (along the fracture). As far as we are aware, the corresponding analyses for the type of variability shown in Figure 3-9a (variability perpendicular to the fracture) have not been undertaken previously. As a preliminary step, new Monte Carlo simulations were undertaken to assess the potential impact.

The simulations consider flow along a 10 m long fracture. One mole of radionuclide is injected into the upstream side of the fracture at t=0. The discharge from the fracture is then calculated for each of multiple realizations of the matrix sorption characteristics and averaged to obtain the expected discharge. The matrix block adjacent to the fracture is 20 cm in extent and is discretized into 10 layers, each of which is 2 cm thick. The matrix retardation value ($R_m = 1 + \dfrac{\rho_b}{\phi} K_d$ where ρ_b is bulk density [kg/m^3] and ϕ is

porosity) in each layer was sampled from a log-normal distribution independent of the other layers to produce a single realization of the R_m field. Given a realization, the semianalytical recursive solution of Cvetkovic (2010) was used to solve for radionuclide discharge from the fracture. Cvetkovic's solution is for the Laplace transform of radionuclide discharge from the fracture and must be inverted numerically to obtain radionuclide discharge. Stehfest's (1970) method was used for the inversion.

Parameters for the six cases examined are shown in Table 3-1. Note that results here will be shown as a function of time shifted by the advective travel time τ. Parameterized this way, the radionuclide discharge (breakthrough) depends on the hydrodynamic transport resistance parameter $\beta = \tau/b$ and not on the advective travel time τ or the fracture half-aperture b individually.

Table 3.1. Parameters for six modeling cases examining the effect of K_d variability in the matrix.

	Case A	Case B	Case C	Case D	Case E	Case F
β [yr/m]	10^5	10^5	10^5	10^5	10^4	2×10^5
R_m^G	10	10	10	10	10	10
$\sigma_{\log R_m}^2$	0.0625	1	2	4	2	2
ϕ	0.01	0.01	0.01	0.01	0.01	0.01
D_e [m^2/s]	3×10^{-13}	3×10^{-13}	3×10^{-13}	3×10^{-13}	3×10^{-13}	3×10^{-13}
L [m]	10	10	10	10	10	10
where $\beta=\tau/b$ [yr/m] is the transport resistance parameter τ is advective travel time [yr] b is fracture half-aperture [m] R_m^G is geometric mean of the matrix retardation factor [-] $\sigma_{\log R_m}^2$ is log-variance of the matrix retardation factor [-] ϕ is matrix porosity [-] D_e is effective diffusion coefficient [m^2/s] L is length of the fracture [m]						

3.4 Consequences of Representing Spatial Variability as Parametric Uncertainty: Technical Results

3.4.1 Single-porosity media

Figures 3-10 to 3-13 show instantaneous breakthrough curves for a pulse release of 1 mole distributed among 10000 particles. The normalized breakthrough curves are widely spread in comparison with the breakthrough curve using a single uniform K_d (equal to the mean value of 3.937 ml/g) for the entire domain. The longer the horizontal correlation length of the sorption coefficient, the wider the normalized breakthrough curve.

Figure 3-14 shows the mean instantaneous and cumulative breakthrough curves for simulations with different K_d horizontal correlation length scenarios (2000 m, 1000 m, 500 m and no correlation). Also shown in Figure 3-14 are results using a parametric uncertainty approach in which K_d was treated as a random constant, i.e., being a constant spatially in each realization but randomly sampled from K_d distribution. The parametric uncertainty case is noisy at the ends of the curve because of the limited number of realizations used, but the general trends are clear. The parametric uncertainty case results in a broader breakthrough for this pulse release and a slightly higher peak of the mean discharge compared with the spatial variability cases. The parametric uncertainty case also results in much earlier breakthrough, which could produce an overly pessimistic picture of geosphere performance for decaying radionuclides (i.e. breakthrough before time to decay).

Ignoring spatial variability altogether and replacing the spatially variable K_d with a uniform value overestimates the peak of the mean breakthrough. However, the effect is relatively modest (factor of 2-3).
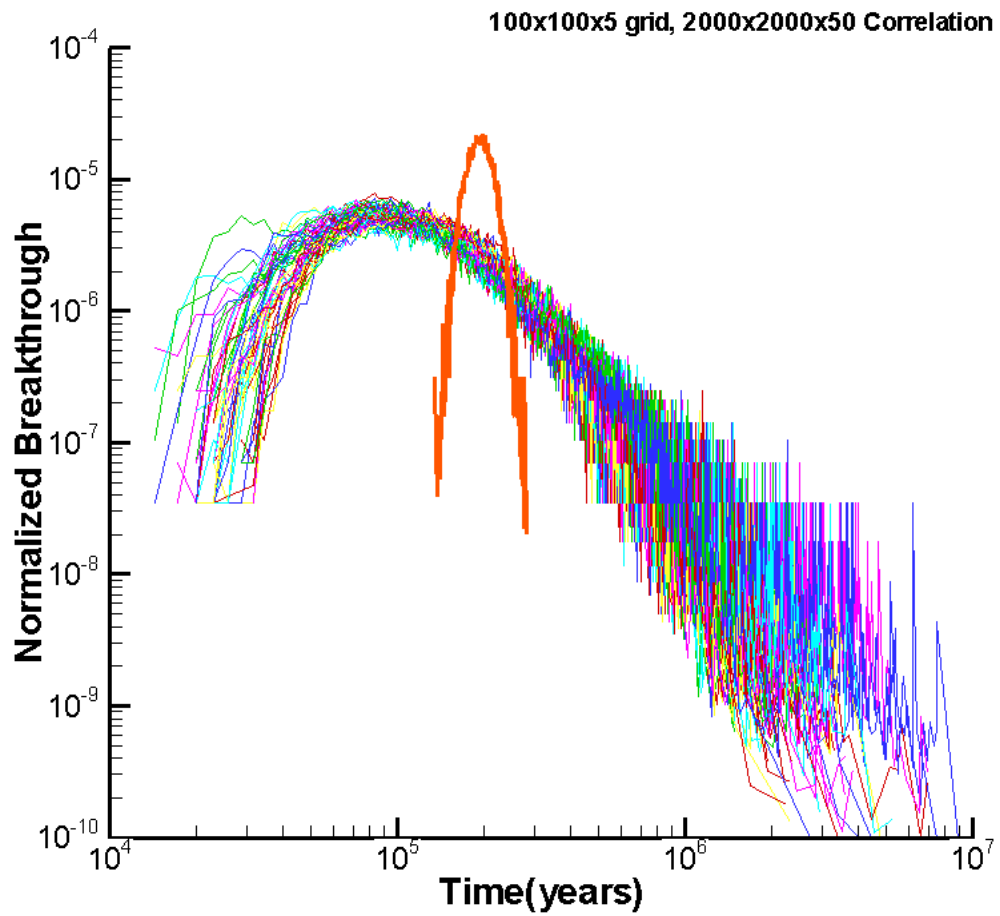
Figure 3-10. Instantaneous breakthrough curves for horizontal K_d correlation length of (2000m $\times$ 2000m $\times$ 50m) in comparison with uniform K_d scenario (using mean K_d value of 3.937 ml/g, red line).
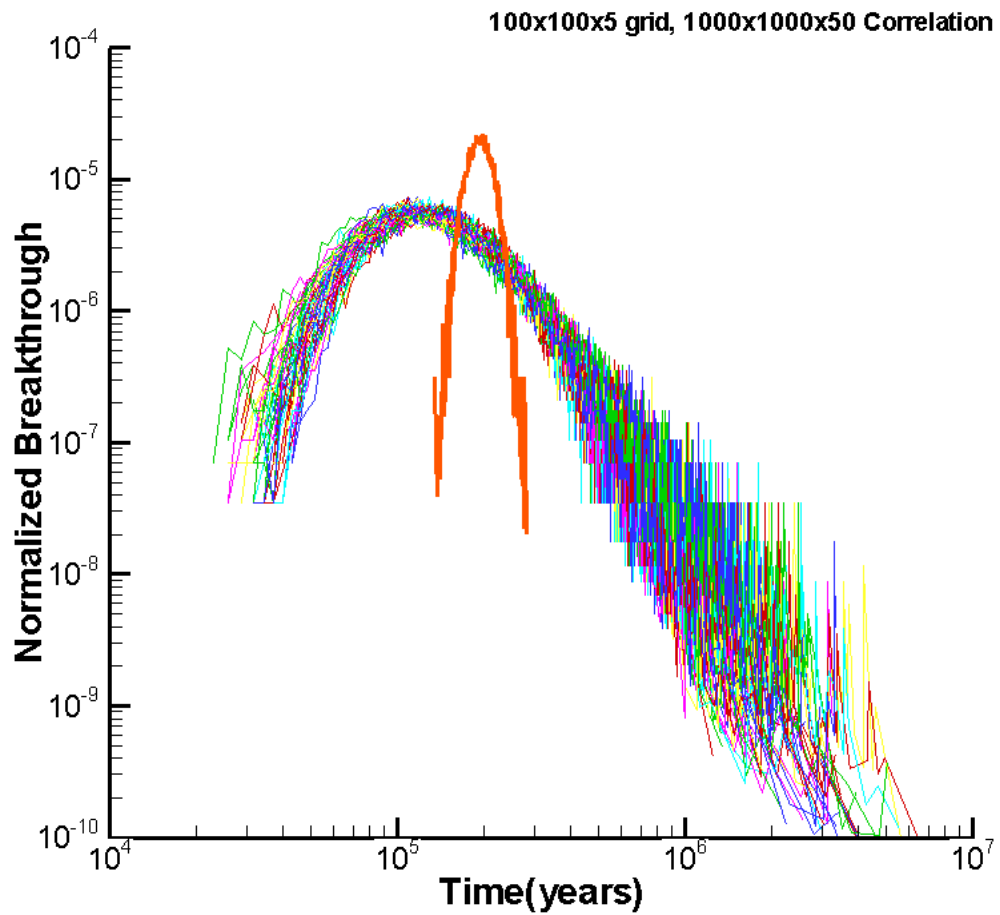
Figure 3-11. Instantaneous breakthrough curves for horizontal K_d correlation length of (1000m $\times$ 1000m $\times$ 50m) in comparison with uniform K_d scenario (using mean K_d value of 3.937 ml/g, red line).
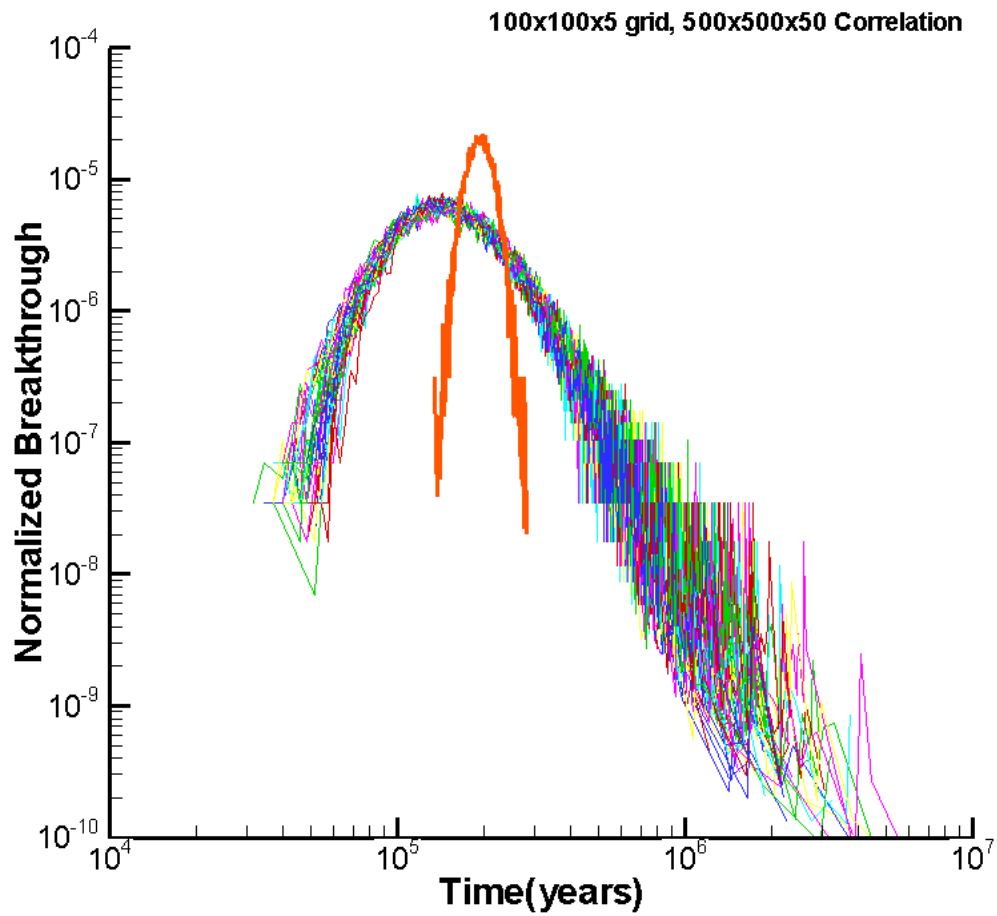
Figure 3-12. Instantaneous breakthrough curves for horizontal K_d correlation length of (500m $\times$ 500m $\times$ 50m) in comparison with uniform K_d scenario (using mean K_d value of 3.937 ml/g, red line).
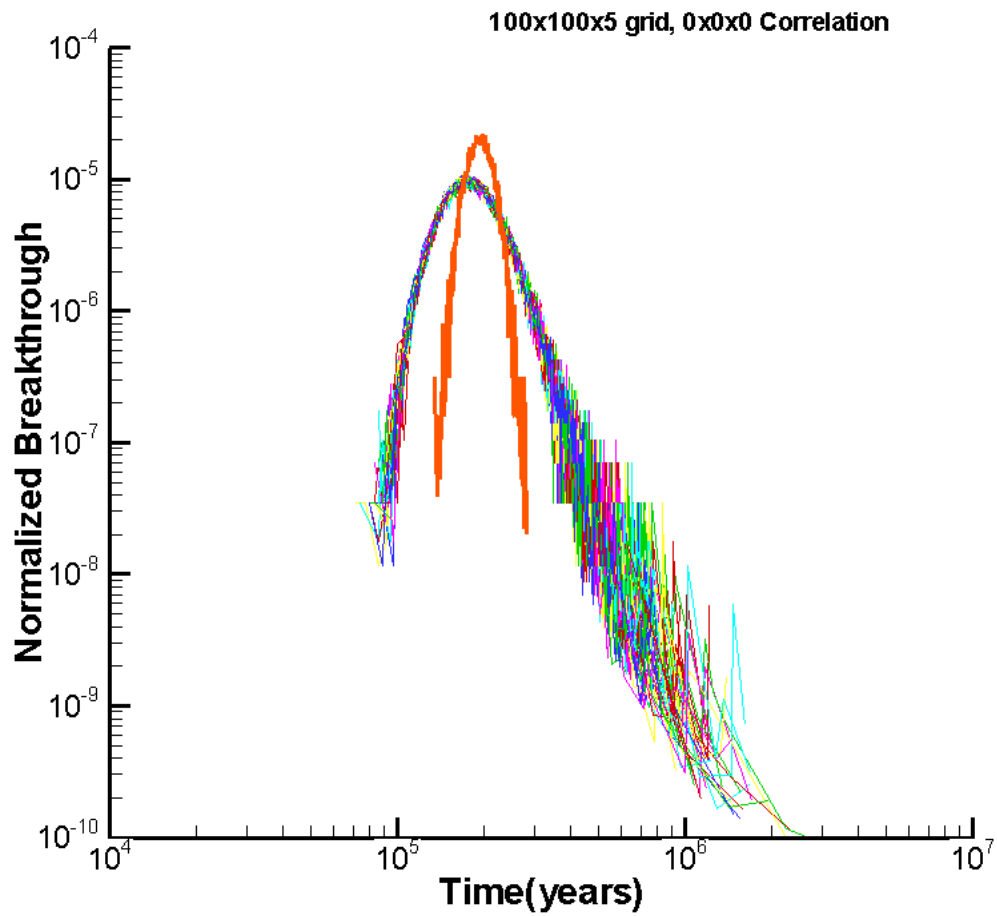
Figure 3-13. Instantaneous breakthrough curves for K_d without correlation in comparison with uniform K_d scenario (using mean K_d value of 3.937 ml/g, red line).
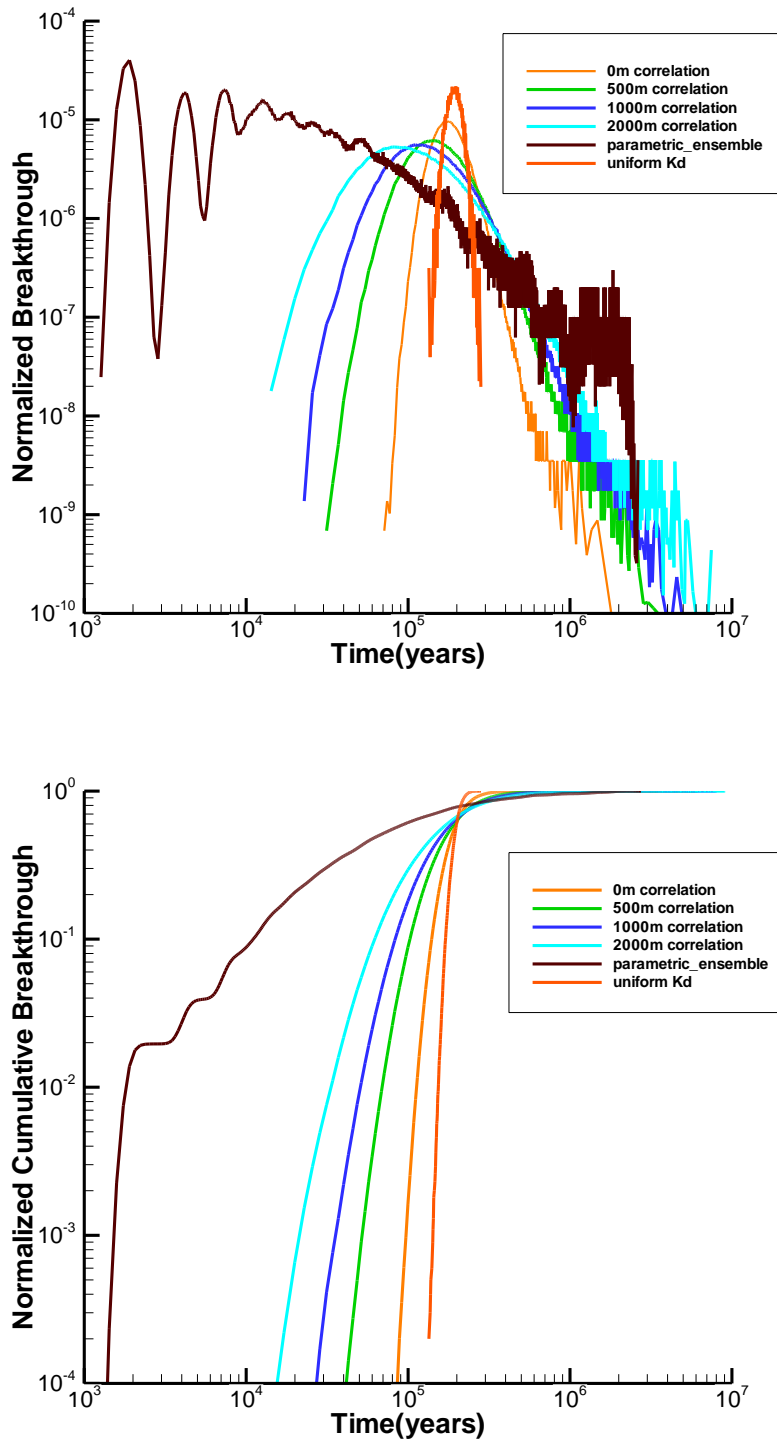
Figure 3-14. Mean breakthrough curves [top (a): instantaneous; bottom (b): cumulative] for heterogeneous distributed K_d with different horizontal correlation lengths in comparison with uniformed K_d run (using mean K_d value of 3.937 ml/g, red line), and ensemble of 51 realizations treating K_d as an uncertain parameter (brown line).

3.4.2   Fractured media

Figure 3-15 shows results for different degrees of variability in K_d, characterized by log-variance in matrix retardation factor R_m. In each plot, the green curve is the result with spatial variability in R_m, the black curve is the result with a single constant R_m value, and the blue curve is the result of treating R_m as an uncertain parameter. Note that rock density and porosity are treated as constant, so R_m variability is directly related to K_d variability. When the variability in R_m (or, equivalently, K_d) is small there is little difference between the three curves, as expected. As R_m variability increases, differences among the different R_m representations become apparent. Parametric R_m results in the largest peak breakthrough and earliest peaks, followed by spatially variable R_m and then constant R_m.

Figure 3-16 shows results for different values of the transport resistance parameter β. These two cases (E corresponding to $\beta=10^{-4}$ yr/m and F corresponding to $\beta=2 \times 10^{-5}$ yr/m) should be compared with case C ($\beta=10^{-5}$ yr/m).

Although there is clear separation among the three curves for all but the smallest of variability, the effect on the peak of the expected discharge is relatively modest unless the log-variance is large, in which case the parametric uncertainty case results in significantly higher peak of the mean. Significantly, the peak of the expected discharge is very similar between the spatial variability cases and the constant R_m cases. However, the time at which the peak occurs is smaller for the spatially variable R_m cases. These cases do not include radionuclide decay. For the cases with significant separation in the time of the peak expected discharge, including decay would enhance the differences between the constant K_d and spatially variable K_d results.
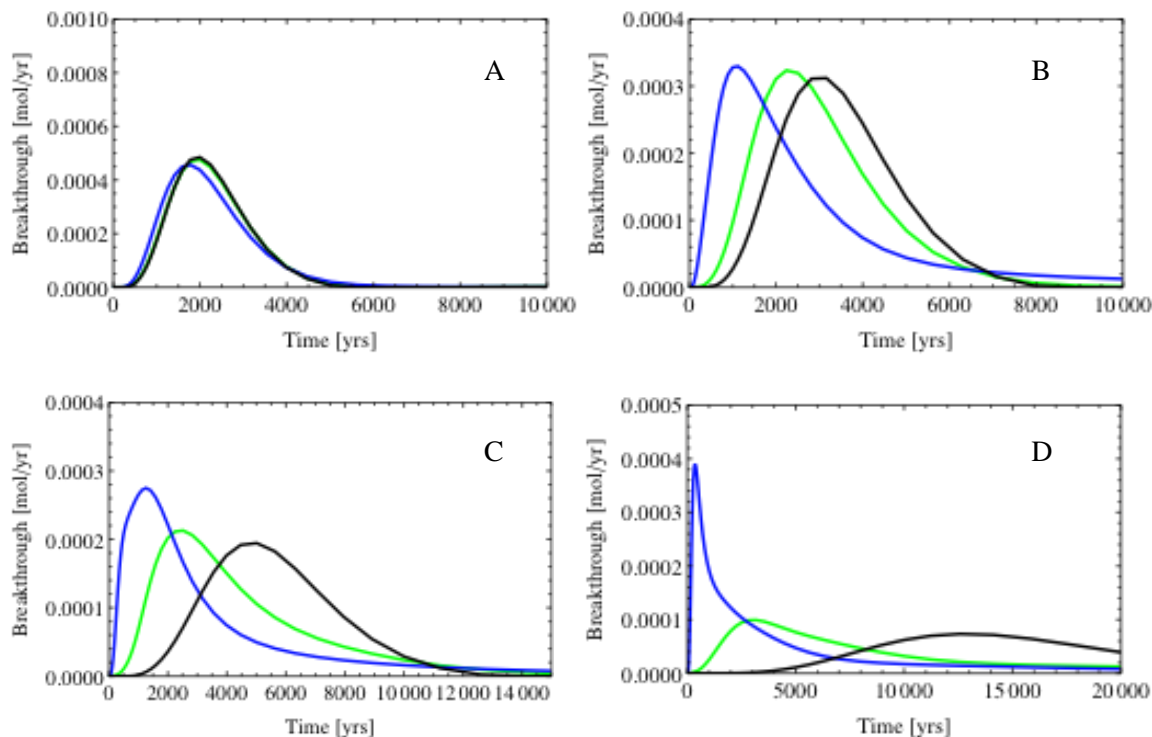
Figure 3-15. Effect of different K_d representations on calculated expected discharge for different levels of K_d variability. In each plot, the green curve is for spatial variability in matrix K_d, the blue curve is for parametric uncertainty in K_d, and the black curve is for constant K_d (no variability, no uncertainty). See Table 3-1 for parameter values for the A-D cases.
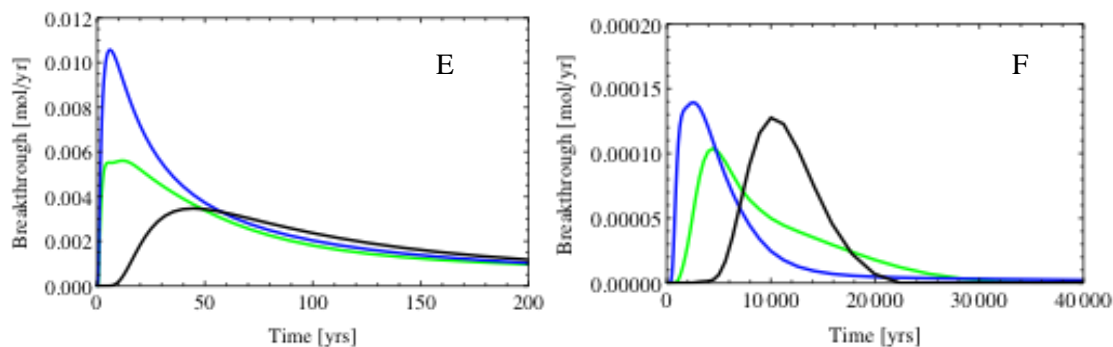
Figure 3-16. Effect of different K_d representations on calculated expected discharge for different values of the retention parameter β. In each plot, the green curve is for spatial variability in matrix K_d, the blue curve is for parametric uncertainty in K_d, and the black curve is for constant K_d (no variability, no uncertainty). See Table 3-1 for parameter values for the E and F cases.

3.5   Conclusions

3.5.1   Single Porosity Media

Single porosity media is likely to form the final leg of the radionuclide transport paths for many sites, irrespective of the repository host medium. Although significant results exist in a general theoretical context, the overwhelming majority of those studies do not specifically address impact on peak of the mean radionuclide discharge in a waste disposal context. Based on the preliminary studies presented here, the previous results of Painter et al. (2001), and general understanding gained in a more general theoretical context, several conclusions can be drawn.

The appropriate treatment of K_d in a performance assessment context depends on the spatial correlation length relative to the length of the transport path. If the correlation length is short relative to the length of the transport path, then the effective upscaled K_d approximates the mean K_d. In this situation, a constant K_d equal to the mean K_d gives good results. Conversely, if the correlation length is long compared to the travel distance, then K_d is essentially an uncertain parameter. The size of the correlation length is site dependent but should be expected to be short compared to the travel distance in most applications of interest. Moreover, the numerical experiments summarized here and in Painter et al (2001) suggest that constant K_d provides a reasonable approximation even when the correlation length is not zero. Thus, a deterministic and spatially constant K_d is appropriate for generic studies provided the only K_d uncertainty is caused by spatial variability. Moreover, substituting parametric uncertainty for spatial variability could lead to significant overestimation of peak of the mean radionuclide discharge into the biosphere.

For intermediate values of the correlation length, results from Lagrangian-based theoretical studies allow the effects of K_d variability to be included without resorting to numerical simulations. However, the Lagrangian approach neglects transverse dispersion and leads to analytical result only when the K_d variability is small. Moreover, existing results presume a single-mode random space function model for K_d variability and are unconditional (i.e. do not consider "conditioning" on measured K_d values on or near the flow paths). These restrictions are not significant limitations for generic studies, but do limit applicability for site-specific applications. Stochastic simulations based on geostatistical methods are recommended for site-specific applications.

3.5.2   Fractured Media

Comparatively few results exist on the effects of matrix K_d variability for fractured media. The preliminary results shown here and previous results of Dai et al. (2009) and Deng et al. (2010) suggest that the effect of K_d variability is modest. However, further study is warranted in light of the significant complexity in real fractured rock masses. Additional complications arise due to the spatial variations of the aperture field within fractures, which cause channeling and preferential transport and typically lead to more complex solute distributions in the rock matrix as well (Neretnieks, 2006). Complexity of the fracture network topology is another factor that will require a more complex theoretical analysis. In realistic fractured rock masses that incorporate the above complexities, a more general approach to deriving effective transport parameters could involve starting from the local-scale governing equations in the fracture and matrix domains viewed as stochastic partial differential equations (due to the random fields of fracture aperture, matrix porosity, retardation and tortuosity), and employing upscaling techniques such as those employed by Gelhar (1993) and Cvetkovic et al. (2007).

3.6   References

Allen-King R. M., Halket R. M., Gaulord D. R., and Robin M. J. L. (1998), Characterizing the heterogeneity and correlation of perchloroethene sorption and hydraulic conductivity using a facies-based approach, *Water Resources Research*, 34(3), 385-396.

Allen-King R. M., Divine D. P., Robin M. J. L., Alldredge J. R., and Gaylord D. R. (2006), Spatial distributions of perchloroethylene reactive transport parameters in the Borden Aquifer, *Water Resources Research*, 42, W01413, doi:10.1029/2005WR003977.

Andersson P., Byegard J., Tullborg E. L., Doe T., Hermanson J., and Winberge A. (2004), In situ tracer tests to determine retention properties of a block scale fracture network in granitic rock at the Aspo Hard Rock Laboratory, Sweden, *Journal of Contaminant Hydroogy*, 70(3), 271–297.

Bellin A., Rinaldo A., Bosma W., van der Zee S., and Rubin Y. (1993), Linear Equilibrium Adsorbing Solute Transport in Physically and Chemically Heterogeneous Porous Formations 1. Analytical Solutions, *Water Resources Research*, 29(12), 4019-4030.

Berkowitz B., Cortis A., Dentz M., and Scher H. (2006), Modeling non-Fickian transport in geological formations as a continuous time random walk, *Reviews of Geophysics*, 44, RG2003, doi:10/1029/2005RG000178.

Burr D. T., Sudicky E. A., and Naff R. L. (1994), Nonreactive and reactive solute transport in three-dimensional heterogeneous porous media: Mean displacement, plume spreading, and uncertainty, *Water Resources Research*, 30(3), 791–815.

Chao C.-H., Rajaram H., and Illangasekare T. H. (2000), Intermediate-scale experiments and numerical simulations of transport under radial flow in a two-dimensional heterogeneous porous medium, *Water Resources Research*, 36(10), 2869–2884.

Cushman J. H., Bennethus L. S., and Hu B. X. (2002), A primer on upscaling tools for porous media, *Advances in Water Resources,* 25(8-12), 1043-1067.

Cvetkovic V. and Dagan G. (1994), Transport of kinetically sorbing solute by steady random velocity in heterogeneous porous formations, *J. Fluid Mech.*, 265(1), 189–215.

Dagan G. (1989), *Flow and Transport in Porous Formations*, Springer, New York.

Dai Z., Ritzi R.W., Huang C., Rubin Y.N., and Dominic D. F. (2004), Transport in heterogeneous sediments with multimodal conductivity and hierarchical organization across scales, *Journal of Hydrology*, 294(1-3), 68-86.

Dai Z., Wolfsberg A. V., Lu Z., and Ritzi R. W. (2007a), Representing aquifer architecture in macrodispersivity models with an analytical solution of the transition probability matrix, *Geophysical Research Letters*, 34, L20406, doi:10.1029/2007GL031608.

Dai Z., Wolfsberg A. V., Lu Z., and Reimus P. W. (2007b), Upscaling matrix diffusion coefficients for heterogeneous fracture media, *Geophysical Research Letters*, 34, L07408, doi: 10.1029/ 2007GL029332.

Dai Z., Wolfsberg A. V., Lu Z., and Deng H. (2009), Scale dependence of sorption coefficients for radionuclide transport in saturated fractured rock, *Geophysical Research Letters*, 36, L01403, doi:10.1029/2008GL036516.

Deng H., Dai Z., Wolfsberg A., Lu Z., Ye M., Reimus P. (2010), Upscaling of reactive mass transport in fractured rocks with multimodal reactive mineral facies. *Water Resources Research* 46, doi:10.1029/2009WR008363.

Deng H., Dai Z., Wolfsberg A. V., Lu Z., and Ye M. (in review), Upscaling retardation factor for hierarchical porous media with multimodal sorption coefficients and conductivity, *SIAM Multiscale Model. Simul., in review,* 2011.

Deutsch C.V., and Journel A.G. (1992) GSLIB: Geostatistical Software Library. Oxford Univ. Press, New York, NY.

DyKaar B., and Kitanidis P. K., (1992), Determination of the effective hydraulic conductivity for heterogeneous porous media using a numerical spectral approach: 2. Results, *Water Resources Research*, 28(4), 1167-1178.

Fernàndez-Garcia D., Illangasekare T. H., and Rajaram H. (2005), Differences in the scale dependence of dispersivity and retardation factors estimated from forced-gradient and uniform flow tracer tests in three-dimensional physically and chemically heterogeneous porous media, *Water Resources Research*, 41, W03012, doi:10.1029/2004WR003125.

Fokker P. A. (2001), General anisotropic effective medium theory for the effective permeability of heterogeneous reservoirs, *Transport in Porous Media*, 44(2), 205-218.

Frampton A. and Cvetkovic V. (2007), Upscaling particle transport in discrete fracture networks: 2. Reactive tracers, *Water Resources Research*, 43, W10429, doi:10.1029/2006 WR005336.

Gelhar L.W., Welty C. W., and Rehfeldt K.R. (1992), A critical review of data on field scale dispersion in aquifers, *Water Resources Research*, 28(7), 1955-1974.

Gelhar L. W. and Axness C. L. (1983), Three-dimensional stochastic analysis of microdispersion in aquifers, *Water Resources Research*, 19(1), 161-180.

Gelhar, L.W. (1993), *Stochastic Subsurface Hydrology*, Prentice-Hall, Englewood Cliffs, NJ.

King P. R. (1989), The use of renormalization for calculating effective permeability, *Transport in Porous Media*, 4(1), 37-58.

Horung U. (1997), *Homogenization and Porous Media*, Springer, New York, 279pp.

Huang H. and Hu B. X. (2000), nonlocal nonreactive transport in heterogeneous porous media with interregional diffusion, *Water Resources Research*, 36(7), 1665-1675.

Huang H. and. Hu B. X. (2001), Nonlocal reactive transport in heterogeneous dual-porosity media with rate-limited sorption and interregional diffusion, *Water Resources Research*, 37(3), 639-747.

Liu H. H., Zhang Y. Q., and Molz F. J. (2007a), Scale dependence of the effective matrix diffusion coefficient: some analytical results. *Vadose Zone Journal*, 6(3), 679-683.

Liu C., Zachara J. M., Qafoku N. P., and Wang Z. (2008), Scale-dependent desorption of uranium from contaminated subsurface sediments, *Water Resources Research*, 44, W08413, doi:10.1029/2007 WR006478.

Molz F. J., Rajaram H., and Lu S. (2004), Stochastic fractal-based models of heterogeneity in subsurface hydrology: origins, applications, limitations, and future research questions, *Reviews of Geophysics*, 42, RG1002, doi:10.1029/2003RG000126.

Neretnieks I. (2006), Channeling with diffusion into stagnant water and into a matrix in series, Water Resour. Res., 42, W11418, doi:10.1029/2005WR004448.

Noetinger B. (1994), The effective permeability of a heterogeneous porous media, *Transport in Porous Media*, 15(1), 99-127.

Noetinger B. and Estebenet T. (2000), Up-scaling of double porosity fractured media using continuous-time random walks methods, Transport in Porous Media, 39(3), 315-337.

Neuman S. P. (1990), Universal scaling of hydraulic conductivities and dispersivities in geological media, *Water Resources Research*, 26(8), 1749-1758.

Painter S. and Paterson L. (1994), Fractional Lévy motion as a model for spatial variability in sedimentary rock, Geophys. Res. Lett., 21(25), 2857–2860, doi:10.1029/94GL02035.

Painter S., Cvetkovic V. and Turner D. R (2001) Effect of heterogeneity on radionuclide retardation in the alluvial aquifer near Yucca Mountain, Nevada, *Ground Water*, 39(3), 326-338.

Painter S., Cvetkovic V., (2005), Upscaling discrete fracture network simulations: An alternative to continuum transport models, *Water Resources Research*, 41, doi:10.1029/2004WR003682.

Rajaram H. (1997), Time and scale dependent effective retardation factors in heterogeneous aquifers, *Advances Water Resources*, 20(4), 317-230.

Renard P. and de Marsily G. (1997), Calculating equivalent permeability: a review, *Adv. Water Resour.*, 20(5), 253-278.

Robin M. J. L., Sudicky E. A., Gillham R. W., and Kachanoski R. G. (1991), Spatial variability of strontium distribution coefficients and their correlation with hydraulic conductivity in the Canadian forces base Borden aquifer, *Water Resources Research*, 27(10), 2619–2632.

Rubin Y. (2003), *Applied Stochastic Hydrogeology*, Oxford Univ. Press, New York.

Samper J. and Yang C. (2006), Stochastic analysis of transport and multicomponent competitive monovalent cation exchange in aquifers, *Geosphere*, 2(2), 102-112, doi: 10.1130/GES00030.

Sanchez-Vila X., Carrera J., and Girardi J. P. (1996), Scale effects in transmissivity, *Journal Hydrology*, 183(1), 1-22.

Sanchez-Vila X., Guadagnini A., and Carrera J. (2006), Representative hydraulic conductivities in saturated groundwater flow, *Reviews of Geophyics*, 44, RG3002, doi:10.1029/2005RG000169.

Slattery J. C. (1967), Flow of viscoelastic fluids through porous media, *AIChEJ*, 13(6), 1066-1071.

Stehfest H. (1970), Numerical inversion of Lapalce transforms, Communications ACM, 13, 47–49.

Stoller-Navarro Joint Venture (2007), *Phase I contaminant transport parameters for the groundwater flow and contaminant transport model of Corrective Action Unit 97: Yucca Flat/Climax Mine, Nevada Test Site, Nye County, Nevada*, Revision No.: 0, September 2007, S-N/99205-096.

Stoller-Navarro Joint Venture (2009), *Phase I Transport Model of Corrective Action Units 101 and 102: Central and Western Pahute Mesa, Nevada Test Site, Nye County, Nevada* (draft), S-N/99205-111.

Tompson A. F. B. (1993), Numerical simulation of chemical migration in physically and chemically heterogeneous porous media, *Water Resources Research*, 29(11), 3709–3726.

Turner D. R and Pabalan R. T. (1999), Abstraction of mechanistic sorption model results for performance assessment calculations at Yucca Mountain, Nevada. *Waste Management* 19, 375-388.

Wang Y. (2011), *Research & Development Plan for Used Fuel Disposition Campaign (UFDC) Natural Systems Evaluation and Tool Development*, U.S. DOE Used Fuel Disposition Campaign, May 25, 2011.

Whitaker S. (1967), Diffusion and dispersion in porous media, *AIChEJ*, 13(3),420-427.

Zavarin M., Carle S. F., and Maxwell R. M. (2004), *Upscaling Radionuclide Retardation-Linking the Surface Complexation and Ion Exchange Mechanistic Approach to a Linear Kd Approach*, UCRL-TR-204713, Lawrence Livermore National Laboratory, Livermore, California.

Chapter 4: Radionuclide Sorption on Clays: From Dilute to Highly Compacted Systems

4.1   Introduction

Clay minerals are ubiquitous in the environment and have been intensely studied for decades. More recently, clays have grown in importance as they exhibit several useful properties in the context of natural or engineered barriers for nuclear waste or CO_2 sequestration. These properties can include: low permeability, high sorption capacities, and the ability to swell. In describing these systems, a conceptual model is required that can encompass and describe the relative impacts from a long list of interrelated processes. These processes include the geomechanical processes related to stresses, pressures, and temperatures at depth, as well as the hydrological concerns of water/fluid flow, and the geochemical processes of reaction. Such a conceptual model is quite ambitious, as each of these disciplines has individualized limitations and questions that remain to be answered; the combination of these processes encompasses these unanswered questions and also creates new realms of interfacial inquiry based on overlapping or interacting processes.

This chapter addresses Topics P2 and P10 of the R&D Plan for the UFDC Natural Systems Evaluation and Tool Development (Wang, 2011; Chapter 1). The focus of this chapter is to consider how chemical reactions couple with geomechanical compaction under conditions relevant to nuclear waste disposal. Specifically, the chemical reaction that will be considered is radionuclide sorption/ion exchange to individual and natural clay minerals. From a geochemical perspective, the degree of compaction ranges from the single clay particle or dilute suspensions up to heavily compacted clay columns. This range of systems allows for a broad range of chemical variability based on the degree of particle-particle interaction even though the chemistry of the solid phase may be consistent throughout. This review begins with a general discussion of chemistry in physically restrictive environments. This general discussion will then be applied to the more specific case of radionuclide sorption to clays. Many aspects of sorption will be considered including: acid/base chemistry of clays, surface charge, and models that have been derived to describe the interactions. The review will also cover descriptions and experiments involving sorption and diffusion in highly compacted clays, and will end with several perspectives on the state of the science and future directions.

4.2   Background

The addition of chemical reactions to a thermal-hydrological-mechanical-chemical (THMc) model framework is an explicit attempt at joining the physical and chemical realms. Much of this paper is devoted to what is already known in linking these two realms. One level of interaction between these two realms is illustrated in Table 4-1. At their simplest, clays are metal oxides. They contain both a metal or metalloid (Al, Mg, or Si) bound to either oxygen or hydroxide. And yet there is much to distinguish clays from, for example, quartz. Much of these differences relate to the physical and chemical properties of these two types of minerals. Traditional metal oxides are very simple from a chemical perspective. Ignoring any impurities, there are only two or three atomic species controlling the chemical behaviors, including the metal, oxygen, and hydrogen. All of the variation in observed chemical behaviors stems from different physical environments. When a crystal is cleaved, there are local alterations in the number of bonds exposed to solution based on the physical structure that is created. In other words, pits, edges,

corners, and any other physical micro-shape the crystal takes gives rise to surface heterogeneity that can be observed in sorption experiments. Clays, however, have both chemical and physical heterogeneities. Not only do they contain some mixture of Al and/or Mg with Si, but these species are separated into tetrahedral and octahedral layers. Even within these layers, there are often a significant amount of substitutions where one of those central ions is replaced by another species such that an individual layer is not pure Si-O, or Al-O. Furthermore, these layers can be bound together in a variety of ways giving rise to different morphologies of the different clay minerals. For example, the individual 2:1 layers in sepiolite invert in a regular pattern forming fibers and large void spaces filled with water. Other clays, for example kaolinite, form continuous sheets leading to a voidless, platy morphology. All of this chemical and physical complexity can lead to behaviors unobserved in traditional metal oxides, most notably ion exchange. Many of the experimental techniques, elaborated on below, are taken directly from the study of more traditional metal-oxides (e.g., goethite, gibbsite, quartz, etc.). Despite furthering knowledge of clay minerals, this application of experimental techniques is at times hindered by the fundamental differences between traditional metal oxides and clays. All of the relationships discussed so far are 'internal' in nature; they arise from the fundamental atomic arrangements to yield observable effects in the solution phase.

Table 4-1. List of physical and chemical properties of traditional metal oxides and clays

	Traditional Me-Oxide	Clays
Physical	• Crystal shape (cubic, tetrahedral, etc.) • Imperfections (pits, etchings, etc.)	• Layered (1:1 vs. 2:1) • Imperfections (stack irregularities, etchings, etc.) • Morphological variations (fibrous, platy, etc.)
Chemical	• Homogenous (2 or 3 species make up crystal ignoring imperfections)	• Heterogeneous mixture (Al, Si, and Mg-oxides) • Lattice substitutions

In THMc modeling, there are also 'external' effects. These effects are largely not derived from an internal structure, but they represent a force acting on the clay which may or may not have an effect on the chemical relationships between the mineral and the solution. For example, these processes could include hydrothermal alterations to mineral phases (Alba et al., 2010; Zheng and Samper, 2008), or compaction and mineral dissolution/alteration (Dewers and Ortoleva, 1990). The connection between 'external' effects and chemistry is probably the weakest connection in THMc modeling. In a conceptual rendering of THMc modeling (Zheng and Samper, 2008), no direct connection is currently shown between chemical and mechanical processes. However, there is broader evidence from other disciplines that external forcing may lead to alterations in surface chemical reactions in clay-based systems.

Figure 4-1 shows a plot conceptualizing the relationship between surface chemical behaviors and constricted space. The x-axis shows a continuum between Al-O and Si-O endmembers with clay minerals being a mixture of the two. For some clays it makes more sense to have a Mg-O endmember instead of the Al-O. For the purposes of this discussion either are viable options, but there is more experimental data for nanoporous Al-O than Mg-O. The y-axis shows a continuum between constrained space and infinite space. Location within this space relates to the chemical behavior for the set of conditions given. For example, the Al-O endmember in infinite space can be thought of as an Al-O particle in a stirred batch solution. In this case, the space between individual solid particles is large enough such that particle-particle interactions can be neglected and space is 'infinite'. By contrast, nanoporous Al-O have been

shown to have chemical behaviors quite different from that of well-dispersed particles (Baca et al., 2008; Wang et al., 2002). Thus, despite having an identical chemical nature, the constrained space that occurs in the nanoporous regime alters the way that chemistry proceeds. That is why these two areas are separated in the figure. Similar arguments hold for the Si-O phases (Campen et al., 2010; Dove and Craven, 2005) (see also Wang et al., 2011 for a broader view of nanoporous materials in earth systems). However, clays are unique from these purer phases. From the figure, dispersed clays are slightly lower on the space axis. Due to the interlayer formation of clays, nanoconfined environments are possible even in dispersed systems due to the internal properties of the clay minerals. Thus attaining the infinite space in the same way that other Me-O particles do is not likely. Furthermore, as these clays are compacted, the amount of nanoconfinement is likely to increase unlike most other metal oxides. Clays have been found to have a dual porosity type nature (Lloret et al., 2003; Musso et al., 2003). These two different porosities also change independently of each other as a function of increasing compaction. The inter-aggregate pore space decreases with increasing compaction, while the intra-aggregate pore space does not (Lloret et al., 2003). This means that as compaction increases, the total pore space is increasingly dominated by the smaller intra-aggregate pores (<100nm). The effect of confinement is demonstrated in Figure 4-1 by moving from the dispersed clay particles down to the compacted clays. This same movement through the defined space also changes the system from where there are purely internal controls on chemistry, in the dispersed systems, to where there are both internal and external controls on chemistry, in the compacted or nanoporous systems.

Figure 4-1. Chemical behaviors as a function of chemical and physical environments

In moving from the unrestricted to restricted environments, there is a transition that occurs which is pictured in Figure 4-2. This figure considers clay behaviors as a continuum of solids concentration ranging from single particle/diffuse systems up to highly compacted clay environments. Over this range, the physical and chemical environments change as the particle-particle interactions become increasingly important. Using the definitions presented here, there is an increasingly external component controlling ion behavior. These changing environments have much in common with mesoporous materials in the sense that the surface environment of the clay particle increasingly deviates from the non-curved infinite plane conceptual model upon which most surface complexation theory is based.

Internal Processes:
Physical/chemical processes based only on the atoms present and their interactions

Internal/External Processes:
Physical/chemical processes based on internal processes and on interactions with an external forcing function

Single/Many Particle(s)
• Fundamental characterization and descriptions

Concentrated Suspension of Particles
• Colloidal interactions

Highly Compacted Columns
• Highly forced particle-particle interactions

Dilute Suspension of Particles
• Continuum scale information
• Observable chemical reactions

Semi-Compacted Columns
• Forced particle-particle interactions

• As solids concentration increases chemical (and charge) environment changes
  • Single/Many Particles: No particle-particle interactions (by definition)
  • Dilute Suspensions: No particle-particle interactions (by assumption)
  • Concentrated Suspensions: DLVO type interactions, possible polymerization of clay particles
  • Semi-Compacted Column: Overlapping double layers
  • Highly-Compacted Columns: Overlapping double layers and compression of the interparticle space
• No current geochemical model can take this changing environment into account
  • Severe lack of data spanning this range
  • Lack of consensus on charge description models

Figure 4-2. Clay behaviors as a function of increasing solids concentration

The remainder of this paper is split into two main parts. The first part will discuss internal structure-function relationships and the state of the science with respect to how clay structures are probed experimentally as well as the modeling that is used to interpret the data. The second part will discuss what is known about external structure-function relationships with a special focus on the relationship between clay compaction and chemical reactions, and how chemical reactions proceed in constrained environments.

4.3   Internal Structure-Function

From the internal perspective, there are three main variables that require attention when considering ion interaction with clays. These variables are: the general structure and chemical composition of the clay mineral, surface charge development and alterations as a function of solution conditions, and ion

complexation and interaction with the clay particles. Each of these variables can be characterized using a suite of techniques. For general characterization this can include microscopy techniques (e.g., TEM, HRTEM, AFM, etc.) as well as high energy techniques (e.g., XRD, XANES, etc.). Surface charge is studied through electrokinetic experiments and both continuous and discontinuous surface titrations. Ion complexation is generally probed through batch and diffusion experiments with specific surface complexes being confirmed with spectroscopic techniques. In this section we will synthesize the knowledge gained from all of these techniques with the exception of the diffusion experiments. The discussion of diffusion experiments will occur in the External Structure-Function section, below.

In an attempt to visually map out the text in this chapter, experimental and modeling techniques can be conceptualized as shown in Figure 4-3. Figure 4-3 shows two separate Venn diagrams representing the progression and overlaps between both experimental and modeling techniques found in the literature. On the experimental side, the first circle represents electrokinetic experiments. The next circle represents surface titrations to determine surface charge characteristics. The overlap between these two circles represents studies which performed both electrokinetic and surface titration experiments and attempt to combine the information from both techniques into a common theory. On the right hand side of Figure 4-3, a similar diagram is shown for modeling techniques. The difference in the overall structure of the left and right hand sides reflects the differences in studies that have been completed to date. For example, there are no experimental diffusion studies which also measure electrokinetic behaviors. However, on the modeling side, there are studies which describe diffusion and surface charge but not surface complexation (e.g., Na^+ diffusion in clay), as well as diffusion studies which consider surface complexation without considering surface charge (e.g. Sr^{2+} complexation and diffusion described with a non-electrostatic K_D based approach). But there are no experimental diffusion studies which are modeled with molecular dynamic simulations. The modeling part of the diagram will only be discussed relative to the experimental work. Common to both the experimental and modeling techniques are many of the basic characterization techniques used to constrain both models and experiments, hence why they are listed in the middle of the diagram. In this chapter we will start with the common characterization techniques, and then discuss other experimental approaches, with the modeling being discussed within the context of the experiments.
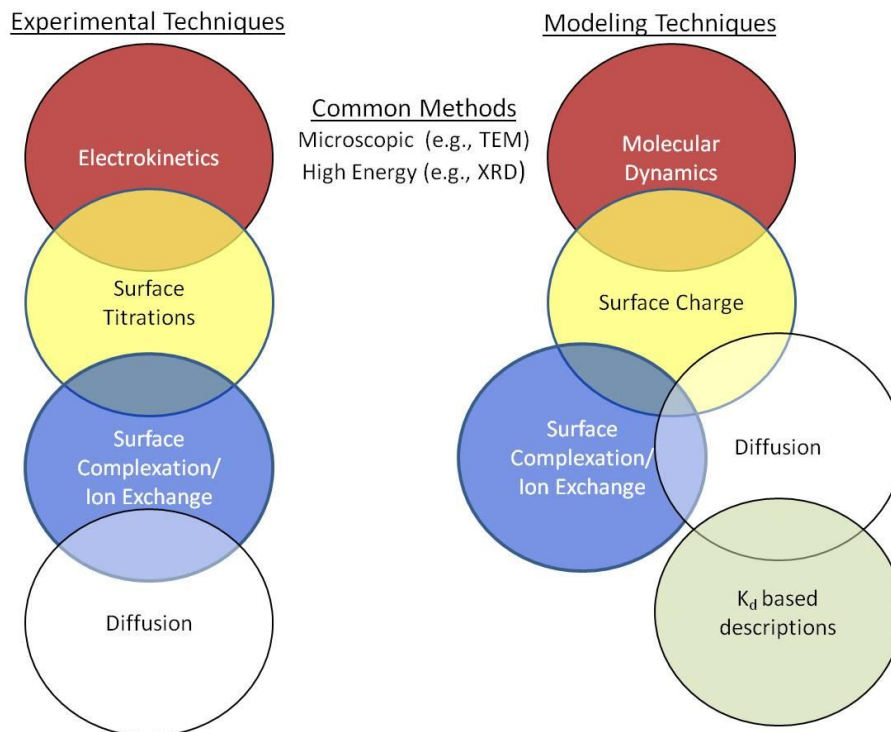
Figure 4-3. Pictorial representation of overlaps in experimental and modeled domains. The vast majority of references in this chapter are associated with only one area in either the experimental or modeling diagram. Thus there are studies where surface titrations and electrokinetic experiments are performed, but no studies where electrokinetics and surface complexation/ion exchange experiments are performed.

4.3.1   Clay Characterization

One of the most common uses of characterization techniques is to use the information gained to either rule out impurity mineral phases or to constrain model parameters. XRD is most commonly used to identify impurities (Coppin et al., 2002; Tournassat et al., 2004b; Chipera and Bish, 2001). But, it has also been used to determine the following: number of water layers in bentonite interlayer spaces (Melkior et al., 2009), the expansion of the basal spacing upon organic adsorption within the interlayers (Dultz et al., 2005), as well as determining whether there has been any mineralogical alterations over the course of an experiment (Coppin et al., 2002) or due to the clay mineral purification procedure (Bektas et al., 2004). Another characterization technique, X-ray absorption near edge structure (XANES), has been used both to determine iodine redox speciation sorbed to a series of minerals including biotite (Fuhrmann et al., 1998) and to characterize differences in Mg binding structure between two similar clays, sepiolite and palygorskite (Sanchez del Rio et al., 2005). Polarized extended X-ray absorption fine structure (p-EXAFS) has been used to characterize the sorption mechanisms of metals onto clay mineral structures. An earlier p-EXAFS work with Zn and hectorite showed Zn proceeding through a fast outer sphere complex on a basal plane ion exchange site, followed by a slow transition to an inner sphere complex on an edge site occurring either through surface diffusion or release and re-adsorption (Schlegel et al., 2001). A more recent work with Ni and montmorillonite showed that the diffusion pathway is unlikely (Dahn et al., 2003). Various types of advanced microscopies (SEM, TEM, and high resolution-TEM [HRTEM]) have also been used to characterize clay minerals. SEM has shown that Pb sorption to palygorskite causes an immediate morphological change in the clay particles (Chen and Wang, 2007). TEM has been used to

visually identify and show $Al(OH)_3$ alteration products of kaolinite located on the basal plane of the clay platelet (Thompson et al., 1999). In a different study with HRTEM, a smectite-like outer layer was observed for a field derived kaolinite (Ma and Eggleton, 1999) and physical channels and other deviations from a 'smooth' face on a kaolinite platelet were also found with atomic force microscopy (AFM, Brady et al., 1996). HRTEM has also found a large degree of physical defects in clay minerals, including dislocations of platelet stacks, lateral layer terminations, and deformation of particles from perfectly stacked layers (Krekeler and Guggenheim, 2008; Ma and Eggleton, 1999). And finally, HRTEM has been used to characterize textural variations as a function of solution chemistry in bentonite (Melkior et al., 2009). This study found that bentonite exposed to a NaCl solution forms a 'gel phase,' and that the presence of the gel phase has implications on both tritium and Na^+ diffusion rates. When the bentonite is exposed to a $CsCl_2$ solution the 'gel phase' does not form.

Much of the micro- and nano-characterization of clay particles has been compiled and considered by Drits (Drits, 2003) and Johnston (Johnston, 2010). Johnston makes many connections between clay physical structures and both molecular dynamic simulations and charge distributions. Drits focuses on the structural and chemical heterogeneity of individual and ensembles of clay particles. The message from much of this information is that clay particles have physical and chemical heterogeneities at a range of scales. At the atomic scale the degree and exact physical locations of isomorphous substitution in any of the clay layers is nearly impossible to measure directly. This necessitates a feedback between molecular dynamic simulation with advanced microscopies and spectroscopies to determine atom scale heterogeneities (Drits, 2003). At the micron scale, clay particles can take on a variety of morphologies depending on the size and interaction of the individual platelets and chemical conditions in solution. Thus the conceptual model of clays being a regularly ordered, layered mineral with known chemical composition is difficult to justify. In many ways this is the inspiration of Table 1. From an applied perspective, characterization of the physical and chemical heterogeneities in a nuclear waste repository, even for a single clay mineral, is effectively impossible to carry out. The question becomes how to use microscopic information in light of the known inconsistencies between these heterogeneous systems and homogenizing model practices. This question will be elaborated on below in the sections relating to chemical behaviors measured in batch and diffusive studies.

4.3.2 Surface charge characteristics

The microscopic and spectroscopic techniques just discussed are used both to constrain experimental and modeled systems. We now move to the experimental Venn diagram in Figure 4-3, and will start at the top with electrokinetic and titration experiments.

Surface charge in clays is derived from the two separate components of isomorphous substitution and amphoteric behavior of the edge sites. Isomorphous substitution occurs when an element with a lesser charge replaces one with a higher charge without significant alteration to the lattice structure of the clay particle. Most often, Al^{3+} replaces Si^{4+} in the tetrahedral layer or Mg^{2+} replaces Al^{3+} in the octahedral layer; although, other substitutions are common. This elemental substitution creates a positive charge deficit which exhibits itself by giving clay particles an overall negative charge. This charge is compensated by interlayer cations, generally the alkali(ne) earth elements K^+, Na^+, Ca^{2+}, or Mg^{2+}. The amphoteric charge is created by the surface sites along the edges of a clay particle. These sites behave similarly to other metal oxides being able to consume of release protons as shown in equations 1-3 where represents a surface complexation site, and Me can be:

$$(4\text{-}1)$$
$$(4\text{-}2)$$
$$(4\text{-}3)$$

Al or Si. These two different sources of surface charge are often distinguished with electrokinetics and surface titrations.

From a fundamental surface chemistry perspective, electrokinetic experiments are limited in that they can only access the charge present at the shear layer, or, from more traditional metal oxide studies, at the inner boundary of the double layer (see Alkan et al., 2005a for an explanation and schematic). Results from electrokinetic experiments, zeta potentials, are only a proxy for surface charge; however, a common thread when performing zeta potential determinations on clay is that the potentials tend to be negative across a range of chemical conditions. When there is a charge reversal of zeta potential, it is generally caused by either a low pH (Alkan et al., 2005b), or from large concentrations of multi-valent ions (Alkan et al., 2005a; Alkan et al., 2005b). However, unlike more traditional metal oxides, ionic strengths of up to 2M of common 1:1 electrolytes are insufficient to cause a reversal of zeta potential (Kosmulski and Dahlsten, 2006). The consistently negative zeta potentials as a function of pH and ionic strength are often attributed to the fixed charge of the clay particle associated with the isomorphous substitution. The presence of the positively charged edge sites is generally insufficient to cause a zeta potential reversal. However, it has been found that larger changes in zeta potential as a function of pH vary inversely with cation exchange capacity (CEC, (Sondi et al., 1996)). In other words, the higher the proportion of edge sites, the more capable they are of neutralizing the effects of the fixed charge sites. Relating zeta potential to surface charge requires a model capable of considering the CEC, the protonation state, and the zeta potential. Fitting a model with this many variables requires not just zeta potential data but also surface titration experiments.

Surface titrations are a very common method for probing surface charge and complexation behavior of metal-oxides. They essentially consist of performing a titration with (sample) and without (blank) a solid phase present. The effect of the blank can be mathematically removed, and the proton interaction with the surface can be derived. Avena and De Pauli (Avena and De Pauli, 1998) completed both titrations and zeta potential measurements, and were able to describe the charging and ion behavior of a Na-montmorillonite. Their conceptual model consists of an internal plane where the negative charge is located. The charge from this plane interacts with the solution only through a discrete number of ion exchange sites. The ion exchange sites are co-located with the amphoteric sites in a plane between the internal plane and the solution phase. Mass action expressions are derived for the complexation of Na^+ and H^+ at both the exchange and amphoteric sites and were fit using the titration experiments. The model shows that H^+ and Na^+ exchange as a function of pH essentially offset leading to a semi-constant value of uncomplexed exchange sites. Because the amphoteric sites are only 5% of the total number of sites, their contribution to charge is negligible. Thus, charge on the internal plane, and subsequently zeta potential, is approximately constant as a function of pH. Similar results in terms of H^+/Na^+ offsets were found by Tournassat et al. (Tournassat et al., 2004b). Thus models relating internal chemical controls to zeta potential have been derived. More recently however, external controls on zeta potential have been found to also have an effect. Using a field sample from the Savannah River site consisting of a mixture of several clays and metal oxides, zeta potential was found to increase (become less negative) as a function of increasing solids concentration up to 25 wt.% (Guerin et al., 2004). Also, particle size was found to increase as a function of increasing solids concentration, suggesting aggregation and increased particle-particle interactions. Titrations not only allow for a bridge between zeta potential and surface charge, they are also used as a critical component of model fitting for metal sorption to clays.

Since clays are a viable choice as a material in nuclear waste disposal, quantitative descriptions of interactions between radionuclides and clays are desirable. Thus, surface titrations of clay minerals have become increasingly common as a first step in describing metal sorption. An extensive review (Duc et al., 2005a) and critical laboratory examination (Duc et al., 2005b) of the limitations of this method has been completed. The conclusion of this review is that the clay mineral isolation method, clay mineral storage

conditions, and the amount of time that the clay was stored all have an impact on the nature of the titration curves. These impacts are most often exhibited by increased hysteresis. In (Duc et al., 2005b), only the use of continuous titrations is considered. However, in the broader literature one of the major distinguishing characteristics between titration methods is whether they are performed continuously (Brady et al., 1996; Douch et al., 2009; Frini-Srasra et al., 2007; Kriaa et al., 2008; Rozalen et al., 2009; Sinitsyn et al., 2000; Vico, 2003), or discontinuously (Baeyens and Bradbury, 1997; Bradbury and Baeyens, 2009a; Huertas et al., 1998; Tournassat et al., 2004b). Continuous titrations are performed in a single vessel with a single sample of clay with acid and base additions most often being performed by an autotitrator; discontinuous titrations are identical to batch reactors where a series of vessels are filled with identical clay samples and varying aliquots of acid/base are added to achieve some desired equilibrium pH. The advantage of the continuous titrations is that they are fast, and effects of kinetically hindered dissolution are minimized. The advantages of a discontinuous titration are the ability to quantify and correct for dissolution through solution analysis of cations, as well as removing any doubt that the protonation state of the clay is not at equilibrium. The difference between continuous and discontinuous techniques has been explicitly compared. The pH in discontinuous experiments has been found to drift for at least 168 hours and the slope of the charging curve was much steeper than that in continuous experiments (Tertre et al., 2006). However, this is directly contradicted by other experiments where there was no change in pH between 24 and 168 hour timepoints (Baeyens and Bradbury, 1997). The reasons for these discrepancies are unclear, but differences in clay purification methods are a likely reason. The goal of both the continuous and discontinuous titration studies is to create a model describing the protonation state of the edge sites (Eqs. 1-3) in order to describe metal complexation. In the next section we will address this final variable when considering internal structure-function relationships, ion complexation.

4.3.3   Ion Complexation

There are two main types of experiments used for exploring ion complexation to clays: batch experiments and diffusion experiments. In general, batch experiments allow for the determination of ion behaviors and the fitting of an ion exchange/surface complexation model (internal processes), while diffusion experiments allow for the analysis of behaviors under application relevant conditions (with internal and external processes). Moving further down on the Venn diagram in Figure 4-3, this section is focused on connecting the characteristics of surface charge with ion behavior, and diffusion experiments are considered in their own section, below.

It has long been recognized that cation sorption to almost any clay mineral is ionic strength dependent at low pH, and transitions to being ionic strength independent and pH dependent as the pH increases. This is most often attributed to the presence of the two types of surface charge. The fixed charge dominates at low pH and the degree to which that charge is distributed into solution is ionic strength dependent. At higher pH the fixed charge is still present, but the edge sites become more negative and dominate sorption due to stronger chemical interactions with ions. The interaction between the cation and clay at low pH are dominated by electrostatic interactions and the surface complex formed is generally outer sphere in nature. At higher pH, the interaction is more analogous to the interactions between cations and other metal oxides where actual chemical bonds are formed between the cation and the edge surface site. This generalized behavior has been observed for a range of clay minerals and cationic sorbents (Baeyens and Bradbury, 1997; Bradbury and Bradbury, 1997; Bradbury and Baeyens, 2009a; Bradbury and Baeyens, 2009b; Vico, 2003; Sinitsyn et al., 2000; Kulik et al., 2000; Rabung et al., 2005; Bradbury et al., 2005; Gu et al., 2010; Turner et al., 1996). When considering a range of sorbents with a single sorbate including transition metals and actinides, linear free energy relationships have been found between the aqueous hydrolysis constant of the metal and the complexation constant for an ion binding to a strong edge site (Bradbury and Baeyens, 2009b). This suggests some level of thermodynamic consistency of ion behavior across a range of experimental approaches. However, there are a few exceptions to this behavior most

notably in how alkali(ne) earth metals interact with clays. Sr^{2+} sorption to smectite is ionic strength dependent but independent of pH; the same is true for Sr^{2+} sorption to illite except at pH>9 (Missana et al., 2008). Furthermore, when the ionic strength is dominated by sodium, uranium sorption to smectite follows the expected trend, but when the ionic strength is dominated by calcium, the ionic strength dependence is far weaker (Turner et al., 1996).

Anion interactions with clay minerals are far less studied, and far less understood. Because the focus of this paper is on nuclear waste repositories, we will limit the anion discussion to common anions and oxyanions found in nuclear waste, including: I^-, IO_3^-, SeO_3^{2-}, and TcO_4^-. Relative to the cations sorption of all of these anions to any clay mineral is very weak and often much slower (Fuhrmann et al., 1998; Jan et al., 2007; Vinsova et al., 2004; Vinsova et al., 2006; Couture and Seitz, 1983; Kaplan et al., 2000). For example selenite required a minimum of 5 days to reach equilibrium with illite and smectite (Missana et al., 2009), and iodide required at least 7 days (Kaplan et al., 2000). Both the rate and extent of anion sorption are consistent with charge repulsion between the fixed negative charge on clays with the anion. However what is surprising is the wide range of variation between the anions. I^- and IO_3^- are often studied in parallel as the oxidation state under field relevant conditions is not always clear (Hu et al., 2005; Fox et al., 2010; Glaus et al., 2008). Indeed the oxidation state in lab studies is not always clear. Using an I^- tracer, significant sorption to various iron oxides has been found. However, when probed using XANES, it was found that the sorbed species was more likely IO_3^- (Fuhrmann et al., 1998). Thus either the sorption process forced oxidation or the iodide oxidized in solution and was subsequently taken up by the solid. I^-/IO_3^- sorption to any of the clay minerals was too low for spectroscopy to be used. Selenium sorption to montmorillonite and kaolinite increase slightly as a function of pH until the pH is circum-neutral. Above that pH sorption drops to near zero (Wang et al., 2001). Selenium sorption to smectite decreases nearly linearly with pH while it is basically constant as a function of pH when reacted with illite (Missana et al., 2009). Technetium, the least studied of the three, exhibits a maximum of ~15% sorption to bentonite at neutral pH, and a fairly weak pH dependence in general (Wang et al., 2001). The small amounts of sorption observed tend to exacerbate errors in model fitting of complexation constants. All of this information is summarized in Table 4-2.

Before proceeding to discuss diffusion experiments, we would like to summarize the modeling methods used to date to describe the internal chemical behaviors and characterization discussed so far: spectroscopic evidence, surface charge characteristics, and ion complexation. From the right side of Figure 4-3, we will be discussing all of the modeling techniques except for models where diffusion is considered.

Table 4-2. Summary of K_d values obtained from batch sorption exaperiments

Ref.	Clay	Major Clay mineral (%)	Other Mineral	Ions Studied	K_d	IX/SCM ?	Notes
(Bazer-Bachi et al., 2006)	Callovo-Oxfordian #1	Illite/Smectite (30-35)	Illite, Kaolinite, Chlorite, Quartz, Calcite, Pyrite	Cl			
	Callovo-Oxfordian #2						
	Callovo-Oxfordian #1				1.50E-01		Concentration dependant I retention, values for [I]=5E-6, sample 1 and 8e-6, sample 2; max value for each
	Callovo-Oxfordian #2			I	3.70E-01	N	
(Vinsova et al., 2006)	Bentonite	Montomorillonite	Calcite, Quartz	Tc	2.58E+03	N	Bentonite/Fe mixture; All three are anaerobic
					1.68E+03		Bentonite/FeS mixture
					5.57E+02		Bentonite and Activated Carbon
(Vinsova et al., 2004)	Bentonite			Tc	0.1-2.7	N	Bentonite alone; All three under aerobic conditions
					9.1-4731		Bentonite and Activated Carbon
					5.9-6186		Bentonite/Fe
(Jan et al., 2007)	Bentonite	Quartz, montmorillonite		Cs	1.50E+02		
				Sr	2.50E+01		
				I	0-1		
	Laterite	Quartz, Hematite, Kaolinite, Goethite		Cs	2.50E+02		
				Sr	1.80E+02		
				I	0-1		
	Quartz			Cs	0-1		
				Sr	0-1		
				I	0-1	N	
(Bradbury and Baeyens, 2009a)	Illite du Puy	Illite		Ni	3.16E+03	Y	Paper performs sorption envelope experiments for the ions given; K_d values reported here are approximated from the envelope at pH 7 and I = 0.1M

Table 4-2. Summary of K_d values obtained from batch sorption exaperiments (cont.)

Ref.	Clay	Major Clay mineral (%)	Other Mineral	Ions Studied	K_d	IX/SCM ?	Notes
(Bradbury and Baeyens, 2009b)	Illite Du Puy	Illite		Am	3.16E+05		Paper performs sorption envelope experiments for the ions given; Kd values reported here are approximated from the envelope at pH 7 and I = 0.1M
				Th	3.16E+05		
				Pa	1.00E+05		
				U	1.00E+05		
				Np	1.00E+01	Y	
(Missana et al., 2008)	FEBEX Bentonite	Smectite	Quartz, Plagioclase, Cristobalite, Feldspar, Calcite, Tridymite		1.78E+04		Sorption envelopes created, values given for pH 7; I = 0.01M
				Sr	1.58E+02		I = 0.1M
	Silver Hill Illite	Illite			1.41E+02		I = 0.1M
				Sr	8.91E+01	Y	I = 0.2M
(Couture and Seitz, 1983)		Kaolinite		IO_3^-	1.25E-03		pH = 5.2
				IO_3^-	9.17E-04		pH = 4.1
				I	1.75E-04		pH = 5.7
				I	3.48E-05		pH = 3.9
				IO_3^-	1.61E+01		pH = 7.0
			Hematite	I	6.80E-04	N	pH = 6.6
(Kaplan et al., 2000)			Calcite	I	-1.00E-01		
		Chlorite		I	-2.20E-01		
			Goethite	I	7.00E-02		
		Illite		I	2.77E+01		
		Montmorillonite		I	-3.30E-01		
			Quartz	I	-4.00E-02		
		Vermiculite		I	8.00E-01	N	

Table 4-2. Summary of K_d values obtained from batch sorption exaperiments (cont.)

Ref. #	Clay	Major Clay mineral (%)	Other Mineral	Ions Studied	K_d	IX/SCM ?	Notes
(Coppin et al., 2002)		Kaolinite		Ln series (no Pm)	1.00E+04		pH = 6.6, At I = 0.025 entire Ln series behaved similarly, at I = 0.5 Kd increased with increasing atomic number over a range spanning an order of magnitude
		Kaolinite		Ln series (no Pm)	1.00E+03		pH = 4.5
		Kaolinite		Ln series (no Pm)	2.51E+02		pH = 3.1
		Smectite		Ln series (no Pm)	1.00E+04		pH = 7.4
		Smectite		Ln series (no Pm)	3.16E+04		pH = 6.3
		Smectite		Ln series (no Pm)	1.00E+04	N	pH = 3.9
(Baeyens and Bradbury, 1997; Bradbury and Bradbury, 1997)		Na-Montmorillonite		Ni	1.78E+03		Sorption envelope created, value given for pH = 7, I = 0.1M
				Zn	6.31E+04		Sorption envelope created, value given for pH = 7, I = 0.1M
				Mn	1.78E+03	Y	Sorption envelope created, value given for pH = 7, I = 0.5M
(Gu et al., 2010)		Montomorillonite		Cd	3.25E+00		Sorption envelopes created, value estimated for pH = 7, I = 0.01M
				Cu	3.25E+00		Sorption envelopes created, value estimated for pH = 7, I = 0.01M
				Ni	3.25E+00		Sorption envelopes created, value estimated for pH = 7, I = 0.01M
				Pb	undefined		100% ion sorption at pH 7
				Zn	3.25E+00	Y	Sorption envelopes created, value estimated for pH = 7, I = 0.01M

Table 4-2. Summary of K_d values obtained from batch sorption exaeriments (cont.)

Ref. #	Clay	Major Clay mineral (%)	Other Mineral	Ions Studied	K_d	IX/SCM ?	Notes
(Missana et al., 2009)		Na-Illite (100)		Se	6.00E+01		Sorption envelopes created, value estimated for pH = 7, I = 0.1M
		Na-Smectite (100)		Se	1.55E+02		Sorption envelopes created, value estimated for pH = 7, I = 0.1M
		Na-Illite (30)/Na-Smectite (70)		Se	1.25E+02		Sorption envelopes created, value estimated for pH = 7, I = 0.1M
		Na-Illite (43)/Na-Smectite (57)		Se	1.05E+02	Y	Sorption envelopes created, value estimated for pH = 7, I = 0.1M
(Bradbury et al., 2005; Rabung et al., 2005)		Ca-Montmorillonite		Eu	1.26E+04		Sorption envelopes created, value estimated for pH = 7, I = 0.1M
				Cm	1.78E+06		Sorption envelopes created, value estimated for pH = 7, I = 0.1M
		Na-Illite		Eu	3.98E+05	Y	Sorption envelopes created, value estimated for pH = 7, I = 0.1M
(Bektas et al., 2004)		Sepiolite		Pb	7.06E+00		Kd values obtained from Freundlich isotherm for pH = 4, I = unspecified
				Pb	7.18E+00		Kd values obtained from Freundlich isotherm for pH = 5, I = unspecified
				Pb	6.10E+00	N	Kd values obtained from Freundlich isotherm for pH = 6, I = unspecified

4.3.4   Modeling Techniques

To complement the three main variables studied in titrations and batch experiments, there are three main components that can be included in conceptual models of clay systems, including: surface charge, ion complexation, and some connection to internal structure. Models describing all three components have been completed, although to varying degrees.

Starting at the smallest scale, molecular electrostatic potential calculations have been completed describing the charge characteristics of kaolinite (Brady et al., 1996). The outcome of this effort was that the surface charge of an individual clay grain 10 unit cells in size is segregated with significant differences between basal and edge locations. At more directly observable scales, more generalized models are derived including the one described earlier to link zeta potential to surface charge (Avena and De Pauli, 1998). In this model the fixed charge was located in a single plane within the clay structure, and that layer was separated from the aqueous phase by another layer containing all of the chemically reactive sites responsible for ion exchange and variable charge properties. A slight extension of that model is to consider the clay particle not as a series of planes, but instead a porous solid where the fixed charge is located at a variety of depths within the solid (Kraepiel et al., 1998). This creates a potential curve both into solution and into the solid phase, a double-double layer. This model has been used to describe the charging behavior of kaolinite and for montmorillonite (Kraepiel et al., 1999). The addition of the interior negative charge allows for the description of decreasing isoelectric pH values as a function of increasing ionic strength, a common experimental observation. A similar porous medium approach has also been generalized such that application can be extended to any microporous material (Revil and Linde, 2006).

Earlier ion complexation models took the form of hard-soft acid-base models (HSAB, (Auboiroux et al., 1998; Xu and Harsh, 1990a; Xu and Harsh, 1990b), a far more comprehensive description of clay complexation models through time is given in (Teppen and Miller, 2006)). HSAB models were based on several fundamental parameters such as electronegativity, ionization potentials, and ionic radii. However, when mathematically combined there are two global fitting parameters which are physically meaningless. Despite that drawback, the HSAB models could accurately predict ion selectivity to a number of minerals and ion exchange resins. More recently, surface complexation models (SCM) have dominated ion sorption descriptions to clays. SCM have been discussed and explained by others (Davis et al., 1998), but a brief introduction is given here. Surface complexation modeling based on simpler metal-oxides treat the surface of a mineral as amphoteric in nature. For example, an aluminum oxide surface could be described using the reactions shown in equations (4-1) and (4-2) above. The protonation state of the surface is pH dependent, and thus so is the charge and ion complexation reactions. This idea was generalized and applied to mineral mixtures where the contributions of individual components are simply averaged into a single set of complexation constants [GC, generalized composite approach (Davis et al., 1998; Honeyman, 1984)]. The major extension in the use of this type of model with respect to clays, is the addition of a generic ion exchange site (generally denoted   ). The complexation behavior of this site is largely independent of pH, and represents the contribution to particle charge from the isomorphous substitutions. For clays, it is generally sufficient to use these three surface sites: an amphoteric Al site, a neutral or negative Si site, and an exchange site. A slightly lesser used method is to use the GC approach, and simply assign a series of generic sites which do not correspond to the two main types of sites present in clays. This often requires a 'strong' and 'weak' generic site in order to obtain sufficient fits. The clay surface can be mathematically fit with either of these structurally independent models. This type of modeling has been applied to a wide array of clays, under broad sets of aqueous conditions and for a wide range of metal sorbents.

One of the major distinguishing factors between the models is the assumption made with respect to how the charge is calculated. These assumptions range from a non-electrostatic model (charge not distributed

into solution, (Bradbury and Baeyens, 2009b; Bradbury et al., 2005; Bradbury and Bradbury, 1997; Gasgova and Bukaty, 2008; Missana et al., 2009)), to the constant capacitance model (charge decays linearly into solution, (Gu et al., 2010; Rozalen et al., 2009; Vico, 2003)), to the diffuse double layer model (partial charge neutralization in one layer due to sorbed cations and parabolically decaying charge in the second layer, (Avena and De Pauli, 1998; Tertre et al., 2006; Wang et al., 2001)), to the triple layer model (inner sphere complexation in the first layer, outer sphere complexation in the second and a diffuse swarm in the third, (Kulik et al., 2000; Turner et al., 1996)), and finally to the MUSIC model (a model based on bonding principles and the physical structure of a mineral surface, (Tournassat et al., 2004a)). Despite the importance of charge in clay systems, all of these models are capable of being fit to the data. However, the use of such an array of models precludes any inter-model comparison of complexation constants. In order to get the linear free energy relationships described earlier (Bradbury and Baeyens, 2009b) a large amount of data had to be re-modeled using a consistent approach. Since all of these models are capable of describing surface interactions, the appropriateness of each model is based on 'softer' considerations such as ease of use. The relative popularity of the non-electrostatic and constant capacitance models is unsurprising as they are conceptually the simplest, and are the easiest to use. In a study which transcends the molecular to observable scales, molecular dynamic simulations were used to test several assumptions associated with the use of triple layer models (Tournassat et al., 2009); this model was even extended to describing electrokinetic data. The use of molecular dynamics allowed for the constraining of TLM and Stern Model parameters, as well as showing significant agreement between the output of the different modeling techniques.

For the purposes of this chapter, we are interested in the models most capable of connecting internal and external processes. Due to the linkages to underlying structure, it would appear for now that the MUSIC model is the most likely candidate (Tournassat et al., 2004a). When applied to montomorillonite, this model used 27 total site types which correspond to individual binding environments based on a crystallographic representation of a montmorillonite platelet. The model constrains many of the fitting parameters through structural considerations, and actually has less fitting parameters than many of the structurally independent models. What remains to be seen is if this internal based model would be sufficiently robust to respond to an external force. In other words, if compaction puts montmorillonite platelets in close proximity such that the 27 possible sites start to interact, does the model still describe behavior? The lack of a description of charge interaction is a shortcoming in both the MUSIC and other surface complexation models. By definition, structurally independent models cannot describe local spatial variations in charge present on a clay particle between the basal surfaces and edge sites. Even in the structurally grounded MUSIC model, equations do not exist to describe how positive/negative charge on an edge can interact with the fixed negative charge located on a basal plane. Some have suggested that the titration techniques generally in use are not sensitive enough to distinguish edge and basal behaviors (Brady et al., 1996). Experimentally this problem would be difficult to approach, as it would necessitate clay particles that were either all edge, or all basal planes, which would of course change the nature and behavior of the particle. Alternatively it may require instrumental techniques with resolution to separate basal plane behavior from edge site behavior (McKinley et al., 2004; Zhao et al., 2008). Molecular modeling may be better suited to distinguish between these two disparate environments. Concerns with modeling of surface charge are re-considered in the diffusion section below.

4.4   External Structure-Function

The focus of this section is to review and discern what can be learned with respect to how chemistry proceeds when reactive environments are constrained from external factors. In order to maintain focus on nuclear waste repositories, much of the discussion will be centered on diffusion-based studies in compacted clays.

4.4.1   Diffusion Experiments

Two main types of diffusion experiments exist, steady-state and non-steady-state, or through diffusion and out diffusion. In through diffusion experiments there are up- and down-gradient reservoirs separated by a compacted clay column. A diffusive gradient is imposed across the column by maintaining a semi-constant tracer concentration in the up-gradient reservoir, while the down-gradient reservoir is kept nearly tracer free. Tracer concentration is monitored in the down gradient reservoir. These experiments are generally continued until the diffusive flux reaches steady state. In out-diffusion experimentation there are two variations on a theme. In the first steady-state flux is first established as just described, then the out-diffusion phase is commenced by replacing the solutions in both reservoirs with tracer-free solutions. In the second variation, a clay column is compacted with an ion source embedded within the clay. The column is saturated, and the ions start to migrate outward from the source. Generally the column is sliced, and the ion is extracted from the solid for analysis. These two types of experiments simulate slightly different conditions, and thus slightly different knowledge can be gained. Through-diffusion experiments simulate the conditions slightly further from a hypothetical waste canister, and the semi-constant boundary conditions allow for simpler fitting of diffusional parameters. The second type of out diffusion experiments more closely simulate conditions much closer to the waste canister where the waste is actively being released. Fitting diffusional terms to the data is often completed with a series of assumptions such as infinite column length or constant source concentration. Diffusion experiments are further distinguished by whether they were using a reactive or non-reactive tracer.

The ultimate non-reactive tracer, tritiated water (HTO), is used by many authors to determine pore volumes, effective diffusion coefficients and geometrically related factors such as tortuosity or capacity factors in compacted clay columns (Appelo et al., 2010; Glaus et al., 2010; Van Loon et al., 2003). Another advantage of using HTO is that the behavior of water in clays can be probed (Van Loon and Jakob, 2005). Slight differences in HTO diffusional properties through illite, montmorillonite, and kaolinite have been found (Gonzalez-Sanchez et al., 2008). Specifically, the effective diffusion coefficients increase in the order Na-montmoriilonite < Ca-montmorillonite < Ca-illite < Na-illite ≤ kaolinite. This behavior is physically interpreted through both changing particle sizes between clay minerals (larger particle sizes allow for lower tortuosity), and through the variations in hydration energy between Ca and Na. So, both chemical and physical internal effects alter HTO diffusion. In another study, sodium and HTO diffusion was measured through Na-, Ca-, and Cs-bentonites (Melkior et al., 2009). In this study, HTO was found to diffuse more quickly in Cs-bentonite, while sodium diffused more quickly in the Ca- and Na-bentonites. Through HRTEM characterization, the authors attribute this to the formation of a 'gel-like phase' in the Ca- and Na-bentonite that is lacking in the Cs form. In this study, an internal morphological change induced by the interaction between cations and the clay particle creates larger scale differences in diffusional properties. HTO diffusion coefficients have also been found to decrease with increasing compaction largely due to changing pore structures (Garcia-Gutierrez et al., 2001). Thus an external change can alter diffusion properties. HTO also acts as an ideal benchmark to explore variations in non-reactive ion diffusion.

Generally the non-reactive ions are the mono-valent halides and alkali earth metals. A long-observed phenomenon is that of cations diffusing faster than expected relative to HTO, and anions diffusing slower. The former is most often explained through 'surface diffusion' (Appelo and Wersin, 2007; Oscarson, 1994) while the latter is often explained through anion exclusion (Yaroshchuk et al., 2007). Surface diffusion can be thought of as a preferential pathway along the negatively charged surface of clays. Due to the negatively charged surface, anions are excluded leading to an enhanced cation concentration gradient and increased diffusion. Recently, a model was derived that separates the surface diffusion from diffusion in the pore space (Gimmi and Kosakowski, 2011). Using this analysis, a scaling factor is derived that is based on the bulk density, K_D value and the porosity of the pore pathway. Using this

scaling factor it appears that diffusional rates are intrinsically determined by the nature of the cation, and not the nature of the clay. Anion exclusion, on the other hand, has been found to vary with bulk density and chemical conditions in solution. For example, chloride diffusion coefficients were nearly an order of a magnitude lower when bulk density was increased from 1300 to 1900 kg*m^{-3}(Van Loon et al., 2007). A linear correlation between the effective diffusion coefficients and the diffusion-accessible porosity suggests that the changes in porosity with increased compaction are the major factor in changing diffusion coefficients. Diffusion coefficients also increase with increasing ionic strength suggesting a masking of surface charge allowing for the anion to use more of the total pore space. Taking this one step further, iodide and chloride diffusion in compacted bentonites have been found to have a fast and slow component (Molera et al., 2003). The capacity factor associated with the fast component decreases with compaction while the compaction factor for the slow process is independent of compaction. Thus, the authors assign the occurrence of the fast process to the inter-aggregate space, and the slow process to the intra-aggregate space. When reactive ions are considered, there is the added complexity of de-convoluting the diffusion and reactive behaviors. Many of the relevant results from diffusion experiments are summarized in Table 4-3.

In stark contrast to the surface complexation/ion exchange models discussed earlier, when sorption reactions are considered in diffusion experiments, data interpretation most often proceeds based on K_d values. Also the most commonly studied reactive species are elements with isotopes of both significant concentration in nuclear waste as well as relatively long-half lives, including several fission products (Cs, Se, Sr, I,Tc, (Appelo et al., 2010; Bazer-Bachi et al., 2006; Glaus et al., 2008; Jansson and Eriksen, 2004; Maes et al., 2008; Molera and Eriksen, 2002; Van Loon and Glaus, 2008)) and actinides (U, Np, Am, (Sato et al., 1992; Yamaguchi et al., 2007)). K_D values must be fit to the data using a conceptual framework. The most common approach is to use a variation of Fick's Law:

$$(\varepsilon + \rho_b K_d)\frac{\delta C}{\delta t} = \frac{\delta}{\delta x}\left(\frac{\varepsilon D}{\tau^2}\frac{\delta C}{\delta x}\right)$$

(4-4)

where ε is the porosity, ρ_b is the bulk density, K_d is the distribution coefficient, C is the aqueous concentration, t is time, x is a spatial coordinate, D is the diffusion coefficient, and τ is the tortuosity. Results from fitting many of these parameters are summarized in Table 4-3. Some authors have extended this analysis to include a dual porosity formulation of Fick's law, with the two different porosities conceptually representing diffusion in the interlayer vs. diffusion in the pore spaces (Bourg et al., 2003; Ochs et al., 2001). Using these models, the basic conclusions of many authors are that as compaction increases, porosity decreases, tortuosity increases, and K_D can either increase or decrease depending on which element is being considered. The K_d value for Cs has been found to decrease as a function increasing compaction [Kunipia-F, (Sato et al., 1992)], and also to increase with increasing compaction [Bentonite MX-80, (Molera and Eriksen, 2002); Volclay KWK, (Van Loon and Glaus, 2008)]. The difference in behavior could be related to slight differences in the application of Fick's Law, but they are most likely related to Na concentrations in the background electrolyte. The decrease in K_d values was found when the column was saturated with distilled water, while the increase in K_D values was found with a sodium rich artificial pore water or swamping $NaClO_4$ solutions. Using a previously developed hydration based model (Teppen and Miller, 2006), the preferential removal of Cs as a function of increasing compaction has been attributed to the coupled processes of hydration/dehydration of the Na and Cs ions (Van Loon and Glaus, 2008). Coupling the hydration energies with the restricted water activity within the interlayer spaces, it is thermodynamically favored to have Cs in the interlayer and Na in the pore fluid. As the system is less compressed, the interlayer and pore waters are more similar, and this energetic favoritism relaxes leading to less Cs sorption. Similar arguments have been cited which relate the solvent structuring ability of individual cations to the development of surface charge on colloidal silica (Dove and Craven, 2005). For species of higher valence, K_d values generally decrease as a function of increasing compaction, with some notable exceptions. Values for Sr follow this trend (Molera

and Eriksen, 2002; Sato et al., 1992), while values for Co are very large, and constant as a function of compaction(Molera and Eriksen, 2002). K_d values decrease slightly for Am, while for Np they start at a value of 0.42 m^3/kg at 200 kg/m^3 decrease to 0.1 at 1200 kg/m^3 and increase to 0.27 at 2000kg/m^3 (Sato et al., 1992). Chemical interpretations of these complex behaviors have yet to be posited. More experimental evidence may be required to extend the hydration/compaction model to poly-valent systems.

Table 4-3. Relevant results summary from diffusion based experiments

Ref.	Clay	Major Clay Mineral (%)	Ions involved	K_d	Diffusion coefficient (m^2/sec)	Compaction	Compaction units	Ion porosity	Notes
(Van Loon et al., 2007)	Bentonite	Montmorillonite	Cl		1.60E-11	1.3	g/cm^3	2.3	All D and porosity values at 0.1M ionic strength, others in reference
					2.30E-12	1.6	g/cm^3	2.1	
					2.40E-13	1.9	g/cm^3	0.7	
(Glaus et al., 2010)		Na-Illite	Na		3.90E-10	1.9	g/cm^3		All values for I = 0.1M, other values given in reference. Since there is no sorption involved the formation factor = porosity
			Cl		2.80E-11	1.9	g/cm^3		
		Na-Montmorillonite	Na		3.80E-10	1.9	g/cm^3		
			Cl		7.20E-14	1.9	g/cm^3		
		Kaolinite (Kga-1b)	Na		3.20E-10	1.9	g/cm^3		
			Cl		2.30E-10	1.9	g/cm^3		
(Van Loon et al., 2003)	Opalinus	Illite (23)/Kaolinite (22)	Cl		5.54E-12	1	MPa		
					3.99E-12	5	MPa		
			I	0.008-0.02	4.57E-12	1	MPa		
					3.22E-12	5	MPa		
(Melkior et al., 2009)	Bentonite	Na-Bentonite	Na		7.50E-11				I = 0.1M
			Na		2.30E-10				I = 0.01M
		Ca-Bentonite	Na		9.90E-11				I = 0.1M
			Na		1.20E-10				I = 0.01M
		Cs-Bentonite	Na		4.80E-11				I = 0.1M
			Na		7.20E-11				I = 0.01M
(Appelo et al., 2010)	Opalinus	Illite (23)/Kaolinite (22)	Na	3.41E+00				0.159	Diffusional factors lumped into a geometrical factor
			Cs	Variable				0.159	
			Sr	2.43E+01				0.159	
			Cl	0				0.077	
			I	0				0.105	
			I	2.90E-02				0.078	
			Br	0				0.105	

Table 4-3. Relevant results summary from diffusion based experiments (cont.)

Ref.	Clay	Major Clay Mineral (%)	Ions involved	K_d	Diffusion coefficient (m^2/sec)	Compaction	Compaction units	Ion porosity	Notes
(Jansson and Eriksen, 2004)	Bentonite MX 80	Montmorillonite	I		5E-14/ 8.6E-11	1.8	g/cm^3		Dual porosity type model, lower diffusive and formation factors value corresponds to intralamellar and larger value corresponds to external water
			Tc		1E-13/ 6E-11	1.8	g/cm^3		
(Molera and Eriksen, 2002)	Bentonite MX 80	Montmorillonite	Na	2.80E+00	3.80E-07	1.8	g/cm^3	0.32	Wider range of ionic strength and packing densities in reference. Porosity determined not for each indiviual ion but for a given amount of compaction
				1.50E+02	3.50E-07	0.8	g/cm^3	0.7	
			Sr	8.00E+01	9.00E-08	1.8	g/cm^3	0.32	
				2.65E+02	6.40E-08	0.8	g/cm^3	0.7	
			Cs	5.80E+02	3.30E-08	1.8	g/cm^3	0.32	
				2.40E+03	1.00E-09	0.8	g/cm^3	0.7	
			Co	2.40E+03	1.00E-10	1.8	g/cm^3	0.32	
(Garcia-Gutierrez et al., 2001)	FEBEX Bentonite	Smectite (93)	Cs	8.23E+02	3.30E-13	1.6	g/cm^3	0.26	Porosity from HTO experiments; Kd and De from analytical model
				9.19E+02	2.64E-13	1.6	g/cm^3	0.26	Kd and De from numerical model
			Se	11/3	6.25e-14/ 1.56e-13	1.6	g/cm^3	0.26	Kd and De from analytical model; Two subfractions observed, thus the two numbers
				1.94E+00	2.81E-14	1.6	g/cm^3	0.26	Kd and De from numerical model
			Sr		5.50E-12	1.6	g/cm^3	0.26	Kd and De from analytical model
				6.95E+02	6.60E-13	1.6	g/cm^3	0.26	Kd and De from numerical model

Table 4-3. Relevant results summary from diffusion based experiments (cont.)

Ref.	Clay	Major Clay Mineral (%)	Ions involved	K_d	Diffusion coefficient (m^2/sec)	Compaction	Compaction units	Ion porosity	Notes
(Sato et al., 1992)	Kunipia-F	Montmorillonite (95)	Sr	9.60E-02	5.10E-11	0.2	g/cm^3		More elements and compaction data in reference
			Tc	3.00E-03	6.90E-10	0.2	g/cm^3		
			I	5.70E-04	8.40E-10	0.2	g/cm^3		
			Np	4.20E-01	1.20E-11	0.2	g/cm^3		
			Sr	-	-	1.4	g/cm^3		
			Tc	1.30E-03	3.20E-11	1.4	g/cm^3		
			I	1.30E-04	8.50E-11	1.4	g/cm^3		
			Np	1.80E-01	3.00E-13	1.4	g/cm^3		
			Sr	1.70E-03	4.30E-12	2.0	g/cm^3		
			Tc	9.40E-04	1.00E-11	2.0	g/cm^3		
			I	6.00E-05	2.40E-11	2.0	g/cm^3		
			Np	2.70E-01	3.00E-14	2.0	g/cm^3		
(Bazer-Bachi et al., 2006)	Callovo-Oxfordian #1	Illite/Smectite (30-35)	Cl		2.70E-11			16.8	
	Callovo-Oxfordian #2				2.00E-11			6.4	
	Callovo-Oxfordian #1		I	1.50E-01	6.60E-12			44.3	Concentration dependant I retention, values for [I]=5E-6, sample 1 and 8e-6, sample 2; max value for each
	Callovo-Oxfordian #2			3.70E-01	2.80E-12			14.7	
(Maes et al., 2008)	Boom Clay	Illite (10-45), Illite/Smectite (10-30), Kaolinite (5-20), Chlorite (0-10), chlorite/smectite (0-5)	Cs	4.10E+03	1.90E-13	~1	MPa	0.37	Duplicated experiments
			Cs	1.50E+03	1.62E-13	~1	MPa	0.37	

Despite widespread application, the use of Fick's Law with K_D based sorption is not applied in a universal manner. For example, Tc and I were treated as non-sorbing by some authors (Ochs et al., 2001), while others treat both as sorbing (Sato et al., 1992; Van Loon et al., 2003). Due to anion exclusion and other charge considerations, the general assumption is that sorption will be minimal. This is substantiated by batch experimentation of I sorption to clay minerals. Small amounts of iodate sorption to kaolinite have been observed, while no sorption of iodide could be measured (Couture and Seitz, 1983). Significant iodide sorption to illite was found ($K_d = 15$ mL/g or 27 mL/g for nontreated and treated samples, respectively), while little to negative sorption was found for montmorillonite or vermiculite (Kaplan et al., 2000). Iodide sorption to the Callovo-Oxfordian argillites (mostly illite and interstratified illite/smectite) was only observed at relatively lower initial iodide concentrations, and over periods of time extending up to 3 months (Bazer-Bachi et al., 2006). Ostensibly this sorption is occurring on positively charged edge sites, although only a weak relationship between pH and K_d has been found for iodide (Kaplan et al., 2000). When iodide has been studied in diffusion experiments, small K_d values (~0.001-2.9 mL/g) are generally required to fit the data (Bazer-Bachi et al., 2006; Jansson and Eriksen, 2004; Van Loon et al., 2003). Also, both I and Tc have decreasing K_D values as a function of increasing compaction (Sato et al., 1992). This is consistent with the conceptual model of clay compaction. An increase in compaction forces the fixed negative charges in closer proximity which acts as a charge barrier to anion sorption. The tremendously low amount of sorption limits the ability to fit SCM/IX models and also precludes the use of spectroscopic techniques. So, exploration of anion sorption to clays is difficult to approach from a mechanistic perspective. Values for diffusion coefficients change depending on whether the anions are assumed to be conservative or reactive. Deciding if anion sorption is actually occurring, or if it is a model artifact, remains a challenge in the surface chemistry of clays.

There remains a significant possibility that the use of K_d based interpretations may be leading to the somewhat contradictory and variable evidence related to individual ions' behaviors as a function of compaction. K_D values in these systems can be considered as a high-level engineered approach at describing some other set of fundamental processes. More mechanistic models that can explicitly describe these fundamental processes may be able to dispel the black box surrounding K_d usage (Bourg and Sposito, 2010; Jougnot et al., 2009; Revil and Linde, 2006). Many of these models are quite recent, and application to large datasets under varying conditions has yet to be completed. Indeed, the only mechanistic approach that combines geometrical effects with charge dissemination (Donnan) with SCM/IX with diffusion is that of Appelo et al. (Appelo et al., 2010). Here Cs, Sr, and I are all treated as sorbing, the reactions are described with a combined SCM/IX model that distributes charge into the pore space using a diffuse double layer/Donnan approach. The model is applied to an *in-situ* test at a single compaction. Application of this and other models to variably compacted systems may help explain the K_d behaviors.

4.5 Conclusions and Perspectives

In considering possible future routes for clay-based repository research, we will divide thoughts at or about the continuum scale. This separation also loosely divides into fundamental knowledge vs. application-driven knowledge.

Continuum scale down: Sub-continuum scale knowledge may allow for the unraveling of observed behaviors at much larger scales, and under a wider range of conditions. Recent applications of FIB-SEM have allowed for the characterization of pore size distributions and connectivity in clay and mudstones (Desbois et al., 2009; Heath et al., 2011). The combined ion beam cutting technique with SEM imaging allows for the creation of a series of image stacks that can be used to re-create the 3-D pore distribution. The total volume this technique uses is on the scale of hundreds of cubic microns, with the pore resolution

reaching down to hundreds of nanometers. What has been found to date is a heterogeneous distribution of various classes of pore shapes. Of interest would be the combination of this technique with chemical characterization of the pore walls. If that could be accomplished, the scale of direct measurement would be approaching the upper scale limits of molecular dynamic simulations.

Another major factor in these constrained spaces is the role of water. With increasing compaction, an increasing proportion of the pore water is contained in nanoporous spaces. In these small pores the water does not act as bulk water; this point is absent in all geochemical models and is only really captured by molecular modelers. The impact of not describing this changing water behavior as a function of constrained space is unknown.

Continuum scale up: While it is true that computing power is increasing exponentially, conceptual models are increasing in complexity nearly as fast. While more fundamental knowledge is always welcome, the application of that knowledge must be metered to the application lest we will always have incomputable descriptions of earth systems. A long standing question in the geo-sciences is how what occurs in a beaker relates to what occurs in the actual system. Knowingly and unknowingly we introduce biases which may in the end be red herrings. For example, in the preceding section, the role of water in confined spaces has been found to be quite different from bulk water through molecular level simulation. However, the question that remains is whether this behavior has any observable effect at the meter to kilometer scales involved with nuclear waste disposal, or if this effect can be ignored. And there is always the question of heterogeneity. If molecular simulations show organized water in small pore spaces, how should that information be incorporated when there is a distribution of pore shapes and sizes? Initial attempts at conceptualizing upscaled models for clay repositories have been completed (Rotenberg et al., 2007). In contrast to porous media systems however, there is a lack of data at large scales (>1m). Shallow contaminated systems have allowed for the collection of data in advective porous media at the 1-1000m scale (Miller et al., 2010). Due to the time scales involved, the only data that can be collected in that range for clay diffusion is through natural analogues (Claret et al., 2010). While certain geochemical information can be gleaned from these systems, the lack of a clear source term will complicate the determination of large scale diffusion coefficients.

The heterogeneity question is also important in extrapolating chemical knowledge. A common comment in the literature is that chemically mechanistic models are necessary to describe sorption/diffusion behavior over the relevant timescales for nuclear waste disposal. In order to get mechanistic models of ion interaction with clays, the clay minerals are subjected to several different flavors of purification; the clay minerals in a repository will not. Regardless of the mechanistic descriptions that may be possible from lab data, the direct extension of mechanistic models to more heterogeneous systems is not clear. This relates both to the chemical interactions as well as the electrostatic interactions. Currently, we do not completely understand the interaction between basal and edge charges on an individual clay particle. What happens when both of those charge domains are also being affected by the charge domain of an impurity mineral or mineral coating? What may be needed are hitherto unconsidered methods to probe clays. These methods may need to be tailored to what we know about clay minerals, and what there is to exploit experimentally, instead of simply using techniques which have worked well with simpler metal oxides. One potential application of this idea is to perform more inter-clay comparison studies with a broader range of clay minerals. Much of the work with respect to nuclear waste repositories focuses on illite and montmorillonite as these are the major minerals in the proposed clay repositories in many countries. Kaolinite is also included often as a chemically simpler system with smaller fixed charge. Clays as a class of minerals exhibit a much broader range of chemical and physical properties, and studies involving less directly applicable clays may either lead to an eventual de-convolution of the chemical and physical properties or to emergent properties of these complex minerals. Another possibility is to exploit the changing conditions present over a range of solids concentrations. Pictorialized in Figure 4-2, changing the solids concentration changes the physical and chemical environment under which ion sorption is

occurring. Experiments of this type may lead to useful representations of clay-ion interactions over a range of conditions.

Making a capital C: THMc modeling has always used the lower-case 'c' as the chemistry that is generally invoked is simplistic in nature, and limited in scope. The range of chemical processes that can be described is only a small sub-set of those involved in citing a repository. This review has largely focused on the connection between the mechanical (compaction) and the chemical. Conceptual representation of the THMc construct usually depicts interrelations between hydrologic and thermal processes as well. While chemistry as a function of increasing temperature is well understood, chemistry as a function of temperature in heterogeneous systems with interconnected processes is not. Furthermore connections between hydrologic and chemical processes, while well studied under conditions of advective mixing, still defy explicit connection. The ideal model is one of a fully coupled multi-process system. In the simplest of terms, we need equations which on the left side of the equation describe, for example, a mechanical process and the right side of the equation describes a chemical process. Determining which mechanical and which chemical process is the first step, and the second is deriving the actual relationship. These steps will need to be completed iteratively and using data that straddles the traditional divides between geo-science disciplines.

4.6   References

Alba, M.D. et al. (2010) Hydrothermal Stability of Layered Silicates in Neutral and Acidic Media: Effect on Engineered-Barrier Safety. *Clays and Clay Minerals*, 58(4): 501-514.

Alkan, M., Demirbas, O., Dogan, M. (2005a) Electrokinetic properties of kaolinite in mono- and multivalent electrolyte solutions. *Microporous and Mesoporous Materials*, 83(1-3): 51-59.

Alkan, M., Demirbas, O., Dogan, M. (2005b) Electrokinetic properties of sepiolite suspensions in different electrolyte media. *Journal of Colloid and Interface Science*, 281(1): 240-248.

Appelo, C.A.J., Van Loon, L.R., Wersin, P. (2010). Multicomponent diffusion of a suite of tracers (HTO, Cl, Br, I, Na, Sr, Cs) in asingle sample of Opalinus Clay. *Geochimica Et Cosmochimica Acta*, 74(4): 1201-1219.

Appelo, J.A.C., Wersin, P. (2007) Multicomponent diffusion modeling in clay systems with application to the diffusion of tritium, iodide, and sodium in opalinus clay. *Environmental Science & Technology*, 41(14): 5002-5007.

Auboiroux, M., Melou, F., Bergaya, F., Touray, J.C. (1998) Hard and soft acid-base model applied to bivalent cation selectivity on a 2 : 1 clay mineral. *Clays and Clay Minerals*, 46(5): 546-555.

Avena, M.J., De Pauli, C.P. (1998) Proton adsorption and electrokinetics of an Argentinean montmorillonite. *Journal of Colloid and Interface Science*, 202(1): 195-204.

Baca, M., Carrier, X., Blanchard, J. (2008) Confinement in nanopores at the oxide/water interface: Modification of alumina adsorption properties. *Chemistry-a European Journal*, 14(20): 6142-6148.

Baeyens, B., Bradbury, M. (1997) A mechanistic description of Ni and Zn sorption on Na-montmorillonite Part I: Titration and sorption measurements. *Journal of Contaminant Hydrology*, 27: 199-222.

Bazer-Bachi, A.R. et al. (2006) Characterization of iodide retention on Callovo-Oxfordian argillites and its influence on iodide migration. *Physics and Chemistry of the Earth*, 31: 517-522.

Bektas, N., Agim, B.A., Kara, S. (2004) Kinetic and equilibrium studies in removing lead ions from aqueous solutions by natural sepiolite. *Journal of Hazardous Materials*, 112(1-2): 115-122.

Bourg, I.C., Bourg, A.C.M., Sposito, G. (2003) Modeling diffusion and adsorption in compacted bentonite: a critical review. *Journal of Contaminant Hydrology*, 61(1-4): 293-302.

Bourg, I.C., Sposito, G. (2010) Connecting the Molecular Scale to the Continuum Scale for Diffusion Processes in Smectite-Rich Porous Media. *Environmental Science and Technology*, 44(6): 2085-2091.

Bradbury, M.H., Baeyens, B. (2009a) Sorption modelling on illite Part I: Titration measurements and the sorption of Ni, Co, Eu and Sn. *Geochimica Et Cosmochimica Acta*, 73(4): 990-1003.

Bradbury, M.H., Baeyens, B. (2009b) Sorption modelling on illite. Part II: Actinide sorption and linear free energy relationships. *Geochimica Et Cosmochimica Acta,* 73(4): 1004-1013.

Bradbury, M.H., Baeyens, B., Geckeis, H., Rabung, T. (2005) Sorption of Eu(III)/Cm(III) on Ca-montmorillonite and Na-illite. Part 2: Surface complexation modeling. *Geochimica et Cosmochimica Acta*, 69(23): 5403-5412.

Bradbury, M.H., Bradbury, B. (1997) A mechanistic description of Ni and Zn sorption on Na-montmorillonite Part II: modeling. *Journal of Contaminant Hydrology*, 27: 223-248.

Brady, P.V., Cygan, R.T., Nagy, K.L. (1996) Molecular Controls on Kaolinite Surface Charge. *Journal of Colloid and Interface Science*, 183: 356-364.

Campen, R.K., Pymer, A.K., Nihonyanagi, S., Borguet, E. (2010) Linking Surface Potential and Deprotonation in Nanoporous Silica: Second Harmonic Generation and Acid/Base Titration. *Journal of Physical Chemistry C*, 114(43): 18465-18473.

Chen, H., Wang, A.Q. (2007) Kinetic and isothermal studies of lead ion adsorption onto palygorskite clay. *Journal of Colloid and Interface Science*, 307(2): 309-316.

Chipera, S.J., Bish, D.L. (2001) Baseline studies of the clay minerals society source clays: Powder X-ray diffraction analyses. *Clays and Clay Minerals*, 49(5): 398-409.

Claret, F. et al. (2010) Natural iodine in a clay formation: Implications for iodine fate in geological disposals. *Geochimica Et Cosmochimica Acta*, 74(1): 16-29.

Coppin, F., Berger, G., Bauer, A., Castet, S., Loubet, M. (2002) Sorption of lanthanides on smectite and kaolinite. *Chemical Geology*, 182: 57-68.

Couture, R.A., Seitz, M.G. (1983) Sorption of anions of iodine by iron oxides and kaolinite. *Nuclear and Chemical Waste Management*, 4: 301-306.

Dahn, R. et al. (2003) Structual evidence for the sorption of Ni(II) atoms on the edges of montmorillonite clay minerals: A polarized X-ray absorption fine edge study. *Geochimica et Cosmochimica Acta*, 67(1): 1-15.

Davis, J.A., Coston, J.A., Kent, D.B., Fuller, C.C. (1998) Application of the surface complexation modeling concept to to complex mineral assemblages. *Environmental Science & Technology*, 32: 2820-2828.

Desbois, G., Urai, J.L., Kukla, P.A. (2009) Morphology of the pore space in claystones - Evidence from BIB/FIB ion beam sectioning and cryo-SEM observations. *eEarth*, 4(1): 15-22.

Dewers, T., Ortoleva, P. (1990) A coupled reaction/transport/mechanical model for intergranular pressure solution, styolites, and differential compaction and cementation in clean sandstones. *Geochimica et Cosmochimica Acta*, 54(6): 1609-1625.

Douch, J., Hamdani, M., Fessi, H., Elaissari, A. (2009) Acid-base behavior of a colloidal clays fraction extracted from natural quartz sand: Effect of permanent surface charge. C*olloids and Surfaces a-Physicochemical and Engineering Aspects*, 338(1-3): 51-60.

Dove, P.M., Craven, C.M. (2005) Surface charge density on silica in alkali and alkaline earth chloride electrolyte solutions. *Geochimica Et Cosmochimica Acta*, 69(21): 4963-4970.

Drits, V.A. (2003) Structural and chemical heterogeneity of layer silicates and clay minerals. *Clay Minerals*, 38(4): 403-432.

Duc, M., Gaboriaud, F., Thomas, F. (2005a) Sensitivity of the acid-base properties of clays to the methods of preparation and measurement 1. Literature Review. *Journal of Colloid and Interface Science*, 289: 139-147.

Duc, M., Gaboriaud, F., Thomas, F. (2005b) Sensitivity of the acid-base properties of clays to the methods of preparation and measurement 2. Evidence from potentiometric titrations. *Journal of Colloid and Interface Science*, 289: 148-156.

Dultz, S., Riebe, B., Bunnenberg, C. (2005). Temperature effects on iodine adsorption on organo-clay minerals II.Structural effects. *Applied Clay Science*, 28: 17-30.

Fox, P.M., Kent, D.B., Davis, J.A. (2010) Redox Transformations and Transport of Cesium and Iodine (-1, 0, +5) in Oxidizing and Reducing Zones of a Sand and Gravel Aquifer. *Environmental Science and Technology*, 44(6): 1940-1946.

Frini-Srasra, N., Kriaa, A., Srasra, E. (2007) Acid-base properties of Tunisian palygorskite in aqueous medium. *Russian Journal of Electrochemistry*, 43(7): 795-802.

Fuhrmann, M., Bajt, S., Schoonen, M.A.A. (1998) Sorption of iodine on minerals investigated by X-ray absorption near edge structure (XANES) and I-125 tracer sorption experiments. *Applied Geochemistry*, 13(2): 127-141.

Garcia-Gutierrez, M. et al. (2001) Solute transport properties of compacted Ca-bentonite used in the FEBEX project. *Journal of Contaminant Hydrology*, 47: 127-137.

Gasgova, O.L., Bukaty, M.B. (2008) Sorption of different cations onto clay minerals: Modelling approach with ion exchange and surface complexation. *Physics and Chemistry of the Earth*, 33: 1050-1055.

Gimmi, T., Kosakowski, G. (2011) How Mobile Are Sorbed Cations in Clays and Clay Rocks? *Environmental Science & Technology*, 45(4): 1443-1449.

Glaus, M.A., Frick, S., Rosse, R., Van Loon, L.R. (2010) Comparative study of tracer diffusion of HTO $^{22}Na^+$ and $^{36}Cl^-$ in compacted kaolinite, illite, and montmorillonite. *Geochimica et Cosmochimica Acta*, 74: 1999-2010.

Glaus, M.A., Muller, W., Van Loon, L.R. (2008) Diffusion of iodide and iodate through Opalinus Clay: Monitiring of the redox state using an anion chromatogrpahic technique. *Applied Geochemistry*, 23: 3612-3619.

Gonzalez-Sanchez, F. et al. (2008) Self-diffusion of water and its dependence on temperature and ionic strength in highly compacted montmorillonite, illite and kaolinite. *Applied Geochemistry*, 23: 3480-3851.

Gu, X., Evans, L.J., Barabash, S.J. (2010). Modeling the adsorption of Cd(II), Cu(II), Ni(II), Pb(II) and Zn(II) onto montmorillonite. *Geochimica et Cosmochimica Acta*, 74: 5718-5728.

Guerin, M., Seaman, J.C., Lehmann, C., Jurgenson, A. (2004) Acoustic and electroacoustic characterization of variable-charge mineral suspensions. *Clays and Clay Minerals*, 52(2): 158-170.

Heath, J.E. et al. (2011) Pore networks in continental and marine mudstones: Characterisitic and contorls on sealing behavior. *Geosphere*, 7(2): 429-454.

Honeyman, B.D. (1984) *Cation and Anion Adsorption in Binary Mixtures of Adsorbents: An Investigation of the Concept of Adsorptive Additivity*. Ph.D. Dissertation, Stanford University, Stanford.

Hu, Q., Zhao, P., Moran, J.E., Seaman, J.C. (2005) Sorption and transport of iodine species in sediments from the Savannah River and Hanford Sites. *Journal of Contaminant Hydrology*, 78: 185-205.

Huertas, F.J., Chou, L., Wollast, R. (1998) Mechanism of kaolinite dissolution at room temperature and pressure: Part 1. Surface speciation. *Geochimica Et Cosmochimica Acta*, 62(3): 417-431.

Jan, Y.-L. et al. (2007) Coupled mechanics, hydraulics and sorption properties of mixtures to evaluate buffer/backfill materials. *Physics and Chemistry of the Earth*, 32: 789-794.

Jansson, M., Eriksen, T.E. (2004) In situ anion diffusion experiments using radiotracers. *Journal of Contaminant Hydrology*, 68(3-4): 183-192.

Johnston, C.T. (2010) Probing the nanoscale architecture of clay minerals. Clay Minerals, 45: 245-279.

Jougnot, D., Revil, A., Leroy, P. (2009) Diffusion of ionic tracers in the Callovo-Oxfordian clay-rock using the Donnan equilibrium model and the formation factor. *Geochimica Et Cosmochimica Acta*, 73(10): 2712-2726.

Kaplan, D.I., Serne, R.J., Parker, K.E., Kutnyakov, I.V. (2000). Iodide Sorption to Subsurface Sediments and Illitic Materials. *Environmental Science & Technology*, 34(3): 399-405.

Kosmulski, M., Dahlsten, P. (2006) High ionic strength electrokinetics of clay minerals. *Colloids and Surfaces A-Physicochemical and Engineering Aspects*, 291: 212-218.

Kraepiel, A.M.L., Keller, K., Morel, F.M.M. (1998) On the acid-base chemistry of permanently charged minerals. *Environmental Science & Technology*, 32(19): 2829-2838.

Kraepiel, A.M.L., Keller, K., Morel, F.M.M. (1999) A Model for Metal Adsorption on Montmorillonite. *Journal of Colloid and Interface Science*, 210: 43-54.

Krekeler, M.P.S., Guggenheim, S. (2008) Defects in microstructure in palygorskite-sepiolite minerals: A transmission electron microscopy (TEM) study. *Applied Clay Science*, 39(1-2): 98-105.

Kriaa, A., Hamdi, N., Srasra, E. (2008) Surface Properties and Modeling Potentiometric Titration of Aqueous Illite Suspensions. *Surface Engineering and Applied Electrochemistry*, 44(3): 217-229.

Kulik, D.A., Aja, S.U., Sinitsyn, V.A., Wood, S.A. (2000) Acid-base surface chemistry and sorption of some lanthanides on K^+-saturated Marblehead illite: II. A multisite-surface complexation modeling. *Geochimica Et Cosmochimica Acta*, 64(2): 195-213.

Lloret, A. et al. (2003) Mechanical behaviour of heavily compacted bentonite under high suction changes. *Geotechnique*, 53(1): 27-40.

Ma, C., Eggleton, R.A. (1999) Surface layer types of kaolinite: A high resolution transmission electron microscope study. *Clays and Clay Minerals*, 47(2): 181-191.

Maes, N. et al. (2008) Retention of Cs in Boom Clay: Comparison of data from batch sorption tests and diffusion experiments on intact clay cores. *Physics and Chemistry of the Earth,* 33: S149-S155.

McKinley, J.P. et al. (2004) Microscale Distribution of Cesium Sorbed to Biotite and Muscovite. *Environmental Science & Technology*, 38(4): 1017-1023.

Melkior, T. et al. (2009) Na^+ and HTO diffusion in compacted bentonite: Effect of surface chemistry and related texture. *Journal of Hydrology*, 370: 9-20.

Miller, A.W., Rodriguez, D.R., Honeyman, B.D. (2010) Upscaling Sorption/Desorption Processes in Reactive Transport Models to Describe Metal/Radionuclide Transport: A Critical Review. *Environmental Science & Technology*, 44(21): 7996-8007.

Missana, T., Alonso, U., Garcia-Gutierrez, M. (2009) Experimental study and modelling of selenite sorption onto illite and smectite clays. *Journal of Colloid and Interface Science*, 334(2): 132-138.

Missana, T., Garcia-Gutierrez, M., Alonso, U. (2008) Sorption of strontium onto illite/smectite mixed clays. *Physics and Chemistry of the Earth*, 33: S156-S162.

Molera, M., Eriksen, T. (2002) Diffusion of Na-22(+), Sr-85(2+), Cs-134(+) and Co-57(2+) in bentonite clay compacted to different densities: experiments and modeling. *Radiochimica Acta,* 90(9-11): 753-760.

Molera, M., Eriksen, T., Jansson, M. (2003) Anion diffusion pathways in bentonite clay compacted to different dry densities. *Applied Clay Science*, 23(1-4): 69-76.

Musso, G., Morales, E.R., Gens, A., Castellanos, E. (2003) The role of structure in the chemically induced deformations of FEBEX bentonite. *Applied Clay Science*, 23(1-4): 229-237.

Ochs, M., Lothenbach, B., Wanner, H., Sato, H., Yui, M. (2001) An integrated sorption-diffusion model for the calculation of consistent distribution and diffusion coefficients in compacted bentonite. *Journal of Contaminant Hydrology*, 47: 283-296.

Oscarson, D.W. (1994) Surface diffusion: Is it an important transport mechanism in compacted clays? *Clays and Clay Minerals*, 42(5): 534-543.

Rabung, T. et al. (2005) Sorption of Eu(III) on Ca-montmorillonite and Na-illite Part 1: Batch sorption and time-resolved laser fluorescence spectroscopy experiments. *Geochimica et Cosmochimica Acta*, 69(23): 5393-5402.

Revil, A., Linde, N. (2006) Chemico-electromechanical coupling in microporous media. *Journal of Colloid and Interface Science*, 302(2): 682-694.

Rotenberg, B., Marry, V., Dufreche, J.-F., Giffaut, E., Turq, P. (2007) A multiscale approach to ion diffusion in clays: Building a two-state diffusion-reaction scheme from microscopic dynamics. *Journal of Colloid and Interface Science*, 309: 289-295.

Rozalen, M., Brady, P.V., Huertas, F.J. (2009) Surface chemistry of K-montmorillonite: Ionic strength, temperature dependence annd dissolution kinetics. *Journal of Colloid and Interface Science*, 333: 474-484.

Sanchez del Rio, M. et al. (2005) Mg K-edge XANES of sepiolite and palygorskite. *Nuclear Instruments and Methods in Physics Research B*, 238: 55-60.

Sato, H., Ashida, T., Kohara, Y., Yui, M., Sasaki, N. (1992) Effect of Dry Density on Diffusion of Some Radionuclides in Compacted Sodium Bentonite. *Journal of Nuclear Science and Technology*, 29(9): 873-882.

Schlegel, M.L., Manceau, A., Charlet, L., Hazemann, J.L. (2001) Adsorption mechanisms of Zn on hectorite as a function of time, pH, and ionic strength. *American Journal of Science*, 301(9): 798-830.

Sinitsyn, V.A., Aja, S.U., Kulik, D.A., Wood, S.A. (2000) Acid-base surface chemistry and sorption of some lanthanides on K^+-saturated Marblehead illite: I. Results of an experimental investigation. *Geochimica Et Cosmochimica Acta*, 64(2): 185-194.

Sondi, I., Biscan, J., Pravdic, V. (1996) Electrokinetics of pure clay minerals revisited. *Journal of Colloid and Interface Science*, 178(2): 514-522.

Teppen, B.J., Miller, D.M. (2006) Hydration energy determines isovalent cation exchange selectivity by clay minerals. *Soil Science Society of America Journal*, 70(1): 31-40.

Tertre, E., Castet, S., Berger, G., Loubet, M., Giffaut, E. (2006). Surface chemistry of kaolinite and Na-montmorillonite in aqueous electrolyte solutions at 25 and 60C: Experimental and modeling study. *Geochimica Et Cosmochimica Acta*, 70: 4579-4599.

Thompson, H.A., Parks, G.A., Brown, G.E. (1999) Dynamic interactions of dissolution, surface adsorption, and precipitation in an aging cobalt(II)-clay-water system. *Geochimica Et Cosmochimica Acta*, 63(11-12): 1767-1779.

Tournassat, C., Chapron, Y., Leroy, P., Bizi, M., Boulahya, F. (2009) Comparison of molecular dynamics simulations with triple layer and modified Gouy-Chapman models in a 0.1 M NaCl-montmorillonite system. *Journal of Colloid and Interface Science*, 339(2): 533-541.

Tournassat, C., Ferrage, E., Poinsignon, C., Charlet, L. (2004a) The titration of clay minerals II. Structure-based model and implications for clay reactivity. *Journal of Colloid and Interface Science*, 273: 234-246.

Tournassat, C., Greneche, J.-M., Tisserand, D., Charlet, L. (2004b) The titration of clay minerals I. Discontinuous backtitration technique combined with CEC measurements. *Journal of Colloid and Interface Science*, 273: 224-233.

Turner, G.D., Zachara, J.M., McKinley, J.P., Smith, S.C. (1996) Surface-charge properties and UO_2^{2+} adsorption of a subsurface smectite. *Geochimica Et Cosmochimica Acta*, 60(18): 3399-3414.

Van Loon, L.R., Glaus, M.A. (2008) Mechancial Compaction of Smectite Clays Increases Ion Exchange Selectivity for Cesium. *Environmental Science & Technology*, 42(5): 1600-1604.

Van Loon, L.R., Glaus, M.A., Muller, W. (2007) Anion exclusion effects in compacted bentonites: Towards a better understanding of anion diffusion. *Applied Geochemistry*, 22: 2536-2552.

Van Loon, L.R., Jakob, A. (2005) Evidence for a second transport porosity for the diffusion of tritiated water (HTO) in a sedimentary rock (Opalinus clay-OPA): Application of through- and out-diffusion techniques. *Transport in Porous Media*, 61(2): 193-214.

Van Loon, L.R., Soler, J.M., Bradbury, M.H. (2003) Diffusion of HTO, $^{36}Cl^-$, and $^{125}I^-$ in Oplainus Clay samples from Mont Terri Effect of confining pressure. *Journal of Contaminant Hydrology*, 61: 73-83.

Vico, L.I. (2003) Acid-base behaviour and Cu2+ and Zn2+ complexation properties of the sepiolite/water interface. *Chemical Geology*, 198(3-4): 213-222.

Vinsova, H., Konirova, R., Koudelkova, M., Jedinakova-Krizova, V. (2004) Sorption of technetium and rhenium on natural sorbente under aerobic conditions. *Journal of Radioanalytical and Nuclear Chemistry*, 261(2): 407-413.

Vinsova, H., Vecernik, P., Jedinakova-Krizova, V. (2006) Sorption characterisitcs of ^{99}Tc onto bentonite material with different additives under anaerobic conditions. *Radiochimica Acta*, 94: 435-440.

Wang, P., Anderko, A., Turner, D.R. (2001) Thermodynamic Modeling of the Adosrption of Radionuclides on Selected Minerals. II: Anions. *Industrial and Engineering Chemical Research*, 40(20): 4444-4455.

Wang Y. (2011) *Research & Development Plan for Used Fuel Disposition Campaign (UFDC) Natural Systems Evaluation and Tool Development*, U.S. DOE Used Fuel Disposition Campaign, May 25, 2011.

Wang, Y., Gao, H., Xu, H. (2011) *Nanogeochemistry: Nanostructures and Their Reactivity in Natural Systems*. In: Harmon, R.S., Parker, A. (Eds.), Frontiers in Geochemistry: Contribution of Geochemistry to the Study of the Earth. Wiley-Blackwell Publishing Ltd., pp. 200-220.

Wang, Y.F. et al. (2002) Interface chemistry of nanostructured materials: Ion adsorption on mesoporous alumina. *Journal of Colloid and Interface Science*, 254(1): 23-30.

Xu, S., Harsh, J.B. (1990a) Hand and Soft Acid-Base Model Verified for Monovalent Cation Selectivity. *Soil Science Society of America Journal*, 54: 1596-1601.

Xu, S., Harsh, J.B., (1990b) Monovalent Cation Selectivity Quantitatively Modeled According to Hard/Soft Acid/Base Theory. *Soil Science Society of America Journal*, 54: 357-363.

Yamaguchi, T., Nakayama, S., Nagao, S., Kizaki, M. (2007) Diffusive transport of neptunium and plutonium through compacted sand-bentonite mixtures under anaerobic conditions. *Radiochimica Acta*, 95(2): 115-125.

Yaroshchuk, A., Glaus, M.A., Van Loon, L.R. (2007) Studies of electrochemical properties of compacted clays by concentration potential method. *Journal of Colloid and Interface Science*, 309(2): 262-271.

Zhao, H.Y. et al. (2008) Probing Surface Charge Potentials of Clay Basal Planes and Edges by Direct Force Measurements. *Langmuir*, 24(22): 12899-12910.

Zheng, L., Samper, J. (2008) A coupled THMC model of FEBEX *mock-up* test. *Physics and Chemistry of the Earth*, 33: S486-S498.

Chapter 5: Experimental Study of Radionuclide Mobility and Colloid Formation

5.1   Introduction

Plutonium (Pu) and Neptunium (Np) have been identified as dominant long-term dose contributors under certain nuclear waste repository scenarios (Kaszuba and Runde, 1999; Management, 2002). The transport of Pu is expected to occur by natural or anthropogenic colloids. While the migration of Np(V) will likely be controlled by its weak sorption to mineral surfaces, colloid-facilitated transport of the reduced form [Np(IV)] may also be possible (Hakanen and Lindberg, 1993). The dominant anthropogenic colloids are likely to be iron oxides produced as a result of steel corrosion (Management, 2002). The mineralogy of natural colloids will be a function of the host rock mineralogy. However, aluminosilicate clays are ubiquitous in nature and are commonly observed as mobile colloids due to their inherently small particle size (Kersting et al., 1999).   The proposed use of bentonite within engineered barrier systems for underground nuclear waste repositories provides additional importance to understanding Pu and Np interaction with smectite aluminosilicate minerals (Sabodina et al., 2006).

Host rock minerals such as smectite and iron oxide minerals are known to sorb Np and Pu (Bertetti et al., 1998; Keeney-Kennicutt and Morse, 1985; Kozai et al., 1996; Kozai et al., 1993; Lujaniene et al., 2007; Powell et al., 2004, 2005; Powell et al., 2008b; Sabodina et al., 2006; Sanchez et al., 1985; Turner et al., 1998), which will result in actinide immobilization or retention. However, actinide sorption to these same minerals in colloid size may also result in transport (e.g. Kersting et al., 1999). Iron oxides and smectite clays represent key phases that will control transport of Pu and Np in repository near fields and far fields. As such, they are the focus of the effort summarized in this chapter.

A major challenge in predicting the mobility and transport of actinides in the natural environment is to determine the dominant geochemical processes that control their transport behavior. The reaction chemistry of Pu (*i.e.*, aqueous speciation, solubility, sorptivity, redox chemistry, and affinity for colloidal particles, both abiotic and microbially-mediated) is particularly complicated. Its migration is known to be oxidation-state dependent and facilitated by transport on particulate matter (*i.e.*, colloidal particles). Despite the recognized importance of colloid-facilitated transport, very little is known about the geochemical and biochemical mechanisms controlling Pu-colloid formation and stability. The interest in understanding the behavior of Pu in the natural environment encompasses both high concentrations expected at the source location and extremely low concentrations encountered at significant distances from the source. Its behavior must be understood over a 10 order of magnitude concentration range, from solubility–controlled [$>5 \times 10^{-9}$ M, Neck et al. (2007)] near-field concentrations to sorption-controlled (10^{-12}-10^{-18} M) far field concentrations. The relevant processes that control the behavior of Pu in the subsurface are not the same across this large range of concentrations and experimental results at high concentrations cannot simply be scaled to low concentrations. For example, at higher concentrations, Pu tends to form intrinsic nano-colloids (Neck et al., 2007); it is not known whether these nano-colloids are produced or are stable at very low (e.g. femtomolar) concentrations. The source locations at future radioactive waste repositories will also likely involve environments at elevated temperatures. Thus, the effect of elevated temperature on the stability and sorptivity of monomeric and colloidal Pu needs to be understood.

This chapter addresses Topics P10 and P11 of the R&D Plan for the UFDC Natural Systems Evaluation

and Tool Development (Wang, 2011; Chapter 1). The focus of this chapter is to evaluate the sorption behavior of Pu at elevated temperatures in the presence of relevant minerals and over a range of concentrations that span environmental conditions in the near-field and far-field. Our effort in FY10 focused on the behavior of two common forms of Pu: aqueous Pu(IV) and intrinsic Pu(IV) nano-colloids. We examined the sorption behavior of these two forms of Pu with iron oxide (goethite, α-FeOOH) at 25 and 80°C. In early FY11, we characterized the morphology of Pu sorbed to goethite using transmission electron microscopy (TEM). A second set of experiments was initiated in FY11 to investigate the behavior of Pu in the presence of clays (montmorillonite) and study the stability of sorbed and nano-particulate Pu. The elevated temperature experiments are leveraged by a parallel on-going effort at Lawrence Livermore National Laboratory (LLNL) to understand the geochemical mechanisms that control Pu transport at ambient temperatures funded by the Office of Science Subsurface Biogeochemical Research (SBR) program in the Office of Biological and Environmental Research (BER).

5.2   State of the Art

Reactive transport models that address geochemical processes occurring at the mineral-water interface are still in their infancy for multi-phase systems (U.S. Department of Energy, 2007). Generally, existing transport models have ignored the coupled factors of redox chemistry and microbial activity and have relied on empirical equilibrium or rate-limited K_d models to address actinide retardation and colloid-facilitated transport (*e.g.* Glynn, 2003; Pickett, 2005; Tien and Jen, 2007). Experimental data from Powell and others (Demirkanli et al., 2008; Kaplan et al., 2004; Kaplan et al., 2006; Powell et al., 2005) suggest that these simplified models cannot adequately predict Pu transport because they do not capture the coupled processes controlling Pu uptake and release. Significant breakthroughs in our conceptual model of Pu transport will only occur through an improved understanding of the geochemical processes and associated kinetics that occur at the mineral-water interface (e.g. sorption, desorption, colloidal formation) at a range of concentrations and relevant environmental conditions.

In our most recent work, we examined the behavior of Pu in the presence of goethite and quartz (Powell et al., 2011). Transmission electron microscopy (TEM) was used to characterize the morphology of Pu associated with these mineral phases. Plutonium was added to goethite and quartz suspensions either as intrisic Pu nano-colloids or as aqueous Pu(IV). Plutonium nano-colloids that formed on goethite from aqueous monomers underwent a lattice distortion relative to the ideal fluorite-type structure, fcc, PuO_2, resulting in the formation of a bcc, Pu_4O_7. This structural distortion resulted from an epitaxial growth of the plutonium colloid on goethite, leading to stronger binding of plutonium compared with other minerals such as quartz where the distortion was not observed. The results suggest that the morphology of Pu associated mineral surfaces will vary and affect its sorption/desorption behavior. An understanding of the stability and kinetics of the resulting Pu association is critical to predicting its long-term colloid-facilitated transport behavior (Cvetkovic, 2000; Cvetkovic et al., 2004; Missana et al., 2004; Saiers and Hornberger, 1996; Steefel, 2008).

The importance of sorption/desorption reversibility and kinetics in predicting actinide transport was most recently discussed in Powell et al. (2008b) (Np and Pu) and Tinnacher et al. (2011) (Np). Tinnacher et al. (2011) evaluated the relevance of aging, hysteresis and irreversible sorption for Np(V) sorption/desorption on goethite via kinetic modeling of a complex and long-term flow-cell experiment. The results indicated that Np(V) desorption rates were much slower than the (ad)sorption rates, and that the rates decreased over the course of the experiment. The modeling effort required a multi-reaction model including an equilibrium Freundlich site, a kinetically-controlled first-order site, and a transition state theory-related parameter $\psi_{2,de}$, which affected the desorption rate from the kinetically-controlled site. The $\psi_{2,de}$ parameter provided a mechanistic basis for a dependence of desorption rates on the net

111

direction of surface reactions. It suggests that the activation complexes or reaction pathways controlling sorption and desorption are unique and affect the observed kinetics. Based on these modeling efforts, aging processes were found to be relevant, while hysteresis and irreversible sorption could be neglected within an experimental desorption time-frame of ~1 month. Thus, desorption reactions appeared to be slow, but not irreversible. If the assumption of irreversible Np(V) sorption to goethite in transport models is not justifiable, the relevance of colloid-facilitated Np(V) transport may be negligible. However, the colloid facilitated transport of reduced forms of Np and Pu may still be significant.

The work documented here builds on our recent work and tests the hypothesis that sorption/desorption behavior of Pu is controlled by the morphology of Pu deposited on mineral substrates which, in turn, depends on the conditions under which Pu was deposited (e.g. Pu concentration, form, oxidation state, temperature, etc.). We predict that sorption can be categorized as mononuclear adsorption, surface precipitation, or weak electrostatic interaction between intrinsic Pu nano-colloids or amorphous precipitates and mineral surfaces. The rates of formation and stability of each form will be dependent on solution conditions, substrate characteristics, and temperature. Down-gradient transport of Pu will be determined by its stability as a colloidal form (intrinsic or otherwise). The results of these efforts will provide a clearer understanding of how Pu can migrate over significant temporal and spatial scales (e.g. Kersting et al., 1999; Novikov et al., 2006; Xu et al., 2006).

5.3   TECHNICAL APPROACH

5.3.1 Pu sorption to goethite at 25 and 80°C

In FY10, we began testing our hypothesis by examining the behavior of Pu in the presence of goethite (α-FeOOH), an iron oxyhydroxide commonly found in subsurface sediments. Two series of batch sorption experiments were conducted. In the first series, aqueous Pu(IV) was reacted with goethite at 25 and 80°C. The experiment was intended to test whether the affinity or morphology of sorbed Pu was temperature dependent. The experiment was performed under identical solution conditions used in an earlier 25°C sorption isotherm experiment (0.1g/L goethite, pH 8, 5 mM NaCl/0.7 mM NaHCO$_3$) (Zhao et al., 2010). However, in the present case, samples were equilibrated for three months rather than two weeks. Comparison of the present data to earlier isotherm data allowed us to evaluate the kinetic aspects of aqueous Pu(IV) sorption.

In the second set of experiments, intrinsic Pu(IV) nano-colloids were reacted with goethite at 25 and 80°C. The intrinsic Pu(IV) nano-colloid sorption experiment was intended to test whether the initial form of Pu affects its sorption behavior and evaluate the stability of Pu(IV) nano-colloids as a function of temperature. Our previous experiments have shown that sorption of aqueous Pu(IV) and Pu(V) to goethite at 25°C results in identical sorption affinities and surface products. We extend our examination to the sorption behavior of intrinsic Pu(IV) nano-colloids here.

At the end of the three month batch sorption experiments, Pu concentrations in the liquid phase were measured and compared to published amorphous PuO$_2$ (PuO$_2$(am, hyd)) solubility measurements (Neck et al., 2007) and sorption affinities (Zhao et al., 2010). In addition, a detailed characterization of the Pu associated with the goethite mineral surface was conducted using TEM. The combination of liquid phase and surface characterization was used to evaluate the effect of temperature and the comparative behavior of aqueous Pu(IV) versus intrinsic nano-colloid Pu(IV) on Pu sorption characteristics.

Pu stock solution: Alpha-emitting [242]Pu (> 99.8% by mass) was used in the experiments. The major isotopes contributing to alpha activities are [238]Pu, [239,240]Pu and [242]Pu with activity percentages of 15.9%, 5.2% and 78.9%, respectively. The Pu stock solution (7.6×10^{-4} M Pu(IV) in 2.06 M HCl) was purified using AG1x8 100-200 mesh anion exchange resin and filtered through a 3kD molecular weight cut-off (MWCO) filter. The oxidation state of Pu was confirmed using both UV/VIS and solvent extraction. The aqueous Pu(IV) working solution was prepared by diluting the stock solution to 1.9×10^{-4} M Pu(IV) in 1N HCl. The intrinsic Pu(IV) nano-colloid working solutions was prepared by adding 1 mL 1N NaOH and 0.39 mL pH 8 buffer (5 mM NaCl/0.7 mM NaHCO$_3$) to 0.53 mL of the Pu(IV) stock. Another 0.06 mL of 1N NaOH was added gradually to adjust the pH to ~8.5 and induce PuO$_2$(am, hyd.) precipitation . The final Pu(IV) nano-colloid concentration (including the precipitate) was 1.5×10^{-4} M. The majority of Pu(IV) in the working solution was retained by 3kD MWCO filter. Thus, we estimate that the intrinsic nano-colloid size was generally >1 nm. The fundamental particle size of intrinsic Pu nano-colloids prepared in this manner is 2-5 nm (Figure 5-1). However, aggregation of these intrinsic nano-colloids is commonly observed such that the aggregate size is larger (Powell et al., 2011).
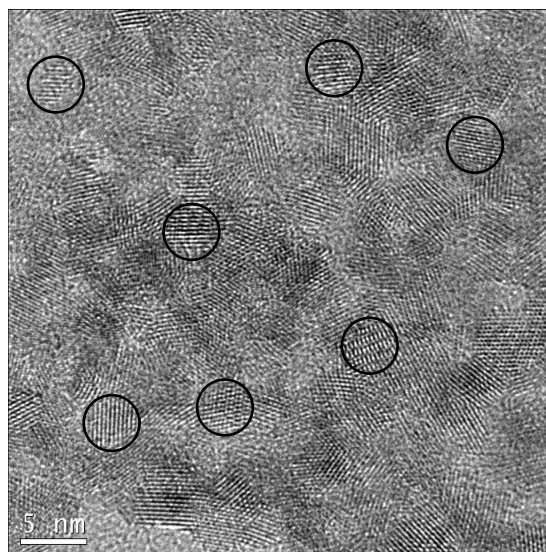
Figure 5-1. HRTEM of aggregated intrinsic Pu(IV) intrinsic nano-colloids. Circles denote individual Pu(IV) nano-colloid locations. The composition of particles was determined by EDX and the structure by high resolution transmission electron microscopy.

Goethite material: Goethite was synthesized from Fe(NO$_3$)$_3$•9H$_2$O as described by Schwertmann and Cornell (1991). Goethite was washed with a 5 mM NaCl/0.7 mM NaHCO$_3$ buffer solution, sonicated for 5 minutes, and centrifuged for 60 minutes at 3500 rpm three times until constant pH was reached. Based on a spherical particle sedimentation estimate (Gee and Bauder, 1986), the goethite particle size retained was >100 nm. X-ray diffraction confirmed goethite as the major phase, the point of zero salt effect was 8.5 ± 0.1 and the BET surface area was 16 m^2/g. Additional characterization details can be found in Powell et al. (2008).

Batch experiments: All batch experiments were conducted in 10 mL Nalgene* Oak Ridge polycarbonate centrifuge tubes with sealing caps. Either aqueous Pu(IV) or intrinsic Pu(IV) nano-colloids were spiked into 9 mL of 5 mM NaCl/0.7 mM NaHCO$_3$ in which goethite (solid to liquid ratio of 0.1g/L) had previously been added. Goethite-free Pu solutions were prepared in parallel. For the aqueous Pu(IV) experiments, an equivalent amount of NaOH was added before adding the Pu spike to ensure a final

solution pH of 8. The 10 mL tubes were submerged in 50 mL polypropylene conical centrifuge tubes filled with MQ water to minimize evaporative losses and provide secondary containment to the radioactive samples. Over the course of the experiment, the 25°C sample tubes were stored vertically in a hood. The 80°C sample tubes were submerged in a heated water bath. Samples were periodically (weekly) shaken and weighed to check for fluid evaporative losses; no significant loss of fluid was observed over the course of the experiment.

Three initial Pu concentrations were used in each of the two sorption experiment series (Table 5-1) such that the resulting equilibrium Pu concentration would be below, above, and near the PuO_2(am, hyd) solubility (~5×10^{-9} M) (Neck et al., 2007). Two goethite-free solutions (spiked blanks) with initial Pu concentrations below and above PuO_2(am, hyd) solubility were used for comparison with sorption experiments. All solutions were allowed to react for 103 days.

At the conclusion of each experiment, two samples were taken from each tube. The pH was measured and found to decrease only slightly from 8.1 of the start to 7.7 at the ned of experiment. The samll decrease in pH was equilent at both temperatures. The first supernatant sample was taken after the goethite was allowed to settle out for 60 hrs. Based on sedimentation rates, we estimate that the supernatant included particles < ~250 nm on average (Table 5-2). The second supernatant sample was collected after centrifugation at 5000 rpm for 90 minutes *at room temperature*. In this case, the supernatant included particles < ~25 nm on average. Because the 80°C sample centrifugation occurred at 25°C, there is a possibility that this decrease in temperature could affect the results. Centrifugation was expected to effectively remove goethite particles. Sedimentation was also expected to remove the majority of goethite from solution. Nevertheless, Fe in solution was monitored by ICP-MS. In all cases, Fe concentrations were low enough such that the contribution of goethite to the measured Pu solution concentration was predicted to be negligible (<0.2% of Pu in solution). Neither sedimentation nor centrifugation was expected to quantitatively remove dispersed Pu(IV) nano-colloids from solution. However, centrifugation would likely remove most aggregated nano-colloids. A comparison of the sedimentation and centrifugation supernatants provides information on the presence of intermediate-sized colloid particles in solution (25-250 nm). These may be small goethite particles with sorbed Pu but are more likely large aggregated intrinsic Pu nano-colloids.

Table 5-1. Experimental conditions for Pu(IV) samples at 25 and 80°C

Sample Number	Pu form	Initial Pu	Goethite concentration	*Predicted* equilibrium aqueous Pu[a]	*Predicted* surface load on goethite[b]
		mol/L	g/L	mol/L	fraction
1	Aqueous	7.3×10^{-11}	0	-	-
2	Aqueous	8.0×10^{-7}	0	-	-
3	Colloidal	9.6×10^{-11}	0	-	-
4	Colloidal	7.3×10^{-7}	0	-	-
5	Aqueous	3.8×10^{-9}	0.1	3.8×10^{-12}	0.0005
6	Aqueous	7.8×10^{-7}	0.1	7.8×10^{-10}	0.1
7	Aqueous	3.8×10^{-6}	0.1	3.8×10^{-9}	0.5
8	Colloidal	3.1×10^{-8}	0.1	3.1×10^{-11}	0.005
9	Colloidal	7.3×10^{-7}	0.1	7.3×10^{-10}	0.1
10	Colloidal	3.7×10^{-6}	0.1	3.7×10^{-9}	0.5

[a] Based on a Pu K_d of 3×10^6 mL/g from Powell et al. (2008).

[b] Surface loading estimated using 0.1 g/L goethite, 16 m^2/g, and a site density of 2.31 sites/nm^2 (Dzombak and Morel, 1990).

Table 5-2. Particle segregation methods and associated particle size cut-offs

Particle segregation method	Particle	Temperature	Particle size cut-off[a]
		°C	nm
Sedimentation	Goethite	25	375
Sedimentation	PuO_2(am, hyd)	25	225
Sedimentation	Goethite	80	250
Sedimentation	PuO_2(am, hyd)	80	125
Centrifugation	Goethite	25	35
Centrifugation	PuO_2(am, hyd)	25	19

[a] Sedimentation rates were calculated using goethite and PuO_2 densities of 4.27 and 11.5 g/cm^3. Fluid viscosity used at 25 and 80°C were 8.90×10^{-4} and 3.55×10^{-4}, respectively. The fluid density used at 25 and 80°C was 0.997 and 0.972 g/cm^3, respectively. Sedimentation was rounded to the nearest 25 nm.

Pu analysis: Both liquid scintillation counting (LSC) and ICP-MS measurements were used to determine Pu concentration. The LSC was used for samples with high Pu and ICP-MS used for samples in which Pu concentrations were below LSC method detection limit ($\sim 3 \times 10^{-10}$ M) . It is important to consider the fact that sedimentation and centrifugation only segregate particles greater than the associated particle size cut off. Thus, the measured Pu concentration in solution represents both aqueous Pu and Pu nano-colloids (or aggregates) smaller than the cutoff size for sedimentation or centrifugation (i.e. Table 5-2).

TEM sample preparation and analysis: At the conclusion of each experiment, the solid phases were washed in MQ (>18 MΩ) water three times by sequentially centrifuging at 5000 rpm for 90 minutes, decanting the supernatant, and replacing it with fresh MQ water. The washing was performed to remove salts from solution. The solids were re-suspended in MQ water by sonicating for 5 minutes and diluting 10× to produce a 0.01g/L suspension. A volume of 2 to 5 uL of each suspension was deposited on TEM carbon-coated copper grids and dried in a glass desiccator. All analyses were performed on a Philips CM 300 FEG TEM operating at 300kV and equipped with a Gatan Imaging Filter (GIF) with a 2k × 2k CCD camera and an EDX detector.

5.3.2   Pu sorption to montmorillonite at 25 and 80°C – a novel approach

Batch sorption has been the most common method used to measure the affinity of a contaminant for a mineral surface. Traditionally, a known amount of adsorbate is added to a liquid suspension containing a sorbent, and the aqueous concentration of adsorbate is measured after equilibrium is reached. The resulting affinity of the adsorbate for the sorbent is reported using the following formula:

$$K_d = (C_{init} - C_{final})/C_{final}) *V/m \qquad\qquad (5-1)$$

where C_{init} and C_{final} are initial and final aqueous concentration of adsorbate (mol/L), respectively, V is volume of liquid (mL), and m is the mass of adsorbent (g). However, if the adsorbate is involved in processes other than sorption (i.e. colloid formation or precipitation) the apparent K_d cannot address the fundamental processes controlling the reaction and may lead to a misinterpretation of experimental observations. This is particularly true in the case of Pu which is known be insoluble when in the reduced (IV) oxidation state and prone to formation of intrinsic nanoparticles (e.g. (Powell et al., 2011)). In order

to distinguish between precipitated, colloidal, and sorbed states of Pu, a technique by which precipitates and intrinsic colloids can be segregated from the sorbent is needed.

Dialysis membranes are commonly used to separate suspended solutes or particles of different dimensions in a liquid mixture. Dialysis membranes are used in biological applications, such as macromolecular purification, protein concentration/separation, and solute fractionation. They are also commonly used as part of the washing step in mineral synthesis (Schwertmann and Cornell, 1991) or to produce homoionic end-members of ion-exchanging mineral phases (e.g. Zavarin et al., 2011). Desirable size separation by dialysis can be achieved by selecting the membrane pore size molecular weight cut off (MWCO). Membrane pore sizes can range from 0.5 to 50 kiloDaltons that is approximately equivalent to 1 to 50 nanometer pore sizes. In the case of Pu, dialysis membranes provide a unique opportunity to segregate aquo (<1 nm), intrinsic nano-colloids (2-5 nm), and sorbed pseudocolloids or precipitates (>100 nm mineral phases).

In FY11, dialysis membranes were used to separate intrinsic Pu nano-colloids from montmorillonite colloids (sorbent), while allowing soluble Pu(IV) species to interact with both phases simultaneously. The experimental design and concepts are illustrated in Figure 5-1. This novel experimental design enables us to test the stability of intrinsic colloids relative to adsorbed species and surface precipitates. By taking samples as a function of time, we are also able to quantify reaction kinetics as the solutions approached equilibrium.

Two sets of experiments were performed as part of this study and are currently on going. In the first set of experiments, the sorption affinity, kinetics, and morphology of aqueous Pu(IV) sorption to montmorillonite and the effects of temperature (25 and 80°C) and adsorbate concentration were examined. In the second set of experiments, intrinsic Pu(IV) nano-colloids were reacted with montmorillonite. For comparative purposes, one intrinsic Pu nano- colloid/goethite sorption experiment was also conducted at 25°C. This goethite sorption experiment could be directly compared with earlier (FY10) batch sorption experiments (in the absence of a dialysis membrane). This is the first attempt to test intrinsic Pu nano-colloid stability using a dialysis membrane. The results are used to determine the relative stability of intrinsic- versus pseudo-colloids as a function of temperature and time. Quantifying the stability of the colloidal forms of Pu is critical to accurately predicting the down-gradient transport behavior of Pu. All experiments were performed under identical solution conditions used for Pu-goethite experiments (pH 8, 5 mM NaCl/0.7 mM NaHCO$_3$) but with a clay concentration of 1g/L. In the present study, samples were taken as a function of time for up to three months.
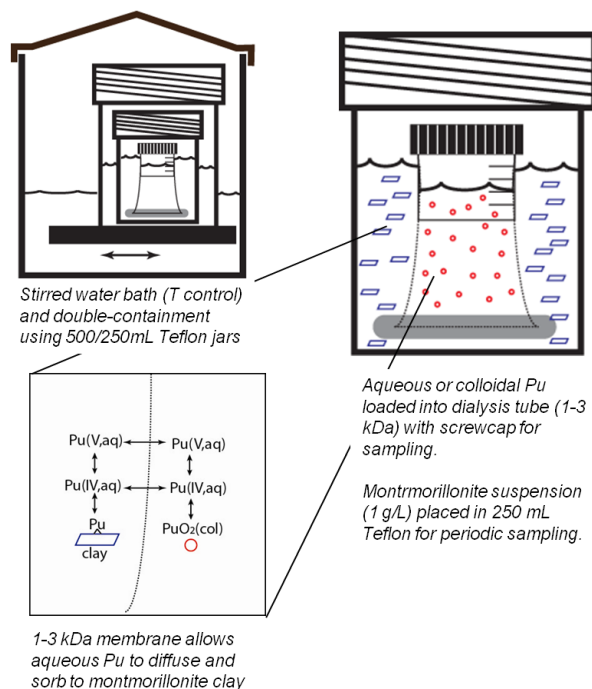
Figure 5-1. Novel experimental design using dialysis membrane to separate intrinsic Pu colloids from pseudo Pu/mineral colloids and the processes that form them.

Pu stock solution: Pu stock solutions with two different Pu isotopic ratios were used. A relatively pure alpha-emitting ^{238}Pu stock solution was used in low and intermediate Pu concentration samples. The isotopic ratios in mass percentage for ^{238}Pu, ^{239}Pu, ^{240}Pu and ^{241}Pu were 76.83%, 21.03%, 2.01% and 0.142%, respectively. The major isotope contributing to alpha activity in this stock was ^{238}Pu (~99.87% by activity). Second Pu stock, used in high Pu concentration experiments, was a ^{242}Pu solution spiked with ~1% of the ^{238}Pu stock. The mass percentages of the resulting ^{242}Pu stock for ^{238}Pu, ^{239}Pu, ^{240}Pu and ^{241}Pu and ^{242}Pu were 0.75%, 0.21%, 0.13%, 0.04% and 98.87%, respectively. The major isotopes contributing to alpha activity in this stock were ^{238}Pu (96.75%) and ^{242}Pu (2.93%). Pu stock solutions were purified using AG1x8 100-200 mesh anion exchange resin and filtered through a 3kD molecular weight cut-off (MWCO) filter. The oxidation state of Pu was confirmed using both UV/VIS and solvent extraction. The aqueous Pu(IV) starting solution was prepared by diluting the stock solution into a pH 8 buffer solution and gradually adding micro liters of NaOH (1N or 6N) to adjust pH to ~pH 8. The intrinsic Pu(IV) nano-colloids were prepared by adding NaOH to the Pu(IV) stocks and adjusting the pH to pH 9-10 to form Pu colloids. After aging for more than a week, the Pu colloids were centrifuged at an RCF of 9168 for 1hr and the supernatant was removed. The Pu colloid particle size cut-off was 14 nm or higher. However, the fundamental particle size of intrinsic Pu nano-colloids prepared in this manner is 2-5 nm. The Pu colloids were re-suspended in Milli-Q water. The Pu colloid starting solutions were prepared by adding a spike of Pu colloids into the pH 8 buffer solution without further pH adjustment. The concentration of soluble Pu in the Pu colloid starting solutions, measured in 3kD MWCO filtrate by LSC, were around 1~3% of the total colloid concentration.

Montmorillonite material: SWy-1 montmorillonite (Clay Minerals Society) was pre-treated using 1 mM HCl followed by addition of 0.1% of H_2O_2 into HCl solution. The suspension of treated montmorillonite was centrifuged to remove excess liquid and the wet paste was transferred to a 6000-8000 MWCO

dialysis tube suspended in 0.01 M NaCl solution for removal of ion-exchangeable impurities. The clay minerals were dialyzed for 7 days and the NaCl solution was changed at least once per day. The clay minerals were then suspended in Milli-Q water and centrifuged to obtain the fraction of particle sizes between 50 nm to 2 microns. The wet solids were dried at 40°C until a constant weight was obtained. A stock montmorillonite suspension was made by mixing 4 g the dried montmorillonite in 400 mL of pH 8 buffer solution (10 g/L). The surface area of montmorillonite measured by N_2(g)-BET was 31.45 ± 0.17 m^2/g comparable to the reported value of 31.8 m^2/ g (Clay Minerals Repository).

Batch experiments: All batch experiments were conducted in 500 mL Teflon jars with air-tied closures. 225 mL of pH 8 buffer solution was mixed with 25 mL of clay stock suspension to yield a 250 mL clay suspension at a solid to liquid ratio of 1g/L. A dialysis tube containing 30 mL of either aqueous Pu(IV) or intrinsic Pu(IV) nano-colloids was then placed in the 250 mL clay suspension. The dialysis tubes containing Pu were also placed in clay-free buffer solutions (blanks). The 500 mL Teflon jars were submerged in 1 L Teflon containers filled with Milli-Q water to minimize evaporative losses and provide secondary containment to the radioactive samples. Over the course of the experiment, the 25°C samples were placed on a top-loading orbital shaker and 80°C samples were submerged in a heated water bath shaker (Innova 3100) at a speed of 100 rpm. At each sampling time, 2 mL of the clay suspension was taken, mixed with 2.4 mL of Insta-Gel Plus liquid scintillation cocktail and counted to determine total Pu. A second 2 mL sample of the clay suspension was centrifuged at an RCF of 9168 for 1hr (particle size cut-off was 30 nm for the clay, 14 nm for intrinsic Pu colloids, if any) and 1.5 mL of the supernatant transferred into a LSC vial, mixed with 3 mL of Insta-Gel Plus liquid scintillation cocktail and counted to determine aqueous Pu. To monitor clay concentration, the absorbance of a third 0.5 mL sample of the clay suspension was measured using UV-VIS spectrometry (Cary 500, Varian) at a wavelength of 300-500 nm calibrated to a set of standards. The pH of each sample was also measured using this 0.5 mL sample.

Two initial Pu concentrations were used for aqueous Pu(IV) and three initial Pu concentrations were used for colloidal Pu sorption experiment series (Table 5-1) such that the starting Pu concentrations would be below, above, and near the PuO_2(am, hyd) solubility (~5×10^{-9} M) (Neck et al., 2007). Two montmorillonite-free solutions (spiked blanks) with initial Pu concentrations below and near PuO_2(am, hyd) solubility were used for comparison with sorption experiments. All sorption experiments are planned to run for 3 months. At the current reporting time, sorption experiments have run between 15 and 30 days. Pu analysis is being conducted by LSC, as described earlier. At the conclusion of these experiments, solid phases will be characterized by TEM to determine the form of Pu associated with the montmorillonite.

Table 5-3. Experimental conditions for Pu(IV) samples at 25 and 80°C

	Pu(IV,aq)	Swy-1 Montmorillonite	Pu colloid	Swy-1 Montmorillonite	Goethite
	mol/L	g/L	mol/L	g/L	g/L
25C	5.93E-12	1	1.13E-11	1	
	6.20E-10	1	8.31E-10	1	
	6.52E-12	0	2.01E-07	1	
			9.13E-10	0	
			2.01E-07		0.1
80C	5.93E-12	1	1.14E-11	1	
	6.20E-10	1	8.31E-10	1	
	6.52E-12	0	2.01E-07	1	
			9.13E-10	0	

5.4   TECHNICAL RESULTS

5.4.1   Pu sorption to goethite at 25 and 80°C

Pu behavior in the absence of goethite: Spiked-blanks (i.e. goethite-free solutions) were run in parallel with sorption experiments to evaluate loss of Pu to container walls and homogeneous nucleation of PuO_2(am, hyd) precipitates. Both aqueous Pu(IV) and intrinsic Pu(IV) nano-colloid solutions were equilibrated for 103 days at 25 and 80°C. Initial Pu concentrations were either oversaturated (~10^{-6} M) or undersaturated (~10^{-10} M) with respect to PuO_2(am, hyd). The solution concentration data are presented in Figure 5-3. To readily compare these solution concentrations to the solubility of PuO_2(am, hyd), we superimposed our data on the PuO_2(am, hyd) solubility data presented in figure 5 of Neck et al. (2007). In all undersaturated samples, significant losses of Pu from solution occurred (70-90%) over 103 days. However, we presume that the losses were dominated by sorption to container walls; precipitation of PuO_2(am, hyd) was not anticipated. Formation of Pu nano-colloids from aqueous Pu(IV), dissolution of Pu(IV) nano-colloids, or oxidation of Pu(IV) may have occurred in these samples, which needs to be further tested.

In the high concentration (~10^{-6} M) samples, the behavior of intrinsic Pu(IV) nano-colloids and aqueous Pu(IV) was distinct. Intrinsic Pu(IV) nano-colloids "precipitated" from solution (~99.7%) in equal amounts at both temperatures. The Pu concentration remaining in solution was consistent with the solubility of PuO_2(am, hyd) at 25°C as reported in Neck et al. (2007). The loss of Pu(IV) nano-colloids from solution appears to be driven by the aggregation of Pu(IV) nano-colloids and not the formation of large ordered precipitates (e.g. Figure 5-1). The behavior of aqueous Pu(IV) appeared to be temperature-dependent. At 103 days, the Pu concentration at 80°C was two orders of magnitude lower than at 25°C (Figure 5-3). The underlying reason for this is not known. Temperature may affect nano-colloid precipitation rates. However, Neck et al. (2007) results indicate that 100 days is sufficient to expect equilibrium. The aggregation behavior of nano-colloids can also be affected by temperature and solution

conditions (e.g. pH, ionic strength) (Garcia-Garcia et al. (2009)). Regardless of temperature, it is clear that homogeneous nucleation and precipitation of PuO_2(am, hyd) will occur under these oversaturated solution conditions and at both temperatures.

Sample initially spiked with Pu(IV), 25°C
Sample initially spiked with intrinsic Pu(IV) nano-colloids, 25°C
Sample initially spiked with Pu(IV), 80°C
Sample initially spiked with intrinsic Pu(IV) nano-colloids, 80°C
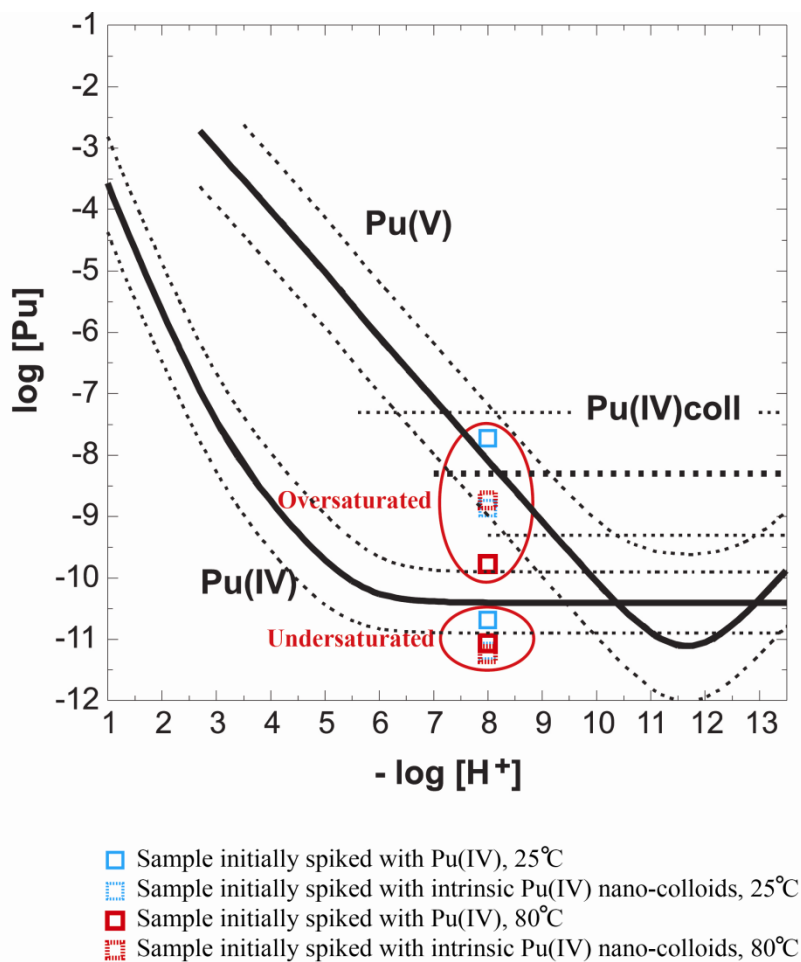
Figure 5-3. Pu concentrations in eight goethite-free spiked blanks oversaturated (initially ~10^{-6} M) and undersaturated (initially 10^{-10} M) with respect to PuO_2(am, hyd). Data are superimposed over PuO_2(am, hyd) solubility model reported in Figure 5 from Neck et al. (2007). Homogeneous nucleation and precipitation of aqueous Pu(IV) and intrinsic Pu(IV) nano-colloids is evident. Pu concentrations in supernatants from sedimentation and centrifugation samples yielded similar results.

Pu behavior in the presence of goethite: Figure 5-4 presents the 25°C data for the sorption of aqueous Pu(IV) and intrinsic Pu(IV) nano-colloid to goethite. For each form of Pu, data at three concentrations are presented. For simplicity, we designate these as low, intermediate, and high concentration samples. For comparison, Figure 5-4 also includes earlier aqueous Pu(IV) isotherm data at 7 and 14 days from an experiment performed over a much wider Pu(IV) concentration range while using the identical mineral and solution conditions (Zhao et al., 2010). Solution concentration data (and associated solid concentrations) are presented based on measured Pu supernatant concentrations after sedimentation (approximately <250 nm) and centrifugation (approximately <25 nm) procedures (Table 5-2). Differences between measured Pu supernatant concentrations from these two procedures are an indication that Pu is present in substantial quantities associated with particles in the 25-250 nm range. This may be a combination of Pu sorbed to goethite nanoparticles and aggregated intrinsic Pu(IV) nano-colloids. However, based on ICP-MS measurements of Fe in solution, we believe that the goethite was effectively removed and the majority of those particles are aggregated intrinsic Pu(IV) nano-colloids.

The present aqueous Pu(IV) sorption data are in excellent agreement with the earlier isotherm data. First, the low concentration aqueous Pu(IV) sample matches previous isotherm data (small black symbols), indicating that equilibrium sorption was reached within 7 days. Second, the intermediate concentration aqueous Pu(IV) sample matches the previous data at 14 days, indicating that sorption/surface precipitation reached equilibrium within 14 days. Third, the highest concentration aqueous Pu(IV) sample ($1.1 \times E^{-9}$M) resulted in a solution concentration lower than the earlier 14 day sample, (3.8×10^{-9}M) indicating that equilibrium had not been reached within 14 days. For the intermediate and high aqueous Pu(IV) concentration samples, solubility considerations suggest that precipitation of PuO_2(am, hyd) may occur (initial Pu concentrations were 8×10^{-7} and 4×10^{-6} M, respectively, Table 5-1). However, equilibrium solution concentrations are slightly lower than expected based on thermodynamic estimates alone [range of PuO_2(am, hyd) solubility predicted by thermodynamic constants and associated uncertainties from Neck et al. (2007) identified in Figure 5-4 by grey zone]. Neck et al. (2007) suggest that a mixture of colloidal PuO_2 and aqueous Pu(V) will be the predominant forms of Pu in solution. However, the concentration of colloidal PuO_2 is conditional, depending on the choice of particle size range that is considered "colloidal". In the case of Neck et al. (2007), the colloidal fraction was defined as the fraction collected by a 10 kD (~1.5 nm pore size) filter from a "clear supernatant". The upper limit of the particle size considered "colloidal" is not strictly defined. In our case, the sedimentation data produces a particle size upper limit of ~250 nm. If a higher upper limit was used in our case, the apparent Pu concentration in solution would be higher.

The behavior of intrinsic Pu(IV) nano-colloids differs significantly from that of aqueous Pu(IV) only in the low concentration sample. A substantial difference between Pu concentration in solution after sedimentation (2.4×10^{-10} M) versus centrifugation (9.8×10^{-12} M) indicates that large (25-250 nm) aggregated intrinsic Pu(IV) nano-colloids are present and do not have a strong affinity for the goethite surface (Figure 5-4). It suggests that intrinsic Pu(IV) nano-colloids at low concentrations may not be subject to sorption processes that would retard their migration. However, the intermediate and high concentration samples do not exhibit this same behavior. The intermediate and high concentration intrinsic Pu(IV) nano-colloid sorption samples result in solution concentrations similar to aqueous Pu(IV) sorption samples, driven most likely by aggregation processes.

Figure 5-5 presents the 80°C sorption data for aqueous Pu(IV) and intrinsic Pu(IV) nano-colloids. The 80°C aqueous Pu(IV) sorption data are similar to the 25°C data. However, larger differences in solution Pu concentrations between sedimentation and centrifugation suggest that large 25-250 nm aggregated intrinsic Pu(IV) nano-colloids may be more stable at higher temperatures. Evaluating the desorption and stability characteristics of adsorbed and surface precipitated Pu(IV) will be the focus for FY12 studies. Morphological and crystallographic characteristics of Pu(IV) sorbed to goethite are discussed in the following section.
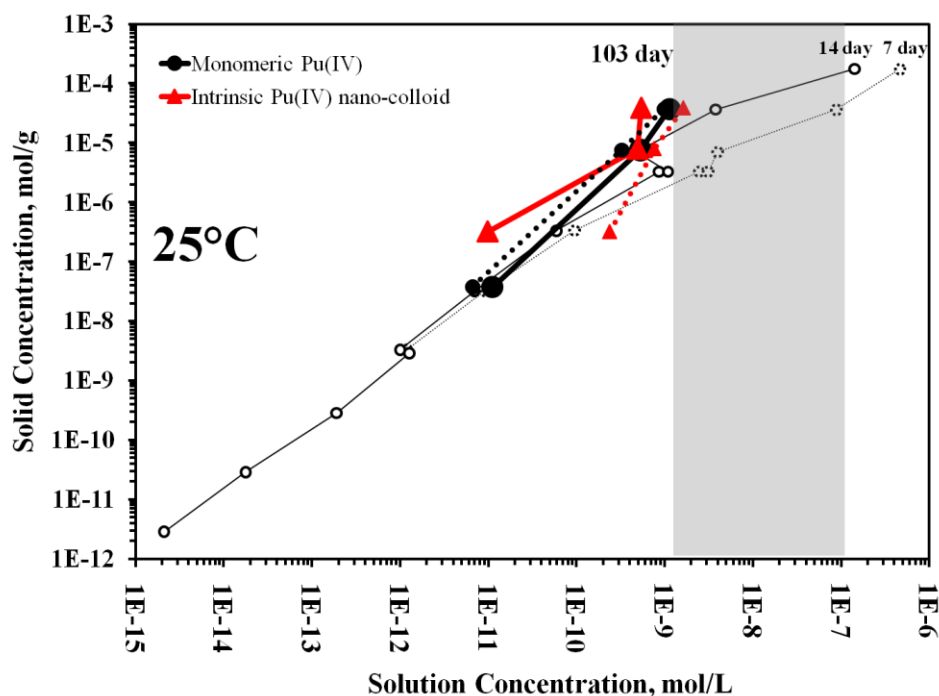
Figure 5-4. Sorption of aqueous Pu(IV) (black) and intrinsic Pu(IV) nano-colloids (red) to goethite at 25°C. Pu includes both aqueous and colloidal Pu with the specified particle size cutoff based on sedimentation (<250 nm, dashed line) and centrifugation (<25 nm, solid line). The 7 day and 14 day aqueous Pu(IV) sorption experiments (small black circles) were performed earlier under identical solution conditions. Gray zone is estimated total Pu concentration in equilibrium with PuO_2(am, hyd) reported in (Neck et al., 2007) for pH 8 solution (dominated by aqueous Pu(V) and >1.5 nm PuO_2 colloids).
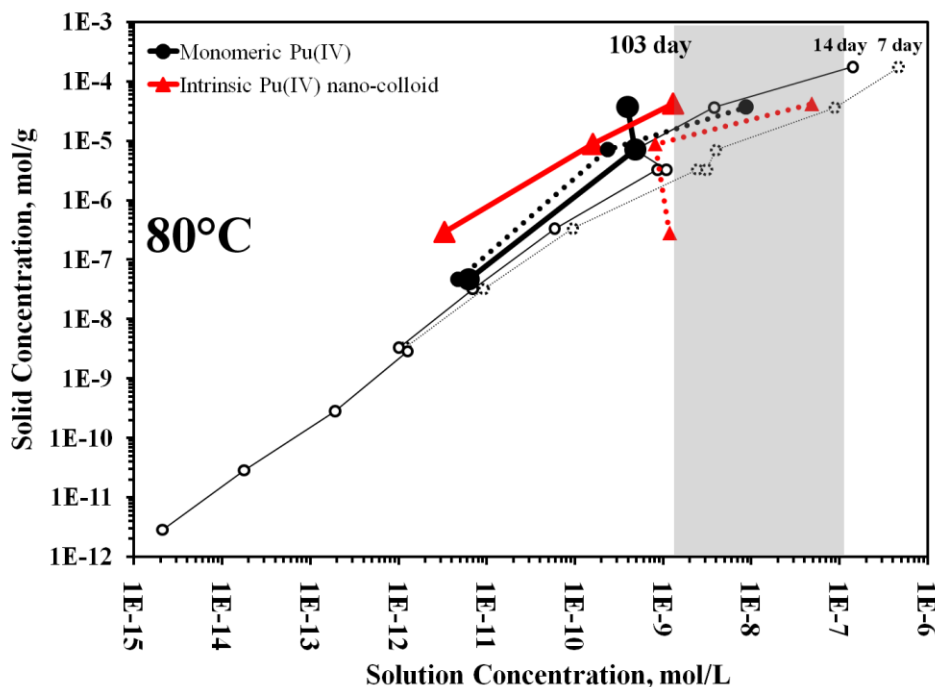
Figure 5-5. Sorption of aqueous Pu(IV) (black) and intrinsic Pu(IV) nano-colloids (red) to goethite at 80°C. Aqueous concentration based on sedimentation (<250 nm, dashed line) and centrifugation (<25 nm, solid line). The 7 day and 14 day aqueous Pu(IV) sorption experiments (small circles) were performed earlier under identical solution conditions. Gray zone is estimated total Pu concentration in equilibrium with PuO_2(am, hyd) reported in (Neck et al., 2007) for pH 8 solution (dominated by aqueous Pu(V) and >1.5 nm PuO_2 colloids)

TEM observations of Pu morphology

25 °C aqueous Pu: In the presence of goethite and at 25°C, aqueous Pu(IV) has been shown to grow epitaxially, forming bcc Pu_4O_7 nano-colloids in the 2-5 nm particle size range (Powell et al., 2011). In all cases, structure determination was based on High-Resolution Transmission Electron Microscopy (HRTEM). While previous observations were made on samples reacted for short durations, the Pu_4O_7 nano-colloids appear to be stable over the longer experiment timeframe examined here (103 days). In the intermediate concentration sample, Pu_4O_7 nano-colloids are widely distributed over the goethite surface and dominated by isolated (dispersed) 2-5 nm nano-colloids (Figure 5-6). In the high concentration sample, both dispersed Pu_4O_7 nano-colloids and aggregated fcc PuO_2 nano-colloids exist (Figure 5-7). Importantly, the fundamental crystalline size remains in the 2-5 nm size range for both forms of Pu nano-colloid and in all samples. In the high concentration sample, nano-colloid aggregation is more pronounced. It cannot be ascertained whether this aggregation is purely a physical/electrostatic interaction or a chemical one. However, that difference may have a pronounced effect on the transport behavior of intrinsic Pu nano-colloids as well as the transport behavior facilitated by iron oxide colloids. Importantly, aggregated nano-colloids appear to be dominated by PuO_2 nano-colloids precipitated directly from solution and weakly associated with the goethite surface. From a bulk solution chemistry standpoint, this would be characterized as precipitation of PuO_2(am, hyd). At the nanoscale, it is characterized as aggregation of PuO_2 nano-colloids.

124

Figure 5-6. TEM/HRTEM of aqueous Pu(IV) sorbed to goethite at 25°C for 103 days at the intermediate concentration. The 1,800 ppm Pu on goethite represents ~10% surface load. Arrows and circles identify locations where dispersed Pu_4O_7 nano-colloids (identified by high resolution transmission electron microscope) are present.

Figure 5-7. TEM/HRTEM of aqueous Pu(IV) sorbed to goethite at 25°C for 103 days, of the high concentration samples. The 8,900 ppm Pu on goethite represents ~50% surface load. Arrows and circles identify locations where aggregated (Agg) PuO_2 and dispersed (Disp) Pu_4O_7 nano-colloids are present.

25°C intrinsic Pu nano-colloids: Unlike aqueous Pu(IV) sorption, intrinsic Pu(IV) nano-colloids sorption to goethite is dominated by aggregated mats of PuO_2 nano-colloids (Figure 5-8). These mats were observed in both the intermediate and high concentration samples. The Pu_4O_7, 2-5 nm, colloids growing on the goethite surface (Figure 5-6 & 5-7) that were observed in the aqueous Pu-experiments were not observed in any of the intrinsic Pu experiments. Only PuO_2 nano-colloids were observed. The bulk solution chemistry data (Figure 5-3) suggest that the same behavior would be observed at the low Pu concentration as well. However, TEM characterization at low surface loading is exceedingly difficult; it was not attempted for the low concentration sample.

Because these mats are located both on and off goethite (Figures 5-9 and 5-10), it is clear that the interaction between intrinsic PuO_2 nano-colloids and the goethite surface is much weaker than in the case of aqueous Pu(IV) sorption. The state of the weak interaction between intrinsic PuO_2 nano-colloids and the goethite surface (electrostatic or otherwise) cannot be ascertained at this time.

It appears that intrinsic PuO_2 nano-colloids, once formed, will not alter to the epitaxial Pu_4O_7 on goethite under these conditions. From the bulk solution chemistry data alone, the complex and diverse interaction of aqueous Pu(IV) and intrinsic Pu(IV) nano-colloids with goethite could not be discerned. Only through careful TEM analysis can we begin to understand the aqueous vs. intrinsic nature of Pu. The aggregation of intrinsic PuO_2 nano-colloids appears, from bulk solution chemistry data, to represent precipitation of PuO_2(am, hyd). However, the ordered PuO_2 does not appear to grow beyond its initial 2-5 nm crystalline size.

Figure 5-8. TEM/HRTEM of intrinsic Pu(IV) nano-colloids sorbed to goethite at 25°C for 103 days at the intermediate concentration. The 1,900 ppm Pu on goethite represents ~10% surface load. Circles identify locations where aggregated (Agg) PuO_2 nano-colloids are present.

Figure 5-9. TEM of intrinsic Pu(IV) nano-colloids sorbed to goethite at 25°C for 103 days in the high concentration sample. The 9,400 ppm Pu on goethite represents ~50% surface load. Arrows identify locations where aggregated (Agg) PuO_2 nano-colloids are present.
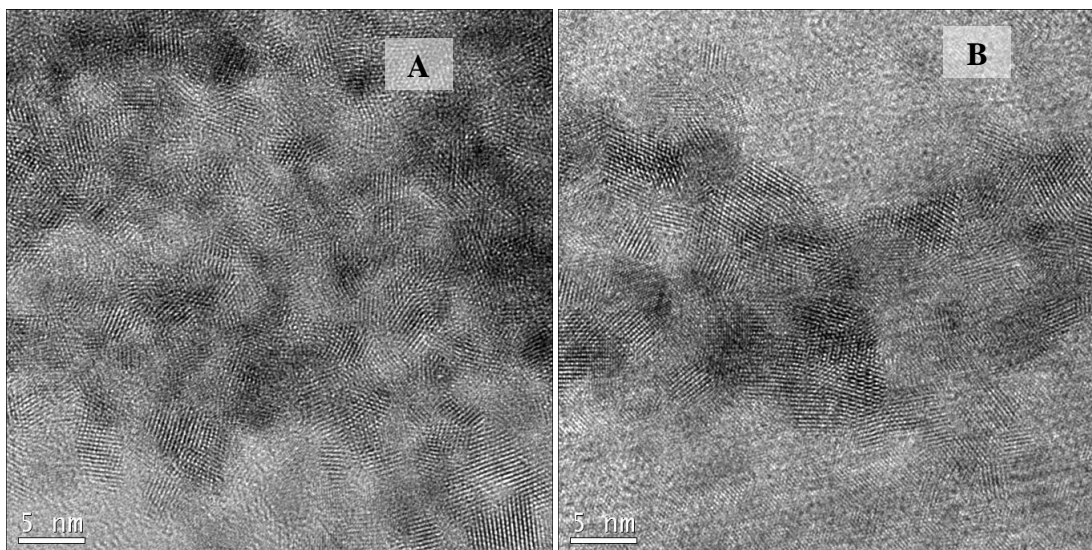
Figure 5-10. HRTEM of intrinsic Pu(IV) nano-colloids sorbed to goethite at 25°C for 103 days. 9,400 ppm Pu on goethite (~50% surface load). Aggregated fcc PuO_2 colloids on carbon support film (A) and aggregated fcc PuO_2 colloids on goethite (B).

80°C aqueous Pu: The characteristics of Pu associated with goethite at 80°C are not substantially different from those at 25°C. The intermediate concentration aqueous Pu(IV) sample is dominated by dispersed Pu_4O_7 nano-colloids that are in the 2-5 nm size range (Figure 5-11; compare to Figure 6). In the high concentration sample, both aggregated PuO_2 nano-colloids and dispersed Pu_4O_7 nano-colloids are present (Figures 5-12 and 5-13; compare to Figure 5-7). The aggregated PuO_2 nano-colloids are located both on and off the goethite surface while the Pu_4O_7 nano-colloids are strictly associated with the goethite surface. At 80°C, the size of the aggregated PuO_2 nano-colloids appears to be larger. This is consistent with Pu concentrations measured in solution (Figure 5-5) which suggest a significant fraction of intrinsic Pu(IV) nano-colloids are aggregated and in the 25-250 nm particle size range.

80°C intrinsic Pu nano-colloids: The behavior of intrinsic Pu(IV) nano-colloids at 80°C is dominated in both intermediate and high concentration samples by the formation of aggregated PuO_2 nano-colloids and little if any association with the goethite surface (Figures 5-13 to 5-15). The high concentration sample is dominated by large mats of aggregated PuO_2 nano-colloids with sizes in the 2-5 nm range. In terms of bulk solution chemistry, these would be considered precipitates of PuO_2(am, hyd). HRTEM images and electron diffraction analysis indicates that the mats are composed of 2-5 nm nano-colloids with a fcc PuO_2 structure. Importantly, the results suggest that the relationship between colloidal and precipitated forms of PuO_2(am, hyd) is controlled by degree of aggregation of 2-5 nm nano-colloids. Aggregation of nano-colloids is controlled primarily by the solution conditions in which they are present [Pu concentration, solution composition (e.g. ionic strength, pH) and temperature]. Thus, the concentration of dispersed intrinsic PuO_2 nano-colloids in solution will most likely be controlled by the physical aggregation behavior of PuO_2 nano-colloids.
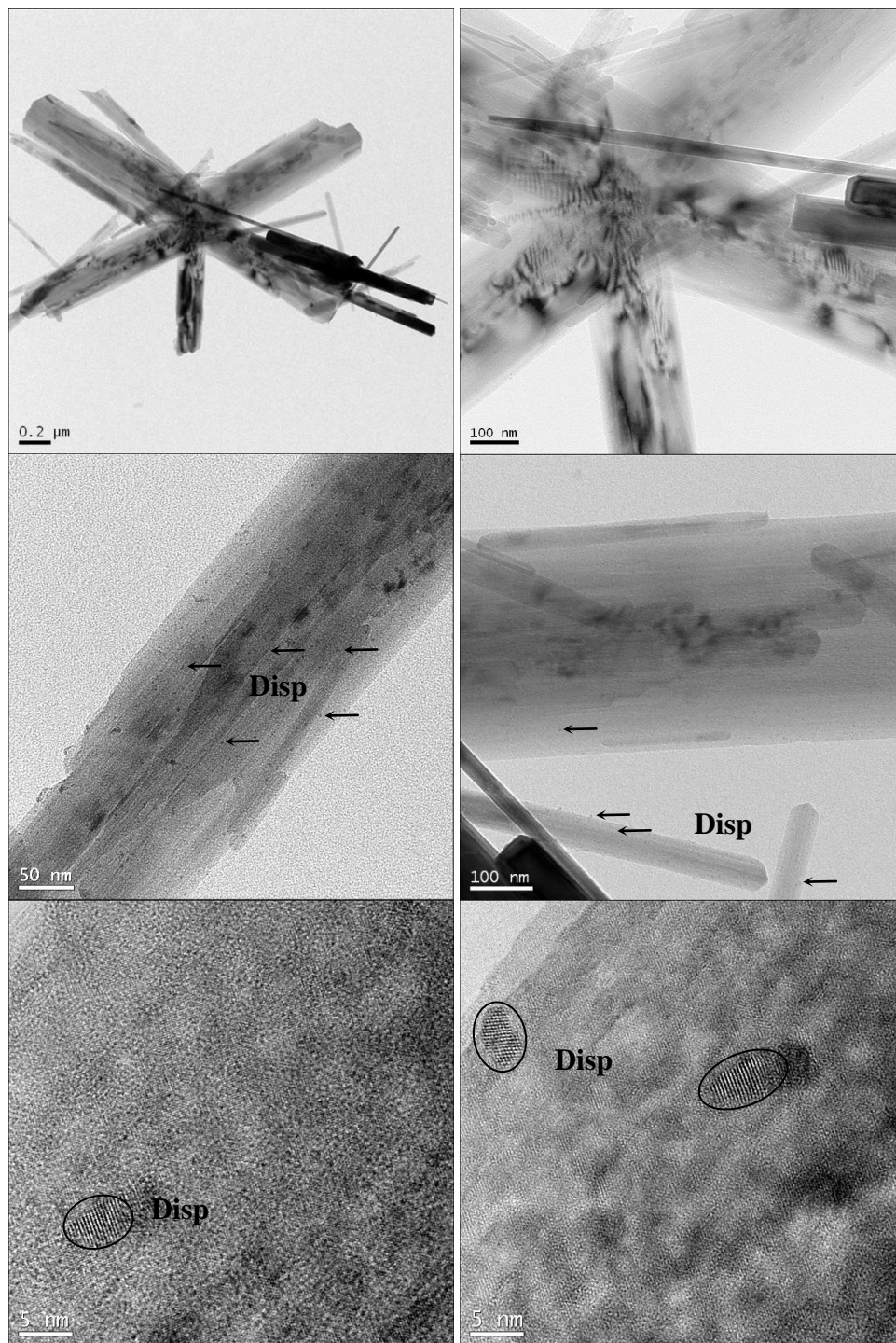
Figure 5-11A. TEM/HRTEM of aqueous Pu(IV) sorbed to goethite at 80°C for 103 days. 1,700 ppm Pu on goethite (~10% surface load). Arrows and circles identify locations where dispersed (Disp) Pu_4O_7 nano-colloids are present.
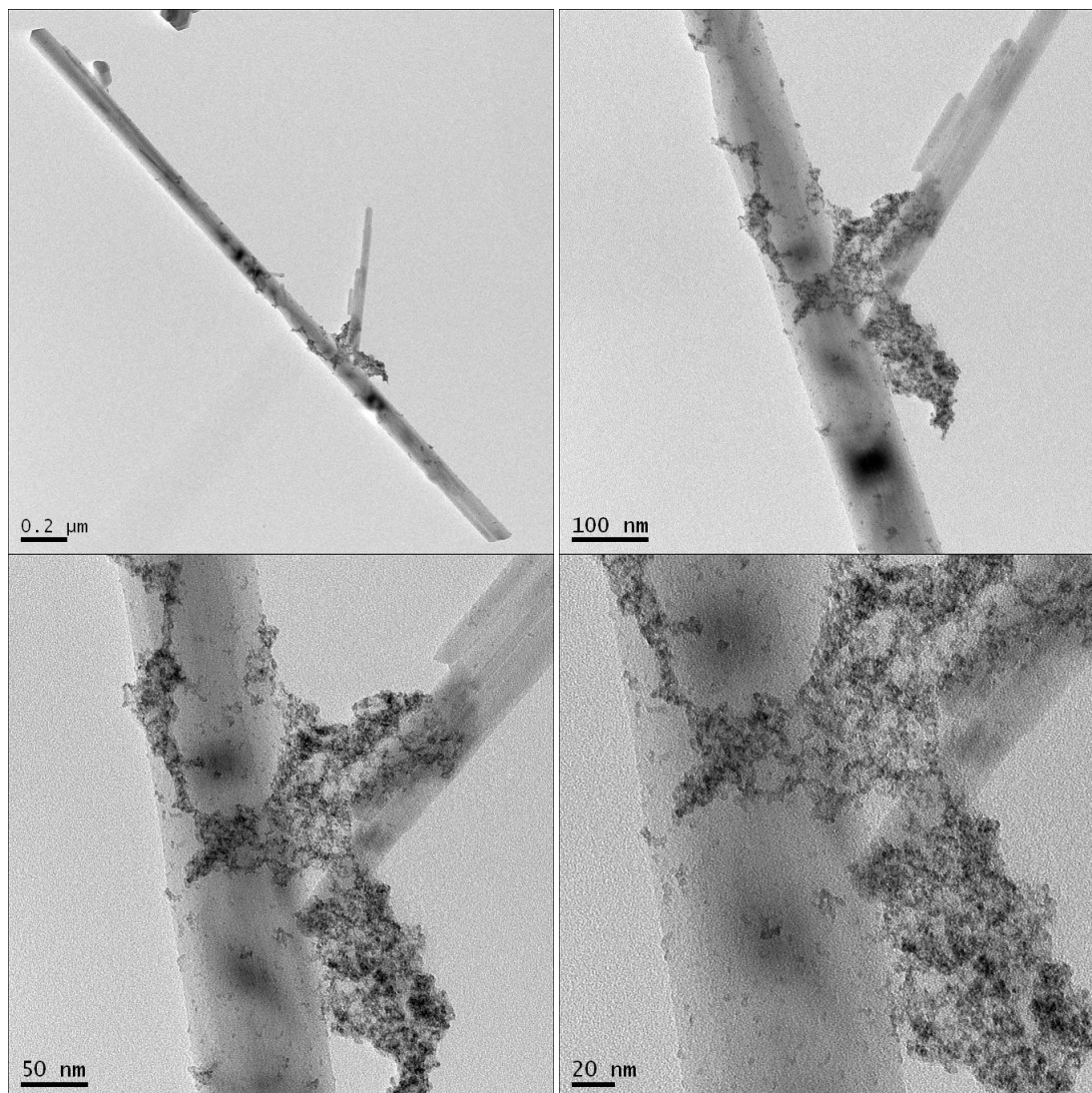
Figure 5-11B. TEM of aqueous Pu(IV) sorbed to goethite at 80°C for 103 days for the high concentration sample. The 8,900 ppm Pu on goethite represents ~50% surface load. Arrows and circles identify locations where aggregated (Agg.) PuO_2 and dispersed (Disp) Pu_4O_7 nano-colloids are present.
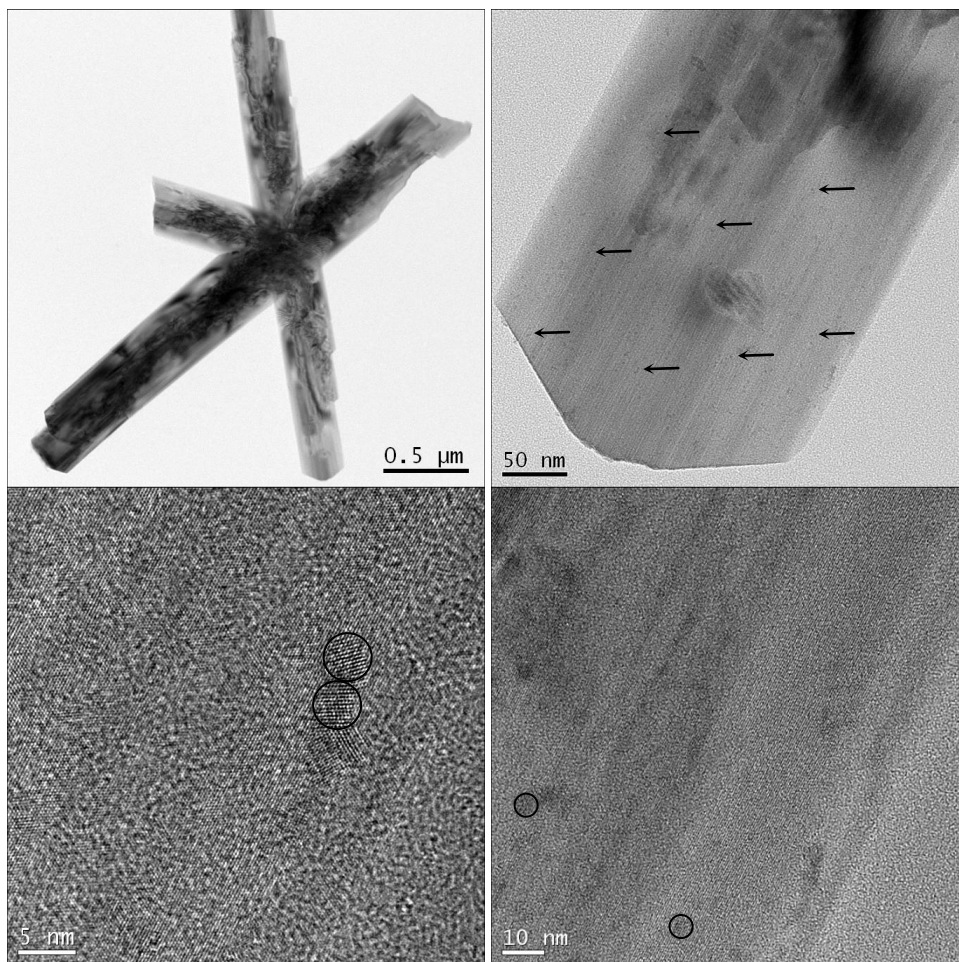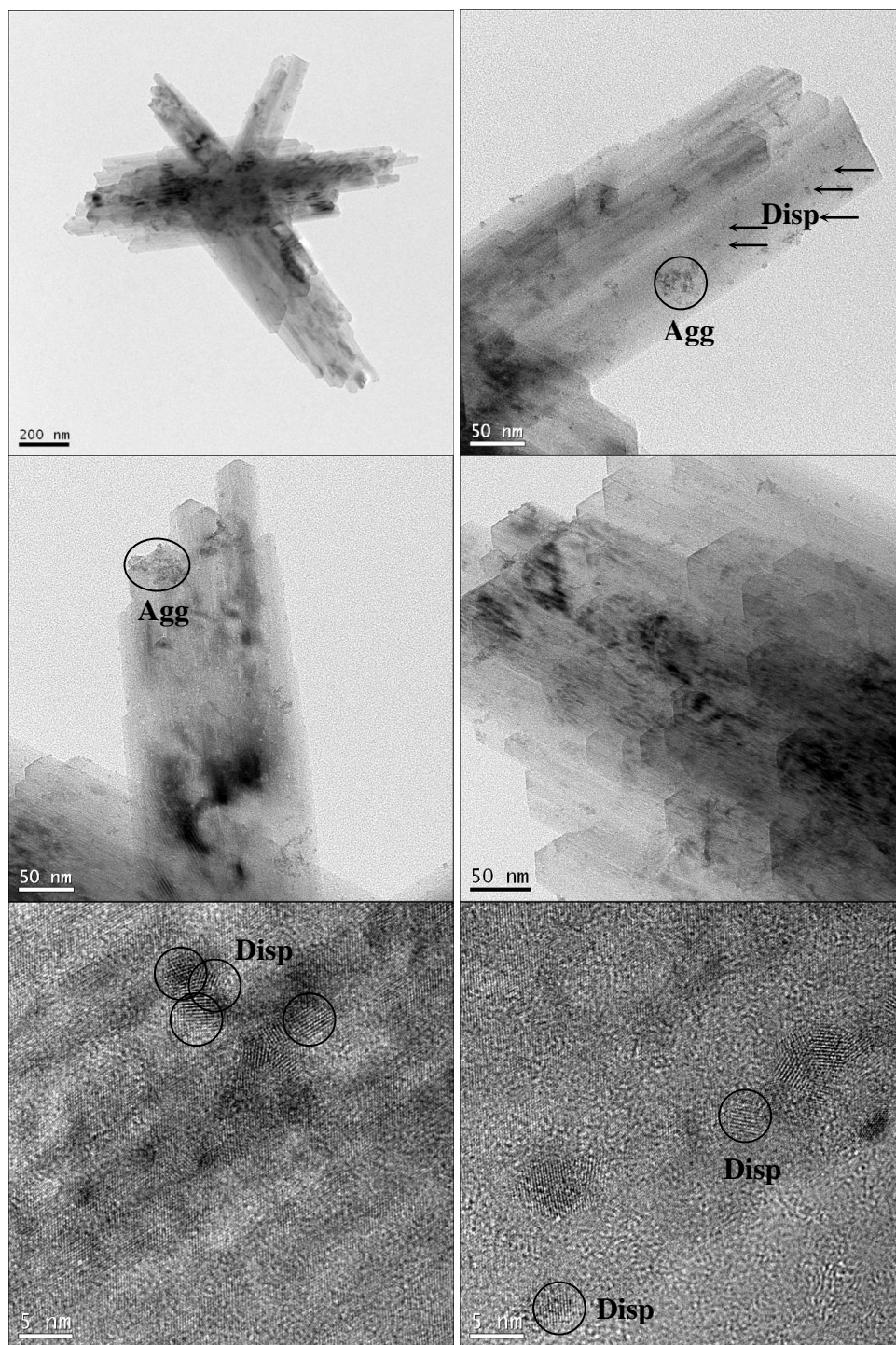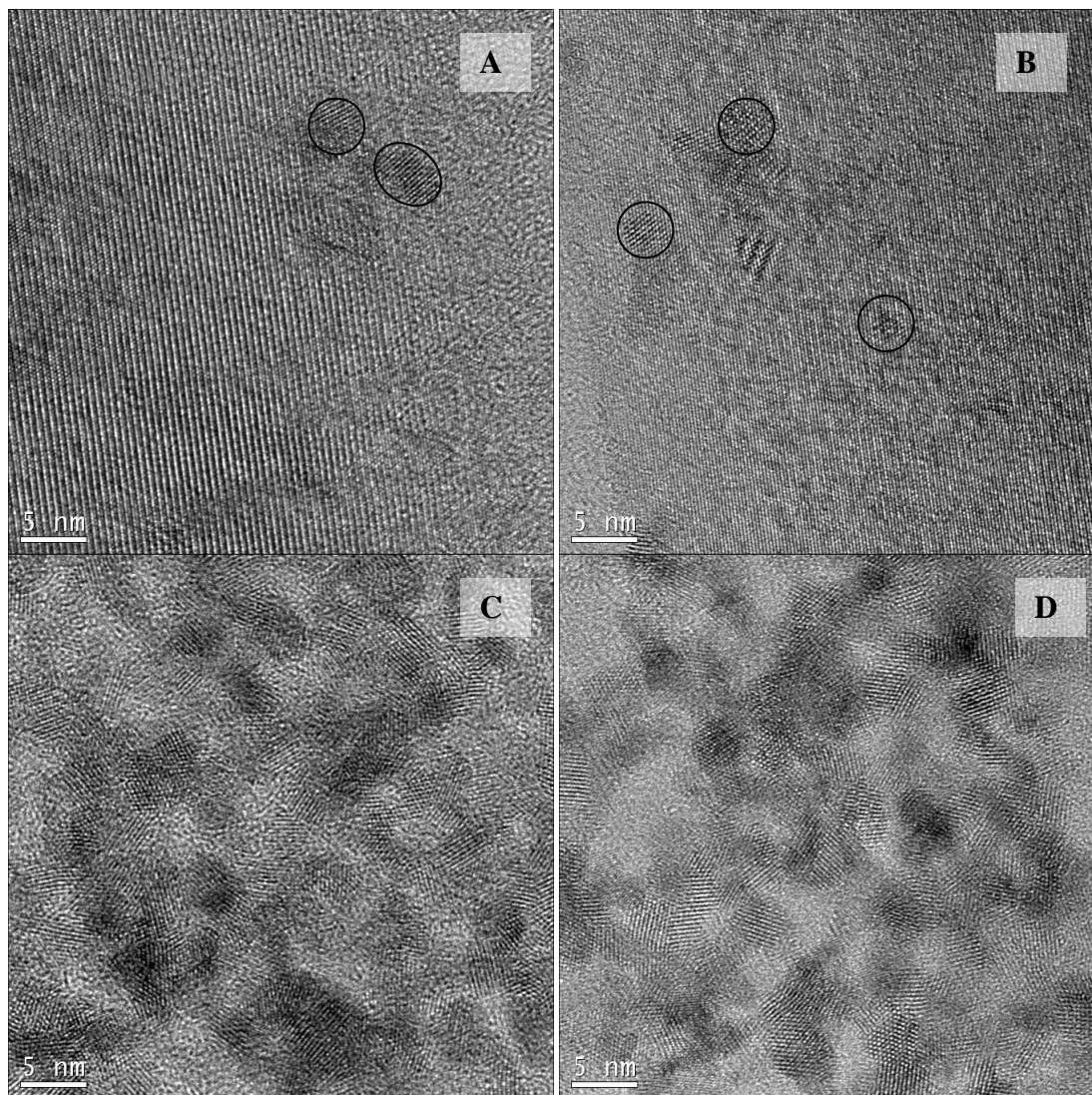
Figure 5-12. HRTEM of aqueous Pu(IV) sorbed to goethite at 80°C for 103 days for the high concentration sample. The 8,900 ppm Pu on goethite represents ~50% surface load. Both dispersed (Disp) Pu_4O_7 nano-colloids (A, B) and aggregated (Agg) PuO_2 nano-colloids (C, D) are present.
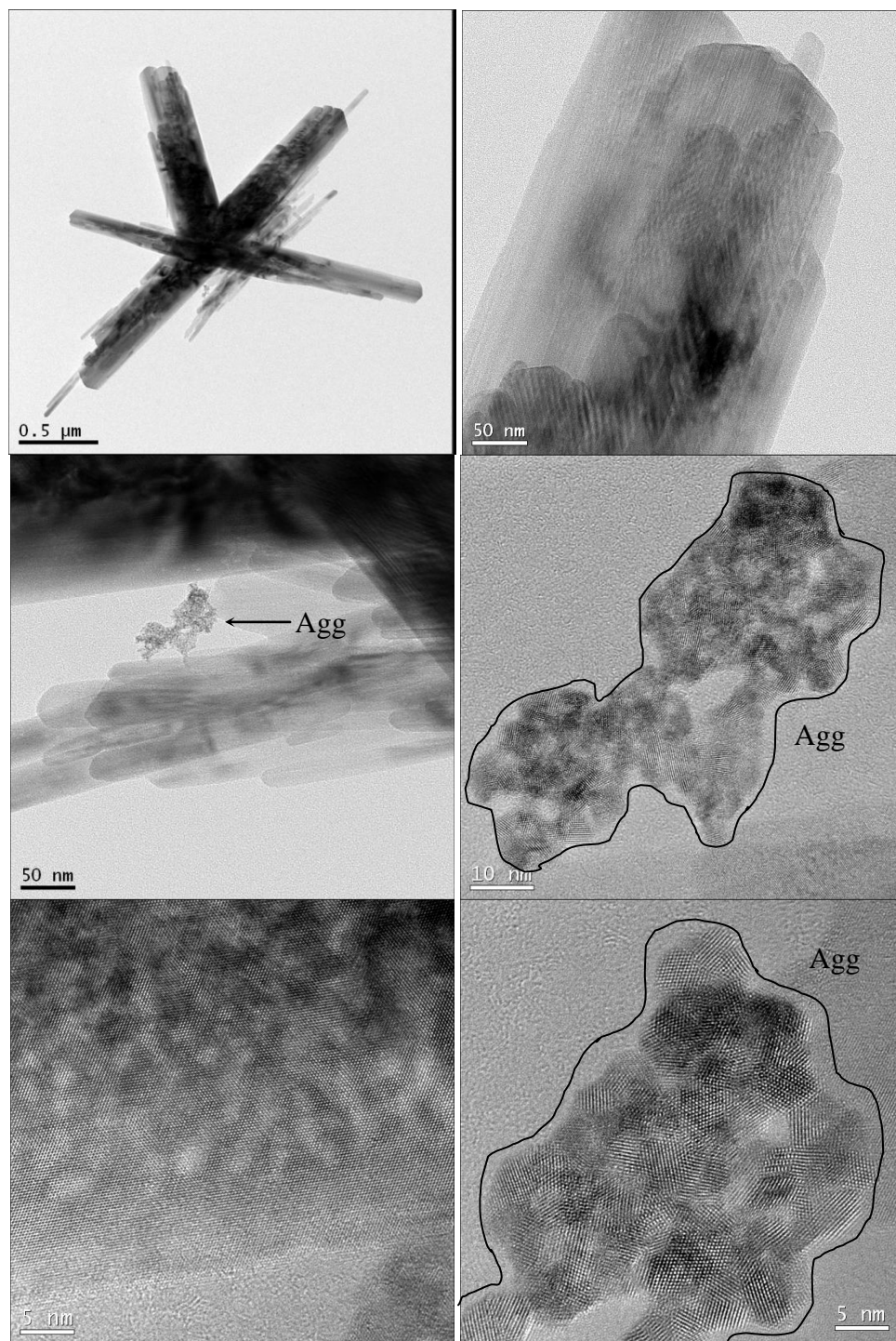
Figure 5-13. TEM/HRTEM of intrinsic Pu(IV) nano-colloids sorbed to goethite at 80°C for 103 days of the intermediate sample. The 2,100 ppm Pu on goethite represents ~10% surface load. Arrows and circles identify locations where aggregated (Agg) nano-colloids are present. Goethite surfaces had no identifiable Pu nano-colloids present. Some aggregated Pu nano-colloids were observed weakly associated with goethite. HRTEM images show aggregated fcc PuO_2 colloids.
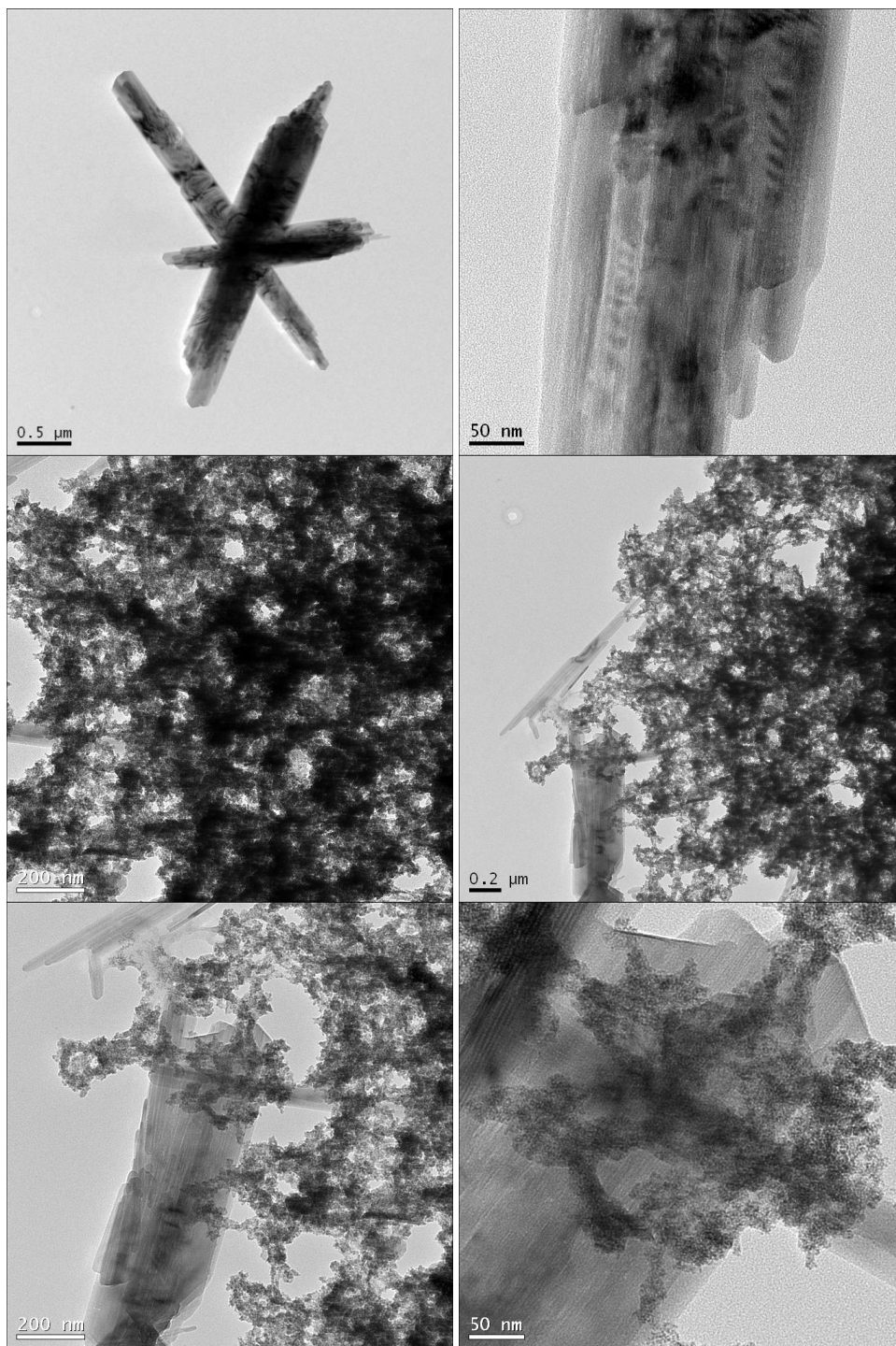
Figure 5-14. TEM of intrinsic Pu(IV) nano-colloids sorbed to goethite at 80°C for 103 days of the high concentration sample. The 10,000 ppm Pu on goethite represents ~50% surface load. Goethite surfaces have no identifiable Pu nano-colloids present. Aggregated Pu(IV) nano-colloids are weakly associated with goethite.
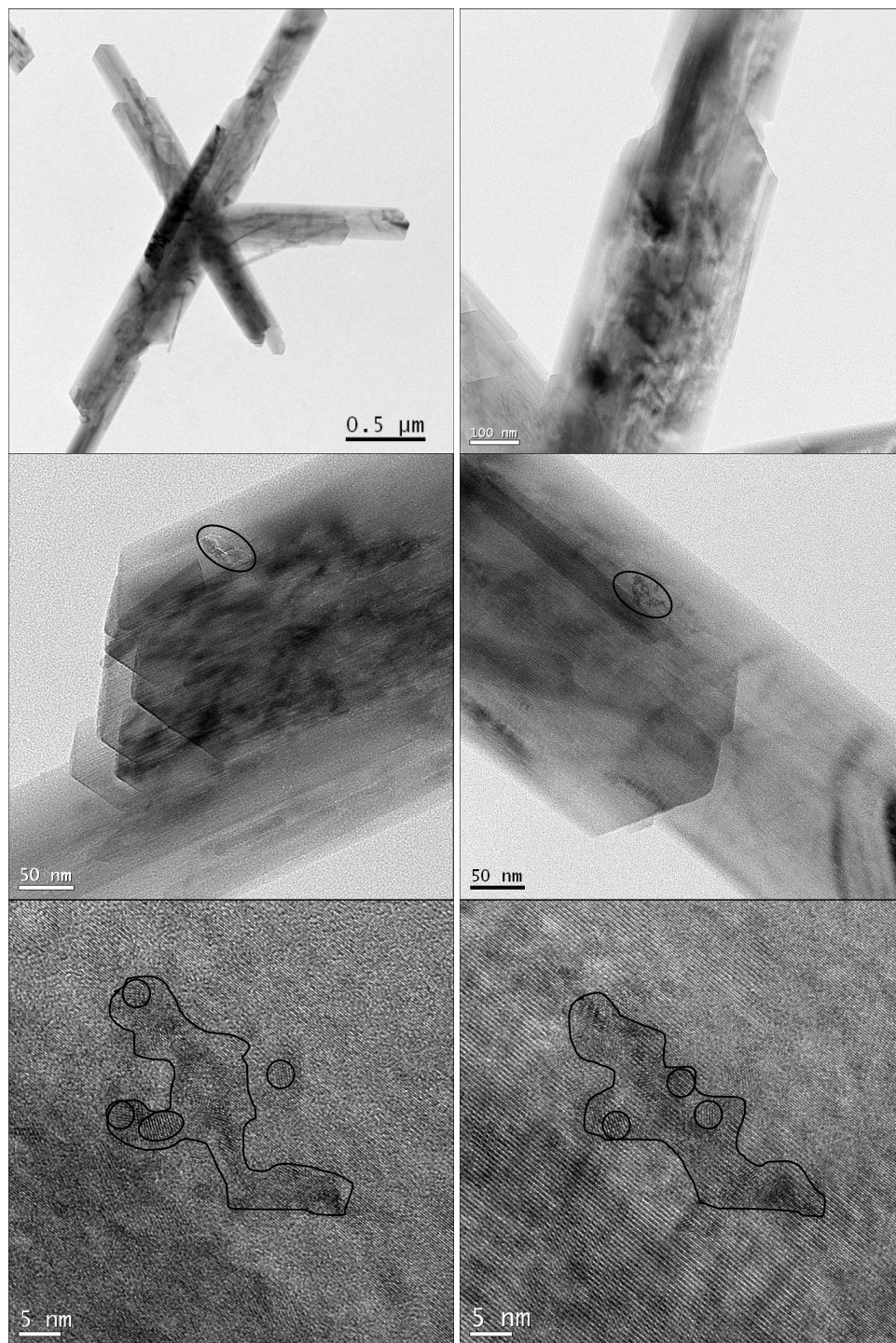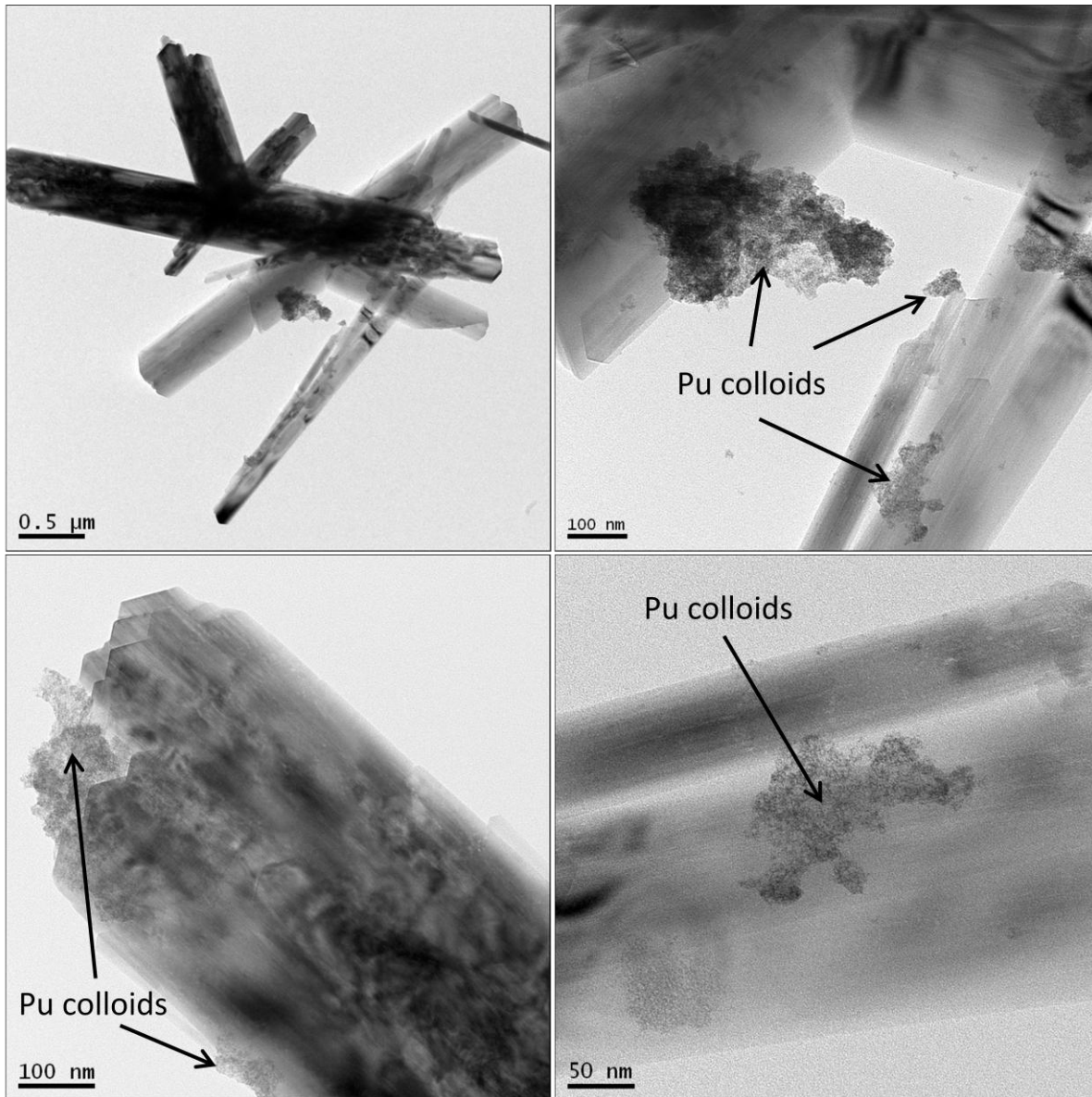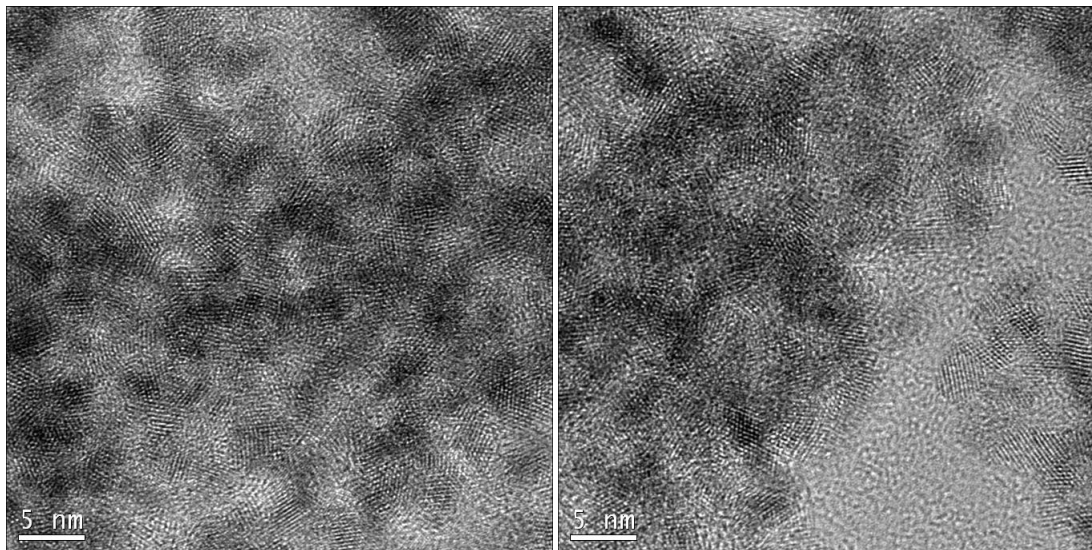
Figure 5-15. HRTEM of intrinsic Pu(IV) nano-colloids sorbed to goethite at 80°C for 103 days of a high concentration sample. The 10,000 ppm Pu on goethite represents ~50% surface load. The aggregated 2-5 nm Pu nano-colloids have a fcc PuO$_2$ crystal structure.

5.4.2   Pu sorption to montmorillonite at 25 and 80°C

The Pu-montmorillonite sorption experiments are underway and will be completed at the end of FY11. The low and intermediate Pu concentration aqueous Pu(IV) and colloidal Pu experiments have run for ~30 days; the high concentration colloidal Pu experiments have run for ~15 days. The results to date indicate that:
- The novel dialysis design is an effective experimental set-up to separate intrinsic colloids from larger pseudo-colloids and dissolved species.
- Pu sorption to montmorillonite is affected by temperature and
- the transformation of intrinsic Pu colloids to pseudo (Pu/montmorillonite) colloids occurred over a wide range of Pu concentrations (10^{-12} to 10^{-7} M)

In this report, we focus only on the low Pu concentration experiment for which we have preliminary data. A complete analysis of all the data, including morphological characterization of Pu associated with the montmorillonite surface, will be forth coming in FY12.

Aqueous Pu(IV) sorption at 25°C and 80 °C: The low concentration (6×10^{-12} M) aqueous Pu(IV) sorption experiments were carried out well below the solubility of PuO$_2$(am, hyd.) (Neck et al., 2007). Thus, the potential for Pu(IV) precipitation or nano-colloid formation in these samples is minimal. Conceptually, sorption in this system is expected to take place in two sequential steps. First, aqueous Pu (in its original +4 state or an oxidized form) diffuses through dialysis membrane (see Figure 1). The rate of diffusion will be a function of temperature and the membrane pore size and density. Following diffusion, aqueous Pu can sorb to montmorillonite outside the dialysis bag. However, sorption to container walls or the dialysis membrane may also occur.

Figure 5-16 is a plot of the Pu concentration in the clay suspension (solid symbols) and in the supernatant (open symbols) at 25°C and 80°C as function of time. The red dashed line is the calculated total Pu concentration in the system. The data indicate that aqueous Pu diffuses across the membrane within a few

days. The initial diffusion is followed by a decrease in the Pu concentration. This loss may be the result of sorption to container walls and is under further investigation. Nevertheless, the long-term trend suggests that Pu will eventually migrate to the montmorillonite surface. Interestingly, sorption appears to reached steady state faster at 25°C (~ 12 days) than that at 80°C (>20 days). The K_ds at 25°C and 80°C were calculated to be $1x10^4$ and $3x10^4$ ml/g based on measured aqueous and suspension concentrations. It is notable that the Pu concentrations in aqueous phase at both 25 and 80°C were very similar. Additional data are needed to confirm whether a true equilibrium has been reached and these experiments are on-going. Furthermore, characterization of the montmorillonite and a mass balance of the Pu is needed. These analyses will be completed in the latter part of FY11.
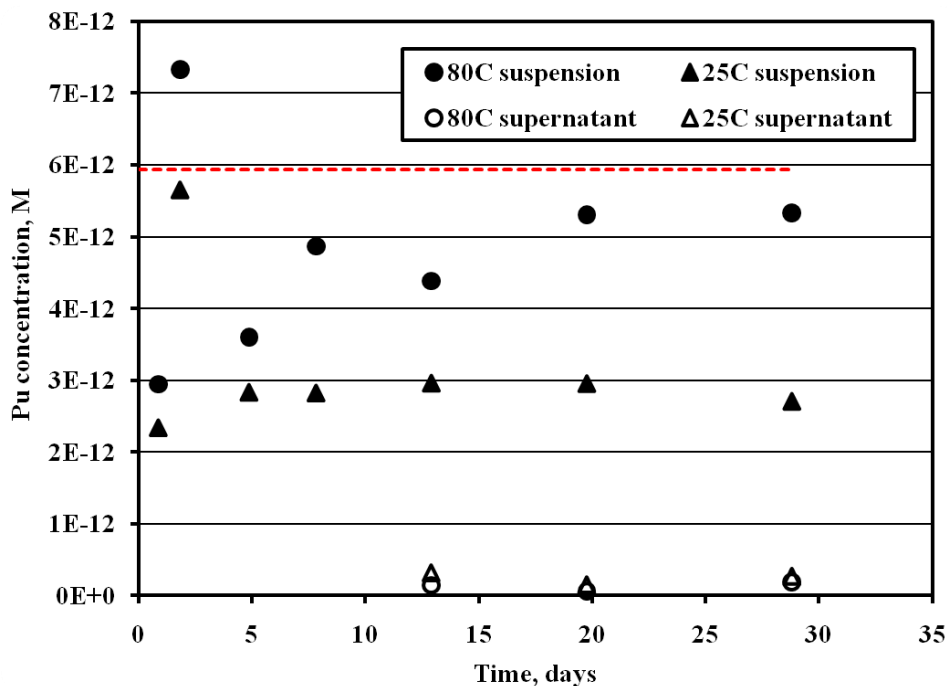
Figure 5-16. Aqueous Pu(IV) concentrations in montmorillonite suspension and its supernatant at 25 °C and 80 °C as function of time. Red line indicates total initial Pu concentration.

Pu(IV) Nano-Colloid Stability and Aqueous Pu(IV) Sorption at 25 °C and 80 °C: The stock solution containing intrinsic Pu(IV) nano-colloids was spiked into the dialysis bag at total concentration of at $1x10^{-11}$ M. At this low total concentration, the thermodynamic driving force in this system should drive intrinsic Pu(IV) nano-colloids towards dissolution. Conceptually, sorption to montmorillonite must include the following steps: dissolution of nano-colloids, diffusion across membrane, and sorption to montmorillonite. Figure 5-17 is a plot of the Pu concentration in the clay suspension (solid symbols) and in the supernatant (open symbols) at 25°C and 80°C and as function of time. Figure 5-17 also includes the calculated initial total intrinsic Pu nano-colloid (red dash line) and aqueous Pu (orange dash line) concentrations. At 80°C, it appears that Pu colloids dissolved in less than 2 days. Furthermore, the time dependence follows the behavior of Pu(IV,aq) very closely, suggesting that the dissolution of Pu(IV) nano-colloids were not rate limiting (Figure 16). At 25°C, the behavior of colloidal and aqueous Pu is markedly different. While intrinsic Pu(IV) nano-colloids are dissolving, diffusing, and sorbing to montmorillonite, the rate appears to be quite slow. An equilibrium has not been reached after 28 days. Importantly, at both temperatures, sorption to montmorillonite appears to provide a sufficient driving force to dissolve Pu(IV) nano-colloids.
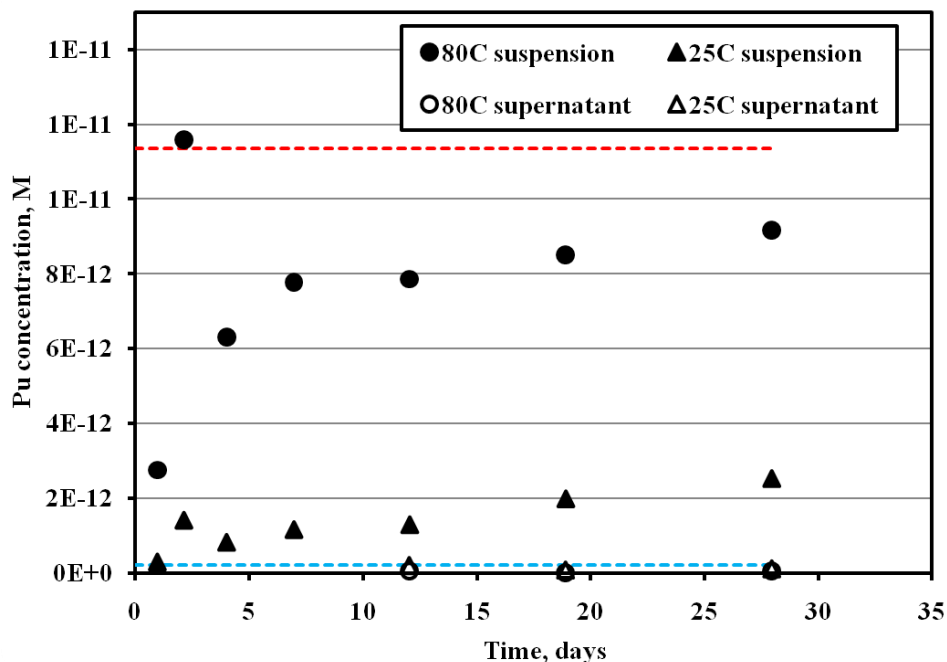
Figure 5-17. Pu(IV) colloids concentrations in montmorillonite suspension and its supernatant at 25 °C and 80 °C as function of time. Red and blue lines indicate total initial colloid and total initial aqueous Pu concentration, respectively.

Aqueous Pu(IV) Behavior in the Absence of Montmorillonite at 25 °C and 80 °C: Figure 5-18 presents Pu concentrations measured outside the dialysis membrane in the absence of montmorillonite. The total initial aqueous Pu(IV) concentration was 6.5×10^{-12} M, well below the solubility of PuO_2(am, hyd.) (Neck et al., 2007). As a result, loss of aqueous Pu from solution should be attributed primarily to sorption to container walls or membrane components. The Pu concentration in the bulk solution and the supernatant are similar, suggesting that the Pu in solution remains in the aqueous form. However, the data are indicative of time-dependent diffusion and Pu losses to container walls and membrane components that will complicate the interpretation of colloid dissolution kinetics. It does not, however, take away from the fact that Pu nano-colloid dissolution kinetics increase substantially with temperature and that the nano-colloids do not appear to be stable even at 25°C in the presence of montmorillonite.
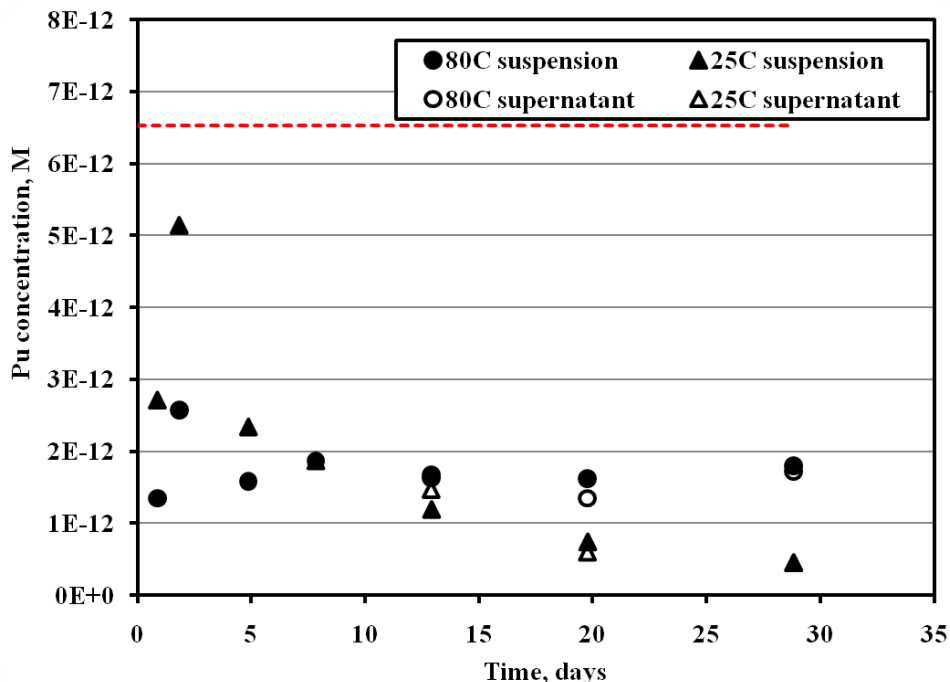
Figure 5-18. Pu(IV) concentrations in the absence of montmorillonite in suspension (no centrifugation) and supernatant at 25 °C and 80 °C as function of time. Red line indicates total initial Pu concentration.

5.5   Conclusions and Future Work

We have examined the behavior of aqueous Pu(IV) and intrinsic Pu(IV) nano-colloids in the presence of goethite at 25 and 80°C and over a range of concentrations from undersaturated to oversaturated with respect to PuO_2(am, hyd). The strong affinity of aqueous Pu(IV) for the goethite surface is explained by the epitaxial growth of bcc Pu_4O_7 nano-colloids on goethite. The behavior is affected minimally by temperature. This strong affinity cannot be achieved when intrinsic Pu(IV) nano-colloids are reacted with goethite over 103 days. The results indicate that the fate of Pu is dependent on its initial form and its subsequent stability under changing geochemical conditions. Epitaxial growth of Pu_4O_7 on the goethite surface will produce a strong association between Pu and goethite, which could also lead to significant colloid-facilitated transport. Both intrinsic colloids and those sorbed to goethite have the potential to be transported with groundwater. The long-term stability and desorption characteristics of these forms of colloidal Pu will be the focus of ongoing research in FY12.

We have begun to examine the behavior of aqueous Pu(IV) and intrinsic Pu(IV) nano-colloids and interaction with clay mineral montmorillonite at 25 and 80°C and over a range of concentrations from undersaturated to oversaturated with respect to PuO_2(am, hyd). Temperature does not appear to greatly affect supernatant Pu concentrations; however, it affects sorption K_d and the stability of intrinsic Pu nano-colloids. In the presence of clay minerals, intrinsic Pu nano-colloids dissolved and transformed into pseudo Pu-montmorillonite colloids. However, at 25°C, the rates of Pu nano-colloid dissolution and sorption to montmorillonite are slow (weeks to months). This may explain why similar observations were not made in the case of Pu nano-colloid sorption to goethite.

The focus of the remainder of FY11will be to complete the Pu sorption kinetic experiments with montmorillonite and characterize the reaction products. A recent study by Zavarin et al. (submitted)

suggests that protonated basal plane ion exchange sites may catalyze Pu(V) reduction on montmorillonite and control sorption. Characterization of the form and location of Pu on montmorillonite surface may help elucidate these and other relevant mechanisms controlling Pu sorption.

The focus of research during FY12 will be on Pu nanoparticle dissolution kinetics using aged Pu nanoparticles and sorbed species from the iron hydroxide (FY10) and clay studies (FY11). Pu nanoparticle dissolution and Pu desorption kinetics must be quantified because these rates are likely to control the colloid-facilitated transport of Pu in the near-field and far-field repository environments. Experimental data summarized in this chapter illustrate the complex reaction chemistry that will control kinetics and the need for a comprehensive conceptual understanding of the underlying mechanisms controlling Pu reactive transport.

5.6   References

Bertetti, F.P., Pabalan, R.T., Almendarez, M.G. (1998) Studies on neptunium(V) sorption on quartz, clinoptilolite, montmorillonite, and a-alumina, in: Jenne, E.A. (Ed.), Adsorption of Metals by Geomedia. Academic Press, San Diego, pp. 131-148.

Cvetkovic, V. (2000) Colloid-facilitated tracer transport by steady random ground-water flow. Physics of Fluids 12, 2279-2294.

Cvetkovic, V., Painter, S., Turner, D., Pickett, D., Bertetti, P. (2004) Parameter and model sensitivities for colloid-facilitated radionuclide transport on the field scale. Water Resour. Res. 40.

Demirkanli, D.I., Molz, F.J., Kaplan, D.I., Fjeld, R.A. (2008) A fully transient model for long-term plutonium transport in the Savannah River Site vadose zone: Root water uptake. Vadose Zone Journal 7, 1099-1109.

Dzombak, D.A., Morel, F.M.M. (1990) Surface complexation modeling : hydrous ferric oxide. Wiley, New York.

Garcia-Garcia, S., Wold, S., Jonsson, M. (2009) Effects of temperature on the stability of colloidal montmorillonite particles at different pH and ionic strength. Applied Clay Science 43, 21-26.

Gee, G.W., Bauder, J.W. (1986) Particle-size Analysis, in: Klute, A. (Ed.), Methods of Soil Analysis: Part I - Physical and Mineralogical Methods. American Society of Agronomy, Inc, Madison, WI, pp. 383-411.

Glynn, P.D. (2003) Modeling Np and Pu transport with a surface complexation model and spatially variant sorption capacities: implications for reactive transport modeling and performance assessments of nuclear waste disposal sites. Computers & Geosciences 29, 331-349.

Hakanen, M., Lindberg, A. (1993) Sorption of neptunium under oxidizing and reduction groundwater conditions. Radiochim. Acta 52/53, 147-151.

Kaplan, D.I., Powell, B.A., Demirkanli, D.I., Fjeld, R.A., Molz, F.J., Serkiz, S.M., Coates, J.T. (2004) Influence of oxidation states on plutonium mobility during long-term transport through an unsaturated subsurface environment. Environmental Science & Technology 38, 5053-5058.

Kaplan, D.I., Powell, B.A., Gumapas, L., Coates, J.T., Fjeld, R.A., Diprete, D.P. (2006) Influence of pH on plutonium desorption/solubilization from sediment. Environmental Science & Technology 40, 5937-5942.

Kaszuba, J.P., Runde, W.H. (1999) The aqueous geochemistry of neptunium: Dynamic control of soluble concentrations with applications to nuclear waste disposal. Environmental Science & Technology 33, 4427-4433.

Keeney-Kennicutt, W.L., Morse, J.W. (1985) The redox chemistry of Pu(V)O2+ interaction with common mineral surfaces in dilute solutions and seawater. Geochim. Cosmochim. Acta 49, 2577-2588.

Kersting, A.B., Efurd, D.W., Finnegan, D.L., Rokop, D.J., Smith, D.K., Thompson, J.L. (1999) Migration of plutonium in ground water at the Nevada Test Site. Nature 397, 56-59.

Kozai, N., Ohnuko, T., Matsumoto, J., Banba, T., Ito, Y. (1996) A study of the specific sorption of neptunium(V) on smectite in low pH solution. Radiochim. Acta 75, 149-158.

Kozai, N., Ohnuky, T., Muraoka, S. (1993) Sorption characteristics of neptunium by sodium-smectite. J. Nuclear Sci. Tech. 30, 1153-1159.

Lujaniene, G., Motiejunas, S., Sapolaite, J. (2007) Sorption of Cs, Pu and Am on clay minerals. Journal of Radioanalytical and Nuclear Chemistry 274, 345-353.

Missana, T., Garcia-Gutierrez, M., Alonso, U. (2004) Kinetics and irreversibility of cesium and uranium sorption onto bentonite colloids in a deep granitic environment. Applied Clay Science 26, 137-150.

Neck, V., Altmaier, M., Seibert, A., Yun, J.I., Marquardt, C.M., Fanghanel, T. (2007) Solubility and redox reactions of Pu(IV) hydrous oxide: Evidence for the formation of PuO2+x(s, hyd). Radiochimica Acta 95, 193-207.

Novikov, A.P., Kalmykov, S.N., Utsunomiya, S., Ewing, R.C., Horreard, F., Merkulov, A., Clark, S.B., Tkachev, V.V., Myasoedov, B.F. (2006) Colloid transport of plutonium in the far-field of the Mayak Production Association, Russia. Science 314, 638-641.

Office of Civilian Radioactive Waste Management (2002) Yucca Mountain Science and Engineering Report: Technical Information Supporting Site Recommendation Consideration, DOE/RW-0539 Rev. 1, U.S. Department of Energy.

Pickett, D.A. (2005) Approach to assessing the potential effects of colloidal radionuclide transport on nuclear waste repository performance. Nuclear Science and Engineering 151, 114-120.

Powell, B.A., Dai, Z., Zavarin, M., Zhao, P., Kersting, A.B. (2011) Stabilization of Plutonium Nano-Colloids by Epitaxial Distortion on Mineral Surfaces. Environmental Science & Technology 45, 2698-2703.

Powell, B.A., Fjeld, R.A., Kaplan, D.I., Coates, J.T., Serkiz, S.M. (2004) Pu(V)O2+ adsorption and reduction by synthetic magnetite (Fe3O4). Environmental Science & Technology 38, 6016-6024.

Powell, B.A., Fjeld, R.A., Kaplan, D.I., Coates, J.T., Serkiz, S.M. (2005) Pu(V)O2+ adsorption and reduction by synthetic hematite and goethite. Environmental Science & Technology 39, 2107-2114.

Powell, B.A., Kersting, A.B., Zavarin, M. (2008) Sorption and Desorption Rates of Neptunium and Plutonium on Goethite, in: Zavarin, M., Kersting, A.B., Lindvall, R.E., Rose, T.P. (Eds.), Hydrologic Resources Management Program and Underground Test Area Project, FY 2006 Progress Report. Lawrence Livermore National Laboratory, Livermore, CA, pp. 90, UCRL-TR-404620.

Sabodina, M.N., Kalmykov, S.N., Sapozhnikov, Y.A., Zkharova, E.V. (2006) Neptunium, plutonium and ^{137}Cs sorption by bentonite clays and their speciation in pore waters. J. Radioanal. Nucl. Chem. 270, 349-355.

Saiers, J.E., Hornberger, G.M. (1996) The role of colloidal kaolinite in the transport of cesium through laboratory sand columns. Water Resour. Res. 32, 33-41.

Sanchez, A.L., Murray, J.W., Sibley, T.H. (1985) The adsorption of plutonium IV and V on goethite. Geochim. Cosmochim. Acta 49, 2297-2307.

Schwertmann, U., Cornell, R., M. (1991) Iron oxides in the laboratory: preparation and characterization. VCH Verlagsgesellschaft mbH, Weinheim.

Steefel, C.I. (2008) Geochemical kinetics and transport, in: Brantley, S.L., Kubicki, J.D., White, A.F. (Eds.), Kinetics of Water-Rock Interaction. Springer, New York, pp. 545-585.

Tien, N.C., Jen, C.P. (2007) Analytical modeling for colloid-facilitated transport of N-member radionuclides chains in the fractured rock. Nuclear Science and Techniques 18, 336-343.

Tinnacher, R.M., Zavarin, M., Powell, B.A., Kersting, A.B. (2011) Kinetics of neptunium(V) sorption and desorption on goethite: An experimental and modeling study. Geochim. Cosmochim. Acta. (in press)

Turner, D.R., Pabalan, R.T., Bertetti, F.P. (1998) Neptunium(V) sorption on montmorillonite: An experimental and surface complexation modeling study. Clays and Clay Minerals 46, 256-269.

U.S. Department of Energy Office of Basic Energy Sciences (2007) Basic research needs for geosciences: facilitating 21st century energy systems. Report from the Workshop Held February 21-23, 2007, Bethesda, MD.

Wang Y. (2011) *Research & Development Plan for Used Fuel Disposition Campaign (UFDC) Natural Systems Evaluation and Tool Development*, U.S. DOE Used Fuel Disposition Campaign, May 25, 2011.

Xu, C., Santschi, P.H., Zhong, J.Y., Hatcher, P.G., Francis, A.J., Dodge, C.J., A., R.K., Hung, C.C., Honeyman, B.D. (2006) Colloidal Cutin-Like SubstancesCross-Linked to Siderophore Decomposition Products Mobilizing Plutonium from Contaminated Soils. Env. Sci. & Tech 42, 211-216

Zavarin, M., Powell, B.A., Bourbin, M., Zhao, P., Kersting, A.B. (2011) Np(V) and Pu(V) Sorption to Montmorillonite as a Function of Ionic Strength, pH, and Time. Environ. Sci. Tech. (submitted)

Zhao, P., Zavarin, M., Tumey, S., Williams, R., Dai, Z., Kips, R., Kersting, A.B. (2010) Isotherm of Pu/Goethite System: Linearity and Sorbent Surface Characterization, AGU Fall Meeting, San Francisco.

Chapter 6: Evolution of Disturbed Rock Zone (DRZ) –Thermal-Hydrologic-Mechanical-Chemical (THMC) Modeling of the Near-Field Evolution of a Clay Repository

6.1   Introduction

Clay/shale has been considered as potential host rock for geological disposal of high-level radioactive waste throughout the world, because of its low permeability, low diffusion coefficient, high retention capacity for radionuclides, and capability to self-seal fractures. For example, Callovo-Oxfordian argillites at the Bure site, France (Fouche et al., 2004), Toarcian argillites at the Tournemire site, France (Patriarche et al., 2004), Opalinus Clay at the Mont Terri site, Switzerland (Meier et al., 2000), and Boom clay at the Mol site, Belgium (Barnichon and Volckaert, 2003) have all been under intensive scientific investigation (at both field and laboratory scales) for understanding a variety of rock properties and their relationships to flow and transport processes associated with geological disposal of radioactive waste. Figure 6.1-1 presents the distribution of clay/shale formations within the USA.
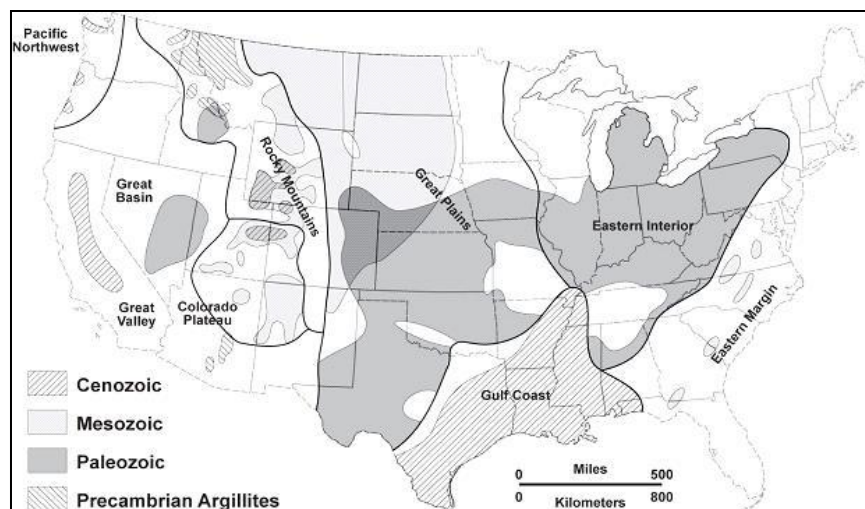
Figure 6.1-1. Clay/shale-formation distribution in the USA (Gonzales and Johnson, 1984)

Clay/shale rocks may be generally classified as indurated or plastic clays (Tsang et al., 2005). The latter (including Boom clay) is a softer material without high cohesion; its deformation is dominantly plastic. For both clay and shale, coupled thermal, hydrological, mechanical, and chemical (THMC) processes are expected to have a significant impact on the long-term safety of a clay repository. For example, the disturbed-rock zone (DRZ) near repository tunnels can modify local permeability (resulting from induced fractures), potentially leading to less confinement capability (Tsang et al., 2005). Because of clay's tendency to swell or shrink (depending on whether the clay is undergoing in imbibition or drainage processes), fracture properties in the DRZ are quite dynamic and evolve over time as hydromechanical conditions change. Understanding and modeling the coupled processes and their impact on repository performance are critical for any defensible performance assessment of a radioactive waste repository in a clay/shale host rock.

This chapter directly and indirectly address a number of research topics identified in *Research & Development (R&D) Plan for Used Fuel Disposition Campaign (UFDC) Natural System Evaluation and Tool Development* (Wang, 2011), including Topics P4, Investigation of water movement and transport in low permeability media (clay formations); P8, Reactive transport modeling of groundwater chemistry evolution and radionuclide transport; P15 Modeling of disturbed rock zone (DRZ) evolution (clay repository), and P18, In-situ testing of DRZ development. This chapter is focused on the development of constitutive relationships for elastic deformation of clay rock (Section 6.2), a THM modeling study (Section 6.3) and a THC modeling study (Section 6.4). The chapter summary and a discussion of future work activities are given in Section 6.5.

6.2   Development of Constitutive Relationships

Constitutive relationships refer to relationships among hydraulic, mechanical, thermal, and mechanical properties. This section documents the progress made in FY11 in developing relationships among stress, strain, and related stress-dependent hydraulic/mechanical properties (Section 6.2.1), as well as the development of an unsaturated property model for non-Darcian flow in clay materials (Section 6.2.2).

6.2.1   An elastic strain-stress relationship under anisotropic stress conditions

6.2.1.1   State of the art

The stress–strain relationship is the most fundamental part of constitutive relationships. Hooke's law has been generally used to describe this stress–strain relationship for elastic mechanical processes. According to Hooke's Law, for an elastic material, the proportionality in the stress-strain relationship should be constant. However, this proportionality is in fact not always constant in many cases, but rather stress-dependent (e.g., Cazacu, 1999; Lionço and Assis, 2000; Brown et al., 1989; Johnson and Rasolofosaon, 1969; Brady, 1969). A number of efforts have been made to relate this stress-dependent behavior to the microstructures of "cracks" in porous rock (Walsh, 1965; Nur, 1971; Mavko and Nur, 1978). An excellent review of these efforts is provided in a chapter entitled "Micromechanical Models" in Jaeger et al. (2007). Because it is generally difficult to characterize small-scale structures accurately and then relate their properties to large-scale mechanical properties that are of practical interest, it is desirable to have a macroscopic-scale theory that does not rely on the detailed description of small-scale structures, and that can physically incorporate the stress-dependent behavior of relevant mechanical properties. A theory of this kind was developed within the framework of Hooke's law by Liu et al. (2009).

Liu et al. (2009) argued that different varieties of Hooke's law should be applied within regions of the rock having significantly different stress–strain behavior, and that a rock body could be conceptualized into two distinct parts. These two parts are called a "hard part" that only experiences small deformation and a "soft part" that experiences large deformation. The natural strain (volume change divided by rock volume at the current stress state), rather than the engineering strain (volume change divided by the unstressed rock volume), should be used in Hooke's law for accurate modeling of the elastic deformation of the soft part of the pore volume, subject to a relatively large degree of relative deformation (i.e., cracks or fractures). This approach permits the derivation of constitutive relationships between stress and a variety of mechanical and/or hydraulic rock properties. The theoretical predictions of this method are generally consistent with empirical expressions (from field data) and also laboratory rock experimental data for sandstone rock (Liu et al., 2009). In FY10, we have primarily demonstrated the validity of Liu et

al.'s (2009) stress-strain relationship for a clay rock. As indicated later in this section and Section 6.2.3 below, consideration of the soft part is important for modeling coupled processes in clay repositories. However, the work of Liu et al. (2009) is limited to isotropic stress conditions corresponding to the hydrostatic stress state. In reality, a clay repository is generally subject to complex, anisotropic stress conditions. In FY11, we have extended the work of Liu et al. (2009) to such conditions.

6.2.1.2 Stress–strain relationship

Stress-strain relationships under isotropic stress conditions

The new stress-strain relationship to be developed herein is based on the work of Liu et al. (2009) for isotropic (or hydrostatic) stress conditions. Thus, for convenience, the results of Liu et al. (2009) are briefly discussed in this subsection.

The major reasoning of Liu et al. (2009) is that the two strains (natural and engineering) should be carefully distinguished, and the natural (or true) strain should be used in Hooke's law for accurately describing material deformation (Freed, 1995). When a uniformly distributed force is imposed on the surface of a homogeneous and isotropic material body subject to elastic deformation, natural (or true)-strain-based Hooke's law can be expressed as:

$$d\sigma_h = -K\frac{dV}{V} = Kd\varepsilon_{v,t} \tag{6.2-1}$$

where V is the total volume of the material body under the current stress state, σ_h is the hydrostatic stress, and K is the bulk modulus. The subscript h refers to hydrostatic (or isotropic) stress conditions, and $\varepsilon_{v,t}$ is the natural volumetric strain. The engineering-strain-based Hooke's law can be expressed as:

$$d\sigma_h = -K\frac{dV}{V_0} = Kd\varepsilon_{v,e} \tag{6.2-2}$$

where V_0 is the unstressed bulk volume, $\varepsilon_{v,e}$ is the engineering volumetric strain. Note that the two strains are practically identical for small mechanical deformations.

In the literature of rock mechanics, the engineering strain has been exclusively used, under the assumption that the elastic strain is generally small. However, Liu et al. (2009) indicated that the strain could be considerably larger within some portion of a rock body because of its inherent heterogeneity, and thus divide the rock mass into two parts to consider the impact of heterogeneity: (1) the portion of pores with different sizes and geometries subject to larger deformation is conceptualized as a "soft" part in the rock body; and (2) the remaining portion subject to small deformation is conceptualized as a "hard" part. For the soft part, the natural (or true)-strain-based Hooke's law is applied. For the hard part, the engineering -strain-based Hooke's law is applied. In this work, we also use subscripts 0, e, and t to denote the unstressed state, the hard part, and the soft part, respectively. According to Liu et al. (2009), the stress-strain relationship for porous and fractured rock under hydrostatic stress state can be expressed as:

$$-\frac{dV}{V_0} = \gamma_e \frac{d\sigma_h}{K_e} + \gamma_t \exp(-\frac{\sigma_h}{K_t})\frac{d\sigma_h}{K_t} \tag{6.2-3}$$

$$dV = dV_e + dV_t \tag{6.2-4}$$

$$V_0 = V_{0,e} + V_{0,t} \tag{6.2-5}$$

$$\gamma_t = \frac{V_{0,t}}{V_0} \tag{6.2-6}$$

$$\gamma_e = 1 - \gamma_t \tag{6.2-7}$$

where K_e and K_t refer to bulk modulus for the hard and soft parts, respectively.

Stress-strain relationship under anisotropic stress conditions

Without losing generality, we consider stress-strain relationships corresponding to the three principal stresses. To extend the work of Liu et al. (2009), we further assume that the principal strain resulting from the soft part is a function of the principal stress along the same direction only, and has nothing to do with the other principal stresses. The validity of this assumption will be evaluated by comparing our results with experimental observations.

Following the procedure of Liu et al. (2009) to derive Equation (6.2-3), we can obtain the expressions for principal strains:

$$d\varepsilon_1 = \frac{\gamma_e}{E_e}\left[d\sigma_1 - \nu(d\sigma_2 + d\sigma_3)\right] + \frac{\gamma_t}{E_t}\exp\left(-\frac{3\sigma_1}{E_t}\right)d\sigma_1$$

$$d\varepsilon_2 = \frac{\gamma_e}{E_e}\left[d\sigma_2 - \nu(d\sigma_1 + d\sigma_3)\right] + \frac{\gamma_t}{E_t}\exp\left(-\frac{3\sigma_2}{E_t}\right)d\sigma_2 \tag{6.2-8}$$

$$d\varepsilon_3 = \frac{\gamma_e}{E_e}\left[d\sigma_3 - \nu(d\sigma_1 + d\sigma_2)\right] + \frac{\gamma_t}{E_t}\exp\left(-\frac{3\sigma_3}{E_t}\right)d\sigma_3$$

where $\sigma_1, \sigma_2, \sigma_3$ are principal stresses, $\varepsilon_1, \varepsilon_2, \varepsilon_3$ are principal strains, ν is Poisson ratio, and E_e and E_t refer to Young's (elastic) modulus for the hard and soft parts, respectively.

The elastic modulus can be related to bulk modulus by :

$$K_e = \frac{E_e}{3(1-2\nu)} \quad K_t = \frac{E_t}{3} \tag{6.2-9}$$

Based on the assumption that strains are zero under unstressed state, principal strains can be solved from Equation (6.2-8) as:

$$\varepsilon_1 = \frac{\gamma_e}{E_e}\left[\sigma_1 - \nu(\sigma_2 + \sigma_3)\right] + \frac{\gamma_t}{3}\left[1 - \exp\left(-\frac{3\sigma_1}{E_t}\right)\right]$$

$$\varepsilon_2 = \frac{\gamma_e}{E_e}\left[\sigma_2 - \nu(\sigma_1 + \sigma_3)\right] + \frac{\gamma_t}{3}\left[1 - \exp\left(-\frac{3\sigma_2}{E_t}\right)\right] \tag{6.2-10}$$

$$\varepsilon_3 = \frac{\gamma_e}{E_e}\left[\sigma_3 - \nu\left(\sigma_2 + \sigma_1\right)\right] + \frac{\gamma_t}{3}\left[1 - \exp\left(-\frac{3\sigma_3}{E_t}\right)\right]$$

In (6.2-8) and (6.2-10), the first term on the right-hand side results from the hard part and the second term on the right-hand side from the soft part. Note that the second term, unlike the first term, is only a function of the corresponding principal stress and not related to other stresses, as a result of the assumption mentioned above. In other words, we ignore Poisson's ratio for the soft part, as demonstrated in (6.2-9).

Our treatment of Poisson's ratio, as the first step, is considered a rough approximation; further research may be needed to refine the treatment by incorporating the Poisson's ratio for the soft part. Poisson's ratio, ν, is defined as the negative of the ratio of transverse strain to the longitudinal strain, under conditions of uniaxial stress (Jaeger et al., 2007). Although the use of approximate or typical values in most rock-mechanics applications does not create significant problems, Poisson's ratio plays an undeniably important role in the elastic deformation of rocks and rock masses subjected to static or dynamic stresses. Furthermore, its effects emerge in a wide variety of rock engineering applications, ranging from basic laboratory tests on intact rocks to field measurements for *in situ* stresses or deformability of rock masses (Gercek, 2007). Poisson (1829) recommended the value of Poisson's ratio as 1/4. Wertheim (1848) recommended the value of Poisson's ratio as 1/3. Franz Ernst Neumann (1798–1895) recommended that the value of Poisson's ratio was not constant, but rather different with different materials. To make the Young's, shear, and bulk modulus of a material positive, the theoretical value of Poisson's ratio must lie in the range -1 and ½ (Jaeger et al., 2007). Moreover, according to Gercek (2007), the values of Poisson's ratio for many elements and materials are between 0 and 0.5. While one may anticipate that the porosity of rock will influence the value of Poisson's ratio, the geometry (size and shape), orientation, distribution, and connectivity of pores are expected to complicate that influence (Gercek, 2007). In this study, we assume that only the hard part of the rock is subject to Poisson's effect. As demonstrated later in this section, this assumption may be adequate for most practical applications in clay and other formations.

Note that our current development is consistent with the work of Liu et al. (2009), in that it is based on the volumetric strain under isotropic conditions. It is well known that the engineering volumetric strain is the sum of three principal strains (Jaeger et al., 2007):

$$d\varepsilon_v = \frac{dV}{V_0} = d\varepsilon_1 + d\varepsilon_2 + d\varepsilon_3$$

(6.2-11)

where ε_v is the volumetric strain. Combining (6.2-8) and (6.2-11) yields:

$$d\varepsilon_v = \frac{\gamma_e\left(1 - 2\nu\right)}{E_e}\left(d\sigma_1 + d\sigma_2 + d\sigma_3\right)$$

$$+ \frac{\gamma_t}{E_t}\exp\left(-\frac{3\sigma_1}{E_t}\right)d\sigma_1$$

$$+ \frac{\gamma_t}{E_t}\exp\left(-\frac{3\sigma_2}{E_t}\right)d\sigma_2$$

$$+ \frac{\gamma_t}{E_t}\exp\left(-\frac{3\sigma_3}{E_t}\right)d\sigma_3$$

(6.2-12)

Inserting (6.2-9) into (6.2-12) will result in the stress-strain relationship (Equation (6.2-3)) reported by Liu et al. (2009) when the three principal stresses are the same. Thus, our current results are a generalization of the work of Liu et al. (2009).

6.2.1.3 Comparisons with experimental observations

To evaluate the validity of our theoretical approach, we use the developed stress-strain relationship (Eq. 6.2-10) to fit the uniaxial compression data presented in Corkum and Martin (2007a) and Olalla et al. (1999) for Opalinus Clay rock. In Corkum and Martin (2007a), rock samples were 83 mm diameter, saw-cut core samples from boreholes BRA-1 and BRA-2, drilled with oil- and air-drilling fluids, respectively (Corkum and Martin 2007a). In Olalla et al. (1999), rock samples were 78 mm in diameter.

To avoid (as much as possible) the non-uniqueness of parameter values determined from curve fitting, we use a simple procedure to estimate parameter values from uniaxial stress versus uniaxial strain data. As shown in Figures 6.2-1 and 6.2-2, measured relationships between stress and strain are very well represented by a straight line for relatively high stresses. The slope of the straight line is used to determine $\dfrac{E_e}{\gamma_e}$, because the exponential terms on the right hand side of (6.2-10) are negligible for high stress values. The strain value at the intersection between the straight line and the strain axis in Figures 6.2-1 and 6.2-2 gives the value of $\dfrac{\gamma_t}{3}$, considering that the straight line represents the first term on the right-hand side of (6.2-10). The above procedure enables direct determination of values for E_e, γ_e and γ_t. The remaining parameter E_t can be estimated using a data point at relatively low stress. As indicted in Figures 6.2-1 and 6.2-2, the data are in excellent agreement with our theoretical results, suggesting that our assumption regarding the Poisson's effect seems to be adequate. Fitted parameter values are given in Table 6.2-1

The curve-fitted results of Opalinus Clay rock indicate that γ_t ranges from 0.036% to 0.48% for the eleven clay rock samples under consideration. It is smaller than the typical porosity of clay rock, which suggests that the so-called soft part is only a small percentage of pore volume, if we consider the soft part to be purely from the pore space. (Note that the nonlinear response of porous rock mainly depends on the soft part rather than the entire pore space.) As shown in Table 6.2-1, E_t ranges from 0.6 MPa to 3.6MPa, which, as expected, is much smaller than E_e. When applied stress loading on a rock frame increases, the shape of the soft-part pores changes, even tending to completely close, whereas the hard-part pores remain hard and resist closure—while the stress-sensitivity or nonlinear response of the rock is generally attributed to the deformation or closure of some pores. Macbeth (2004) also found that the pressure sensitivity of sand stones is due to the closure of intra- and intergranular cracks, small-aspect-ratio pore spaces, and broken grain contacts, none of which consume any significant portion of the pore volume. Shapiro and Kaselow (2005) assumed that the main reason for load-induced changes in the elastic properties of rock is the load-induced deformation of the pore space, and the compliant part of the pore space played the more important role.

Our work here is generally consistent with these previous studies. However, it differs from those studies in that our work is directly based on the notion that Hooke's law should use natural strains and rock mass that can be conceptualized into hard and soft parts. This allows for derivation of our stress-strain relationship, one that can be further used, in a systematic way, to generate formulations for stress-

dependent rock properties with physically defined parameters, whereas most previous studies focus primarily on some specific mechanical parameters, rather than general stress-strain relationships.

Table 6.2-1. Fitted parameter values from the experiment data for Opalinus Clay rock

Specimen	E_e (MPa)	γ_e	E_t (MPa)	γ_t
bra2-2a	2537.5	0.99310	0.9	0.00230
bra1-7a	2643.5	0.99490	2.0	0.00170
bra1-3a	2438.8	0.99640	3.6	0.00120
bra2-2b	2414.4	0.99817	3.0	0.00061
bra1-7b	2682.9	0.99892	2.1	0.00036
9949a	2080.0	0.99520	0.9	0.00480
9963	2448.8	0.99640	0.6	0.00360
9949b	2326.9	0.99703	1.6	0.00297
9972	2164.5	0.99793	1.7	0.00207
9957	2804.4	0.99844	1.8	0.00156
9984b	3345.1	0.99847	1.8	0.00153
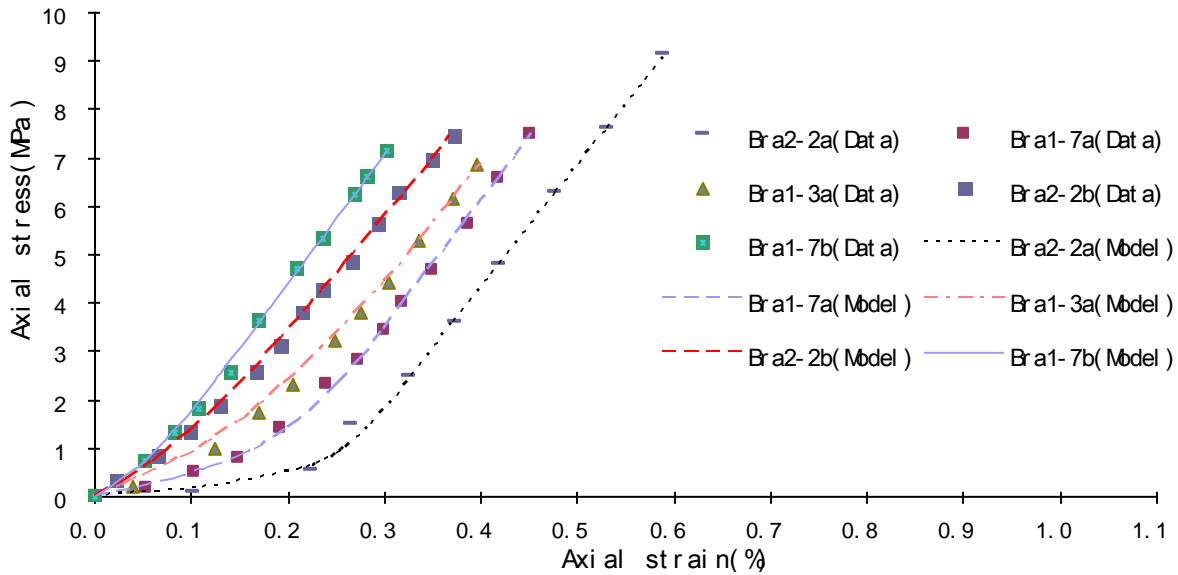
Figure 6.2-1. Matches between results calculated from Eq. (6.2-10) and experimental data from unconfined compression tests on clay rock (Corkum and Martin 2007a)
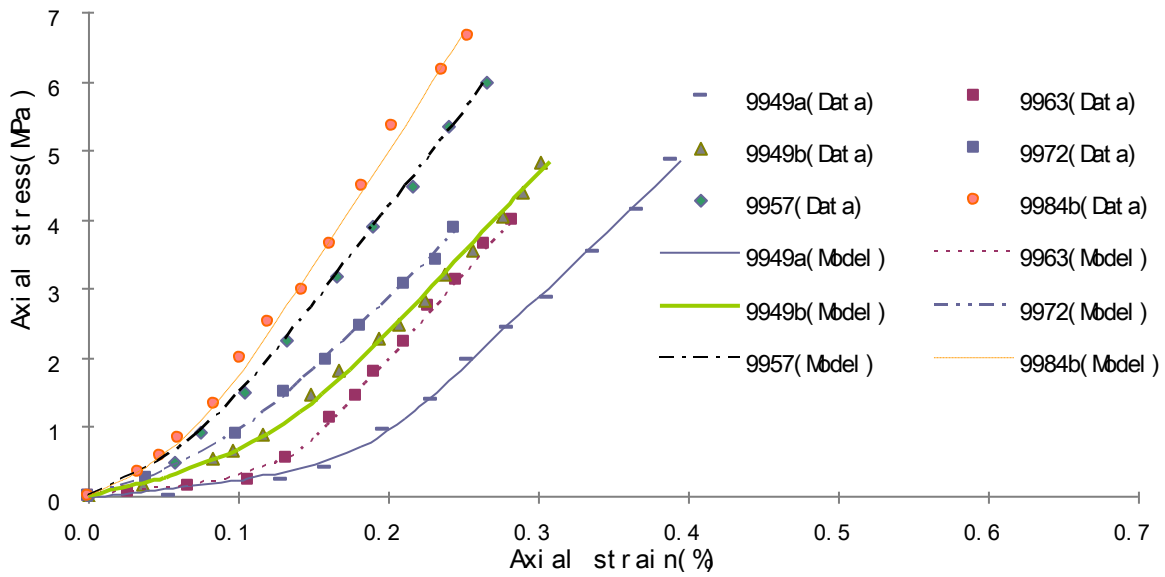
Figure 6.2-2. Matches between results calculated from Eq. (6.2-10) and experimental data from unconfined compression tests on clay rock (Olalla et al., 1999).

To further evaluate the impact of the soft part on rock mechanical deformation, Figure 6.2-3 shows strain-stress curves calculated from (6.2-10) by considering the hard part only, soft part only, and hard part + soft part, respectively. Clearly, the soft part has a larger strain than the hard part at the early stage of uniaxial loading, even though the volumetric ratio γ_t is much lower than that for the hard part. The curves in Figure 6.2-3 also suggest that the soft-part strain is important for porous rock, especially at low stresses.

(a)

(b)

(c)

(d)
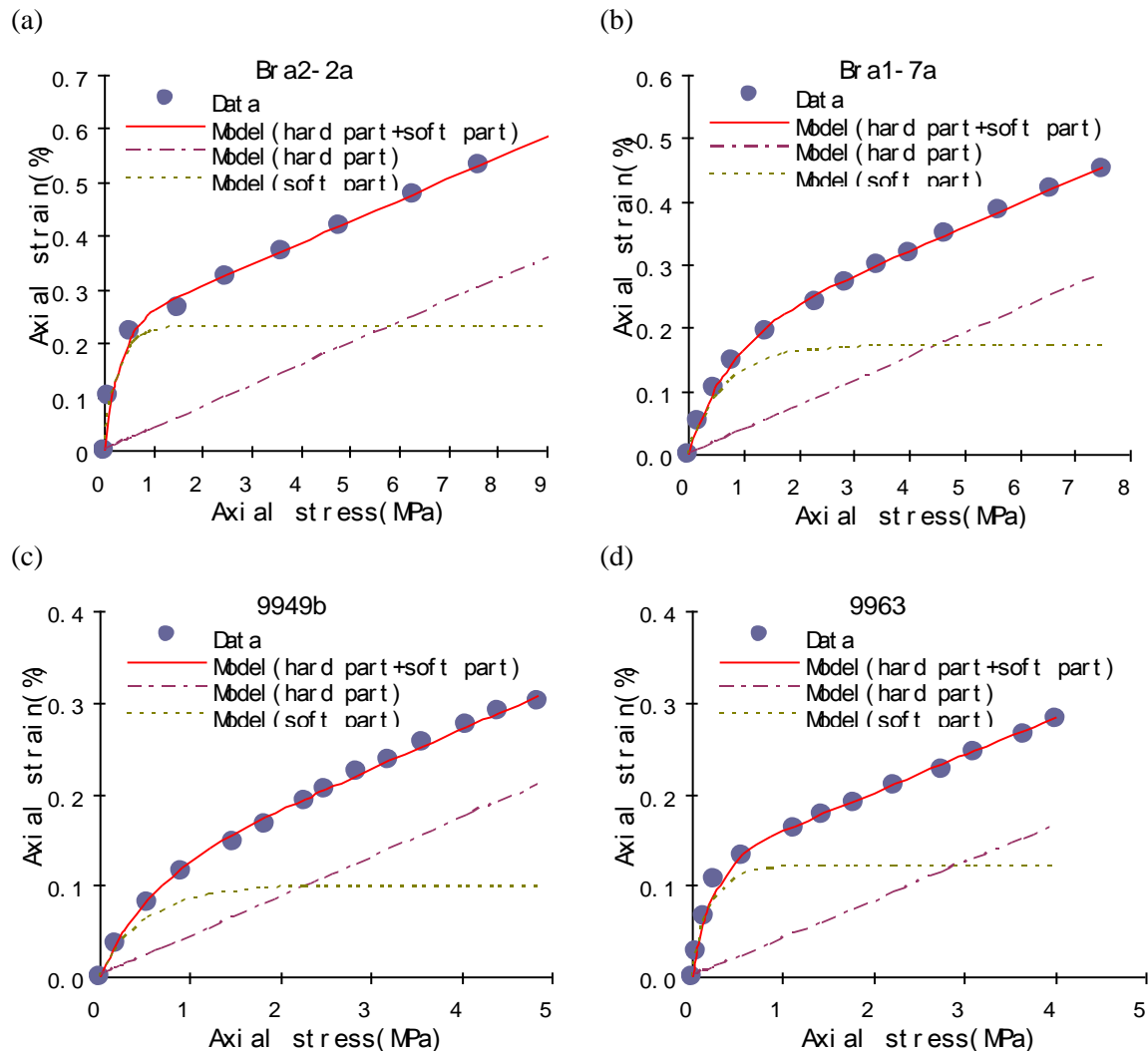
Figure 6.2-3. Comparisons between hard part strain and soft part strain

To further verify our stress-strain relationship, we compare our theoretical results with data from triaxial compression tests for a porous white sandstone (drilled from a construction site near metropolitan Taipei) (Tien et al., 1990), a shale rock (Xu et al., 2006a), and a conglomerate rock (Hu and Liu, 2004). These triaxial tests involve a cylindrical rock sample subjected to confining pressure σ_c (corresponding to axial strain ε_0), keeping a constant confining pressure and then controlled increases in axial stresses. In these

tests, the measured relationships between deviatoric stress $(\sigma_1 - \sigma_c)$ and axial strain $(\varepsilon_1 - \varepsilon_c)$ are generally reported and used in our evaluation. When the confining pressure is constant, applying Equation (6.2-10) yields:

$$\varepsilon_1 - \varepsilon_c = \frac{\gamma_e}{E_e}(\sigma_1 - \sigma_c) + \frac{\gamma_t}{3}\exp\left(-\frac{3\sigma_c}{E_t}\right)\left[1 - \exp\left(-\frac{3(\sigma_1 - \sigma_c)}{E_t}\right)\right]$$

(6.2-13)

Figures 6.2-4, 6.2-6, and 6.2-8 show the satisfactory matches of (6.2-13) with observed data from rock samples under triaxial compression conditions. The curve-fitted results indicate that the γ_t value ranges from 2.4% to 3.3% for the sandstone rock, from 0.9% to 1.02% for the conglomerate rock, and is 1.65% for the shale rock under consideration. Because different rock samples are used for different stress conditions during triaxial compression tests, some variation in fitted values for rock parameters are observed for a given rock type. The fitted parameter values are listed in Table 6.2-2, 6.2-3 and 6.2-4.

To further demonstrate the relative importance of the soft part, Figures 6.2-5, 6.2-7 and 6.2-9 show the results of both the soft-part strain and the ratio of soft-part strain to the hard-part strain as a function of axial stress. (R denotes the ratio in those figures.) These curves describe the overall deformation behavior of the soft part, showing significant increase in strain with stress initially and then a slow change in strain. All samples show a decrease in R with increased confining pressure for a given deviatoric stress, and with increased axial stress at a given deviatoric stress.
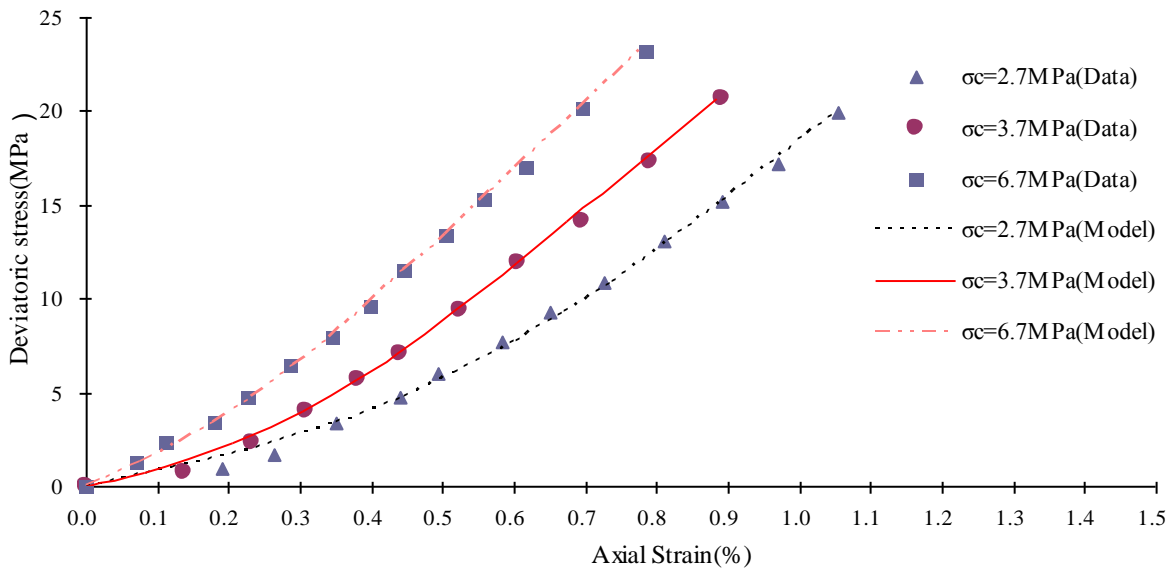
Figure 6.2-4. Matches between results calculated from Equation (6.2-13) and experimental data from triaxial compression tests on a sandstone (Tien et al., 1990)
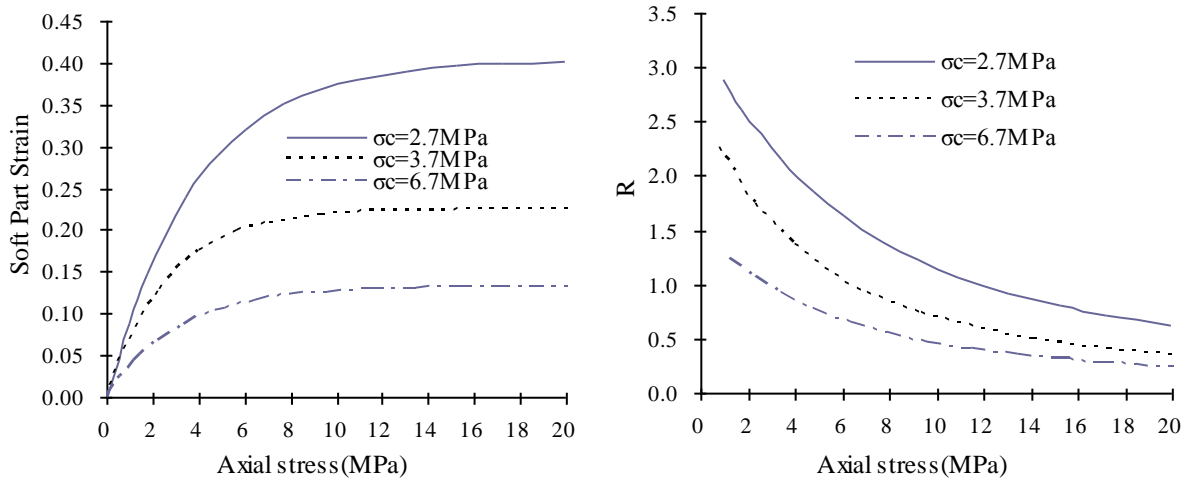
Figure 6.2-5. Soft part strain and R (the ratio of soft part strain to the hard part strain) as a function of axial stress at different confining pressure for a sandstone.

Table 6.2-2. Fitted parameter values from the experimental data for sandstone

Confining pressure(MPa)	E_e(MPa)	γ_e	E_t (MPa)	γ_t
2.7	3070.0	0.97534	11.4	0.02466
3.7	3140.0	0.97343	8.1	0.02657
6.7	3600.0	0.96786	9.6	0.03214
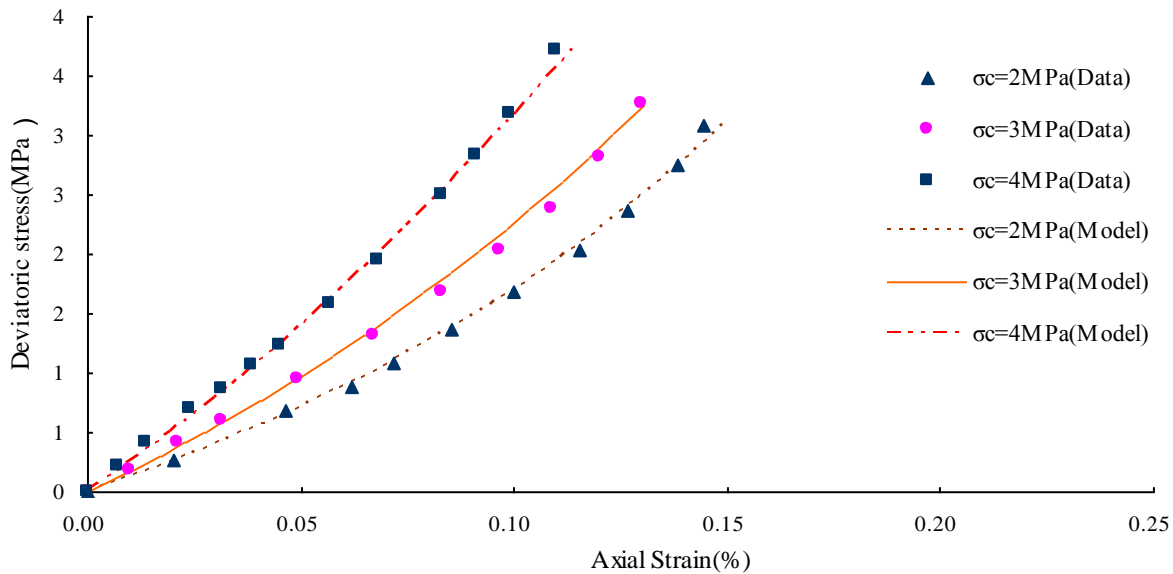
Figure 6.2-6. Matches between results calculated from Equation (6.2-13) and experimental data from triaxial compression tests on a conglomerate rock (Hu et al., 2004)
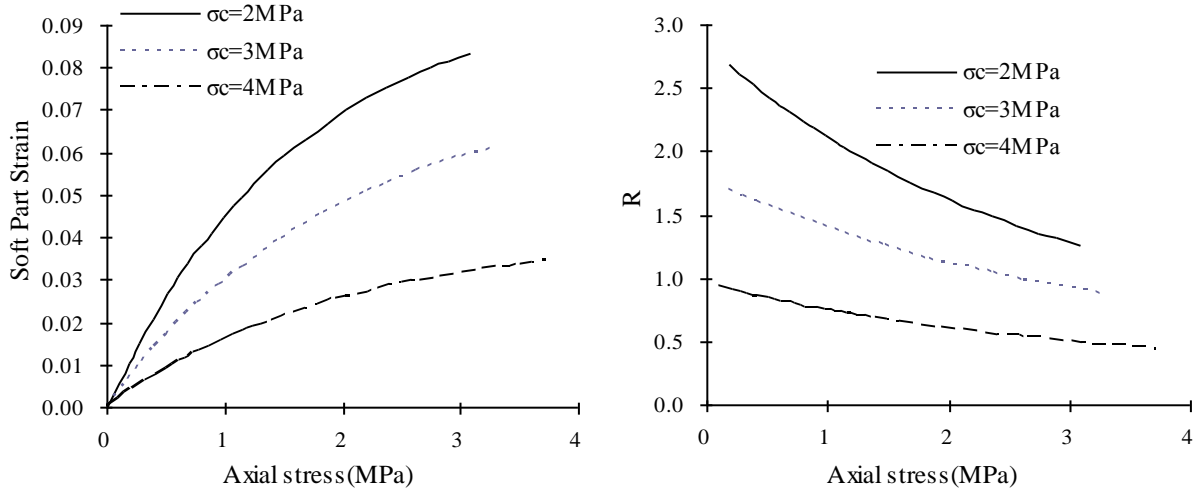
Figure 6.2-7. Soft part strain and R (the ratio of soft part strain to the hard part strain) as a function of axial stress at different confining pressure for a conglomerate rock.

Table 6.2-3. Fitted parameter values from the experimental data for conglomerate rock

Confining pressure(MPa)	E_e (MPa)	γ_e	E_t (MPa)	γ_t
2	4670.0	0.99100	4.8	0.00900
3	4670.0	0.98980	6.0	0.01020
4	4670.0	0.98980	6.0	0.01020
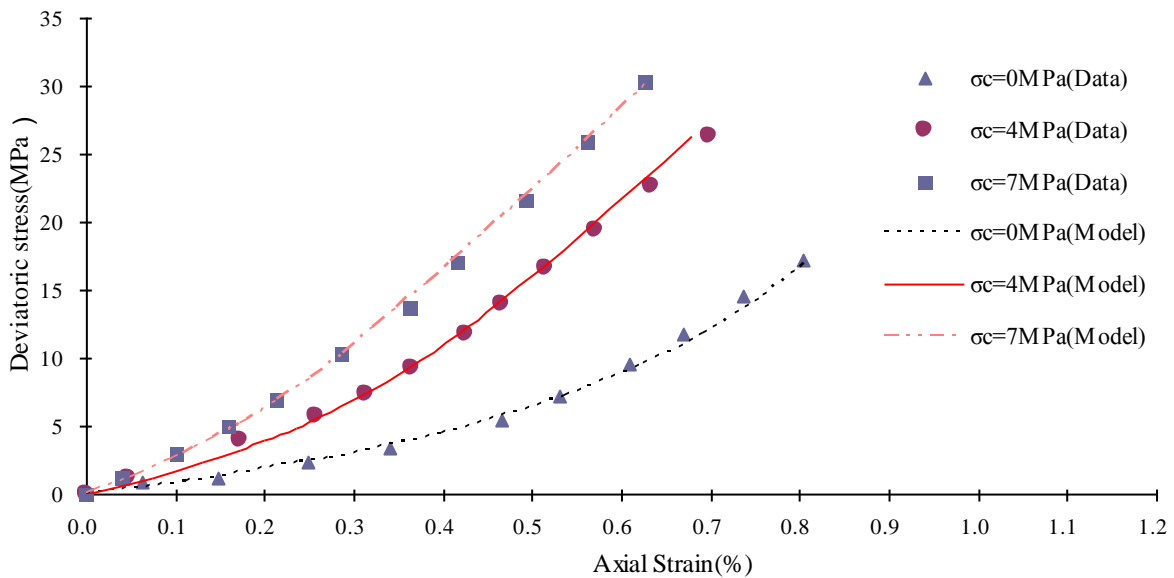
Figure 6.2-8. Matches between results calculated from Equation (6.2-13) and experimental data from triaxial compression tests on shale rock (Xu et al., 2006a).
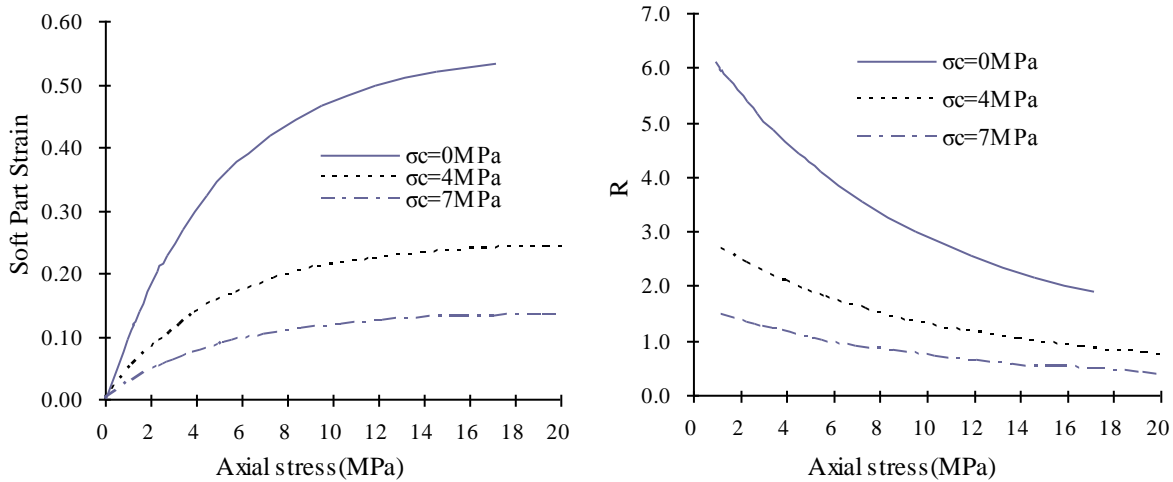
Figure 6.2-9. Soft part strain and R (the ratio of soft part strain to the hard part strain) as a function of axial stress at different confining pressure for a shale rock.

Table 6.2-4. Fitted parameter values from the experimental data for shale rock

Confining pressure(MPa)	E_e (Mpa)	γ_e	E_t (Mpa)	γ_t
0	6100.0	0.98350	15.0	0.01650
4	6100.0	0.98350	15.0	0.01650
7	6100.0	0.98350	15.0	0.01650

6.2.1.4 Stress-dependent mechanical and hydraulic rock properties

Our newly developed stress-strain relationship (Equation 6.2-10) allows derivation of a variety of additional constitutive relationships among mechanical and hydraulic properties. This subsection presents the stress dependence of porosity and compressibility, as illustrative examples. While our focus here is on a clay repository, our developed results can be applied to other geological formations as well. Experimental data for clay rock are generally limited to the stress dependence of rock properties. Therefore, data from sandstones are used here for evaluating the stress-dependence relationships of porosity and compressibility.

Porosity: Rock porosity is an important parameter for modeling coupled hydrological and mechanical processes, because flow processes occur in pore spaces. Following Liu et al. (2009), we assume that the soft part is a fraction of pore space. In this case, the rock porosity is defined by:

$$d\phi = \frac{dV^p}{V} = \frac{dV_e^p + dV_t}{V} \approx \frac{dV_e^p + dV_t}{V_0} \tag{6.2-14}$$

where V is the bulk volume of rock and superscript p refers to pore space. Liu et al. (2009) indicated that for the purpose of calculating porosity, the total rock volume V could be approximated with the undressed volume V_0, because their difference is small in practical applications.

For pores associated with the hard part of the rock, we have:

$$\frac{dV_e^p}{V_0} = \frac{V_{0,e}^p}{V_0}\frac{dV_e^p}{V_{o,e}^p} = -(\phi_0 - \gamma_t)C_e(d\sigma_1 + d\sigma_2 + d\sigma_3)$$

(6.2-15)

To derive the above equation, we use the following relationships:

$$\frac{V_{0,e}^p}{V_0} = \phi_0 - \gamma_t$$

(6.2-16)

and

$$C_e = -\frac{1}{3V_{0,e}^p}\frac{\partial V_e^p}{\partial \sigma_i} \qquad (i = 1, 2, 3)$$

(6.2-17)

where   is the pore volume within the hard part of the rock under unstressed conditions,   is porosity under unstressed conditions, and C_e is pore compressibility (constant).

From Equation (6.2-12) and its derivation procedure, it can be mathematically shown that the porosity change owing to the soft part, —, is the same as the last three terms on the right hand of (6.2-12). Thus, we have:

$$d\phi = -(\phi_0 - \gamma_t)C_e(d\sigma_1 + d\sigma_2 + d\sigma_3) -$$

$$\frac{\gamma_t}{E_t} \times \left[\exp\left(-\frac{3\sigma_1}{E_t}\right)d\sigma_1 + \exp\left(-\frac{3\sigma_2}{E_t}\right)d\sigma_2 + \exp\left(-\frac{3\sigma_3}{E_t}\right)d\sigma_3 \right]$$

(6.2-18)

Using the condition that unstressed porosity is   , we obtain:

$$\phi = \phi_0 - \gamma_t - (\phi_0 - \gamma_t)C_a(\sigma_1 + \sigma_2 + \sigma_3)$$
$$+ \frac{\gamma_t}{3}\left[\exp\left(-\frac{3\sigma_1}{E_t}\right) + \exp\left(-\frac{3\sigma_2}{E_t}\right) + \exp\left(-\frac{3\sigma_3}{E_t}\right) \right]$$

(6.2-19)

We use experimental results from uniaxial tests to verify our porosity-stress relation, or Equation (6.2-19), while relevant data are very limited for more complex stress conditions. Peng and Zhang (2007) reported a data set of porosity (as a function of axial stress) under uniaxial strain conditions for two sandstone specimens cored 1000 m below the sea floor. Satisfactory matches between results calculated from Equation (6.2-19) and porosity data are shown in Figure 6.2-10. The curve-fitted results indicate that

values for γ_t range from 1.77% to 2.04% for the sandstone samples under consideration, and that are 15.0 MPa for E_t (Table 6.2-5). Note that the value for E_t is generally consistent with that reported in Table 6.2-2. However, the estimated γ_t values are much higher than those given in Table 6.2-2, which may be a result of rock porosity values in this part of the study being much higher.
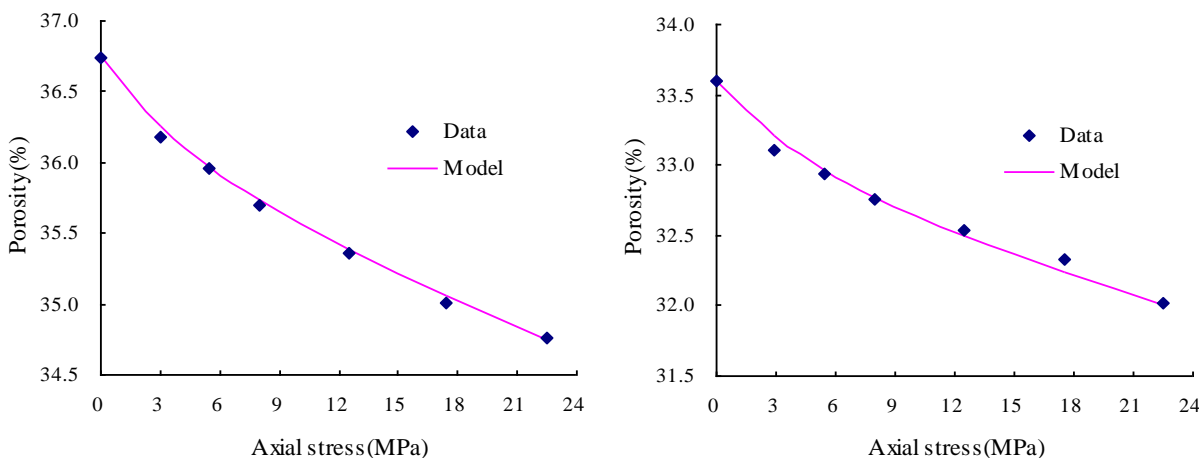
Figure 6.2-10. Comparisons between results calculated from Equation (6.2-19) and experimental data from uniaxial strain tests for two sand specimens (Peng and Zhang, 2007)

Table 6.2-5. Fitted parameter values from the experimental data for sandstone samples

Specimens	ϕ_0 (%)	C_a (10^{-3}MPa^{-1})	E_t (MPa)	γ_t
1	36.75	1.70	15.0	0.0204
2	33.60	1.44	15.0	0.0177

Note that a similar form of relationship between stress and porosity was also reported by Shapiro and Kaselow (2005). They assumed that pore space contains so-called compliant porosity (similar to the "soft part" in this study) and also derived a number of relationships between stress and other mechanical properties under anisotropic conditions (Shapiro and Kaselow, 2005). However, several important differences can be observed when comparing our theory with theirs. First, our theory is based on the natural-strain-based Hooke's law, which is fundamentally different from the physical origin of Shapiro and Kaselow (2005). Second, their theory is theoretically valid only for rock with moderate or small porosity, on the order of 0.1 or less (Shapiro and Kaselow, 2005). As evidenced by the corresponding derivation procedures, our results are not subject to this limitation. Finally, the validity of Shapiro and Kaselow's (2005) theory requires that their compliant porosity must be a very small part of total porosity. Again, our theory is not limited by this, largely because our theory as mentioned above has a different physical origin. It can be applied to cases in which soft porosity is large. For example, Liu et al. (2009) successfully derived the relationship between stress and fracture aperture. Unlike the "soft" part of porous rock, the "soft" part in a fracture corresponds to a much larger portion of fracture voids than the hard part (Liu et al., 2009).

Bulk Compressibility: Bulk compressibility is often used to quantify the ability of a rock to reduce in volume with applied pressure. It may be defined in different ways; in this study, we define bulk compressibility (associated with a principal stress   ) by:

$$C_i = \frac{\partial \varepsilon_v}{\partial \sigma_i} \quad (i=1, 2, 3) \tag{6.2-20}$$

Based on the above equation and (6.2-12), the compressibility can readily be determined as:

$$C_i = \frac{\gamma_e(1-2\gamma)}{E_e} + \frac{\gamma_t}{E_t}\exp\left\{-\frac{3\sigma_i}{E_t}\right\} \quad (i=1, 2, 3) \tag{6.2-21}$$

Morgenstern and Tamuly Phukan (1969) investigated the relationship between modulus of compressibility and stress for Bunter sandstone. We use results from Morgenstern and Tamuly Phukan's (1969) uniaxial tests to verify our compressibility-stress relation (Equation (6.2-21)). For uniaxial tests, we need only consider C_1, because $\sigma_2 = \sigma_3 = 0$. As shown in Figure 6.2-11, our relationship satisfactorily matches the data, further supporting our overall theoretical results developed for anisotropic conditions. The estimated parameter values for sandstone are presented in Table 6.2-6. Note that the compressibility, *C*, defined by Morgenstern and Tamuly Phukan (1969) is three times the compressibility given in (6.2-21). In Figure 6.2-11, the former is used.
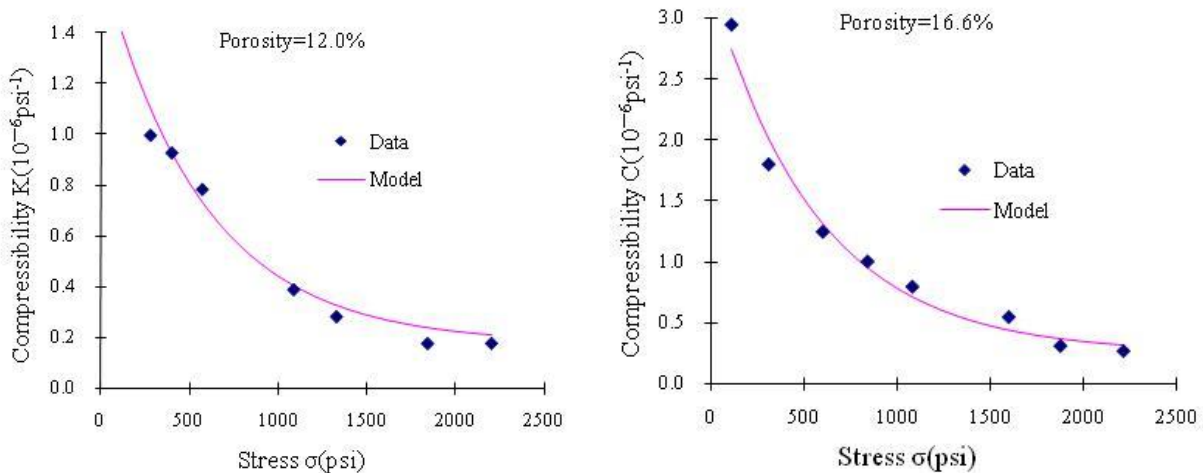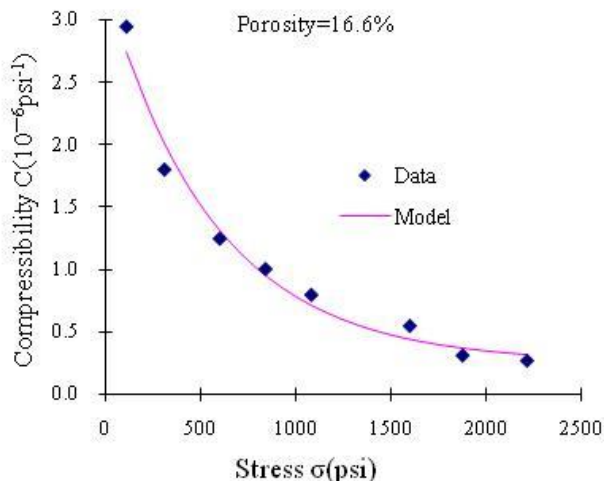
Figure 6.2-11. Comparisons between the uniaxial test data for Bunter sandstone (Morgenstern and Tamuly Phukan 1969) and the compressibility-stress relationship (Equation (6.2-21)).

Table 6.2-6. Fitted parameter values from the experimental data for Bunter sandstone

ϕ (%)	$E_e (10^3 \text{psi})$	γ_e	$E_t (10^3 \text{psi})$	γ_t
12.0	9914.000	0.99914	1.725	0.00086
15.3	7187.544	0.99827	1.725	0.00173
16.8	7187.544	0.99827	1.725	0.00173

6.2.1.5   Conclusions

In FY 2010, we reported a stress-strain relationship for clay and other rocks under elastic and isotropic conditions. In this study, we extend that work to anisotropic stress conditions. It was shown that the new relationship could satisfactorily represent a number of experimental observations. Furthermore, based on this relationship, we derived additional constitutive relationships between stress and selected mechanical or hydraulic rock properties (compressibility and porosity). The consistency between these relations and data further supports the usefulness and validity of our stress-strain relationship, which is a critical input to coupled-process simulators. The constitutive model reported here was not incorporated into the simulations presented in Sections 6.3 and 6.4 because it was only recently developed.

6.2.2   Unsaturated properties for non-Darcian water flow in clay

6.2.2.1 State of the art

Because of the impact of heat-transport processes (caused by radionuclide decay within waste packages) and water-flow processes between clay rock and an engineered barrier, an unsaturated zone generally develops within the near field of a clay repository. Furthermore, in radioactive waste disposal at great depth, compacted expansive clay soils (bentonites) are often considered as buffer materials within an engineered barrier system, to be placed between the radioactive waste and the host rock. The bentonite is usually compacted at low water content, such that it is progressively wetted by water from the host formation. The unsaturated wetting process is accompanied by the bentonite swelling to ensure acceptable sealing of open spaces between waste packages and the corresponding host formation. Therefore, accurately modeling unsaturated flow in clay materials is critical for assessing the performance of both clay rock and buffer materials for isolating radioactive wastes at a disposal site.

It has been documented in the literature that water flow in clays cannot be adequately described by the commonly used Darcy law, which states that water flux is directly proportional to hydraulic gradient. For example, Hansbo (2001) reported that water flux is proportional to a power function of hydraulic gradient when the gradient is less than a critical value, whereupon the relationship between water flux and gradient becomes linear for large gradient values. He explained this behavior by positing that a certain hydraulic gradient is required to overcome the maximum binding energy of mobile pore water. Moreover, Dixon et al. (1999) presented measured hydraulic conductivity data for clays, They found no "critical" or "threshold" gradients from their observations, but did find that there were "transitional" gradients that define two separate regions of Darcian flow. Lower hydraulic conductivities were observed for hydraulic gradients less than the transitional gradient. Dixon et al. (1999) indicated that clay could contain considerable quantities of structured water that shears at gradients above the transitional gradient, allowing it to participate in advective flow. Finally, Zou (1996) proposed a nonlinear flux-gradient relation depending on the activation energy of pore liquid. He assumed that the activation energy of pore water in clay (or fine-grained materials) is not only variable with the distance from the solid particle surface, but also with the flow velocity of pore water. His model, including several empirical parameters, was able to fit a number of data sets that show nonlinear flux-gradient relations at low hydraulic gradients and linear relations at high gradients. More studies of non-Darcian behavior for water flow in clay can be found in references cited in Hansbo (2001), Dixon et al. (1999), and Zou (1996). Although some inconsistency seems to exist among these studies, most studies demonstrated the existence of non-Darcian's flow behavior in clay under conditions of relatively low hydraulic gradients.

Note that such studies are all for saturated flow conditions; investigations for unsaturated flow in clay are very limited. It is expected that non-Darcian flow behavior becomes more significant under unsaturated conditions, because in such conditions, pore water exists as water films or occurs in relatively small pores, and therefore is subject to relatively strong interactions with the clay surface. This seems to be supported by experimental observations recently reported by Cui et al. (2008). They observed non-Darcian behavior for the full range of observed hydraulic gradients under unsaturated conditions.

While several models have been proposed for describing non-Darcian flow in clay in saturated conditions, a systematic investigation of constitutive models for unsaturated flow in clay materials is still lacking. The objective of this work is to develop such a model under unsaturated conditions, by considering pore water as a non-Newtonian fluid.

6.2.2.2 Theoretical model

This section presents a theoretical model describing non-Darcian flow under unsaturated conditions. The model will be verified in the next section with data from a laboratory experiment. Theoretical development of the model is based on the hypothesis that pore water in clay materials is non-Newtonian and that flow is driven by the hydraulic gradient.

Newtonian and non-Newtonian fluids: In general, fluids can be classified as Newtonian or non-Newtonian. The former has a constant viscosity; thus, its shear stress is directly proportional to the shear rate defined as the velocity gradient perpendicular to the plane of shear. For non-Newtonian fluid, the viscosity is not constant anymore, but rather a function of shear rate and/or time. For example, Figure 6.2-12 shows typical relations between shear stress and shear rate for a Newtonian fluid and three non-Newtonian fluids. Pseudoplastic or shear-thinning fluids have a lower apparent viscosity at higher shear rates, and dilatant, or shear-thickening fluids increase in apparent viscosity at higher shear rates (e.g., Wu and Pruess, 1998). Bingham plastic fluids have a linear shear stress/shear strain relationship and require a finite yield stress before they begin to flow. In other words, the plot of shear stress against shear strain does not pass through the origin (Figure 6.2-12).

A relatively simple way to describe non-Newtonian behavior is to express the apparent viscosity (μ_e) as a power function of shear rate $\dfrac{\partial u}{\partial y}$ (e.g., Christopher and Middleman, 1965):

$$\mu_e = \kappa \left(\frac{\partial u}{\partial y} \right)^{n-1} \tag{6.2-22}$$

where κ is a constant, u is water velocity parallel to the plane of shear, y is a coordinate perpendicular to the plane of shear, and n is a dimensionless number. The corresponding fluids are called "power-law fluids." In this case, the shear stress of fluid, τ, is given by:

$$\tau = \mu_e \left(\frac{\partial u}{\partial y} \right) = \kappa \left(\frac{\partial u}{\partial y} \right)^{n} \tag{6.2-23}$$

Equations (6.2-22) and (6.2-23) correspond to pseudoplastic fluid (n <1), Newtonian fluid (n =1), and dilatant fluid (n >1), respectively. In this study, we focus on power-law fluids following Equations (6.2-22) and (6.2-23); Bingham plastic fluid is not considered. As demonstrated below, these equations seem to capture the non-Darcian behavior of pore water under unsaturated conditions reasonably well. Note that the methodology developed in this study can be easily applied to Bingham plastic fluids as well, when needed.
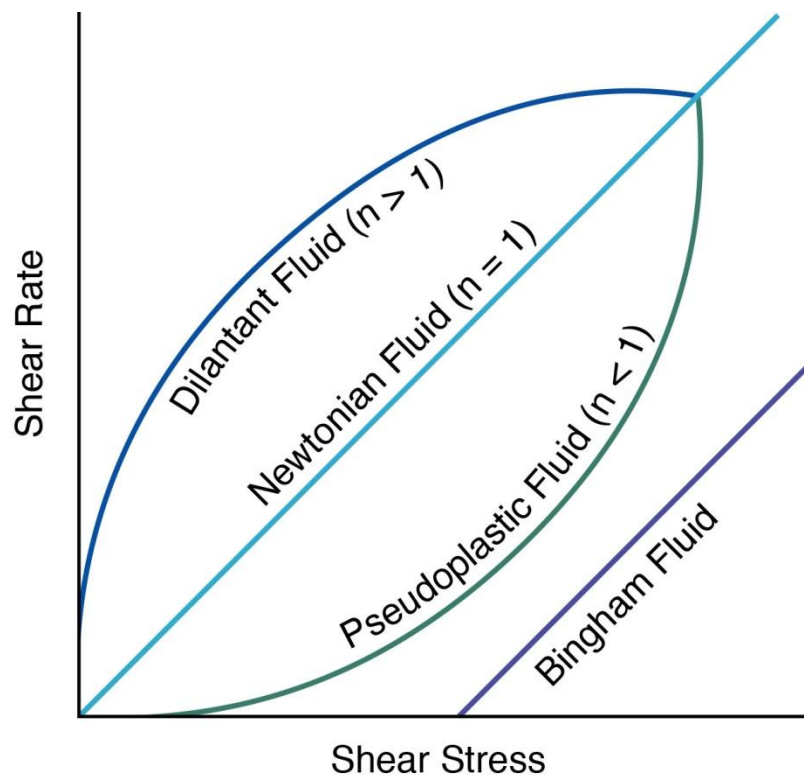
ESD11-020

Figure 6.2-12. Schematic demonstration of relations between shear stress and stress rate for a Newtoniain fluid and three typical non-Newtonian fluids

It is well documented in the literature that water properties will change near the clay surface as a result of water-clay interaction. Like other researchers (e.g., Zou, 1996), we believe that the observed non-Darcian behavior for water flow is caused by non-Newtonian properties of pore water in clay materials. These properties should be a direct result of strong water-clay interaction. However, this argument is largely based on observations at core scales and to the best of our knowledge has not been directly confirmed by measured viscosity and shear rate data at pore scales. Thus, it is appropriate to treat the considered correlation between non-Darcian behavior and non-Newtonian properties as a hypothesis at this point.

Relationship between flux and hydraulic gradient for a capillary tube: In this subsection, we derive a relationship between water flux and hydraulic gradient for a capillary tube with radius R (Figure 6.2-13). This will be used as the basis for developing corresponding relationships for clay materials. For simplicity, we consider a horizontal capillary tube here, while our result can be easily extended to capillary tubes with other orientations.
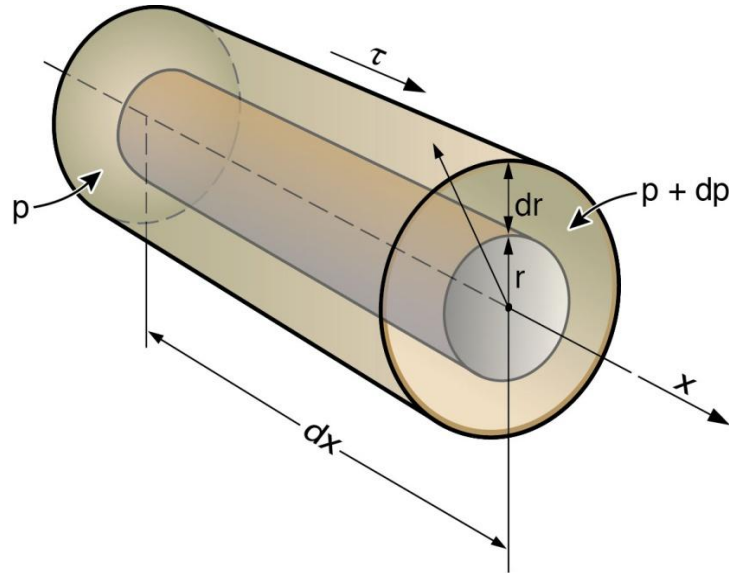
ESD11-021

Figure 6.2-13. A water element in a capillary tube

Considering water to be a non-Newtonian fluid in the capillary tube and using Equations (6.2-22) and (6.2-23), we can write the shear stress relationship as:

$$\tau = \kappa \left(\left| \frac{du}{dr} \right| \right)^n \tag{6.2-24}$$

where r is radius coordinate. For a water surface with radius r and length dx (Figure 6.2-23), the total shearing force is:

$$F = \tau (2\pi r) dx \tag{6.2-25}$$

Then, the net shearing force for a water element with thickness dr within the capillary tube, dF, is given by $dF = 2\pi(dx)d(r\tau)$. For laminar flow, the inertial effect can be ignored. In this case, the shearing force should be balanced by an opposing pressure on the water element that is $(dp)(dr)(2\pi r)$. Therefore, we have:

$$dF = 2\pi(dx)d(r\tau) = (dp)(dr)(2\pi r) \tag{6.2-26}$$

Combining (6.2-24) and (6.2-26) yields:

$$r\frac{dp}{dx} = \frac{d(r\tau)}{dr} = \frac{d\left(r\kappa \left(\left| \frac{du}{dr} \right| \right)^n \right)}{dr} \tag{6.2-27}$$

The above equation can be solved for shear rate (or velocity gradient $\dfrac{du}{dr}$)

$$\frac{r^2}{2}\frac{dp}{dx} + C = \kappa r\left(\left|\frac{du}{dr}\right|\right)^n \tag{6.2-28}$$

where C is a constant and determined to be zero by the following boundary condition (that is a result of symmetry):

$$\left.\frac{du}{dr}\right|_{r=0} = 0 \tag{6.2-29}$$

Note $\left|\dfrac{du}{dr}\right| = -\dfrac{du}{dr}$ for the capillary tube under consideration. Then (6.2-28) can be rewritten as:

$$-\frac{du}{dr} = \left(\frac{dp}{dx}\right)^{1/n}\left(\frac{r}{2\kappa}\right)^{1/n} \tag{6.2-30}$$

Further, using non-slip conditions on the surface of the capillary tube ($u = 0$ at $r = R$), the solution to (6.2-30) is given as:

$$u(r) = \left(\frac{dp}{dx}\right)^{1/n}\int_R^r\left(\frac{r}{2\kappa}\right)^{1/n}dr = \left(\frac{dp}{dx}\right)^{1/n}\left(\frac{1}{2\kappa}\right)^{1/n}\frac{n}{n+1}\left[R^{1+\frac{1}{n}} - r^{1+\frac{1}{n}}\right] \tag{6.2-31}$$

The above equation gives the velocity distribution along the radius direction. The average water flux across the cross-sectional area of the tube is then determined by:

$$q_C = \frac{\displaystyle\int_0^R u(r)(dr)(2\pi r)}{2\pi R^2} = \left(\frac{1}{2\kappa}\right)^{1/n}\frac{n(n+1)}{2(n+1)(3n+1)}R^{1+\frac{1}{n}}\left(\frac{dp}{dx}\right)^{\frac{1}{n}} \tag{6.2-32}$$

Theoretical model for unsaturated clay materials: The pore space in a porous medium is often conceptualized as a group of capillary tubes with different tortuosity values and sizes (van Genuchten, 1980; Burdine, 1953). Thus, Equation (6.2-32) for a single capillary tube can be extended to represent the relationship between water flux, q, and hydraulic gradient $\dfrac{dH}{dx}$ in porous media:

$$q = -K\left(\left|\frac{dH}{dx}\right|\right)^{\frac{1}{n}}i \tag{6.2-33}$$

where H is the hydraulic head, K is hydraulic conductivity, and i is the unit vector for hydraulic gradient.

Note that for a single capillary tube, K is proportional to $R^{1+\frac{1}{n}}$, rather than R^2. (The latter is valid for Newtonian fluids.) The relationship between hydraulic conductivity for a capillary tube and R is the foundation for studying relative permeability under unsaturated conditions. Equations similar to (6.2-33) were also reported by a number of researchers (e.g., Pascal 1983; Wu and Pruess, 1998; Lopez et al., 2003). Most previous studies deal with single-phase fluid flow except Wu and Pruess (1998), who did not consider how non-Newtonian behavior affected unsaturated flow properties. As discussed below, the major focus of this study is on determining how non-Newtonian behavior impacts the unsaturated properties of clay materials.

For unsaturated media, capillary pressure P_c can be related to water saturation by the well-known Brooks-Corey (1964) relationship:

$$S_e = \left(\frac{P_c}{P_d} \right)^{-\lambda} \quad \text{for } P_c < P_d \tag{6.2-34-1}$$

$$S_e = 1 \quad \text{for } P_c \geq P_d \tag{6.2-34-2}$$

In (6.2-34), λ is a fitting factor related to pore-size distribution, P_d is the air entry value, and S_e is the effective saturation defined by:

$$S_e = \frac{\theta - \theta_r}{\theta_s - \theta_r} \tag{6.2-35}$$

where θ, θ_s and θ_r are water content, saturated water content, and residual water content, respectively.

In the literature, the relative permeability for unsaturated media has often been provided by the Burdine (1953) model:

$$K_r = \frac{K}{K_{sat}} = S_e^2 \frac{\int_0^{S_e} P_c^{-2} dS_e}{\int_0^1 P_c^{-2} dS_e} \tag{6.2-36}$$

where K_{sat} is saturated hydraulic conductivity. In Equation (6.2-36), S_e^2 represents tortuosity, and $\frac{1}{P_c}$ characterizes the size (or radius) of the capillary tube (or pore space) under saturation S_e. The power value of -2 in the two integrals results from the fact that, for Newtonian fluids, hydraulic conductivity for a capillary tube is proportional to the square of its radius. Therefore, Equation (6.2-36) is valid for Newtonian fluid only, because for a non-Newtonian fluid, the hydraulic conductivity of a capillary tube is not proportional to the square of the radius. Based on Equation (6.2-32), the Burdine (1953) model needs to be rewritten as:

$$K_r = \frac{K}{K_{sat}} = S_e^2 \frac{\int_0^{S_e} P_c^{-(1+\frac{1}{n})} dS_e}{\int_0^1 P_c^{-(1+\frac{1}{n})} dS_e} \tag{6.2-37}$$

Combining Equations (6.2-34) and (6.2-37) yields:

$$K_r = \left(\frac{P_c}{P_d}\right)^{-(\frac{1}{n}+1+3\lambda)} \tag{6.2-38}$$

and

$$K_r = S_e^{3+\frac{1+\frac{1}{n}}{\lambda}} \tag{6.2-39}$$

In deriving Equations (6.2-38) and (6.2-39), we assumed that pore geometry does not change with saturation or capillary pressure. The hydraulic conductivity change is purely a function of changes in saturation. In reality, clay swells (or shrinks) with changes in saturation. In this case, the relative conductivity is given by:

$$K_r^* = \frac{K}{K_{ref}} = (\frac{K_r}{K_{ref,r}})(\frac{K_{sat}}{K_{ref,sat}}) = \left(\frac{P_c P_{ref,d}}{P_d P_{ref,c}}\right)^{-\left(\frac{1}{n}+1+3\lambda\right)} (\frac{K_{sat}}{K_{ref,sat}}) \tag{6.2-40}$$

The subscript *ref* refers to the reference case in which measurements are available. For mechanically deforming media, it is convenient to define relative hydraulic conductivity respective to a reference case. In this case, relative conductivity can be larger than one. Also, in (6.2-40), we assumed, for simplicity, that pore-size distribution (or parameter λ) remains unchanged during swelling/shrinkage.

Based on the principle of Leverett (1941) scaling, relative changes in pore size can be approximately characterized by those in porosity ϕ. By definition of air entry value P_d and using (6.2-32), we have

$$\frac{P_{ref,d}}{P_d} = \frac{\phi}{\phi_{ref}} \tag{6.2-41}$$

$$\frac{K_{sat}}{K_{ref,sat}} = \left(\frac{\phi}{\phi_{ref}}\right)^{(1+\frac{1}{n})\alpha} \tag{6.2-42}$$

where parameter $\alpha > 1$ accounts for the fact that the porosity ratio may underestimate the corresponding size ratio for those well-connected pores that determine the hydraulic conductivity. Dixon et al. (1999) showed that $\alpha > 2.3$ for some saturated clay materials within a Darcian-flow regime.

Combining (6.2-40), (6.2-41), and (6.2-42), we obtain:

$$K_r^* = \left(\frac{P_c}{P_{ref,c}}\right)^{-\left(\frac{1}{n}+1+3\lambda\right)} \left(\frac{\phi}{\phi_{ref}}\right)^{\lambda-1\left(1+\frac{1}{n}\right)-3\lambda} \qquad (6.2\text{-}43)$$

In the right-hand side of (6.2-43), the first and second terms represent conductivity changes resulting from changes in capillary pressure and swelling (shrinkage), respectively. The second term needs to be determined by measurements or estimated using geomechanical simulators. Equations (6.2-33), (6.2-34), and (6.2-43) give the constitutive relationships required for modeling unsaturated flow in clay materials. Their validity will be evaluated in the next section by examining their consistency with data.

6.2.2.3 A comparison with experimental observations

As previously indicated, non-Darcian flow is a result of non-Newtonian properties of pore water in clay. However, experimental studies of non-Newtonian flow in porous media are very limited for unsaturated flow conditions. Most recently, Cui et al. (2008) reported the measurement results of unsaturated hydraulic conductivity for a compacted sand-bentonite mixture. To the best of our knowledge, this work provided the first reliable data set of water flux as a function of hydraulic gradient under unsaturated conditions.

The tests of Cui et al. (2008) were conducted under two different conditions: constant volume and free swelling. In this study, we focus on the data for constant-volume conditions only, reasoning that under constant-volume conditions and for a given capillary pressure, hydraulic processes and pore structures are approximately the same at different locations within the soil sample (Cui et al., 2008). Experimental determinations of the flux-gradient relationships required the use of this approximation. Cui et al. (2008) used the instantaneous profile method to determine the unsaturated hydraulic conductivity for infiltration tests of a vertical soil column. The soil column (50 mm in diameter, 250 mm high) was directly compacted in the metallic cylinder (50 mm in inner diameter). The bottom of the test cell was connected to a water source, and the upper end to an air source under atmospheric pressure. Capillary pressures were monitored at several locations along the soil column. Under transient water-flow conditions, vertical distributions of capillary pressure were directly measured as a function of time. The relationship between water content and capillary pressure was independently measured under constant volume conditions. This relationship enables us to estimate vertical distributions of water content from capillary-pressure measurements. Based on these vertical distributions at different times, and on the mass balance at each location within the soil column, one could estimate the water flux at that location as a function of capillary pressure and hydraulic gradient. The details of this instantaneous method can be found in Daniel (1982) and Cui et al. (2008).

Figure 6.2-14 shows measured water flux (data points) as a function of hydraulic gradient under several capillary pressures. Obviously, very strong nonlinear (non-Darcian) behavior emerges at all the different capillary pressures, indicating that Darcy's law will not be valid for the range of hydraulic gradients under consideration. Based on Figure 8 of Cui et al. (2008), the unit of hydraulic gradient in Figure 6.2-14 is kPa/m. This seems to support the notion that non-Darcian flow behavior becomes more significant under unsaturated conditions, because in unsaturated materials, pore water exists as water films or occurs in relatively small pores, and therefore is subject to relatively strong interactions with the clay surface, as previously indicated.
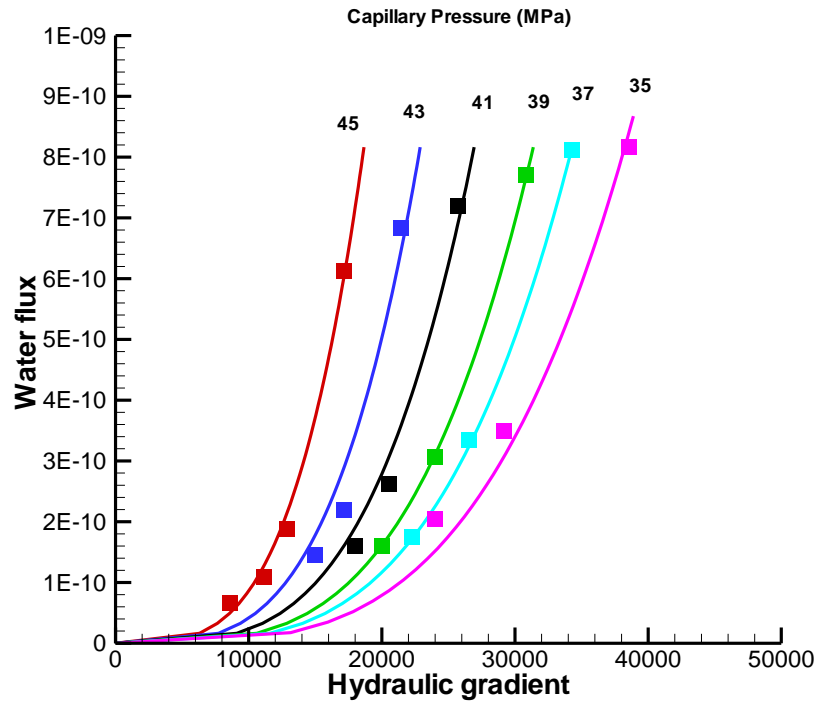
Figure 6.2-14. Comparisons between calculated (solid curves) and measured (data points) water flux as a function of hydraulic gradient for different capillary pressures. The calculation is based on Equation (6.2-33). Data from Cui et al. (2008)

Figure 6.2-14 also matches Equation (6.2-33) (solid lines) with data for the six capillary pressures. The single value of $n = 0.28$ seems to be able to fit all the data points reasonable well. In general, n can be considered a measure of non-Newtonian behavior that may be saturation (or capillary pressure) dependent. Thus, n may also be a function of saturation as well in a general case. At least the data of Cui et al. (2008) support the use of a constant n for different capillary pressures—but more evaluations are needed before the issue can be fully resolved.
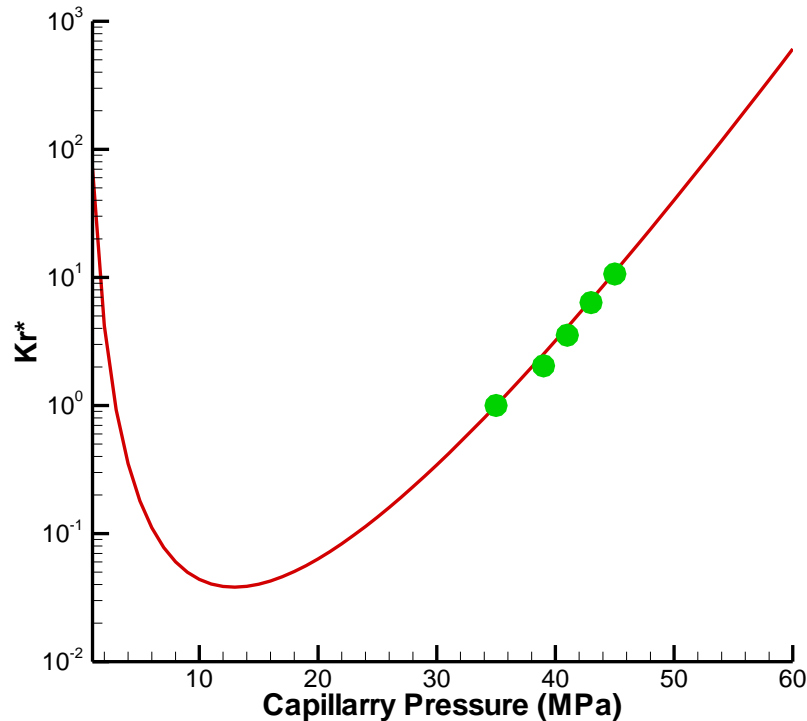
Figure 6.2-15. Calculated unsaturated hydraulic conductivity as a function of capillary pressure. The data points are determined from Figure 6.2-14. The solid curve is calculated from Eqs. (6.2-43) and (6.2-44) as an illustrative case. Data from Cui et al. (2008).

Figure 6.2-15 gives the values for relative hydraulic conductivity defined in Equation (6.2-40). The properties at capillary pressure of 35 MPa are used as reference properties. Thus, $K_r^* = 1$ in Figure 6.2-15 at that capillary pressure. Note that for Darcian unsaturated flow in a rigid material, hydraulic conductivity always decreases with capillary pressure, which is not the case here. This highlights the importance of the fact that conventional unsaturated flow theory and methodology cannot be simply borrowed for clay materials. The data presented in Figure 6.2-15 are from laboratory measurements reported by Cui et al. (2008). They present results for relative hydraulic conductivity versus capillary pressure over a wider range of capillary pressure than shown here. However, because we compute hydraulic conductivity using the non-Darcian constitutive model given in Equation (6.2-33), we require data for flux and hydraulic gradient to establish relative hydraulic conductivity. The flux and hydraulic gradient data provided Cui et al. (2008) needed to compute relative hydraulic conductivity is limited to the capillary pressure range of the data given in Figure 6.2-15.

The observed relationship between hydraulic conductivity and capillary pressure can be explained with Equation (6.2-43), in which the first and second terms represent conductivity changes resulting from changes in capillary pressure and swelling (shrinkage), respectively. For the observed range of capillary pressures, the effects of shrinkage (as a result of increasing capillary pressure) may dominate the changes in K_r^*. To further demonstrate our reasoning, assume that porosity and capillary pressure follow the following relationship:

$$\frac{\phi}{\phi_{ref}} = \exp\left[\beta\left(\frac{P_c}{P_{ref,c}} - 1\right)\right] \qquad (6.2\text{-}44)$$

where β is a fitting factor. The above equation is based on the consideration that the amount of clay swelling seems to be an exponential function of capillary pressure (Pham et al., 2007), and that porosity change is proportional to the amount of swelling (or shrinkage) under constant-volume conditions.

The solid curve in Figure 6.2-15 is calculated using Equations. (22) and (23) with $n = 0.28$ (obtained from Figure 6.2-14), $\lambda = 0.21$ (obtained from Figure 2 of Cui et al., 2008), $\alpha = 3.27$, and $\beta = 1.13$, and matches the observed conductivities. Note that K_r^* decreases with increasing capillary pressure for small levels of capillary pressure and then increases with increasing capillary pressure for higher levels of capillary pressure. This is because for relatively small capillary pressures, the behavior of K_r^* is dominated by the first term on the right-hand side of Equation (6.2-43), and for relatively large capillary pressures, the behavior of K_r^* is dominated by the second term, representing the effects of clay shrinkage. Although the definition of hydraulic conductivity in Cui et al. (2008) is different from ours, their results show similar behavior to the solid curve in Figure 6.2-15. However, it is important to emphasize that the solid curve in the figure should be considered as an illustrative case, because (6.2-44) is based on some rough assumptions. The accurate determination of porosity change under test conditions of Cui et al. (2008) needs to be rigorously based on coupled hydro-mechanical processes. Nevertheless, comparisons between our theoretical results and data (Figures 6.2-14 and 6.2-15) support the usefulness of our approach.

6.2.2.4 Concluding remarks

Unsaturated flow occurs in the engineered barrier and the near field of a clay repository for high-level radioactive waste. Therefore, accurately modeling unsaturated flow in clay materials is important for assessing the performance of a geological repository in isolating the radioactive waste. The non-Darcian behavior of water flow in clay materials has been demonstrated in the literature. While several models have been proposed for dealing with non-Darcian behavior for saturated flow conditions, a systematic study of modeling unsaturated non-Darcian flow is still lacking. Based on the hypothesis that pore water in clay becomes non-Newtonian as a result of water-clay interaction, we proposed constitutive relationships for unsaturated flow, including a relationship between water flux and hydraulic gradient and among capillary pressure, water saturation, and hydraulic conductivity. An evaluation based on a set of laboratory experimental observations supports the usefulness of the proposed relationships. The constitutive model reported here was not incorporated into the simulations presented in Sections 6.3 and 6.4 because it was only recently developed.

6.3   Thm Modeling in Clay/Shale Environment

6.3.1   State of the art

An essential feature that needs to be considered for the long-term safety of a clay repository is the disturbed-rock zone (DRZ) near the repository, and its hydromechanical and geochemical evolution with time. The creation of a DRZ is expected for all man-made openings in geologic formations. Macro- and microfracturing, and in general the rearrangement of rock structures that will occur in this zone, leads to drastic increases in flow permeability through the fractures and cracks induced by excavation, ventilation, and other operational factors. The implications of such high permeability and its time evolution under various repository scenarios need to be evaluated as part of a waste repository safety assessment. Various issues, such as processes creating fractures in the DRZ, the degree of permeability increase, and the potential for sealing or healing (with permeability reduction) in the zone, need to be carefully evaluated.

As reviewed by Tsang et al. (2005), the DRZ evolution is closely related to specific stages of repository development: the excavation stage, the open drift stage, the early closure stage (including resaturation and heating phases), and the late closure stage (including cooling and self-sealing phases). In this research, the stability and associated DRZ mode of the surrounding indurated clay (Opalinus Clay) in the open drift stage are the main concerns. In the open drift stage, the desaturated zone close to the walls of a deep underground repository, excavated into clay rock, could have a detrimental impact on its performance (Ghorbani, et al., 2009; Bock et al., 2010).

Experimental evidence has shown that the process of disaggregation of DRZ could be expected to start as a consequence of seasonal variations in tunnel ventilation (Bock et al., 2010). Desiccation cracks would occur if soil shrinkage was constrained or the induced surface tensile stress exceeded the bonding strength of grains. The presence of cracks in clay significantly modifies the transport processes that occur in the clay profile. For example, in the context of the ventilation experiment at the Mont Terri URL (Mayor et al., 2007; Bock et al., 2010), significant fluctuations in capillary pressure were monitored in the DRZ during drying and wetting periods, respectively. Ventilation of underground openings, particularly if low-humidity air has direct access onto the tunnel wall rock, can cause a desaturation of DRZ rock and transportation of the pore water towards the excavated surface, where it evaporates. For the Opalinus Clay rocks, the desaturation zone in the DRZ rock may be expanded over a depth of no more than a certain distance (about 2 to 4 m) from the tunnel wall, which would have an effect on the short-term and long-term stability of tunnels. Clay is a highly complex material, with cracking behavior governed by a considerable number of factors (e.g., mineral composition, temperature, relative humidity, layer thickness and size, surface plant cover). The essential mechanism of damage and dynamics of DRZ propagation is still not well understood, although in recent years much attention has been paid to the damage phenomenon induced by shrinkage in clay by researchers. While considerable progress has been made in hydromechanical (HM) modeling in the DRZ, some important issues remain unsolved.

One is the mechanical anisotropy and related damage mode. The extension of the desaturated zone parallel to the bedding plane is usually larger than that perpendicular to the bedding plane, due to the high permeability parallel to the bedding in clay rocks and the small Young's modulus perpendicular to the bedding plane, which leads to large displacement under isotropic stress conditions. This could be one of the reasons for breakout after excavation in clay rock. The creation and development of a DRZ is a coupled mechanical-hydraulic process. The former is dominated by the redistribution of the stress around an opening due to mechanical unloading. DRZ development, however, is dominated by hydraulic de-/resaturation due to the ventilation of the opening. This process is also closely related with the rock permeability dependent on damage evolution (Tsang, et al., 2005; Shao et al., 2008).

Variation in the strength and deformability of rocks with increasing/decreasing water content should be further studied. It is commonly accepted that water has a detrimental effect on the mechanical behavior of rock. This has led to a number of investigations on the influence of water content on rock mechanical properties. These investigations have been conducted for a wide variety of rock types, tensile strength, compressive strength (with uniaxial, triaxial or point load), and modulus of elasticity (Towner, 1987; Causarano, 1993; Panayiotopoulos, 1996; Kouakou and Morel, 2009; Erdal et al., 2010). All laboratory observations suggest that adsorbed pore water is a key factor dominating the thermo-hydromechanical properties and processes in indurated clays and a small increase in the water content may lead to a marked reduction in strength and deformability. While most of the previous studies have mainly concentrated on experimental tests, systematic investigations are necessary to identify governing mechanisms, to develop robust constitutive models and related numerical routines, and to quantify precisely the THM behavior of indurated clays under the relevant conditions expected in practical engineering (Zhang et al., 2007).

The stress-strain relationship is fundamental for modeling mechanical deformation and the associated coupled processes in porous and fractured rocks. Laboratory testing indicated that the stress–strain behavior of Opalinus Clay was highly nonlinear, with low stiffness at low stress levels. This is an important aspect of the material's behavior that is not adequately captured by conventional elasto-plastic analyses (Bobet et al., 1998; Corkum and Martin, 2007a, 2007b). A phenomenologically based model, generally called a stress-dependent modulus (SDM), was developed based on observations from field and laboratory studies by Corkum and Martin (2007a). Liu et al. (2009) (see also Section 6.2.1) proposed a more rigorous relationship. The new relationship has satisfactorily represented a number of experimental observations. However, prior to this report, the relationship of Liu et al. (2009) has not yet been used in modeling coupled HM process in clay under field conditions. As the Opalinus Clay is unloaded around an underground opening, the zones with lower stress level come into being, which could correspond to the non-linear behavior of Opalinus Clay. Therefore it's necessary to incorporate the relationship into a coupled-process simulator and use it to find how the non-linear behavior of Opalinus Clay affects the DRZ around the underground opening.

The goal of this study is to use numerical tools to investigate the short-term rock-mass deformation and pore pressure around an underground excavation in Opalinus Clay. The processes of water evaporation, volume shrinkage/swelling, DRZ initiation and propagation are numerically monitored during the entire drying period. The relationships between shrinkage effect, anisotropic properties, and the stress-dependent deformability of clay and DRZ extent are also discussed.

6.3.2   Technical Approach

6.3.2.1   Modeling methodology

The earliest developments of TOUGH-FLAC at the Lawrence Berkeley National Laboratory (LBNL) were presented in Rutqvist et al. (2002) and Rutqvist and Tsang (2003). The simulator has since been applied to studying coupled geomechanical processes under multiphase flow conditions for a wide range of applications, including radioactive waste disposal, CO_2 sequestration, geothermal energy extraction, naturally occurring CO_2 upwelling with surface deformations, and gas production from hydrate-bearing sediments (Rutqvist, 2011).

These applications have been accompanied by recent exploratory code development. The most significant new development is a revised architecture, enabling a more rigorous and tighter coupling procedure with improved computational efficiency. This enhancement was made possible by linking FLAC3D to the newly released TOUGH+ code for analyzing the geomechanical performance of hydrate-bearing sediments and unsaturated soil (Rutqvist et al., 2011). One great advantage of this approach to coupled-processes modeling is that both TOUGH2 and FLAC3D are being continuously developed and widely used, and therefore contain many constitutive and equation-of-state modules that can be readily applied to a wide range of scientific and engineering problems.

The stress-strain relationship is fundamental for modeling mechanical deformation and the associated coupled processes in porous and fractured rock. To capture the constitutive behavior of Opalinus Clay, the theoretical relationship represented by Equation (6.3-1), proposed by Liu et al. (2009) for elastic deformation, was implemented into the TOUGH-FLAC code:

$$K = \begin{cases} \dfrac{1}{\dfrac{\gamma_e}{K_e} + \dfrac{\gamma_t}{K_t}\exp\left(-\dfrac{\sigma_m}{K_t}\right)} & \sigma_m > 0 \\[4em] \dfrac{\gamma_e}{K_e} & \sigma_m \le 0 \end{cases} \qquad (6.3\text{-}1)$$

where K is bulk modulus, K_e and K_t refer to bulk moduli for the hard and soft part, respectively, the parameters γ_e and γ_t are volumetric portion of the hard and soft part under unstressed condition (Liu et al., 2009), and σ_m is mean stress, equal to $(\sigma_1 + \sigma_2 + \sigma_3)/3$. At present, the effects of stress anisotropy, discussed in Section 6.2.1, is not considered in the model and will be incorporated into our future studies.

During drying, the volume of an aggregate in Opalinus Clay decreases, resulting in the formation of shrinkage cracks and surface subsidence. Upon rewetting, the aggregate regains water and swells, cracks close, and the soil surface returns to its original position. The evaluation of the swelling–shrinkage potential of expansive clays is very important. In this study, the Opalinus Clay (rock matrix) surrounding the underground opening becomes practically fully saturated with ventilation. The clay matrix is assumed to behave with a volumetric swelling/shrinkage, and a corresponding stress that depends on the changes in water saturation, ΔS_l, is considered. The incremental swelling/shrinkage stress is calculated according to:

$$\Delta\sigma_s' = 3K\Delta S_l \beta_s \qquad (6.3\text{-}2)$$

where σ_s' is the induced swelling stress (an effective stress), K is the bulk modulus, and β_s is a moisture swelling coefficient. Based on the laboratory tests related to the shrinkage/swelling features of Opalinus Clay (Montes-Hernandez, et al., 2003; Zhang et al., 2008a), it was found that β_s is not a constant, but rather varies with saturation, as shown in Figure 6.3-1. In this study, we assumed that the evolution of β_s conforms to the law formulated by Equation (6.3-3). The direct dependence of the stress variable on suction and saturation degree bears the following coupling: drying, which corresponds to suction increases, will cause an increase in effective stress and therefore shrinkage of the solid matrix. In contrast, wetting is the origin of swelling:

$$\beta_s = \begin{cases} -0.0017 Ln(\Delta S_l) + 0.0219 & \Delta S_l > 0 \\ 0.016 e^{3.2112 \cdot \Delta S_l} & \Delta S_l < 0 \end{cases} \tag{6.3-3}$$
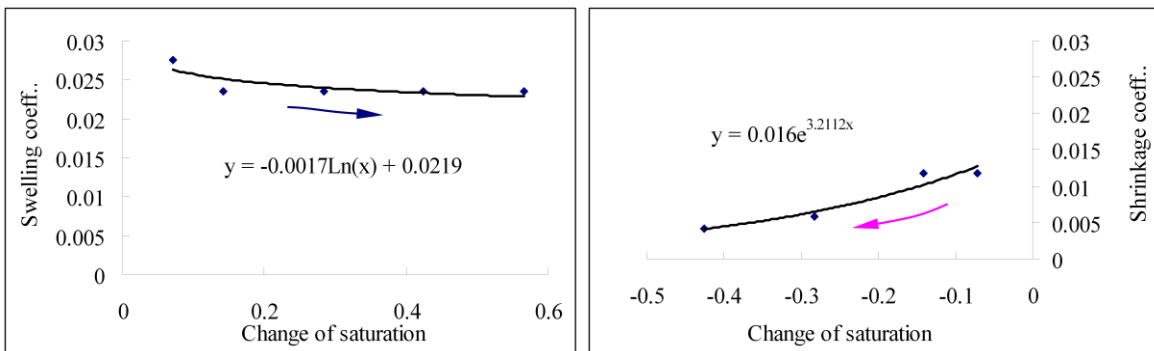
Figure 6.3-1. Swelling/shrinkage coefficient variation with the change in saturation

By changing the water content, the clay rocks exhibit significant variations in strength and deformability (Pham et al., 2007; Zhang et al., 2008a; Erguler and Ulusay, 2009). In order to account for such changes and variations in mechanical parameters in the numerical simulation, the following expressions are incorporated into the TOUGH-FLAC routine:

$$C = 10.0 e^{-0.07 w} \tag{6.3-4}$$

$$\sigma_t = 3.0 e^{-0.07 w} \tag{6.3-5}$$

where C and σ_t are the cohesion and tensile strength of clay, respectively, w is the water content, $w = (\phi/(1-\phi)) \cdot (\rho_l / \rho_m) \cdot S_l$ (ϕ is the porosity of clay, ρ_l is the density of fluid (water), and ρ_m is the density of the clay matrix).

To consider the influence of stress on porosity and permeability, we employed the following equation to represent the porosity of rock matrix (Liu et al., 2009):

$$\phi = (\phi_0 - \gamma_t)(1 - C_e \sigma') + \gamma_t \exp\left(-\frac{\sigma'}{K_t}\right) \tag{6.3-6}$$

174

where ϕ_0 is porosity at zero stress, and C_e is the compressibility for the hard fraction of pore volume.

Once porosity is known, the permeability of a rock matrix can be estimated based on the relationship between permeability and porosity. The relationship between permeability and porosity is a key constitutive equation for modeling subsurface fluid flow and is fundamental to the quantification of a range of geological processes. Based on the analysis of a huge universe of experimental clay-rock data, Yang and Aplin (2010) pointed out that much of the permeability range observed at a given porosity could be explained by variation in lithology. Using clay content as the quantitative lithology descriptor, they proposed that permeability is a function of porosity and clay content:

$$K = \exp(-69.59 - 26.79 F_c + 44.07 F_c^{0.5} + (-53.61 - 80.03 F_c + 13278 F_c^{0.5}) \cdot e$$
$$+ (86.61 + 81.91 F_c - 16361 F_c^{0.5}) \cdot e^{0.5}) \tag{6.3-7}$$

where F_c is the clay content, $e = \phi/(1-\phi)$. In this study, Equation (6.3-7) is employed to represent the permeability of rock matrix.

6.3.2.2.   Model geometry

Among underground openings with different cross-sectional shapes, the o U-shaped cross-sectional opening is the most common form of tunnel. In this study, we construct a numerical model with a geometry containing one U-shaped tunnel and consisting of about 1,452 zones and 3,002 grid points. The configuration of the tunnel, located in the central part of the model, is shown in Figure 6.3-2. To minimize the boundary effect on the areas of interest in the model while limiting the number of model elements to a reasonable size, some simplifications with regard to model size and boundary conditions were selected. Referring to the previous studies on tunnels in Opalinus Clay (Corkum and Martin, 2007b; Shao et al., 2008; Popp et al., 2008), in our study, the Z-axis was set as vertical in the model, while the horizontal Y- and X-axes were aligned parallel and perpendicular to the tunnel, respectively. The dimensions of the model were 60 m in the X-direction, 1 m in the Y-direction, and 60 m in the Z-direction. In simulation, the variations in deformation, saturation, porosity, and permeability in the rock matrix around the tunnel opening were monitored. The figuration of monitoring key points is marked in Figure 6.3-3.
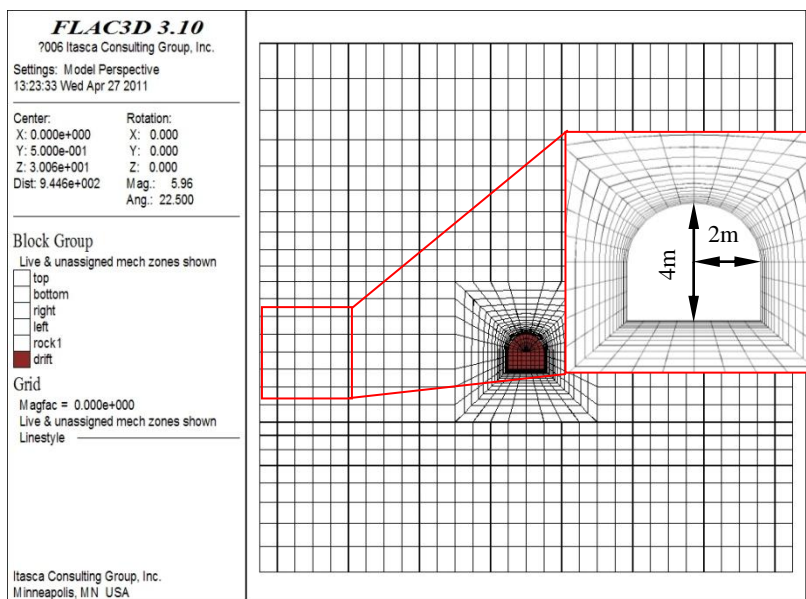
Figure 6.3-2. Numerical model and grid mesh
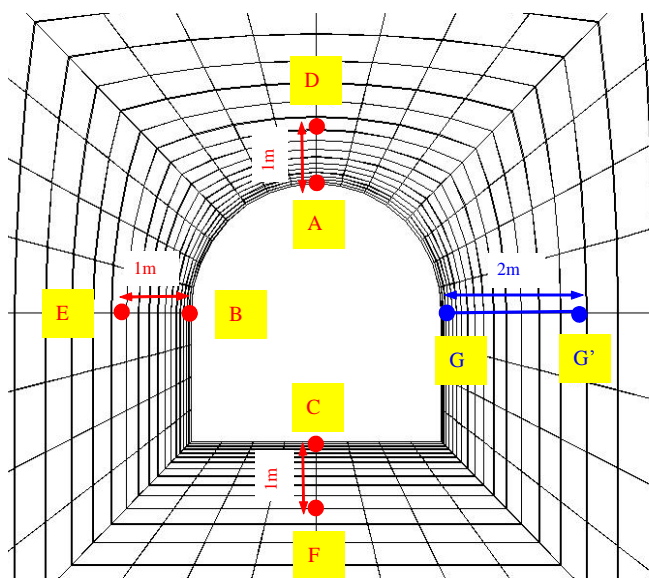
Figure 6.3-3. Location of key points for monitoring parameter variation in numerical simulation

In TOUGH2, the numerical grid is defined by finite volume elements, with one node located within the element boundaries connected to neighboring elements' center nodes. In a FLAC3D numerical grid, on the other hand, corner nodes define the element shapes. The geometry and element numbering should be consistent in TOUGH2 and FLAC3D for a particular problem. In this study, a special FISH routine in FLAC3D has been programmed to produce a mesh consistent with the meshes employed in TOUGH2. The FISH routine can directly translate FLAC3D meshes into TOUGH2 meshes. With the numerical

grids defined, input files are prepared for TOUGH and FLAC3D, including material properties, boundary conditions, and initial conditions.

6.3.2.3. Boundary conditions and material parameters

An accurate assessment of the *in situ* stress conditions is important for analyzing underground excavations. These boundary conditions are particularly significant when the engineering objective is to understand the rock-mass response to excavation. Based on laboratory and field investigations (Bossart et al., 2002; Shao et al., 2008), we assumed that the tunnel is located about 200 m underneath the ground surface. The general mechanical boundary conditions are employed: a total stress of $\sigma_z = 5MPa$, representing the stress induced by the overlying rock layers, is applied on the top boundary of the model, and normal displacements are constrained on the right and left side and bottom boundary.

With regard to ventilation, one of the most important factors influencing the formation of the DRZ may be the humidity level after the excavation of the tunnel. In this study, the grid elements representing the empty tunnel (air) are modeled as an equivalent porous medium. The tunnel is set up with relative humidity at the entrance; then the tunnel is modeled explicitly and the ventilation is imposed with a pressure boundary at the tunnel wall (i.e., the air humidity). The unsaturated zones within the excavation are characterized by relatively high capillary pressures. The corresponding capillary pressure is given by Kelvin's equation incorporating humidity (Edlefsen and Anderson, 1943):

$$P_c = \ln(RH) \cdot \rho_w \frac{RT}{M_w} \tag{6.3-8}$$

where *RH* is the relative humidity, ρ_w is the density of water, *R* is the gas constant, *T* is the absolute temperature (degree Kelvin), and M_w is the molecular weight of water. Field test results show that the humidity of the air within the tunnel varies with the season. In this study, an average relative humidity of 80%, which amounts to a capillary suction pressure of about 30 MPa, is selected (Mayer et al., 2007; Shao et al., 2008). Based on the capillary pressure curve for Opalinus Clay (Zhang et al., 2008b), as shown in Figure 6.3-4, the Opalinus Clay surrounding the tunnel is desaturated.
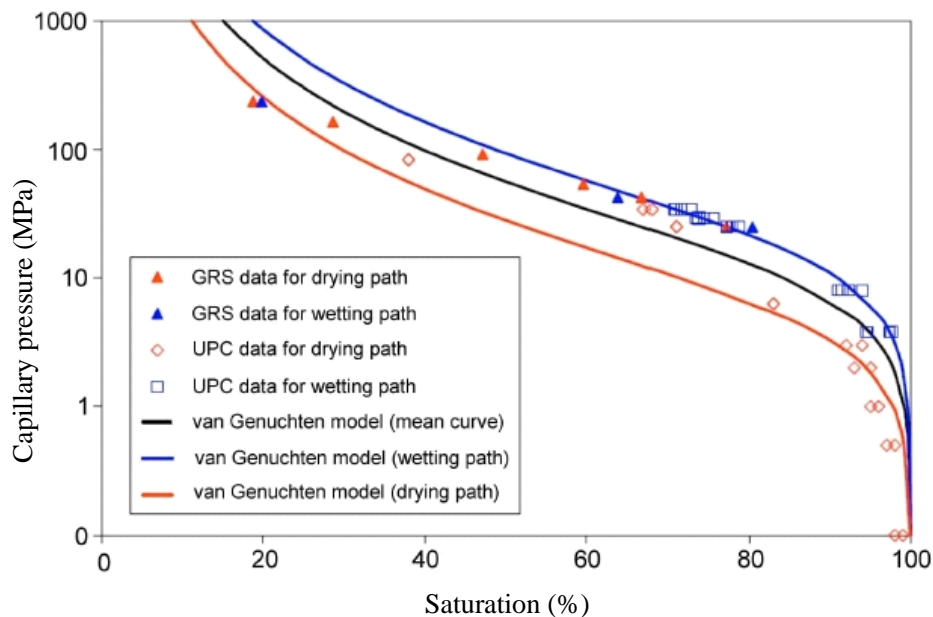
Figure 6.3-4. Relationship between capillary pressure and water saturation (modified from Zhang et al., 2008b)

The underground water table is assumed to be located 100 m underneath the ground surface, and the rock matrix under the water table is saturated initially. A pore pressure, $P_l = 1000000 + (60 - Z)\rho_l g$ Pa (where Z is height), is directly incorporated into the numerical model. The outer boundary condition is an imposed constant pressure. Since the ventilation-induced desaturation and associated mechanical responses are the main concerns in this study, the temperature at the tunnel opening and within the rock matrix are assumed to be a constant, 20°C.

The calculations were performed with a full hydromechanical coupling. For two-phase flow, the van Genuchten function fitted by laboratory data was used. The relationship describing the capillary pressure as a function of the saturation and the water relative permeability as a function of the saturation are given by the van Genuchten (1980) formulation, which has been used successfully to fit the data from the gas injection tests in the Opalinus Clay (Mayer et al., 2007). The capillary pressure as a function of the saturation is given by:

$$P_c = \frac{1}{\alpha} \cdot (S_{ec}^{n/1-n} - 1)^{1/n} \qquad (6.3\text{-}9)$$

$$S_{ec} = \frac{S_w - S_{wr}}{S_{w\max} - S_{wr}} \qquad (6.3\text{-}10)$$

The residual saturation S_{wr} is the minimum value of the water saturation achievable when gas is displacing water. The parameter n is a pore-size distribution index (shape factor), and the parameter $1/\alpha$ is a ''pseudo air entry pressure'' for the gas phase.

Using the integral formulation of Mualem (1976), the relative permeability of the water kr,w (van Genuchten, 1980) is defined as follows:

$$k_{r,w} = S_{ec}^{1/2} \cdot (1 - (1 - S_{ec}^{n/n-1})^{(n-1)/n})^2 \qquad (6.3\text{-}11)$$

The gas phase relative permeability $k_{r,g}$ is arbitrarily chosen as (Pruess et al., 1999):

$$k_{r,g} = (1 - S_e)^2 \cdot (1 - S_e^2) \qquad (6.3\text{-}12)$$

$$S_e = \frac{S_w - S_{wr}}{1 - S_{gr} - S_{wr}} \qquad (6.3\text{-}13)$$

S_{gr} is the residual gas saturation. Note that the non-Darcian flow behavior, discussed in Section 6.2.2, is not considered here yet, but will be incorporated within future studies.

The key flow parameters for Opalinus Clay are presented in Table 6.3-1. The values originate from the extensive laboratory and *in situ* tests performed on the Opalinus Clay (Mayer et al., 2007; Zhang et al., 2008b). The rock matrix (Opalinus Clay) is assumed to be initially almost saturated ($S_l = 0.999$). Comparisons between simulations with 100% and 99% saturation have shown that the impact of the initial saturation of the rock on the simulation results is negligible.

Table 6.3-1. Flow parameters for the Opalinus Clay

Parameter	Value	Unit
Porosity	0.16	
Intrinsic permeability	$1.0e^{-20}$	m^2
Initial liquid saturation	1.0	
Residual water saturation	0.7%	
Residual gas saturation	1%	
Van Genuchten $1/\alpha$ (Gas entry pressure)	$1.0e^7$	Pa
Van Genuchten m = (n-1)/n	0.3	

For the mechanical part, a pore-elastic-plastic model was used. There are thirteen basic constitutive models provided in FLAC3D, arranged into null, elastic, and plastic model groups. The commonly used criteria for plastic model groups are those of Mohr-Coulomb, Hoek and Brown, Cam-Clay, and so on, among which the Mohr-Coulomb model is the conventional one used to represent failure in soils and rocks (Itasca Consulting Group Inc. 2001). For the Mohr-Coulomb model, the main argument against the criterion is that its linear approximation is often not a good enough fit to the experimental strength data, and it cannot adequately characterize the fracture patterns of tensile regions. The arguments in favor of the Mohr-Coulomb criterion are its widespread use in geomechanics, its relative simplicity, its implementation in all pertinent geotechnical computer codes, and its proven suitability for indurated argillaceous media. In this study, the evolution of damage, failure, and post-failure behavior is described by the Mohr-Coulomb criterion (shear yield function) with tension cut-off (tension yield function). The position of a stress point on this envelope is controlled by a nonassociated flow rule for shear failure and an associated rule for tension failure. Note that the application of the Mohr-Coulomb criterion for clay rock needs to be further evaluated, and more advanced constitutive models are under development for clay rock.

Opalinus Clay is of interest not only as a host formation for radioactive waste repositories, but also as a formation through which new transportation tunnels have been constructed. For this reason, a number of investigations have been conducted, and the corresponding results of these studies have been published. The mechanical parameters employed in this study range from laboratory experiments to field research (Corkum et al., 2007b; Zhang et al., 2008b; Bock, et al., 2010; Jobmann et al., 2010). The strength and deformation properties of Opalinus Clay at dried state are shown in Table 6.3-2.

Table 6.3-2. Mechanical parameters for the Opalinus Clay

Parameter	Value	Unit
Bulk density(ρ_m)	2450	kg/m^3
Young's modulus(E)	7	GPa
Poisson's ratio(v)	0.3	
Tensional strength(σ_t)	3	MPa
Cohesion(C)	10	MPa
Friction(φ)	25	°
Clay content (F_c)	60%	

6.3.3   Technical Results

In this section, three cases were considered. In Case 1, the calculation was carried out with the application of an elasto-plastic approach, assuming that the rock matrix was isotropic. In Case 2, the calculation was carried out exclusively with the application of an elastic approach, assuming that the rock matrix was transversely isotropic and the elastic deformation is described by conventional Hooke's law. In Case 3, the calculation was carried out with the application of an elasto-plastic approach incorporated into the constitutive model proposed by Liu et al. (2009), assuming that the rock matrix was isotropic. In each of the cases above, simulation was first conducted for excavation of a U-shaped tunnel opening before simulation of the ventilation effect was conducted.

6.3.3.1 Results for Case 1

Saturation evolution: Particularly if low-humidity air has direct access into the tunnel wall rock, ventilation of underground openings can cause a desaturation of the near-field rock and transportation of the pore water towards the excavated surface, where it evaporates. One of the most important numerical results in this case is the calculated saturation (S_l) around the tunnel opening. Figure 6.3-5 illustrates the progressive change in saturation at two different elapsed times. In this simulation, the initial saturation of liquid (water) is 99.9% within the rock matrix. During the ventilation period, a desaturation zone gradually penetrates into rock matrix although the evolution is slow due to the low permeability of Opalinus Clay. At the start of day 3, the saturation is less than 99% only within a small ring around the tunnel wall (thickness ≈ 9 cm). Even after the end of 3 years, the model indicates that the rock matrix S_l values are lower than 95% only within a small zone around the tunnel walls (thickness ≈ 40cm). These results agree well with the monitoring data for a ventilation test on Opalinus Clay (Mayor et al., 2007).
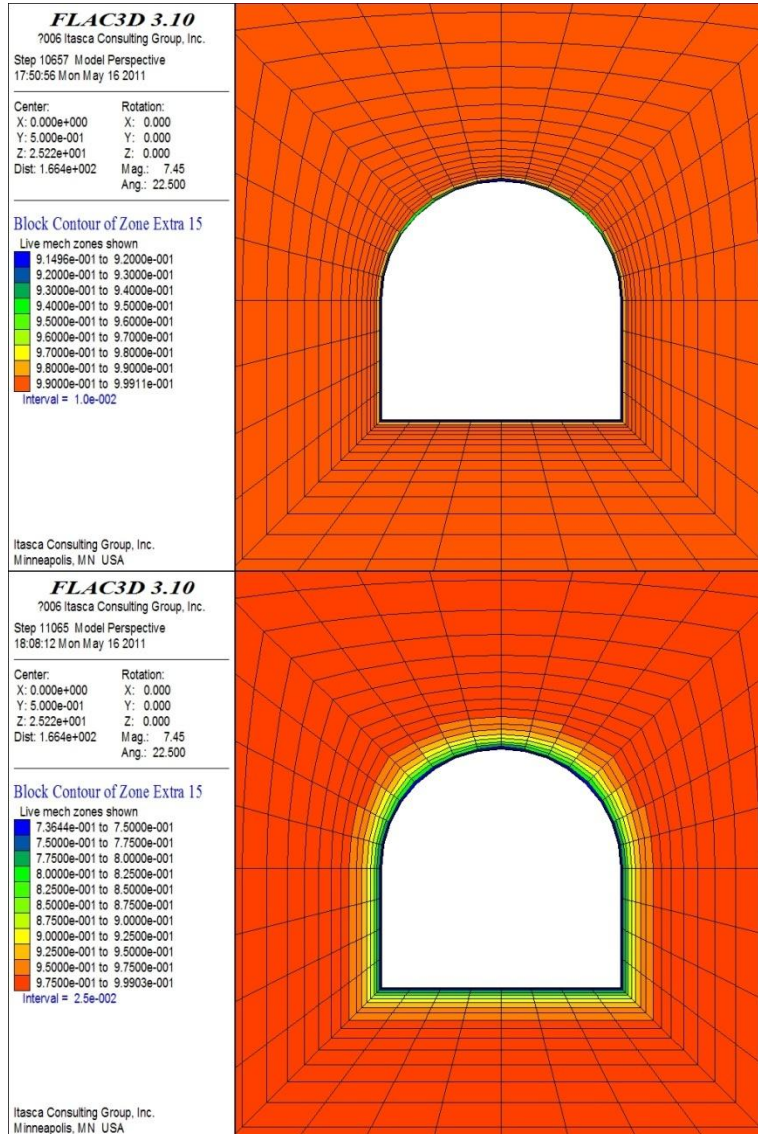
Figure 6.3-5. Saturation evolution with time

Figure 6.3-6 plots the saturation evolution in the typical elements along line G-G' in Figure 6.3-3. The maximum decrease for saturation in the vicinity of the tunnel walls is about 26%. According to the model calculations, the decreasing rate of the saturation is relatively fast, and there is sharply decreasing saturation within the vicinity of the tunnel walls in the early days of ventilation. Although the variation in saturation smoothes after 30 days of ventilation, the desaturation continues to move into the rock matrix, until finally the rock-matrix S_l values are lower than 99% in a relatively wide zone around the tunnel walls (thickness = 1m), which indicate that the shrinkage effect induced by desaturation will continue as ventilation continues.
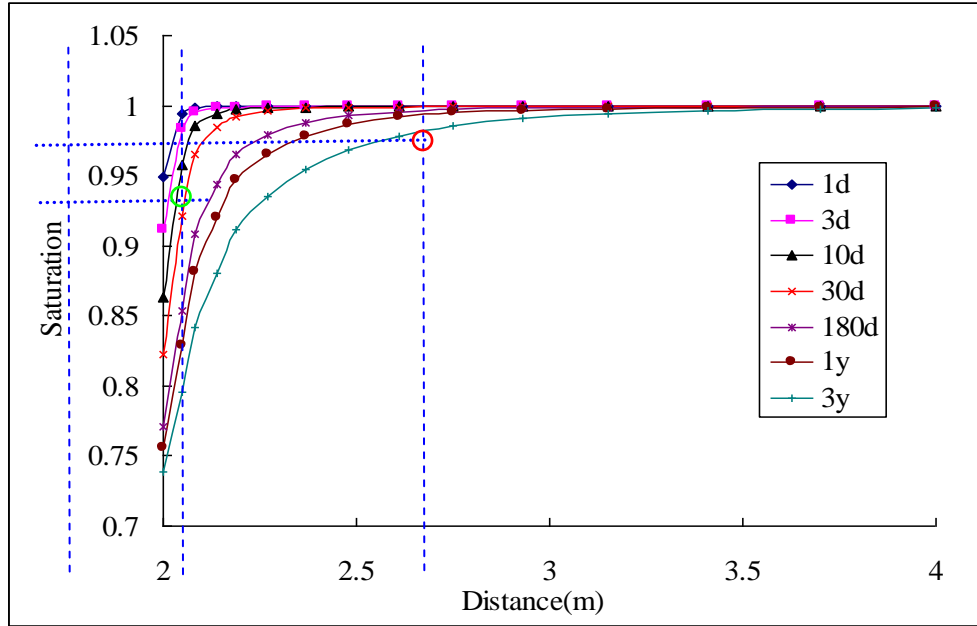
Figure 6.3-6. Saturation variation in the surrounding rock mass along line G-G'

Pore water pressure: *F*igure 6.3-7 presents the calculated pore-water pressure field around the tunnel surface. In the early days of ventilation, the pore pressure shows a very sharp gradient within the zone adjacent to the tunnel surface. Just on the tunnel wall, the calculated value of gas pressure P_g is 0.1 MPa, equal to the atmospheric pressure in the tunnel. At the end of three years of ventilation, the calculated liquid pressure (P_l) isolines around the tunnel show that negative values for P_l develop up to a distance of ~1.8 m from the tunnel walls, indicating that a the rock remains under suction up to such a distance. Beyond 1.8 m from the tunnel walls in rock matrix, the pore pressure evolution shows a tendency to stabilize at a constant value.
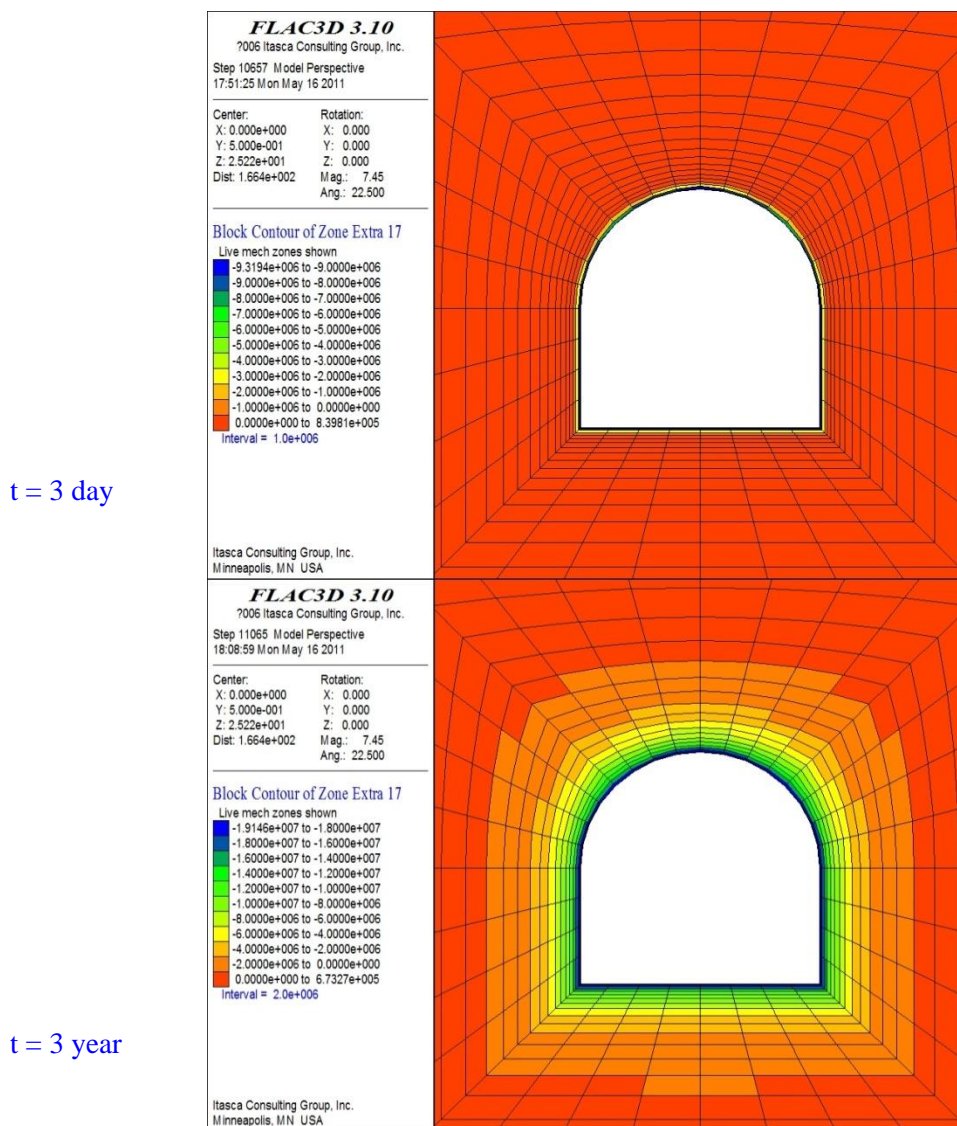
Figure 6.3-7. Pore pressure evolution with time

Stress and displacement: Any excavation of an underground opening (borehole, tunnel, gallery, shaft, etc.) causes a redistribution of the geologic stress field in the vicinity of the new opening. The degree of redistribution could be quite significant, depending on numerous factors such as structure of the host rock, size, shape, and orientation of the excavation, geological stress field, and even the manner in which the excavation was technically carried out. The results based on numerical analysis with TOUGH-FLAC are given in Figure 6.3-8 and 6.3-9 (where the positive sign represents tensile stress and the negative sign represents compressive stress). It is shown that the drying-out process influences the stress distribution as a result of the shrinkage effect. Stress concentration is generally increased at and near the excavation surface where the saturation is relative low. Away from the tunnel walls, the degree of stress concentration gradually lessens until the outer boundary is reached. In the early days of ventilation, the tensile stress zone is mainly found in the roof and floor, while the compressive stress is concentrated near

the vertical sides of the tunnel. During ventilation, the tensile-stress concentrated zone induced by shrinkage gradually moves into the rock matrix. About 10 days after ventilation, evident tensile-stress concentration can be observed within the zone near the vertical sides of the tunnel. Finally, after 3 years, the average value of maximal tensile stress within the zone 0.5 m away from the tunnel surface reaches 2.0 MPa, which has exceeded the tensile strength of the rock matrix.
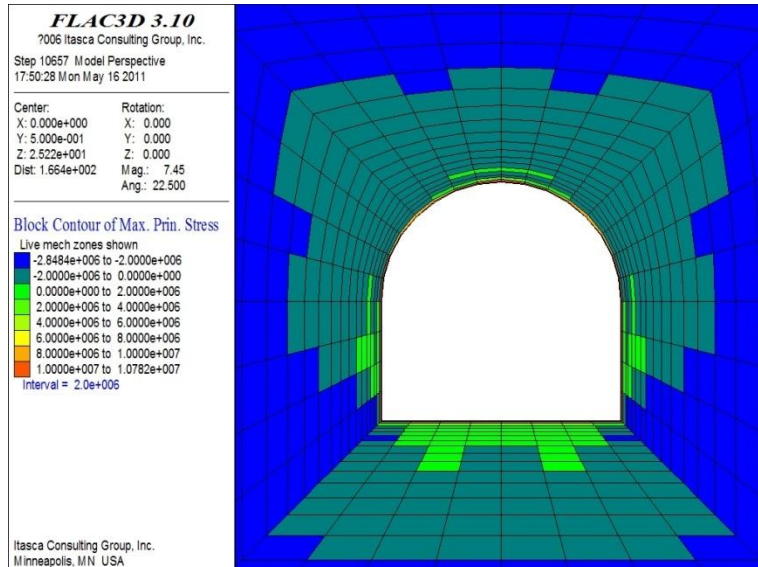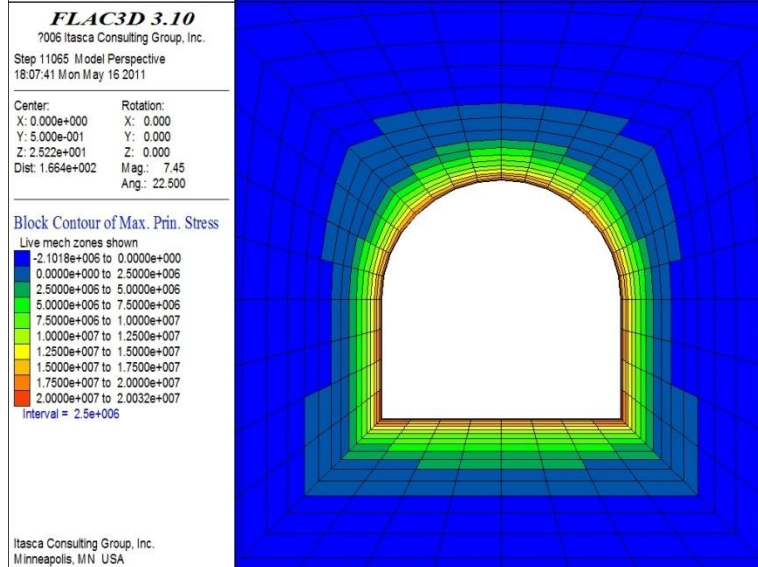
Figure 6.3-8. Maximum principal stress distribution
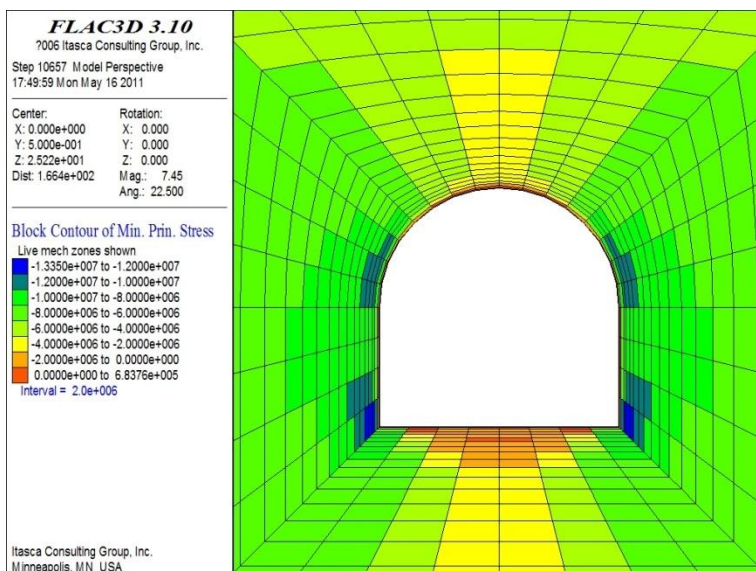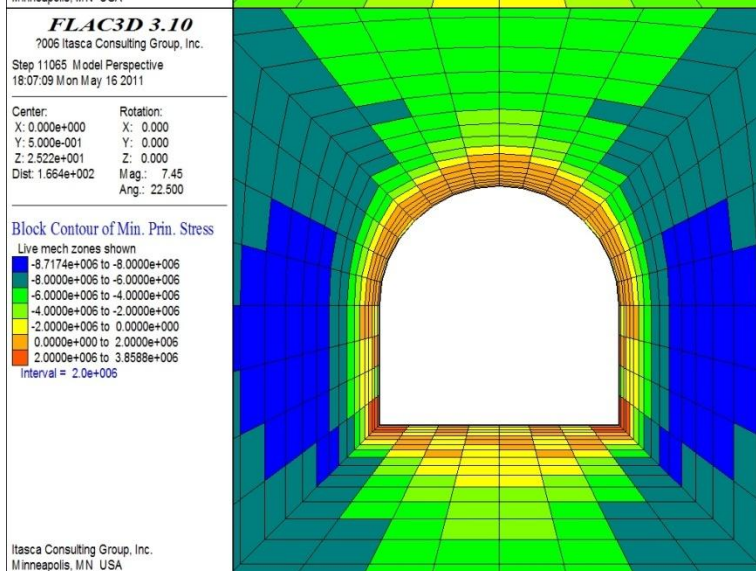
Figure 6.3-9. Minimum principal stress distribution

In general, the deformations measured at points A, B, C, D, E, and F around the tunnel show unique signatures, with all deformations trending towards the tunnel or towards the rock matrix (As shown in Figure 6.3-10, a displacement is designated as positive when the deformation motion is in a positive direction along the axis and negative for a displacement that is in a negative direction along the axis.). Due to the shrinkage of the Opalinus Clay during ventilation, the deformations at points A, B, and C along the tunnel boundary show a slight movement towards the rock matrix and gradually reach a convergence after one year. The deformations at points D, E, and F show an opposite tendency at points A, B, and C with respect to a transition between negative and positive movement. At points D, E, and F, deformation convergence was not observed even after three years. Although the maximal displacement is not beyond 3 mm, it can also be pointed out that the mechanical coupling has an evident effect on the macroscopic behavior of the rock matrix during the desaturation process.

Numerical results show that the evolution of stress is a result of two sources: (1) shrinkage stress caused by saturation changes, and (2) poroelastic stress from average pore-pressure changes under unsaturated conditions. The calculated maximal displacement for the corresponding deformation at points A, B, C, D, E and F, is not beyond 1 mm, as shown in Figure 6.3-11. The shrinkage effect on the mechanical response of the underground opening in the open drift stage is remarkable.
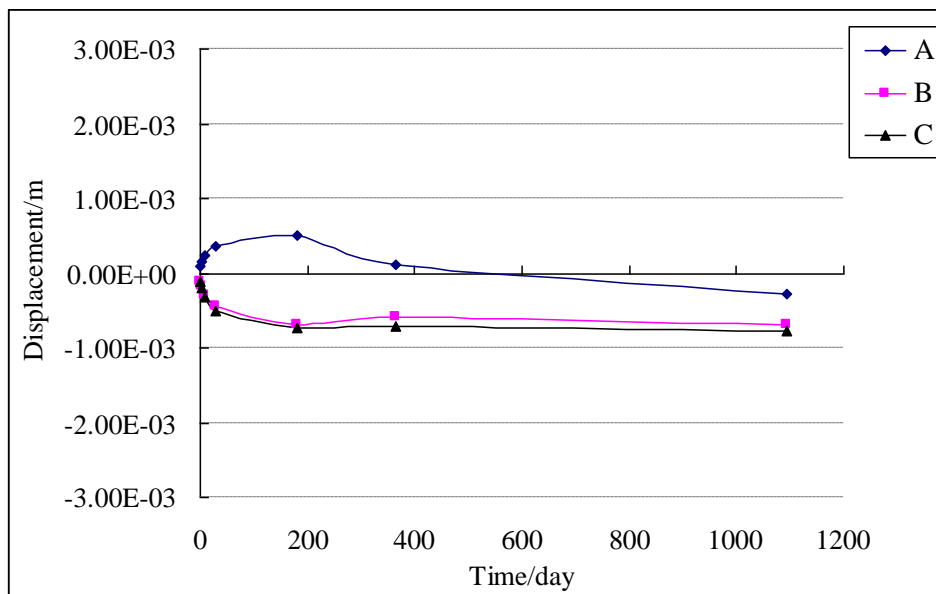
(a) Displacement evolution with time for points A, B, and C, respectively
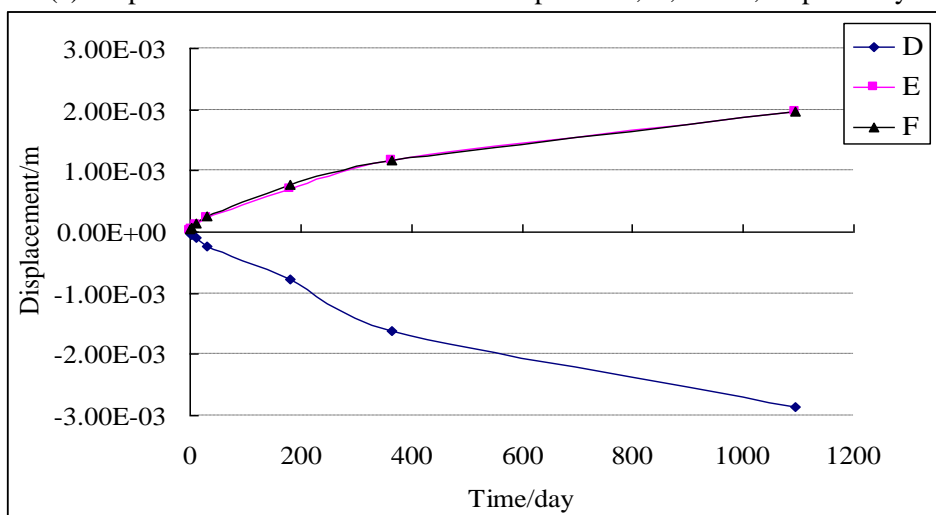
(b) Displacement evolution with time for points D, E, and F, respectively

Figure 6.3-10. Numerically obtained displacement at points A, B, C, D, E and F labeled in Figure 6.3-3.
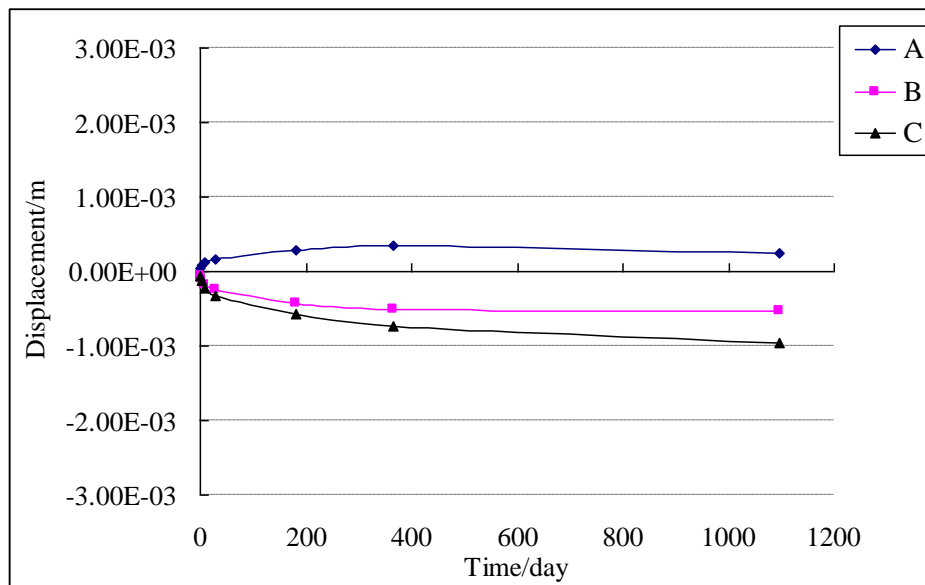
(a) Displacement evolution with time for point A, B and C, respectively
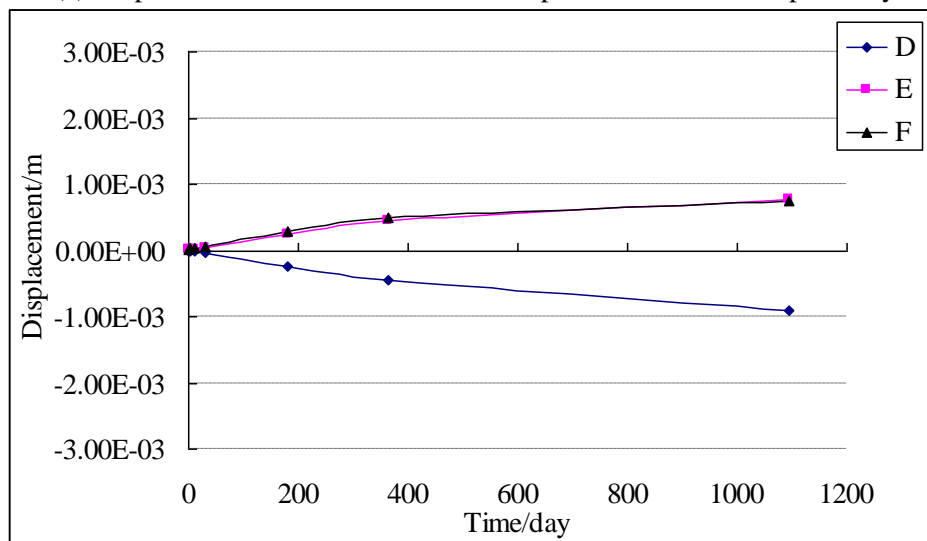
(b) Displacement evolution with time for points D, E, and F, respectively

Figure 6.3-11. Numerically obtained displacement at points A, B, C, D, E and F (the case without considering the shrinkage effect)

With the evolution of stress, changes in porosity and permeability are observed. Figure 6.3-12 plots the porosity and permeability evolution in the typical elements along line G-G'. The results indicate a significant signature of TH-induced change in porosity and permeability; both porosity and permeability first decrease as a result of the compressive stress induced by the overlying rock layers. During ventilation, porosity and permeability gradually increase within the zones adjacent to the tunnel walls, due to tensile stress induced by desaturation. At the end of three years' ventilation, variations in porosity and permeability were limited to a radial distance of about 2.0 m from the tunnel wall.
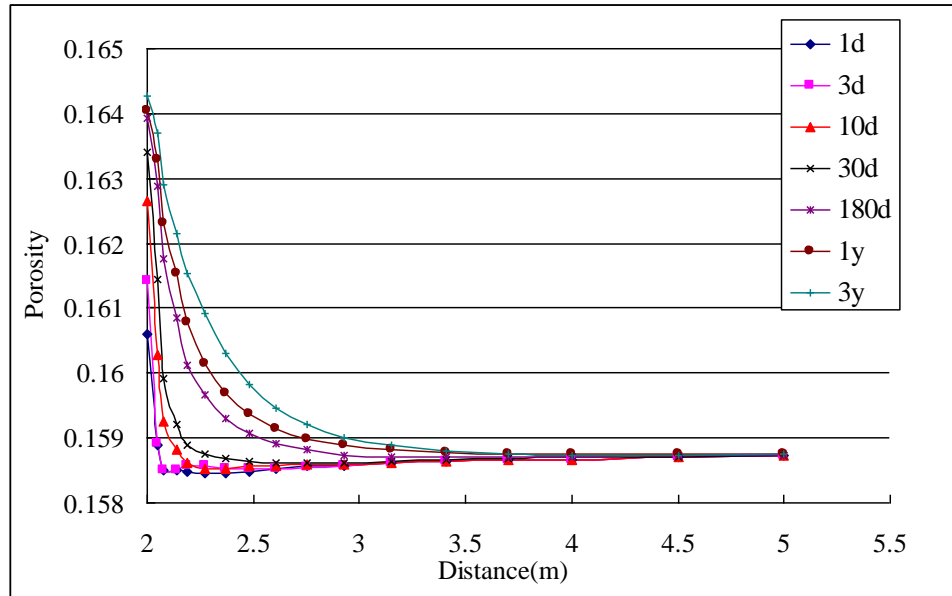
(a) porosity variation
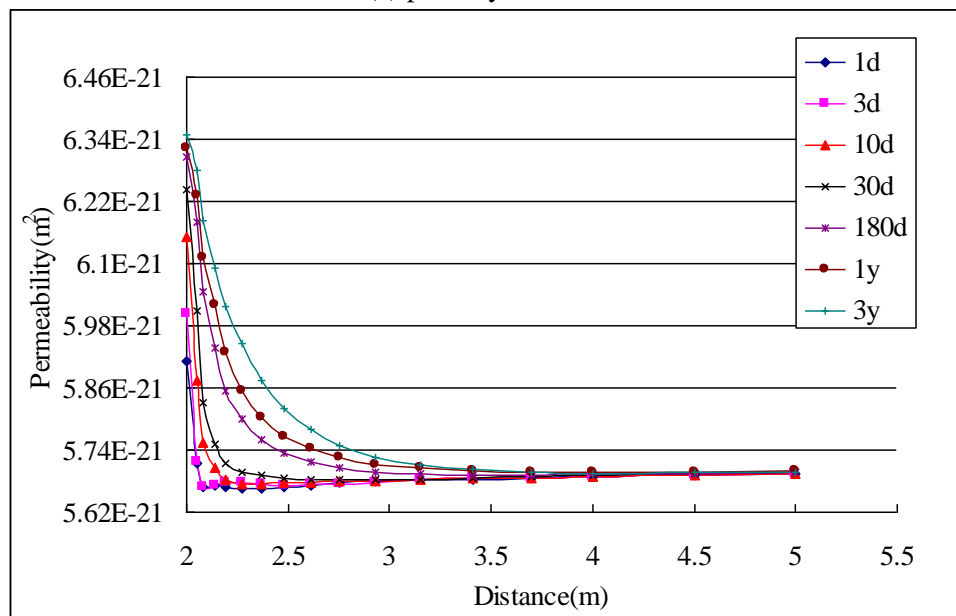
(b) permeability variation

Figure 6.3-12. Porosity and permeability evolution with ventilation

DRZ around tunnel: The DRZ primarily developed in the vicinity of the tunnel surface, as expected. Figure 6.3-13 illustrates the progressive change in the DRZ; the observations are taken at six different ventilation times. In the early days of ventilation, the DRZ growth rate is relatively fast, indicating unstable damage growth, corresponding to the saturation variation and the stress field evolution in the rock matrix. Because shrinkage is the major mechanism of DRZ development, tension is the major form of failure.

During ventilation, the DRZ continues to grow, particularly in the vicinity immediately adjacent to the opening roof and sidewalls (as the DRZ in the floor has expanded quite deeply, as a result of the cross-sectional shape of the tunnel). The extent of the DRZ stays practically constant for relatively long and extreme desaturation periods, despite the suction or pore pressure developed up to a distance of ~2.0 m into the rock matrix. The DRZ extends only about 40 cm from the tunnel surface. Figure 6.3-14 shows the final damage mode for the cases (a) without considering both pore pressure and shrinkage, and (b) considering pore pressure but without shrinkage. It is evident that the creation and development of a DRZ is a coupled mechanical-hydraulic process: with creation dominated by the redistribution of the stress around the tunnel due to mechanical unloading, and with development dominated by hydraulic de-resaturation due to ventilation of the tunnel opening.
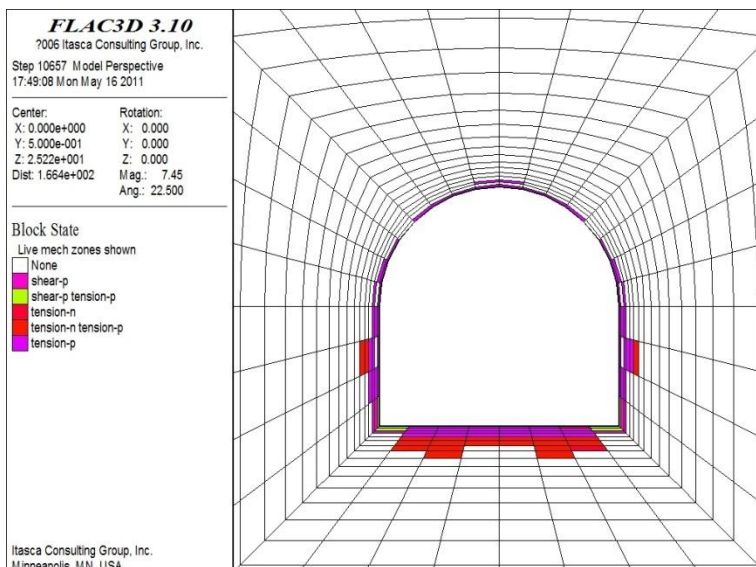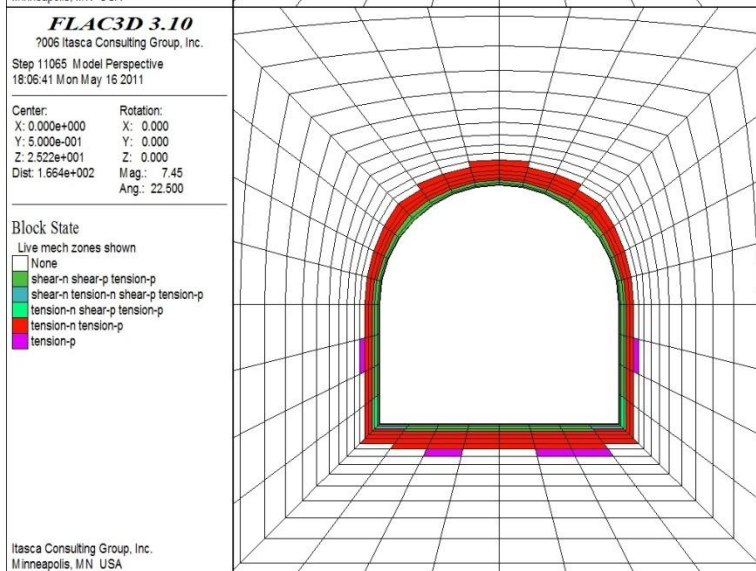
Figure 6.3-13. DRZ (plastic zone) evolution with time
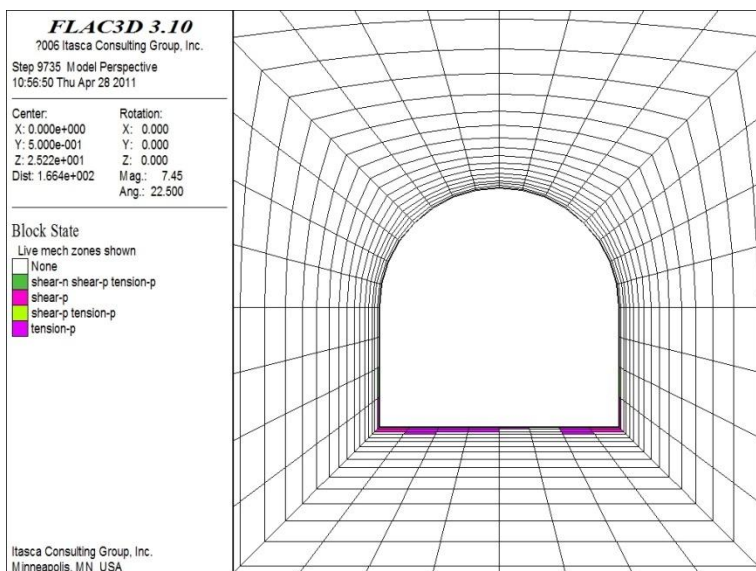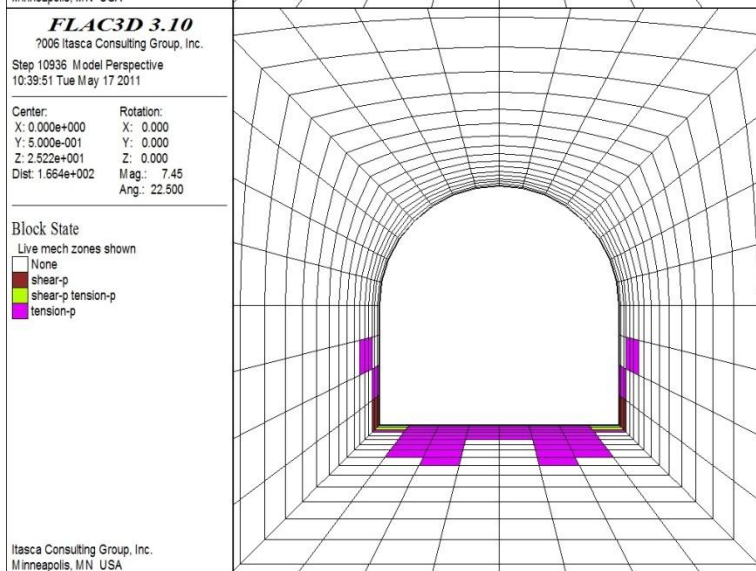
Figure 6.3-14. DRZ (plastic zone) for the cases (a) considering mechanical unloading only, and (b) without considering shrinkage effect

6.3.3.2 Results for Case 2

Bedding in the Opalinus Clay is a prominent geological feature consisting of persistent ubiquitous planes spaced in the millimeter range. This is consequently reflected in the transverse-isotropic nature of the mechanical properties: Young's modulus ranges from 4 GPa perpendicular to bedding to 10 GPa parallel with bedding, which causes the stress redistribution around an underground tunnel to be anisotropic. The interplay of these anisotropic properties and behavior is an open question, one that requires not only model development and study, but also field or laboratory tests to measure such anisotropic effects.

In Case 2, understanding the influence of the bedding planes on the stress distribution and the induced damage map around the tunnel was achieved through a series of numerical simulations. It was decided to

keep the same input parameters as in the model of Case 1, but only consider elastic responses. Two scenarios were modeled to assess the impact of the geological heterogeneities. The first scenario considered a transverse isotropic rock matrix with the isotropic plane inclined at 0° from horizontal. In the second scenario, the bedding anisotropy was represented with the isotropic plane inclined at 90° from horizontal. Given the stiffness properties with respect to bedding orientation, two different deformation properties were considered: Young's modulus of 10 and 4 GPa parallel with and perpendicular to the bedding, respectively. For clarity, only elastic model results are compared in the stress field and deformation plots.

Figure 6.3-15 and 6.3-16 show the developed stress distribution. They clearly demonstrate that the stress distribution depends strongly on the bedding orientation. For the case with horizontal oriented bedding planes (dip=0°), the tensile stress is mainly concentrated within the region adjacent to the side walls of the tunnel, while in the second case, the tensile stress is uniformly distributed around the entire tunnel surface.

(a)

(b)
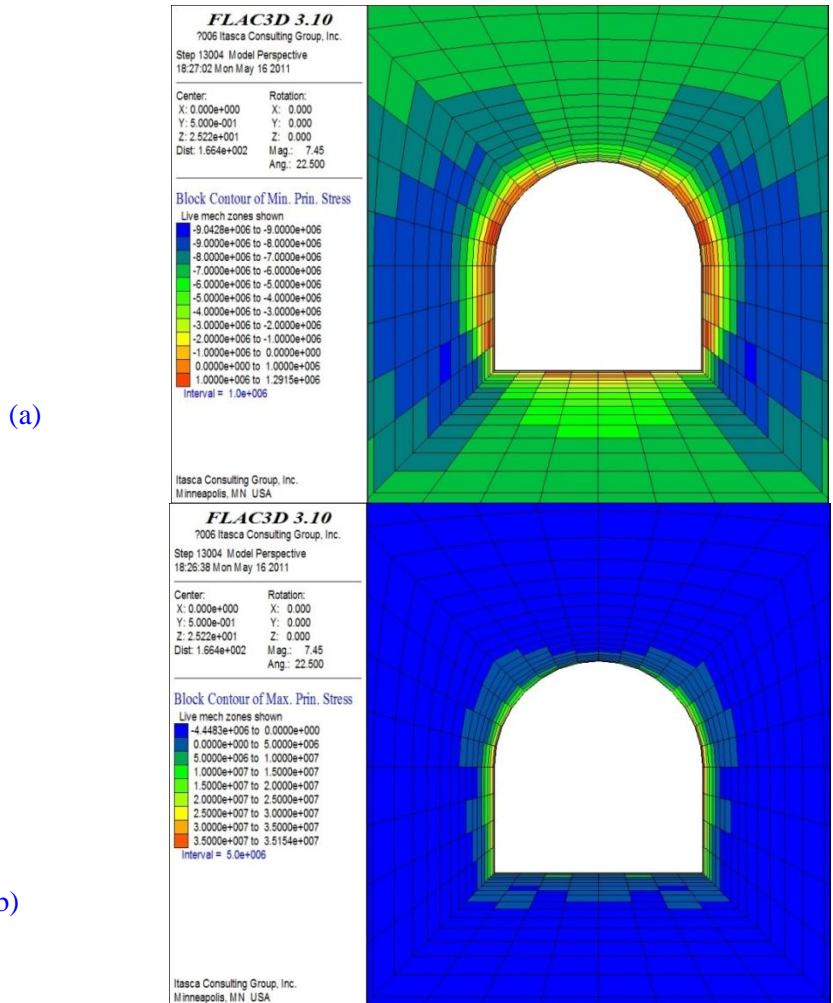
Figure 6.3-15. Stress distribution for the case with horizontal oriented bedding planes (dip=0°)
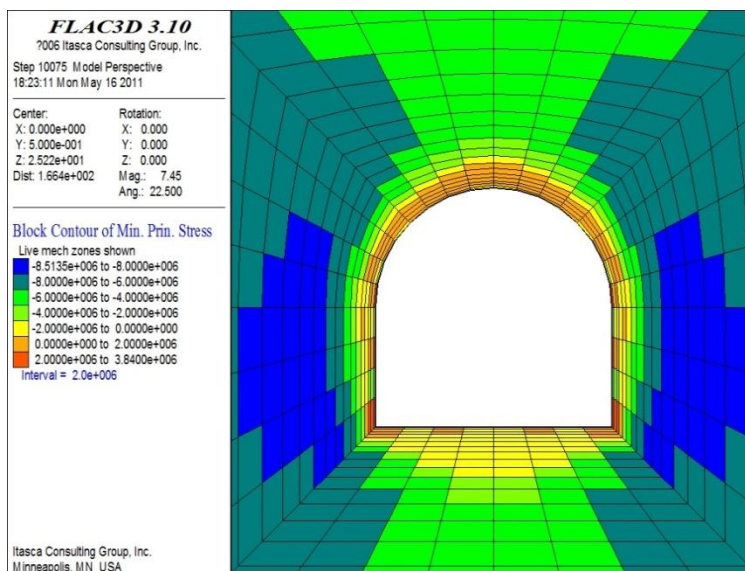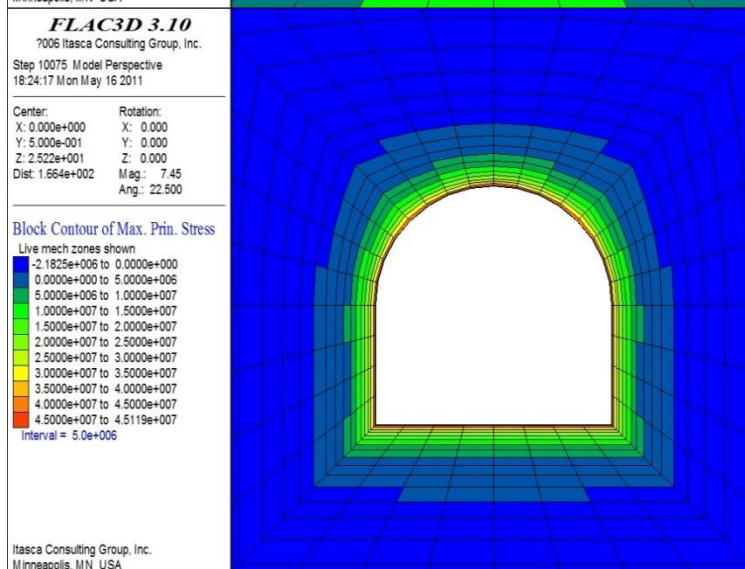
Figure 6.3-16. Stress distribution for the case with vertical oriented bedding planes (dip=90°)

The deformations at points A, B, and C along the tunnel boundary show a slight movement towards the rock matrix, gradually reaching convergence after one year for both cases, as shown in Figure 6.3-17 (a). The deformations at points D, E, and F show an opposite tendency, with a transition between negative and positive movement compared with that at points A, B, and C. Deformation convergence was not observed even after three years, as shown in Figure 6.3-17 (b). Although the general developing trend of deformation is the same, there is an obvious difference in the magnitude, particularly for the displacement in roof and floor zones. The small Young's modulus perpendicular to the bedding plane leads to large displacement under isotropic stress conditions.
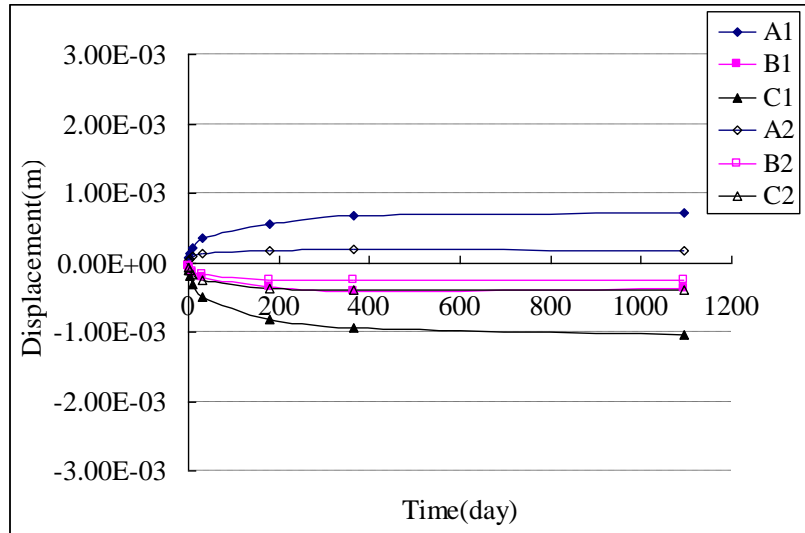
(a)
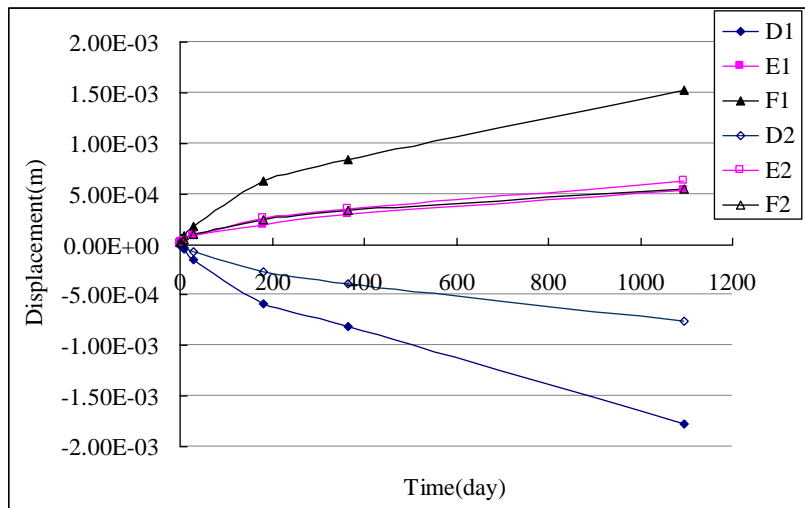
(b)

Figure 6.3-17. Numerically obtained displacement at points A, B, C, D, E, and F

The potential plastic zones (the area enclosed by the red line in Figure 6.3-18), where tensional stress exceeds tensional strength, further depends on the relative orientation of the principal stresses and the stress magnitude within the zones adjacent to the tunnel surface. This is because the zones subjected to tensional stress around the tunnel with parallel bedding planes are obviously smaller than those with perpendicular bedding planes. Only extensional failure is observed at the side walls of the tunnel with horizontal oriented bedding planes, while extensional failure appears symmetrical around the entire tunnel surface for the case with vertical oriented bedding planes. Obviously, the observed failure pattern is caused by the anisotropy of the material parameters, rather than the far field stress.
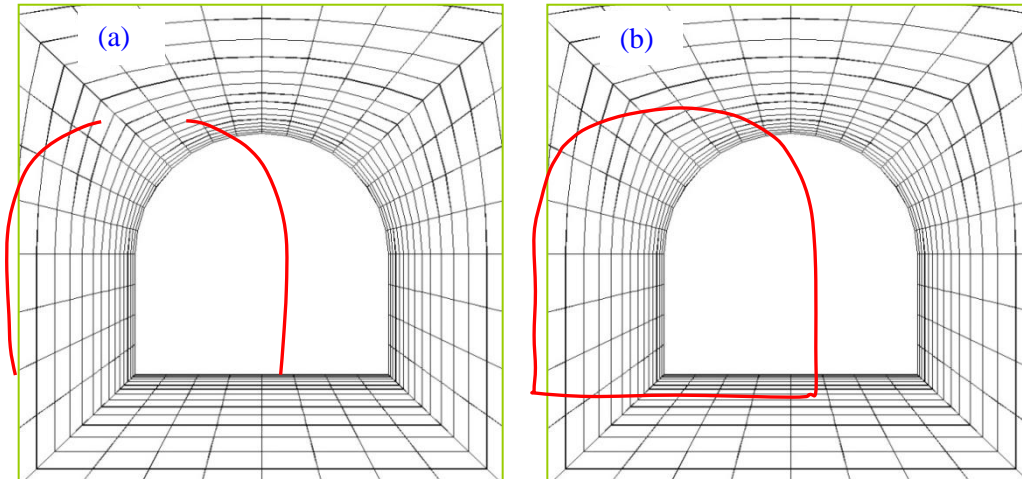
Figure 6.3-18. Numerically obtained potential plastic zones for the cases (a) with the isotropic plane inclined at $0°$ from horizontal, (b) with the isotropic plane inclined at $90°$ from horizontal

6.3.3.3 Results for Case 3

In Case 3, we first validate the model by comparing the stress-strain states in a numerical specimen with available data from the literature (Corkum and Martin, 2007a, 2007b; Liu et al., 2009). Uniaxial tests were numerically performed on the 83 mm diameter core specimen, shown in Figure 6.3-19, with FLAC3D.
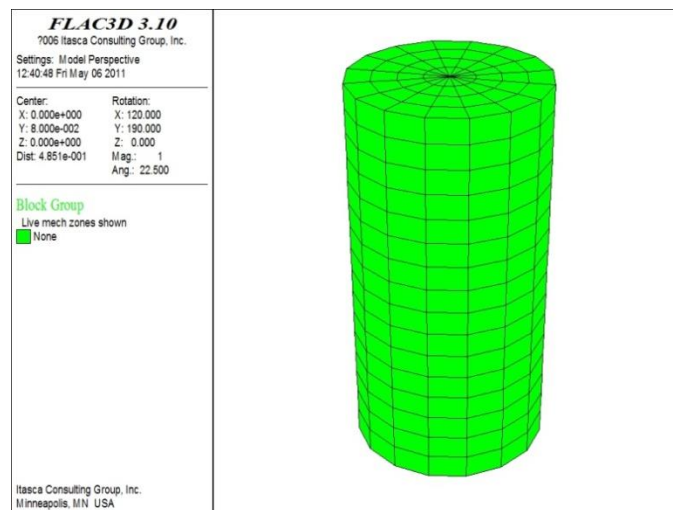
Figure 6.3-19. Numerical specimen for model validation

Stress-strain plots for the three specimens are shown in Figure 6.3-20, indicating a significant low-stiffness, nonlinear response at low stress levels, which indicates that our numerical results are in excellent agreement with the experimental data. Corkum and Martin (2007a) have demonstrated that the mechanical response of Opalinus Clay is unique and reflective of a microstructure dominated by diagenetic bonding and stored latent strain energy. They showed that the low-stress, low-stiffness nonlinear stress–strain response of laboratory samples is the true material behavior. However, it is not fully understood how such nonlinear behavior impacts DRZ evolution around the underground opening. Further analyses are needed to investigate this effect.
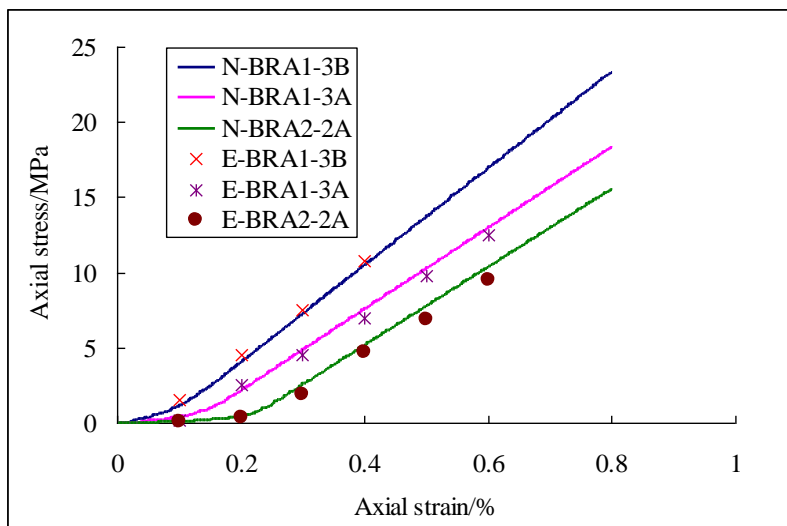
Figure 6.3-20. Comparison between laboratory measurements and values obtained using the numerical method

For the simulation on DRZ features in Case 3, it was decided to keep the same input parameters as in the model of Case 1, but further consider the nonlinear behavior of Opalinus Clay. We compared the numerically obtained (short-term excavation) ventilation-induced mechanical response with that in Case 1. The supplementary parameters are listed in Table 6.3-3.

Table 6.3-3. Supplementary mechanical parameters for Case 3

Parameters	Value	Unit
E_e	3999	MPa
γ_e	0.999	
E_t	1	MPa
γ_t	0.001	

To directly and clearly compare the results of modelling to those in Case 1, the results based on elastic analysis are presented first. This comparison was done using the stress distribution around the tunnel and the deformation variations at points D, E, and F.

After 3 years of ventilation, the final maximum and minimum principal stresses for Case 1 and Case 3 are shown in Figure 6.3-21 and 6.3-22, respectively. Generally, the tensile-stress concentrated zone induced

by shrinkage is located within the region adjacent to the tunnel surface. However there are differences in the stress distribution mode and magnitude. For the case considering nonlinear behavior, the zones with compressive stress evidently increased, particularly near the side walls of the tunnel; the zones with a compressive stress beyond 8 MPa have extended to ~4 m away from the sidewalls of the tunnel.
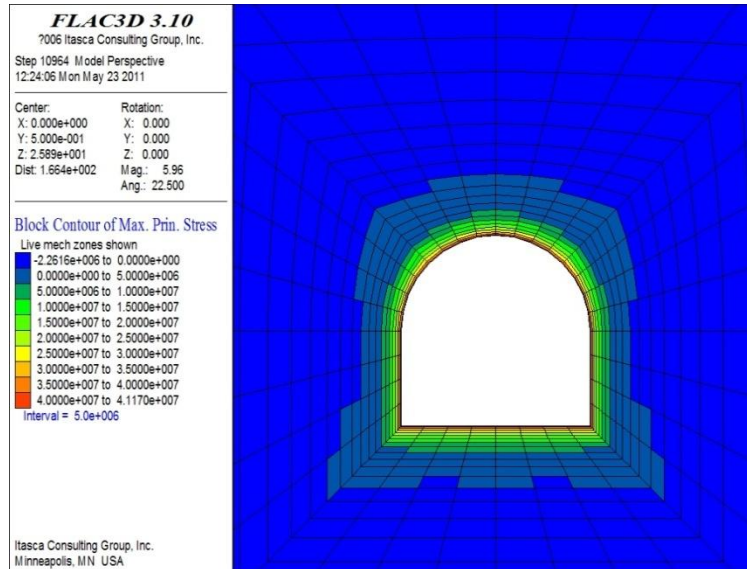
(a)maximum principal stress
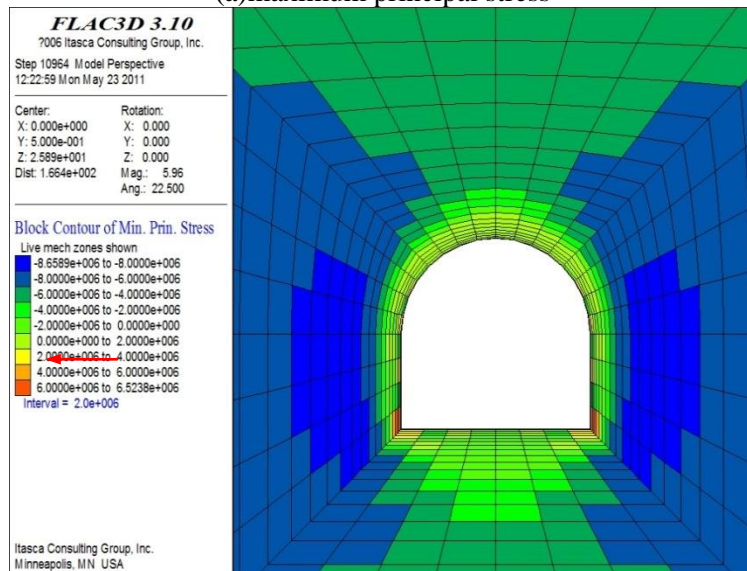
(b)minimum principal stress

Figure 6.3-21. Stress distribution for Case 1 (elastic mode)
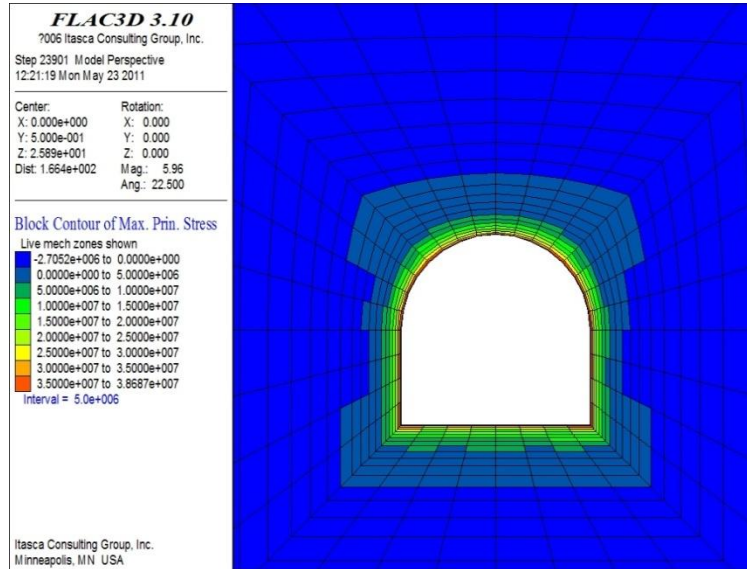
(a)maximum principal stress
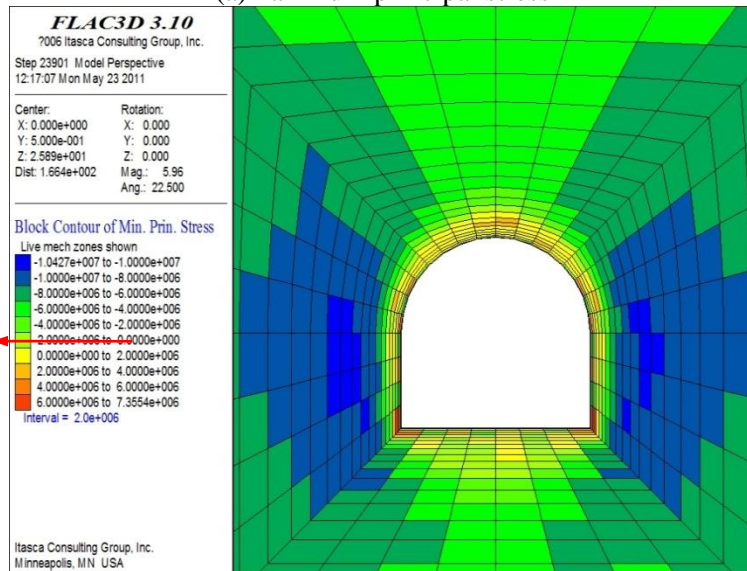
(b)minimum principal stress

Figure 6.3-22. Stress distribution for Case 3 (elastic mode)

Figure 6.3-23 shows the numerically obtained stress variation during the ventilation process. The average values of the compressive stress at point E increased about 1.1 MPa compared with those in Case 1, while the compressive stress at points D and F decreased. For points D and F, the minimum principal stress evolved from a compressive state to a tensional state. Especially at point F, the tensional stress is slightly higher than those in Case 1.

For both cases, the deformations at points D, E, and F show an evident movement towards the tunnel opening, as shown in Figure 6.3-24. Although the general developing trend of deformation is the same, the magnitude is obviously different, particularly for the displacement in roof and floor zones. A relatively large displacement at point F was obtained for Case 3, while the displacements at points D and E are slightly less than those in Case 1.
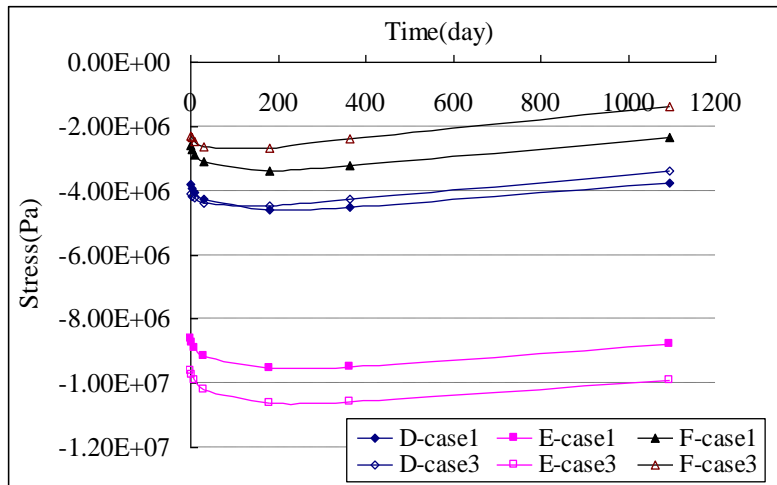
(a) Maximum principal stress evolution with time for point D, E and F, respectively
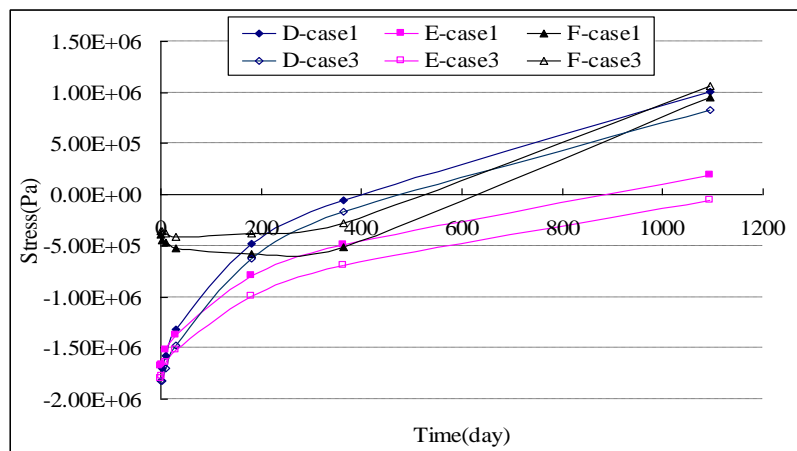
(b) Minimum principal stress evolution with time for point D, E and F, respectively

Figure 6.3-23. Numerically obtained stress at points D, E, and F
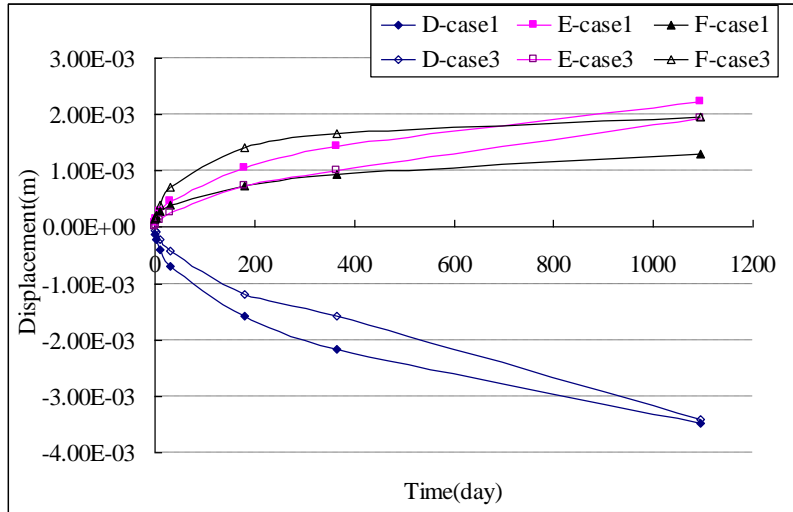
Figure 6-3-24. Numerically obtained displacement at points D, E, and F

As shown in Figure 6.3-25, during the period of ventilation, the variation in porosity and permeability correspond to the evolution of stress. The porosity and permeability gradually increase within the zones adjacent to the tunnel walls, due to tensile stress induced by desaturation. The average values for porosity and permeability at point E are smaller than those in Case 1, while those at point F have evidently increased. The average values for porosity and permeability at point D has changed little, since the variation in stresses at point D was limited.
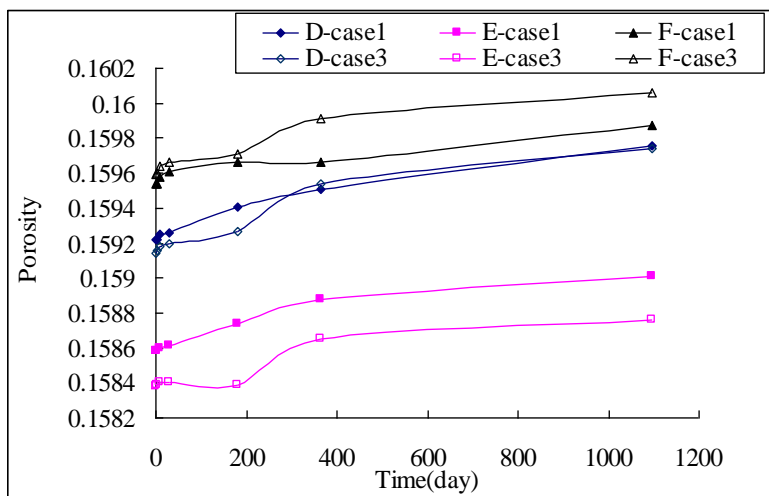
(a) porosity variation
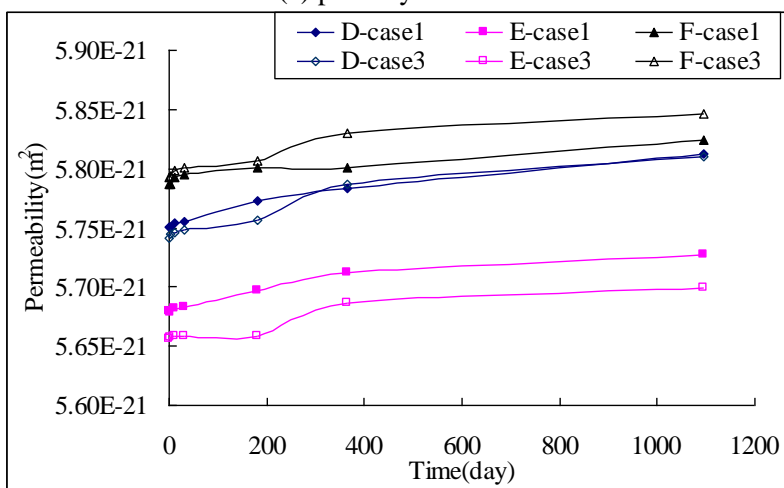
(b) permeability variation

Figure 6.3-25. Porosity and permeability evolution at points D, E, and F

Similarly, the DRZ is mainly developed in the vicinity of the tunnel surface. Figure 6.3-26 illustrates the progressive change DRZ at ventilation times of 3 days and 3 years. Our calculations show that the extent of the DRZ near the tunnel roof decreased slightly, and near the tunnel floor increased slightly as compared with Case 1, and shown in Figure 6.3-13. The DRZ development in this case is dominated by tension failure induced by the hydraulic desaturation due to the ventilation of the tunnel opening. However the employed constitutive law, Equation (6.3-1), in the calculation of this case is the same as the conventional Hooke's law for tensional state, which means that the influence on the DRZ above was obtained by regulating the compressive stress distribution around the tunnel. Nonetheless, based on a comparison of the results, it can be pointed out that the non-linear behavior in the Opalinus Clay has an evident influence on hydromechanical behavior, including stress, displacement, porosity, permeability variation, and DRZ mode around the tunnel.

t = 3 day
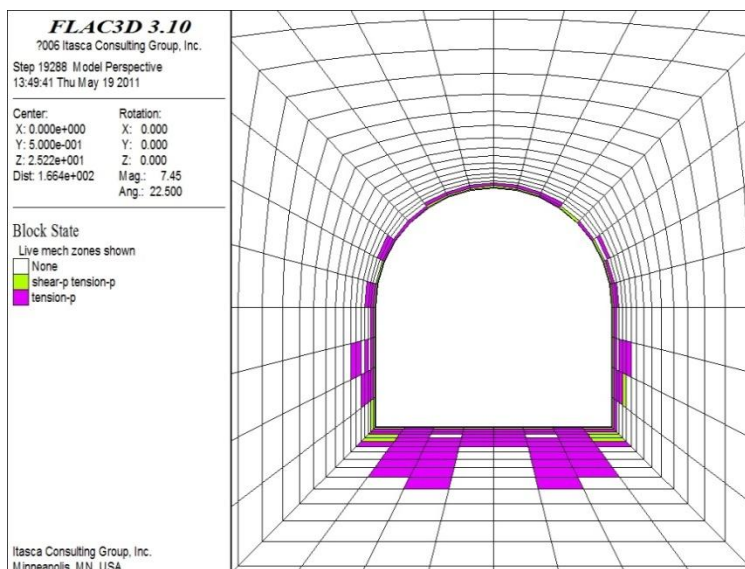
t = 3 year
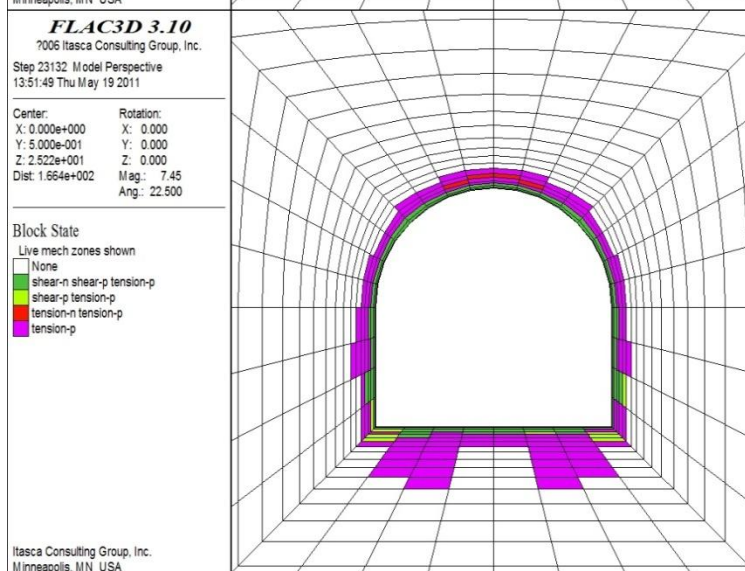
Figure 6.3-26. DRZ mode for Case 3 at time t = 3 days and 3 years

6.3.4. Conclusions

In this study, the near-field coupled HM processes associated with ventilation in a clay repository were investigated with TOUGH-FLAC. In the improved TOUGH-FLAC, a series of relationships reflecting dynamic variations in mechanical parameters are incorporated into the TOUGH-FLAC routine, and a special FISH routine in FLAC3D has been programmed to translate FLAC3D mesh into TOUGH2 meshes, to ensure mesh compatibility between TOUGH2 and FLAC3D.

Numerical simulations indicate that after 3 years of ventilation, the underground tunnel was affected by the ventilation in a narrow zone around the tunnel (thickness less than 40 cm), where the degree of rock saturation was lower than 95%. For the initially saturated Opalinus Clay matrix, the water evaporation

process has three stages: (1) a stage with a rapid desaturation rate, when most of the rock matrix remains saturated and the tunnel surface is dried by air entry suction; (2) a stage with a relatively gentle desaturation rate; and (3) a final, stable stage, in which further ventilation does not result in any more water loss. Correspondingly, tunnel surface damage (DRZ induced by shrinkage stress) generally takes place in three stages: initiation of primary damage; development of subdamage; and then relative stability, with no new damage developing. It is also observed that DRZ development is parallel to the tunnel surface, which is consistent with the desaturation zone development.

DRZ-phenomena are found to be strongly related to the existing lithological rock properties, i.e., rock anisotropy due to the bedding planes. When considering elastic deformation only, we show that the zones subjected to tensional stress around the tunnel with parallel bedding planes are obviously smaller than those with perpendicular bedding planes, and relatively larger displacement occurs in the roof and floor for the tunnel with parallel bedding planes. The potential plastic zones, where tensional stress exceeds tensional strength of rock matrix, depend on the relative orientation of the principal stresses and the stress magnitude within the zones adjacent to the tunnel surface. Only extensional failure is observed at the side walls of the tunnel with horizontally oriented bedding planes (dip=0°), while extensional failure appears symmetrical around the entire tunnel surface for the case with vertically oriented bedding planes (dip=90°).

Experimental tests have shown that the stress–strain curve of Opalinus Clay behaves in a highly nonlinear manner, with low stiffness at low stresses. We have implemented a constitutive model capturing the stress-strain nonlinearity of Opalinus Clay into the TOUGH-FLAC code. The model included both linear and nonlinear components dependent on stress levels, in which the nonlinear component reflected the behavior of Opalinus Clay at low stresses, where most of the deformation around the tunnel occurs. The unloading and ventilation-induced response of Opalinus Clay to tunneling based on numerical modeling was found to be closely related to the nonlinear response of Opalinus Clay observed in laboratory samples. Using our constitutive model, we found a larger radial elastic deformation on the roof and floor of the tunnel, and considerably different stress distributions, porosity-permeability variations, and DRZ modes around the tunnel. By regulating the stress distribution around the tunnel, we found that the mode of damage zones near the tunnel roof and floor showed evident differences with those calculated by the conventional Hooke's law, indicating the importance of incorporating more accurate constitutive models for modeling the coupled processes.

6.4 THC Modeling in a Clay/Shale Environment

6.4.1 State of the art

Clay/shale formations are one of the host rock candidates for radioactive waste disposal throughout the world. These formations have been studied especially extensively in Europe—the Opalinus Clay at Mont Terri (Thury, 2002) and the Callovo–Oxfordian clay at ANDRA's underground research facility, France (Samper et al., 2008; Jougnot et al., 2010). One advantage of emplacing radioactive waste in clay formations is the potential self-sealing capability of clay due to swelling. The self-sealing capability might have particular importance for disturbed rock zones (DRZ). It is therefore necessary to study the changes in swelling properties within clay rock, especially in the near-field area during the disposal of radioactive waste. Because the clay rock is usually in a saturated condition, the swelling-property changes in clay rock are mostly due to the geochemical changes, including (1) changes in ion concentration of the bulk water, which may also change the swelling properties; (2) cation exchange changes in the composition of the water in the interlayer space, and therefore changes in the swelling of the rock and (3)

swelling minerals such as smectite may dissolve (for example, as the pH increases) or precipitate (due to the dissolution of silicates), which subsequently modify the swelling of the rock.

The studies of geochemically induced change in clay swelling properties are relatively limited. Thury (2002) reported that in contact with water, decompressed Opalinus Clay swells; the swelling varies when the swelling tests are carried out with various water types (deionized water, low mineralized water, synthetic pore water and KCl solution). The maximum measured swelling heave (obtained with deionized water) perpendicular to bedding is 9%, and is up to 10 times greater than that parallel to bedding. More highly mineralized waters result in smaller swelling heaves by 2% only. Wakim et al. (2009) experimentally evaluated the effect of aqueous solution chemistry on the swelling and shrinkage of shales under saturated conditions, and reported that the more concentrated solution led to less swelling of shale. Kamei et al. (2005) and Cuadros (2006) indicated that illitization, the transformation from smectites to illite, is usually part of the diagenesis process of clay formation. Illitization apparently changes the swelling properties of clay formation. Several simulations by Montes-Hernandez et al. (2005) have shown that the Na/Ca-montmorillonite-to-Ca-montmorillonite conversion due to cation exchange in the interface was a significant chemical transformation that could change swelling properties. Studies of mixed-ion montmorillonites by El-Swaify and Henderson (1967) showed that the moisture retention in interlayer spacing by osmotic swelling at a particular equilibrium pressure has a near-linear relationship with exchangeable Na percentage. The neo-formation of chlorites (nonswelling clays) (Montes-Hernandez et al., 2005) was also observed as a potential chemical transformation that could also lower the swelling properties of the clay rocks.

Although the possible change in clay-rock swelling properties which has been demonstrated with short term and small-scale lab tests (Thury, 2002; Wakim et al., 2009) and by indirect measurement (such as the occurrence of illitization) (Kamei et al., 2005). Cuadros (2006) point out the need to evaluate the geochemically induced swelling/shrinkage of host clay rock, no such evaluation has been reported, as far as our literature survey has found. In this report, coupled THC models that include EBS and host clay rock are linked with a swelling model based on the Gouy-Chapman diffuse double layer (DDL) theory, in which the changes in swelling properties within the near-field area of host clay rock are evaluated. The coupled THC models provide the geochemical changes in the near-field host rock, and the swelling model calculates the swelling pressure.

6.4.2   Technical Approach

In this report, an approach that combines a coupled THC model with a swelling model based on the Gouy-Chapman DDL theory is adopted to evaluate the changes in swelling properties for near-field host clay rock. First, the change in geochemical parameters (i.e., the concentration of the bulk solution, the exchangeable cations, and the volume fraction of swelling clay minerals) in the host clay rock are calculated with a THC model using TOUGHREACT Version 2, and then the swelling pressure is calculated based on the input from THC model. Eventually, the changes in hydraulic properties are computed and fed back to the THC model as needed.

In this section, the simulator TOUGHREACT V2 is discussed briefly and then the swelling model based on DDL theory is presented, along with some calculation examples.

6.4.2.1 TOUGHREACT Version 2

TOUGHREACT is a numerical simulation program for chemically reactive nonisothermal flows of multiphase fluids in porous and fractured media (Xu and Pruess, 2001; Spycher et al., 2003; Sonnenthal et al., 2005; Xu et al., 2006b; Xu et al., 2011; Zhang et al., 2008c; Zheng et al., 2009). The program was written in Fortran 77 and developed by introducing reactive chemistry into the multiphase fluid and heat flow simulator TOUGH2 (Pruess, 2004). The program can be applied to one-, two- or three-dimensional porous and fractured media with physical and chemical heterogeneity. The code can accommodate any number of chemical species present in liquid, gas, and solid phases. A variety of subsurface thermal, physical, chemical, and biological processes are considered under a wide range of conditions of pressure, temperature, water saturation, ionic strength, and pH and Eh.

Processes for fluid flow and heat transport are the same as in the original TOUGH2 code. Transport of aqueous and gaseous species by advection and molecular diffusion is considered in both liquid (aqueous) and gas phases. Depending on computer memory and CPU performance, any number of chemical species in the liquid, gas, and solid phases can be accommodated. In the 2004 version, aqueous complexation, acid-base, redox, gas dissolution/ exsolution, and single-site cation exchange are considered under the local equilibrium assumption. Mineral dissolution and precipitation can proceed either subject to local equilibrium or kinetic conditions.

Over the last several years, many new capabilities have been developed within different research projects at Lawrence Berkeley National Laboratory. We have incorporated these new capabilities into Version 2 of TOUGHREACT. Major additions and improvements in Version 2 include:
- Intra-aqueous reaction kinetics and biodegradation,
- Surface complexation models, including double layer,
- Multi-site exchange,
- Improvements in the reactive surface area algorithm for mineral-water reactions, and fugacity coefficient corrections for gas-water reactions,
- Improvement in coupling and mass balance between chemistry and physics parts, including changes in rock and fluid properties due to reactions, and accounting for CO_2 fixed as carbonates in flow simulation (for use in the ECON module).
- Improvement in functionalities such as printout mineral reaction rate, and both aqueous component and species concentrations in different unit options,
- Improvement in computational efficiency.

A detailed description of TOUGHREACT Version 2 is given by Xu et al. (2011).

6.4.2.2 Application of DDL theory to calculate swelling pressure

The swelling of clays can be calculated in several ways. Elastoplastic models (Gens and Alonso, 1992; Thomas and He, 1998) such as the Barcelona Basic Model (BBM) (Alonso et al., 1990) and the Barcelona Expansive Model (BExM) (Alonso et al., 1999) are widely used. Recently, chemical components are also incorporated into the stress-strain relation, such as incorporation of the concentration of exchangeable cations (Guimarães et al., 2007) and consideration of the aqueous concentration via chemical potential (Ghassemi and Diek, 2003). Another approach involves a constitutive equation to relate the deformation of compacted bentonite to the distance between two montmorillonite layers based on the DDL theory (e.g., Komine and Ogata, 1996; 2003; Schanz and Tripathy et al., 2009).

To determine the approach for calculating the swelling pressure of the near-field host clay rock, it is necessary to determine the swelling processes that the clay rock might suffer, i.e., what type of swelling we are dealing with. In expansive clay-water-ion systems, there are basically two types of swelling processes: crystalline and osmotic. Crystalline swelling refers to swelling that occurs at relatively low water content and is primarily a consequence of the hydration of interlayer exchangeable cations. Swelling occurs as water enters the mineral interlayer as a sequence of successive molecular layers, which results in a step-wise separation of the interlayer for up to three or four layers of water. Osmotic swelling occurs at higher water contents and is associated with continuing interlayer separation that develops from movement of water into the interlayer due to the difference in ion concentration within the interlayer and within the bulk pore water. Osmotic water adsorption results from concentration differences among dissolved ions between the interlayer pore water (overlapping double layers) and the free (bulk) water. It is a long-range interaction, which mostly depends on ionic concentration, the type of exchangeable ion (e.g., Ca vs. Na), pH of the pore water, and clay mineralogy (van Olphen, 1977). Corresponding osmotic swelling results from the balance of attractive and repulsive forces that develop between overlapping electrical double layers. Crystalline swelling, which occurs mainly in the initial hydration, will be transformed to osmotic swelling when clay approaches full saturation. Wayllace (2008) reported that such transformation will occur when the RH% is around 97; Onikata et al. (1999) indicated, from a microscopic point of view, that the d(001)-value of 20 to 40 Å is probably a critical value, where the electrostatic attractive force between the 2:1 layers by way of the cations is sufficiently weak that the crystalline swelling is transformed into osmotic swelling.

Based on the fact that (1) the host clay rocks that went through a long term diagenesis process are mostly fully saturated and (2) the driving force is mostly the geochemical changes, the clay rocks will undergo osmotic swelling when contacting with EBS. Typically, clay host rock has different chemical compostions from EBS bentonite; this implies that, near the interface area, chemical transport will occur between clay host rocks and EBS bentonite, which will induce a disequilibrium of chemical potential and therefore osmotic swelling.

According to the DDL theory (Bolt, 1956), during the osmotic swelling process, the swelling pressure is the difference between the osmotic pressure in the central plane between two clay plates and the osmotic pressure in the equilibrium solution. In other words, the swelling pressure is the pressure required to keep the clay-water system at the required void ratio, when it is allowed to adsorb water or electrolyte (Tripathy et al., 2004). Bolt (1956) and van Olphen (1977) presented a method for calculating the swelling pressure in a clay–water electrolyte system. Sridharan and Jayadeva (1982) improved on Bolt (1956) and van Olphen (1977) and presented the diffuse double layer theory in a lucid form that could be readily used for understanding the engineering behavior of clays. The equations used by Sridharan and Jayadeva (1982) to determine swelling pressure are as follows:

$$e = G\gamma_w Sd \tag{6.4-1}$$

where e is the void ratio, G is the specific gravity of soil solids, γ_w is the unit weight of water, S is the specific surface area of soil (m^2/g swelling clay), d is half the distance between parallel clay platelets.

$$\int_z^u \frac{1}{\sqrt{(2\cosh y - 2\cosh u)}}dy = \int_0^d d\xi = -Kd \tag{6.4-2}$$

where u is the nondimensional midplane potential, z is the nondimensional potential at the clay surface, y is the nondimensional potential at distance x from the clay surface and x is the distance from the clay surface, ξ is the distance function (= Kx). K (1/m) is the double layer parameter:

$$K = \sqrt{\left(\frac{n(e')^2 v^2}{2\varepsilon kT}\right)} \qquad (6.4\text{-}3)$$

where e' is the elementary electric charge (= 1.6×10^{-19} C), k is Boltzmann's constant (1.3806×10^{-23} j/K), n is the molar concentration of ions in pore fluid (molal), v is the valency of the interlayer cation, T is the absolute temperature, ε is the dielectric constant of the pore fluid, given by $\varepsilon = \varepsilon_0 D$, in which ε_0 is the permittivity of the vacuum (8.8542×10^{-12} C^{2}J^{-1}m^{-1}) and D is the ratio of the electrostatic capacity of condenser plates separated by the given material to that of the same condenser with vacuum between the plates (Mitchell and Soga, 2005):

$$-\left(\frac{dy}{d\xi}\right)_{x=0} = \sqrt{(2\cosh z - 2\cosh u)}$$

$$= \Gamma \sqrt{\left(\frac{1}{2\varepsilon nkT}\right)} \qquad at \quad x = 0, y = z$$

$$= \left(\frac{B}{S}\right)\sqrt{\left(\frac{1}{2\varepsilon nkT}\right)} \qquad (6.4\text{-}4)$$

where Γ is the surface charge density (base exchange capacity per specific surface), and B is the base exchange capacity of the clay (meq/100 g solid):

$$p = 2nkT(\cosh u - 1) \qquad (6.4\text{-}5)$$

where p is the osmotic pressure or swelling pressure (Pa). For any given pore-fluid medium, determination of the swelling pressure using Langmuir's equation (i.e., Equation (6.4-5)) requires the nondimensional midplane potential function, u.

Determination of u is an indirect and time-consuming process. A relationship between u and the nondimensional distance function, Kd, must be established to determine u for any given value of Kd and vice versa. Equations (6.4-2)–(6.4-5) are used for this purpose. Tripathy et al. (2004) illustrate the procedure of obtaining the u-Kd relation clearly, with the flow chart shown in Figure 6.4-1. For any given pressure, u can be found from Equation (6.4-5). For known B, S, n and u values $(dy/d\xi)_{x=0}$ and then z can be calculated from Eq. (6.4-4). From Equation (6.4-2), for known u and z values, Kd can be found. After determining u and Kd values for a series of pressures, an u-Kd relation can be established for one particular group of B, S and n. For any void ratio, e, knowing K from Equation (6.4-3) and d from Equation (6.4-1), Kd can be found. Then the u value for the corresponding Kd value can be determined from the established u–Kd relationship. The swelling pressure can be calculated from Equation (6.4-5).
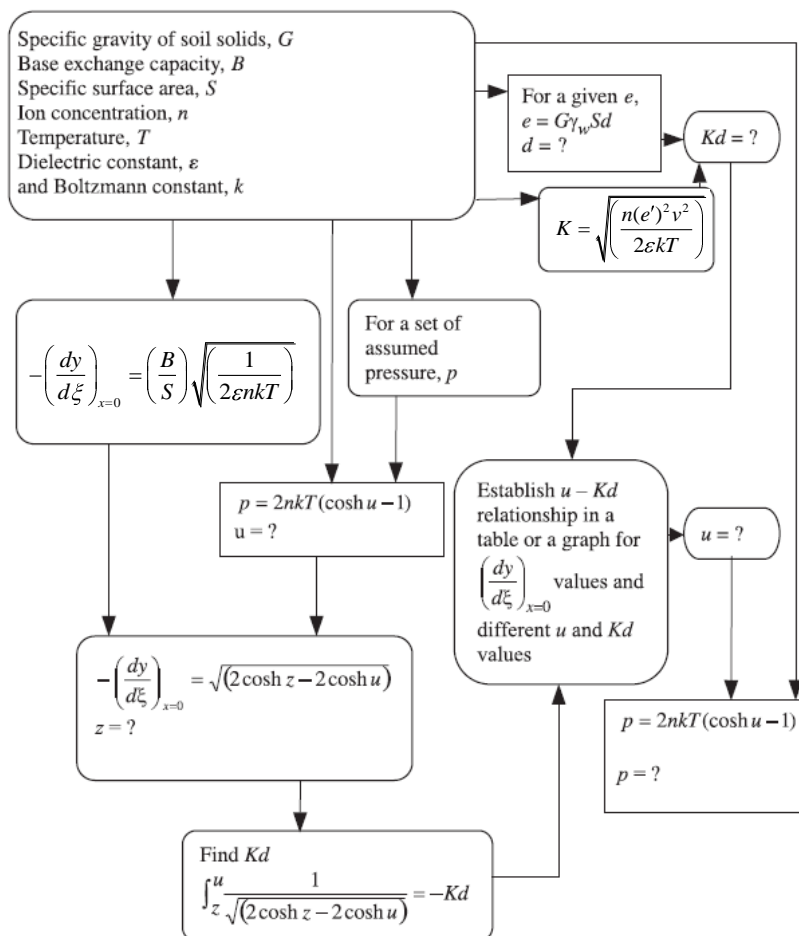
Figure 6.4-1. Flow chart showing the determination of swelling pressure for a given void ratio using the diffuse double layer theory

6.4.2.3 Calculation examples for swelling pressure

Subroutines for calculating swelling pressure based on DDL theory have been implemented in TOUGHREACT V2. In this section, we present two calculation examples: one is for the FEBEX bentonite (ENRESA, 2000), the other is for the lower Dogger opalinum shale in northern Switzerland (Madsen and Muller-vonmoss, 1985). We use the first example to show the importance of u-Kd relations and the second example to illustrate the necessary modification of Eq. (6.4-1) when applying DDL theory to natural clayey sediments.

While DDL theory has been applied extensively to assess the compressibility (or swelling) of initially saturated clays (Bolt, 1956; van Olphen, 1977; Sridharan and Jayadeva, 1982; Madsen and Muller-vonmoss, 1985; Mitchell and Soga, 2005), researchers have also applied the theory to calculate the swelling pressure of unsaturated compacted bentonite that is used in EBS (Komine and Ogata, 1996; Komine and Ogata, 2003; Tripathy et al., 2004; Schanz and Tripathy, 2009). Tripathy et al. (2004) and Schanz and Tripathy (2009) present an extensive review of the application of the DDL theory to compacted bentonite and discussed some of the limitations. Tripathy et al. (2004) applied the DDL theory

to calculate the swelling pressure of FEBEX bentonite (ENRESA, 2000) and tested it against the measured swelling pressure. Here, we seek to reproduce the calculation made by Tripathy et al. (2004) and discuss the importance of *u-Kd* relation.

The key of performing such a calculation is to establish the relationship between *u*, the nondimensional midplane potential, and *Kd*, the nondimensional distance function. Usually, the *u-Kd* relation is given in the following form:

$$u = a + b\log 10(Kd) \tag{6.4-6}$$

where *a* and *b* are fitting constants.

As shown in Figure 6.4-1, in order to establish the *u-Kd* relation, one needs to calculate the *u* from a series of hypothetical swelling pressures and then calculate *Kd* based on Equation (6.4-2). The *u-Kd* relation is affected by the specific surface area (*S*), base-exchange capacity (*B*), and ion concentration of bulk water (*n*). In addition, the range of pressure also slightly affects the *u-Kd* relationship. Tripathy et al. (2004) present a *u-Kd* relation based on a pressure range from 0.05 MPa to 50 MPa and assuming $n = 10^{-4}$ molal:

$$u = 3.07 - 3.664\log 10(Kd) \tag{6.4-7}$$

Table 6.4-1 lists the relevant properties of FEBEX bentonite that Tripathy et al. (2004) used to calculate the swelling pressure. Using the same properties, our code yields a similar *u-Kd* relationship (see *a* and *b* value in Table 6.4-2). Schanz and Tripathy (2009) noted that the difference between the *u-Kd* relationship derived from the DDL theory and those back-calculated from the experimental data is the main reason for the difference between calculated and measured swelling pressure. Figure 6.4-2 shows the swelling pressure calculated based on the theoretical and experimental *u-Kd* relationship. It shows that we must back-calculate the *u-Kd* relationship in order to fit the measured data for compact bentonite.

Table 6.4-1. Properties of FEBEX bentonite that Tripathy et al. (2004) used to calculate the swelling pressure

Specific gravity G	Specific surface area (m2/g)	Base exchange capacity (meq/100 g)	Ion concentration of bulk water (molality)	Weight average of valencies (v)
2.70	725	102	10^{-4}	1.66-1.73
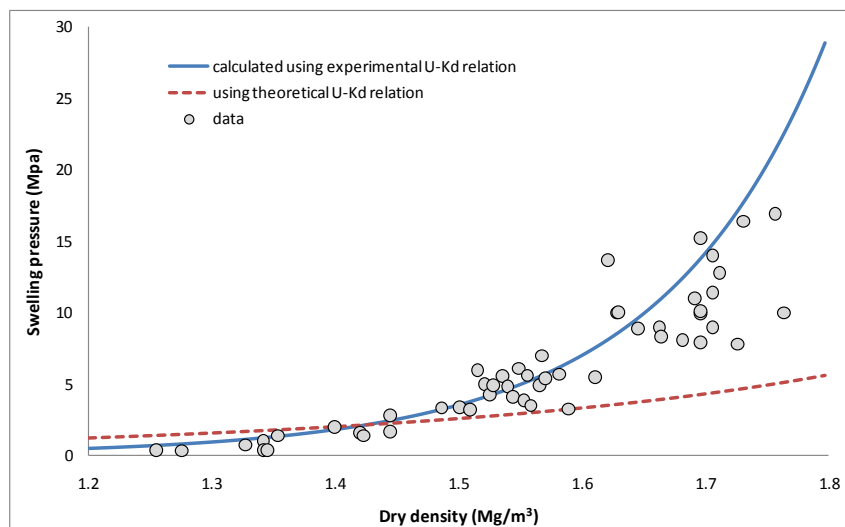
Figure 6.4-2. Comparison of calculated and measured swelling pressure as a function of dry density

The sensitivity of the *U-Kd* relation to specific surface area, base exchange capacity, and ion concentration of bulk water were further checked by varying these parameters. Table 6.4-2 lists parameter *a* and *b* in Equation (6.4-6) under different combinations of parameters. As the *U-kd* relations change, the calculated swelling pressures change correspondingly. Figure 6.4-3 shows the variation in the swelling pressure for those scenarios listed in Table 6.4-2. Note that when the ion concentration increases from 10^{-4} to 10^{-2}, changes in swelling pressure are rather minimal, whereas a further increase in ion concentration to 0.1 lead to remarkable changes in swelling pressure. Figure 6.4-4 also shows that specific surface area and base exchange capacity have significant effects on swelling pressure.

Table 6.4-2. Parameter A and B for U-Kd relation (Equation (6.4-2)) under different combinations of parameters

Run number	Specific surface area (m^2/g)	Base exchange capacity (meq/100 g)	Ion concentration of bulk water (molality)	a	b
Base	725	102	10^{-4}	3.07	-3.71
Run1	725	102	10^{-2}	2.21	-3.66
Run2	725	102	10^{-1}	1.81	-3.43
Run3	725	51	10^{-4}	3.54	-3.17
Run4	362.5	102	10^{-4}	2.67	-4.13
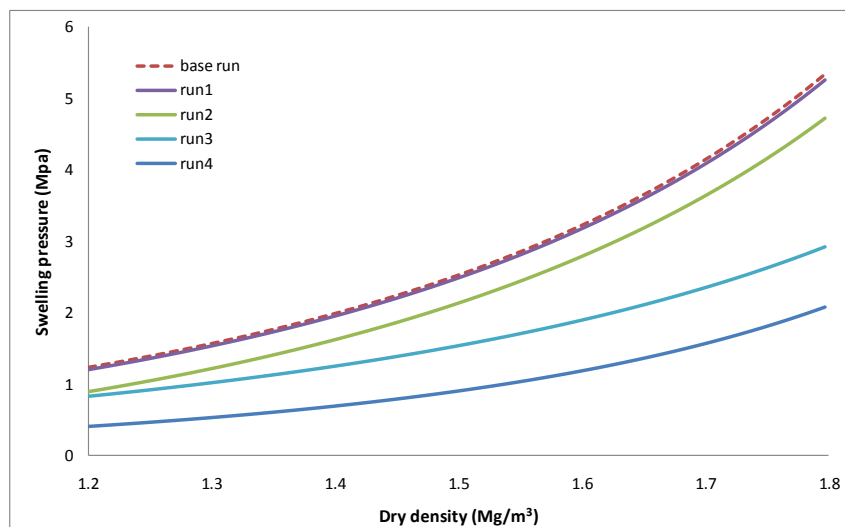
Figure 6.4-3. Calculated swelling pressure as a function of dry density for the different scenarios listed in Table 6.4-2.

Using the DDL theory to calculate the swelling pressure was originally established for pure clay. Natural clay formation, however, is never composed of one type of pure clay mineral. For example, the Opalinus Clay, a candidate for host rock formation for radioactive waste disposal in Europe (Thury, 2002), contains only about 10% illite-smectite mixture. For the clay formations that have a mixture of swelling and nonswelling minerals, Equation (6.4-1) is obviously questionable because the pore space includes not only the interlayer space where the swelling occurs, but also the pore spaces that are surrounded by nonswelling minerals. The derivation of Equation (6.4-1) is based on the assumption that the clay platelets are parallel, as shown in Figure 6.4-4. As we extend the idealized structure of pure swelling clay (Figure 6.4-4) to a mixture of swelling clay and nonswelling minerals (Figure 6.4-5), Equation (6.4-1) will be modified correspondingly.
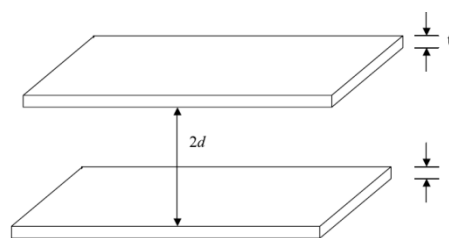
Figure 6.4-4. A representative unit layer separation for parallel clay platelets (Schanz and Tripathy, 2009), where t is the thickness of the swelling clay platelets.
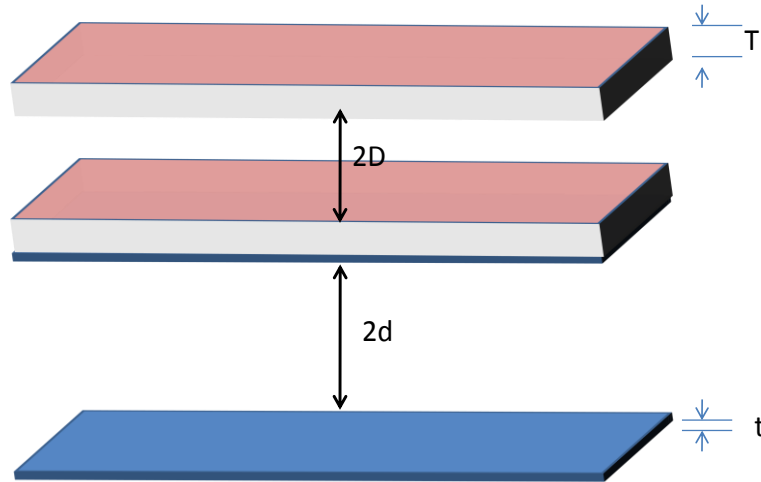
Figure 6.4-5. A representative unit layer structure for parallel swelling clay and nonswelling mineral platelets, where D is the half width between two nonswelling mineral platelets and T is the thickness one nonswelling mineral platelet.

Assuming the platelet (both swelling and nonswelling minerals) has a plan area of A, the volume of the void is

$$V_v = 2A(d + D) \tag{6.4-8}$$

The volume of the solids is

$$V_s = 2A(t + T) \tag{6.4-9}$$

and void ratio is

$$e = \frac{V_v}{V_s} = \frac{d + D}{t + T} \tag{6.4-10}$$

Neglecting the contribution from the edges, the specific area (surface area per unit mass of swelling clay) of the swelling clay is given by

$$S = \frac{2A}{M_t f^s} \tag{6.4-11}$$

where M_t is the total mass of the solid and f^s is the mass fraction of the swelling clay in the mixture. The specific gravity of the solid is given by:

$$G = \frac{M_t}{V_s \gamma_w} \tag{6.4-12}$$

The mass of the solid is

$$M_t = GV_s\gamma_w = \frac{G\gamma_w 2A(d+D)}{e}$$ (6.4-13)

Substituting *Mt* in Equation (6.4-13) to Equation (6.4-11), we have:

$$e = G\gamma_w Sf^s(d+D)$$ (6.4.14)

Taking $f^d = D/d$, then Equation 6.4-14 can be rewritten as:

$$e = G\gamma_w Sf^s d(1+f^d)$$ (6.4-15)

Typically a nonswelling clay mineral such kaolinite or illite has a the basal spacing (d(001)) of around 10 A, whereas a swelling clay (smectite) that suffers osmotic swelling has the d(001) value of 20 to 40 A (Onikata et al., 1999). f^d therefore ranges from 0.25 to 0.5. Note that in a broader sense, f^d represents the ratio of pore space associated with nonswelling minerals to that associated with swelling minerals.

Madsen and Muller-Vonmos (1985) measured the swelling pressure of nineteen drill core samples of the lower Dogger opalinum shale in northern Switzerland. The samples contain around 50% clay-size materials, of which about 30% are swelling clays. The mass fraction of swelling clay, f^s, is therefore equal to 0.3, assuming that swelling clays are smectite, which typically has a cation exchange capacity of 100 meq/100 g and a specific surface area of 800 m^2/g (Sridharan and Jayadeva, 1982). Figure 6 shows the calculated result with two different f^d: 0.25 and 0.5. It seems that the f^d of 0.25 gives a better match with the measured data and is therefore used for the calculations in this report.
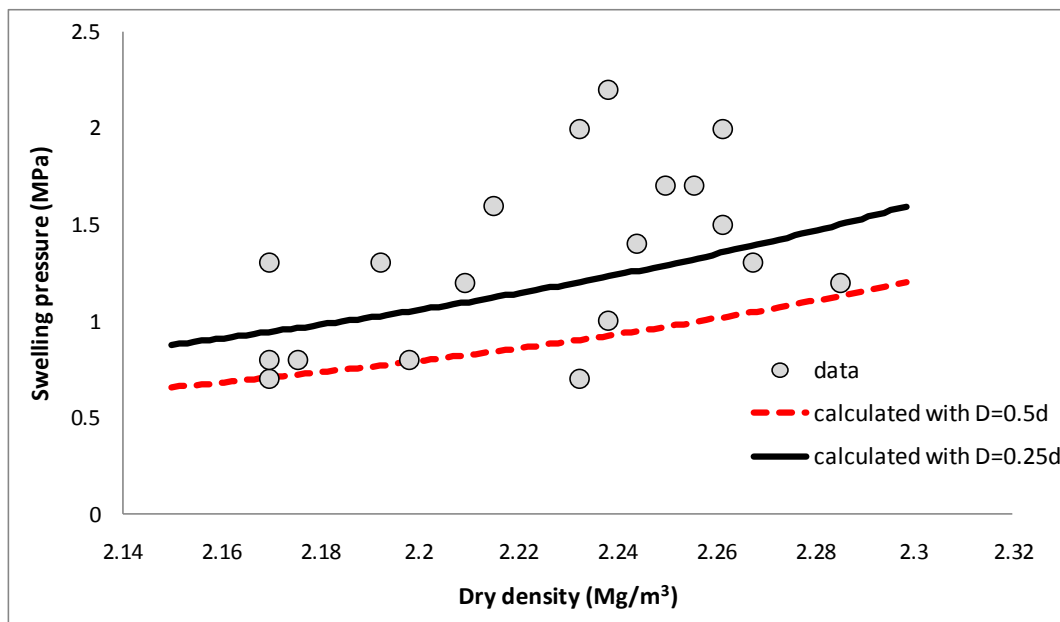
Figure 6.4-6. Comparison of calculated and measured swelling pressure lower Dogger opalinum shale in northern Switzerland (Sridharan and Jayadeva, 1982)

6.4.3   Technical results

6.4.3.1 Model setup

Both the 1-D and 2-D THC models are developed in the calculations presented here. The mesh for the 2-D model is shown in Figure 6.4-7. The mineralogical composition of bentonite (Table 6.4-3) is taken from the Kunigel-V1 bentonite (Ochs et al., 2004). The clay formation is assumed to be Opalinus Clay investigated in the Mont Terri underground rock laboratory in Switzerland (Thury, 2002) and the mineral composition is given in Table 6.4-4.
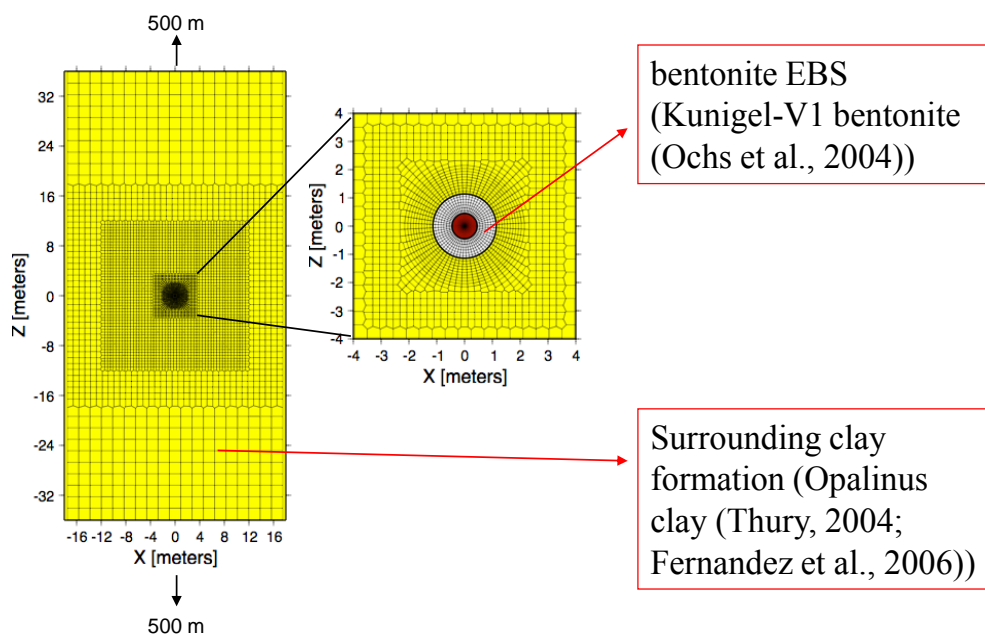
Figure 6.4-7. 2-D mesh used in the THC model

Table 6.4-3. Mineral composition of the bentonite used in the model (taken from the Kunigel-V1 bentonite (Ochs et al., 2004)

Mineral	Abundance (volume fraction)
Smectite-na	0.475
Quartz	0.335
K-Feldspar	0.041
Calcite	0.0235
Dolomite	0.029
Pyrite	0.006

Table 6.4-4. Mineral composition of the clay formation used in the model (taken from the Opalinus Clay (Thury, 2002)

Mineral	Abundance (volume fraction)
Calcite	0.1
Illite	0.223
Kaolinite	0.174
Chlorite	0.1445
Smectite-na	0.1426
Quartz	0.1845
Siderite	0.01256
Ankerite	0.00798
Pyrite	0.01

The pore-water composition of the bentonite (Ochs et al., 2004) and clay formation (Fernandez et al., 2007) are listed in Table 6.4-5.

Table 6.4-5. Pore water composition of EBS bentonite and host clay rock

	EBS Bentonite: Kunigel-V1 (Ochs et al., 2004)	Opalinus Clay (Fernandez et al., 2007)
pH	8.40	7.60
Eh	-0.23	-0.27
Cl	1.50E-05	3.32E-01
SO_4^{-2}	1.10E-04	1.86E-02
HCO_3^-	3.50E-03	5.20E-03
Ca^{+2}	1.10E-04	2.26E-02
Mg^{+2}	5.50E-05	2.09E-02
Na^+	3.60E-03	2.76E-01
K^+	6.20E-05	2.16E-03
Fe^{+2}	1.00E-10	2.96E-07
$SiO_2(aq)$	3.40E-04	1.16E-04
AlO_2^-	3.54E-08	3.89E-06

In our current model, it is assumed that smectite is the only swelling mineral, with a specific surface area of 800 m^2/g smectite (Sridharan and Jayadeva, 1982). The cation exchange capacity is taken from Thury (2002) which is 11.68 meq/100 g solid. The mass fraction of smectite f^s is assumed to be equal to its volume fraction, as shown in Table 4.

Table 6.4-6 lists the thermal and hydrodynamic parameters used in the model. Those for bentonite are taken from Liu et al., (2010), while those for clay formation are mostly taken from Thury (2002).

Table 6.4-6. Thermal and hydrodynamic parameters

parameter	Clay formation	Bentonite
Grain density [kg/m^3]	2700	2700
Porosity ϕ	0.15	0.41
Saturated permeability [m^2]	1.0×10^{-20}	2.0×10^{-21}
Relative permeability, k$_{rl}$	$m = 0.6$, $S_{rl} = 0.01$	$K_{rl} = S^3$
Van Genuchten α [1/Pa]	6.8×10^{-7}	3.3×10^{-8}
Van Genuchten m	0.6	0.3
Compressibility, β [1/Pa]	3.2×10^{-9}	5.0×10^{-8}
Thermal expansion coeff., [1/^{o}C]	0.0	1.0×10^{-4}
Dry specific heat, [J/kg ^{o}C]	800	8000
Thermal conductivity [W/m ^{o}C] dry/wet	2.2/2.2	0.5/1.3
Tortuosity for vapor phase	$\phi^{1/3} S_g^{10/3}$	$\phi^{1/3} S_g^{10/3}$

Mineral dissolution/precipitation are kinetically controlled, except that calcite is assumed to be in equilibrium. The kinetic law for mineral dissolution/precipitation is given in Xu et al. (2006b). The kinetic rate for the mineral considered in our model is given in Table 6.4-7. Note that the surface areas listed in Table 6.4-7 are calculated for tuff (Sonnenthal et al., 2005); their applicability to the clay formation being considered is questionable. Further refinement of the surface area calculation is needed for when the THC model is applied to a realistic scenario.

Table 6.4-7. Kinetic properties for minerals considered in the model (Xu et al., 2006b)

Mineral	A (cm^2/g)	Parameters for Kinetic Rate Law								
		Neutral Mechanism		Acid Mechanism			Base Mechanism			
		k_{25} $(mol/m^2/s)$	E_a (KJ /mol)	k_{25}	E_a	$n(H^+)$	k_{25}	E_a	$n(H^+)$	
Primary:										
Calcite	Assumed at equilibrium									
Quartz	9.8	1.023×10^{-14}	87.7							
K-feldspar	9.8	3.89×10^{-13}	38	8.71×10^{-11}	51.7	0.5	6.31×10^{-12}	94.1	-0.823	
Kaolinite	1.95×10^5	6.91×10^{-14}	22.2	4.89×10^{-12}	65.9	0.777	8.91×10^{-18}	17.9	-0.472	
Illite	6.68×10^5	1.66×10^{-13}	35	1.05×10^{-11}	23.6	0.34	3.02×10^{-17}	58.9	-0.4	
Chlorite	9.8	3.02×10^{-13}	88	7.76×10^{-12}	88	0.5				
Dolomite	12.9	2.52×10^{-12}	62.76	2.34×10^{-7}	43.54	1				
Ankerite	9.8	1.26×10^{-9}	62.76	6.46×10^{-4}	36.1	0.5				
Smectite-Na	5.64×10^5	1.66×10^{-13}	35	1.05×10^{-11}	23.6	0.34	3.02×10^{-17}	58.9	-0.4	
Na-montmorillonite	5.64×10^5	1.66×10^{-13}	35	1.05×10^{-11}	23.6	0.34	3.02×10^{-17}	58.9	-0.4	

6.4.3.2 Base model results

Although the current simulation domain includes both engineered barrier system (EBS) bentonite and natural system (NS) clay rock, we present the model results for host clay rock exclusively, in order to stay focused on the objective of this report—evaluating the geochemically induced changes in swelling properties for the host clay rock in the near-field area. During the period of EBS hydration, chemical species are transported from host clay rock to EBS by advection and diffusion. Figure 6.4-8 shows the spatial distribution of chloride at different times. Chloride is barely affected by chemical reactions in our current model and therefore primarily undergoes advection and diffusion. As illustrated in Figure 6.4-8, a sharp decrease in chloride concentration occurs at the very beginning of hydration, in the area close to the EBS-NS interface. Such a decrease propagates further away from the EBS-NS interface as time increases and the concentration of chloride bounces back, because of the inflow of water from the surrounding far-field area. While affected by the chemical reaction such as dissolution of smectite and cation exchange, sodium exhibits similar behavior to chloride (Figure 6.4-9). As the major ion in the pore water decreases, the ionic strength decreases as well (see Figure 6.4-10). Note that we use ionic strength to represent the ion concentration n (e.g., Eq. (6.4-3)) in the swelling model.
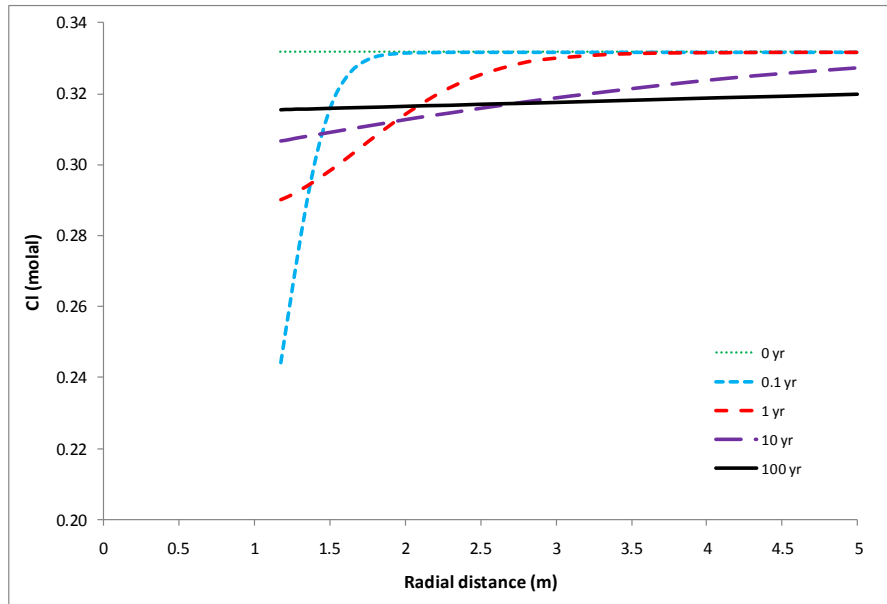
Figure 6.4-8. Spatial distribution of chloride at different times.
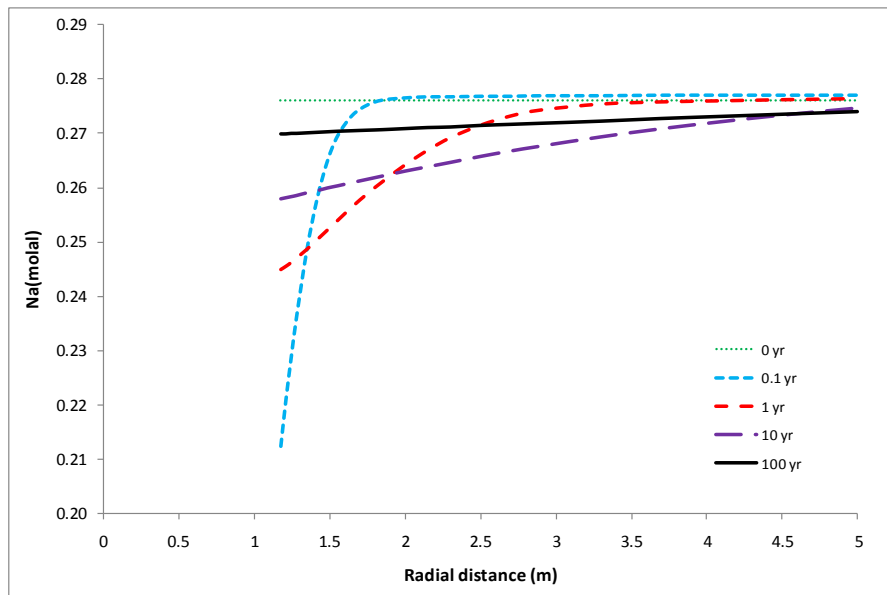
Figure 6.4-9. Spatial distribution of sodium at different times.
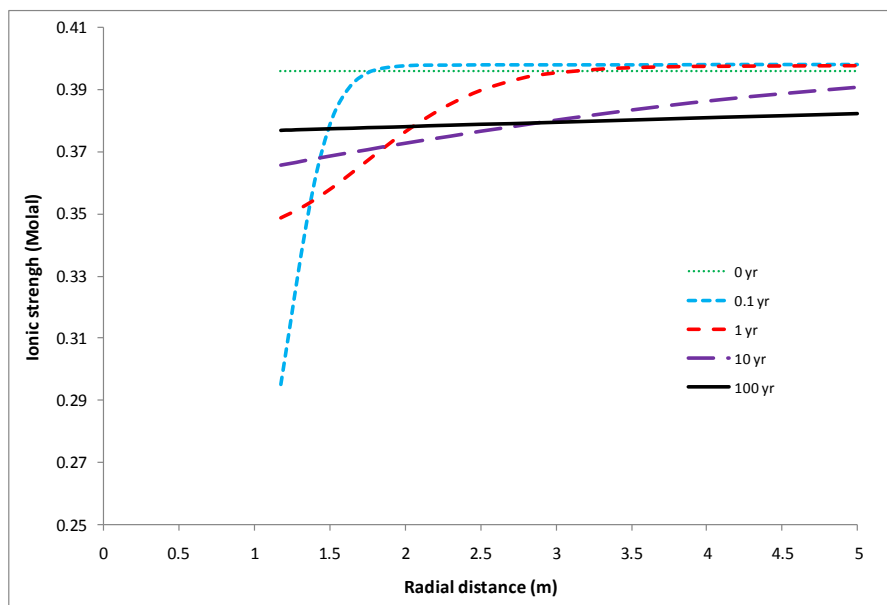
Figure 6.4-10. Spatial distribution of ionic strength at different times.

As mentioned above, illitization, the transformation from smectites to illite, is usually part of the diagenesis process of clay formation (Kamei et al., 2005; Cuadros, 2006). Our current model confirms such a transformation, as illustrated by Figures 6.4-11 and 6.4-12. As a result of smectite dissolution, chlorite precipitates as well (Figure 6.4-13), which leads to a decrease in the concentration of magnesium.
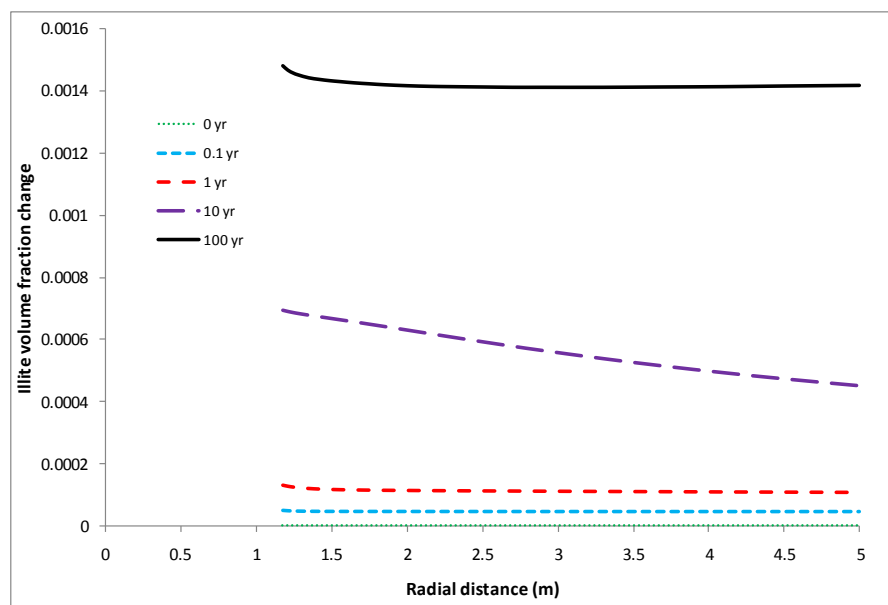
Figure 6.4-11. Spatial distribution of illite volume fraction change (dimensionless) at different times.
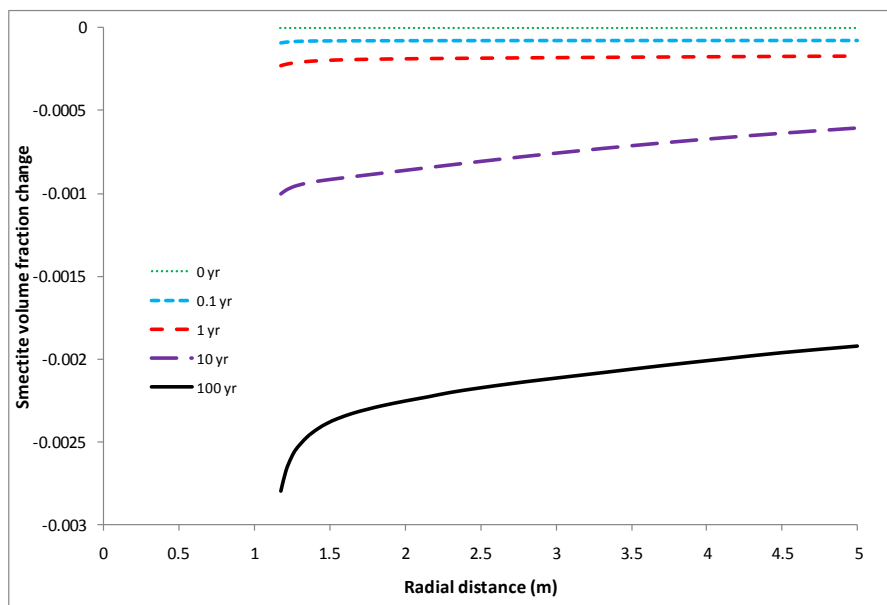
Figure 6.4-12. Spatial distribution of smectite volume fraction change (dimensionless) at different times
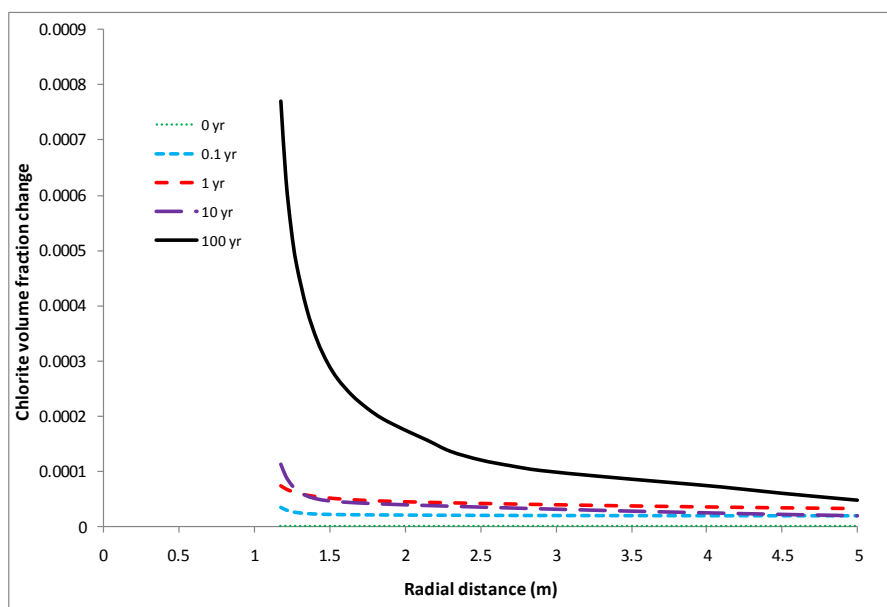
Figure 6.4-13. Spatial distribution of chlorite volume fraction change (dimensionless) at different times

Mineral dissolution/precipitation affects the concentration of aqueous cations, which subsequently induce a change in the composition of exchangeable cations. The concentration of calcium increases because of the dissolution of calcite; the concentration of potassium decreases because of the precipitation of illite; the concentration of magnesium decreases because of the precipitation of chlorite. Figure 6.4-14 shows the concentration of exchangeable cations at the beginning and at 100 years. An increase in aqueous calcium drives the exchangeable calcium to an elevated level, whereas the decrease in aqueous potassium

and magnesium leads to a significant drop in exchangeable potassium and magnesium (see Figure 6.4-15 for a clearer illustration when plotting Figure 6.4-14 in logarithmic scale). Exchangeable sodium also increases, due to the drop in exchangeable potassium and magnesium. In the formulations of DDL to calculate the swelling pressure, the composition of the exchangeable cations is not specifically included. Instead, the weight average of the valence of exchangeable cations (Tripathy et al., 2004) is used to account for the effect of change in exchangeable cations on the swelling pressure. The weighted average of the valence of exchangeable cations at different times is therefore plotted (see Figure 6.4-16), but only minimal changes are observed.
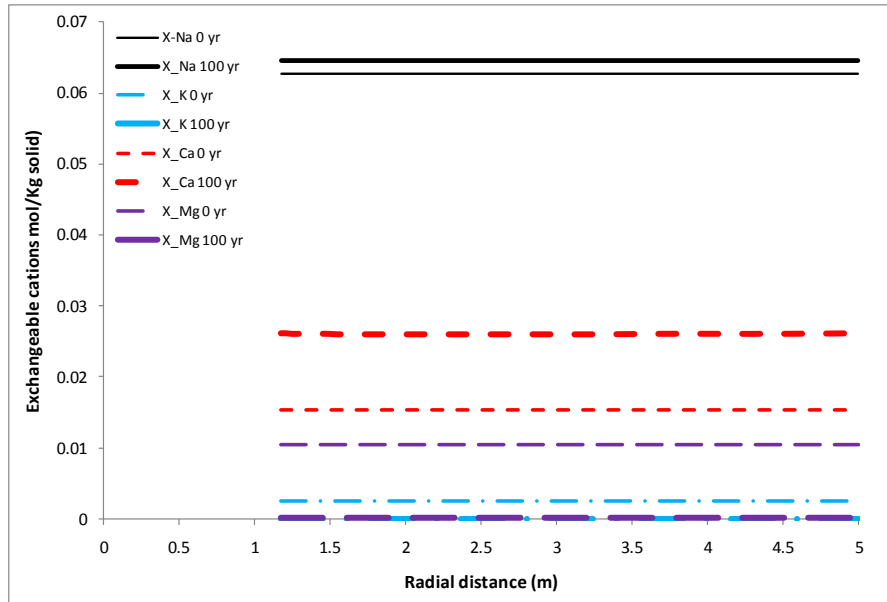
Figure 6.4-14. The concentration of exchangeable cations at the 0 and 100 yr
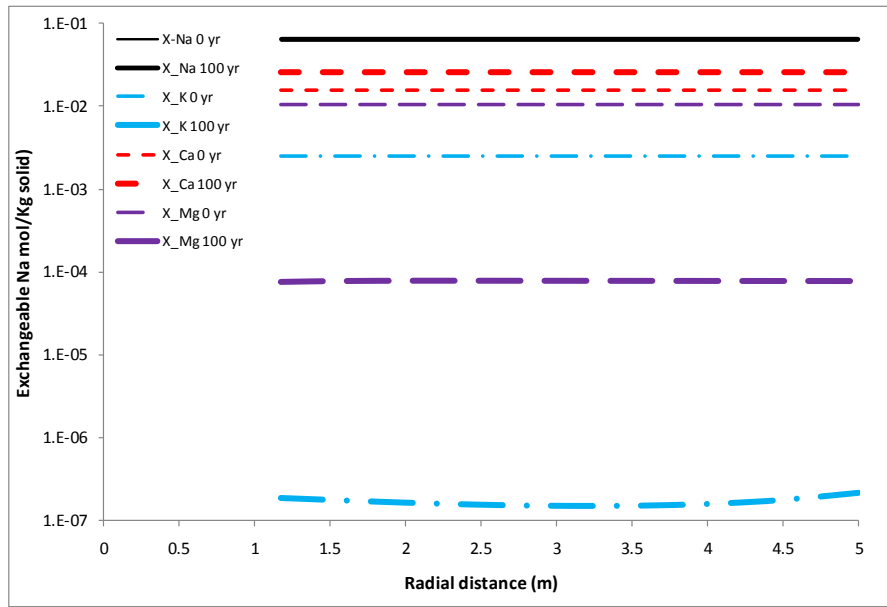
Figure 6.4-15. The concentration of exchangeable cations at the 0 and 100 year, with vertical axis in logarithmic scale
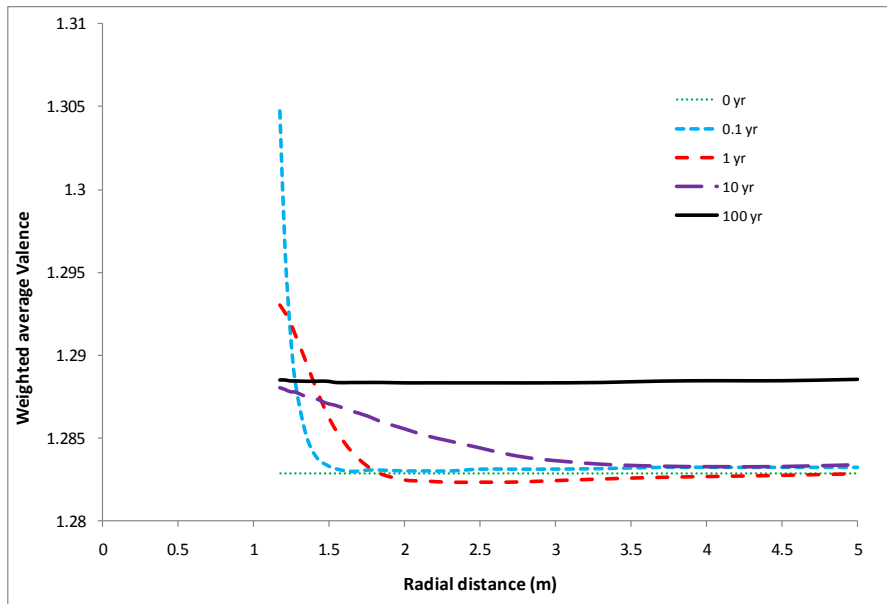
Figure 6.4-16. The weighted average valence of exchangeable cations at different times

The geochemical evolution in the host clay rock—including the decrease in pore-water ionic strength, loss of the smectite due to illitization, and change in exchangeable cations—could lead to a change in the swelling pressure. Figure 6.4-17 shows the calculated swelling pressure at different times. The initial swelling pressure is around 7.5 bar, which is smaller than the measured swelling pressure (about 15 bar) of the lower Dogger Opalinum shale in northern Switzerland (Madsen and Muller-Vonmoss, 1985), because of the higher ion concentration of pore water for Opalinus Clay (0.4 molal in comparison with 0.01 molal for lower Dogger opalinum shale). The temporal and spatial change in swelling pressure follows the change in ionic strength, as shown in Figure 6.4-10. In the area close to the EBS-NS interface, the swelling pressure could rise to 9.5 bar. Figure 6.4-18 gives the relative change in swelling pressure, defined as:

$$(P_s^t - P_s^0)/P_s^0 \times 100 \qquad (6.4\text{-}16)$$

where P_s^0 and P_s^t are swelling pressure initially and at given time t. After 100 years, the swelling pressure increase about 5%.
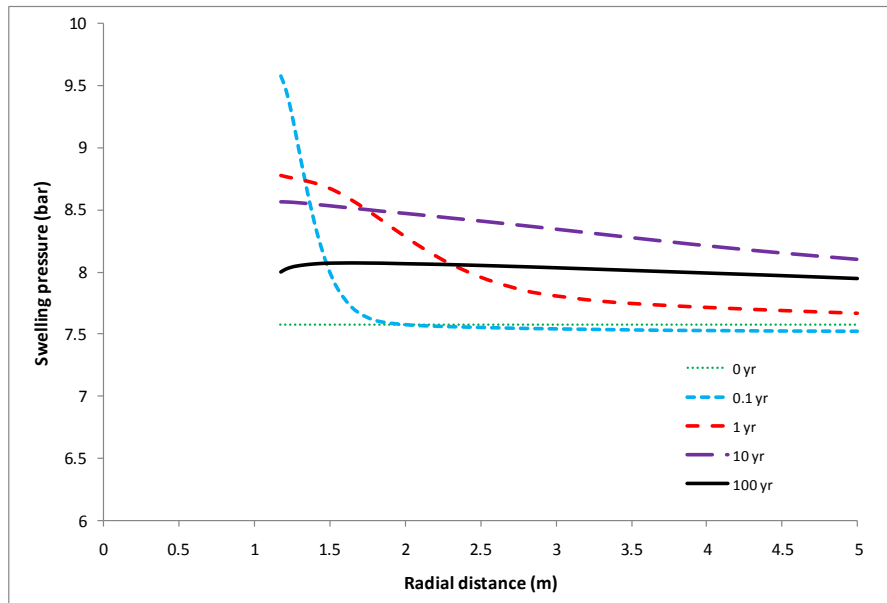
Figure 6.4-17. Spatial distribution of swelling pressure at different times
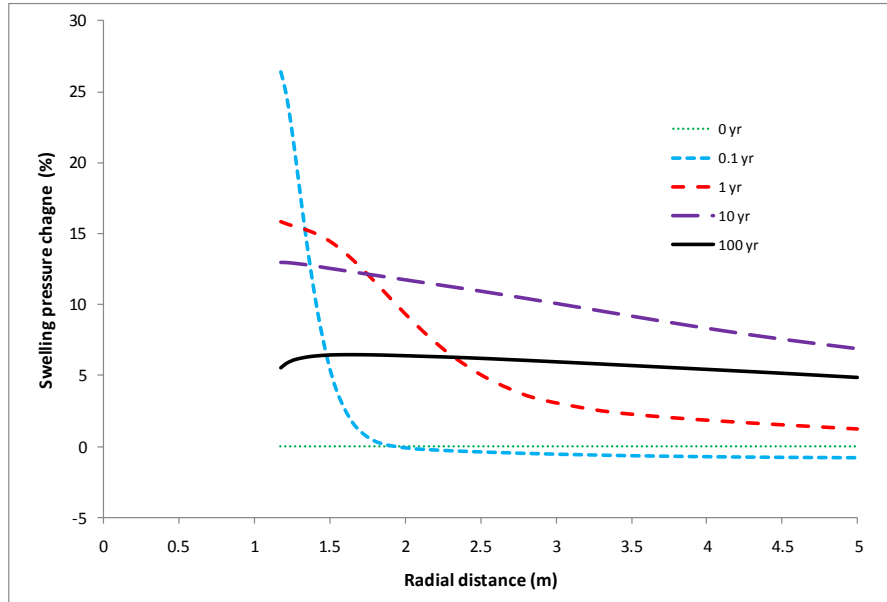
Figure 6.4-18. The percentage of swelling pressure change comparing with initial swelling pressure at different times.

The change in swelling pressure induces the change of porosity. Liu et al. (2010) proposed the following porosity-stress relation:

$$\phi = \phi_e(1 - C_e\sigma) + \gamma_t \exp\left(\frac{\sigma}{K_t}\right)$$ (6.4-17)

$$\phi_e = \phi_0 - \gamma_t$$ (6.4-18)

$$\gamma_t = \frac{V_{0,t}}{V_0}$$ (6.4-19)

where C_e is the compressibility for the hard fraction of pore volume, ϕ_0 is the porosity under the unstressed state, V_0 is the total volume under unstressed state and $V_{0,t}$ is the volume of soft fraction, K_t is the bulk moduli for the soft parts and σ is the stress. Neglecting the soft part and assuming that stress is equal to the swelling pressure, Equation (6.4-4) can be simplified as:

$$\phi = \phi_0(1 - C_e P_s)$$ (6.4-20)

where P_s is swelling pressure (Pa). Writing Equation (6.4-20) in incremental form, we have:

$$\Delta\phi = -\phi_0 C_e \Delta P_s$$ (6.4-21)

Based on Equation (6.4-21), the relative porosity change due to swelling is calculated similarly to the relative swelling pressure change, Equation (6.4-16), and the results are shown in Figure 6.4-19. After 100 years, the porosity decreases insignificantly due to swelling, only about 0.01%. On the other hand, porosity is also changed by mineral dissolution/precipitation (see Figure 6.4-20); there is a 0.14%

porosity increase resulting from geochemical processes, which overshadows the porosity change due to swelling.
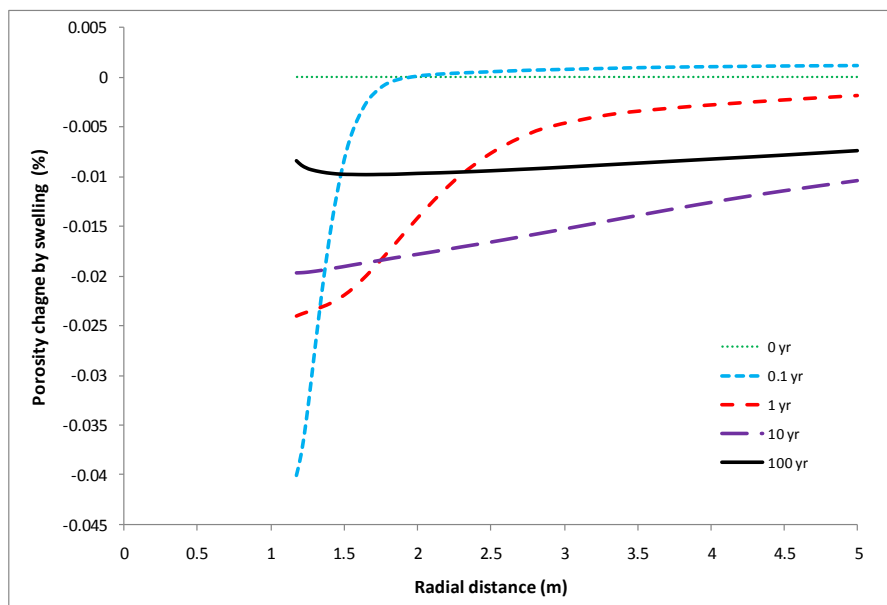
Figure 6.4-19. The change in porosity due to swelling at different times
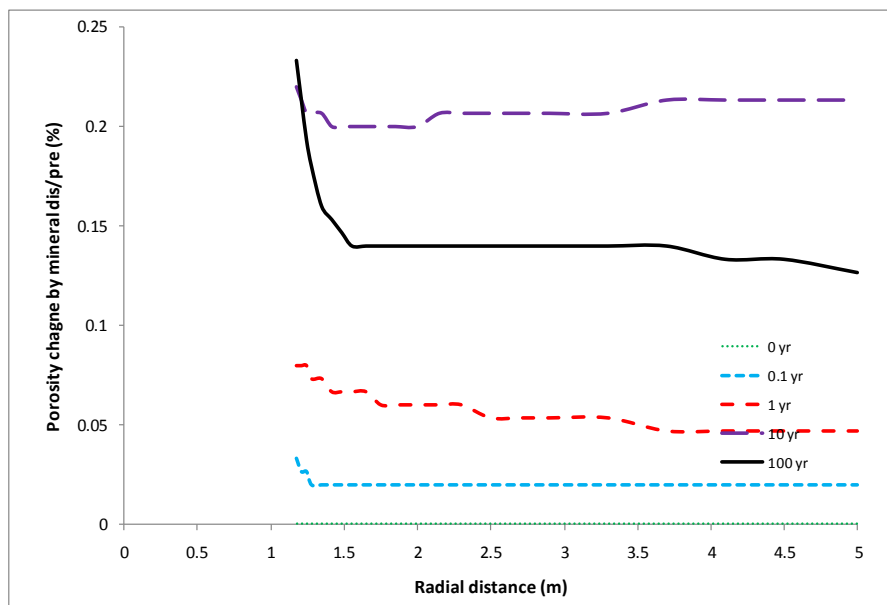
Figure 6.4-20. The change in porosity due to mineral precipitation/dissolution at different times

Just as the 1-D model allows us to analyze the geochemically induced swelling-pressure changes at rather low computational cost, the 2-D model helps us to evaluate the spatial change in swelling pressure. Figure 6.4-21 and 6.4-22 shows the spatial distribution of ionic strength at 1 year and 100 years, while Figures

6.4-23 and 6.4-24 show the spatial distribution of swelling pressure at 1 and 100 years. The 2D model gives similar results to the 1D model. Model results from the 2D model show that the significant change in swelling properties occurs within about 2–3 m from the EBS-NS interface into the host rock.
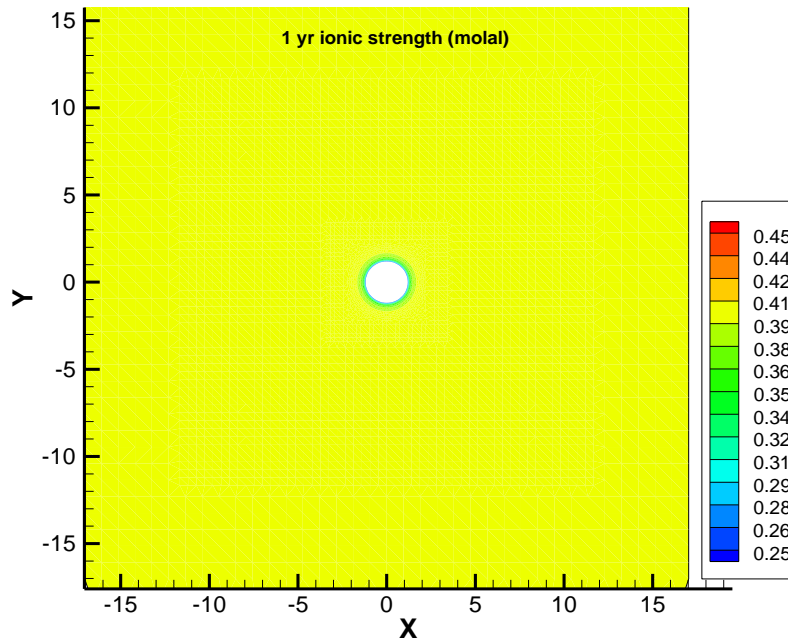
Figure 6.4-21. Spatial distribution of ionic strength at 1 year.
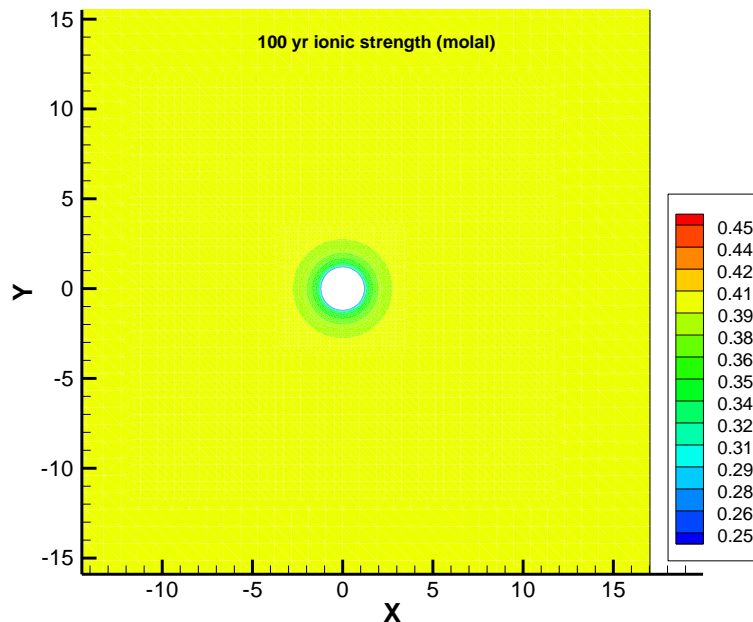
Figure 6.4-22. Spatial distribution of ionic strength at 100 years.
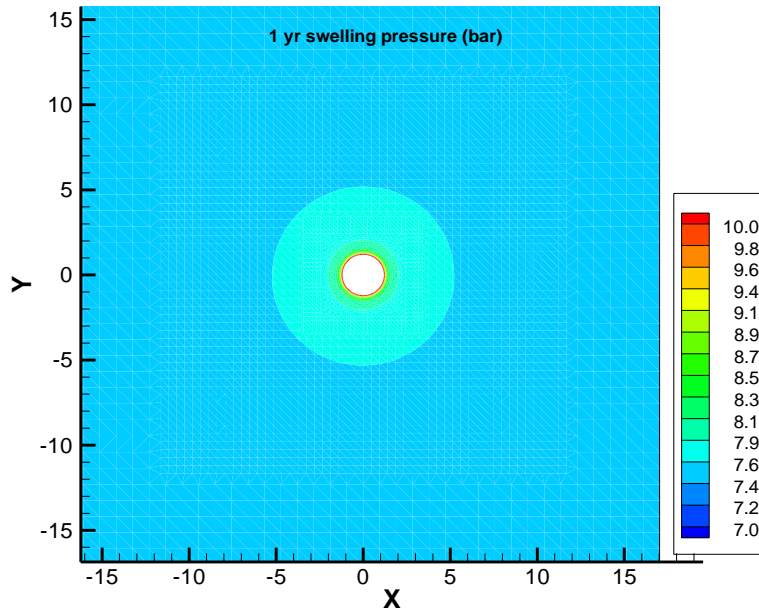
Figure 6.4-23. Spatial distribution of swelling pressure at 1 year.
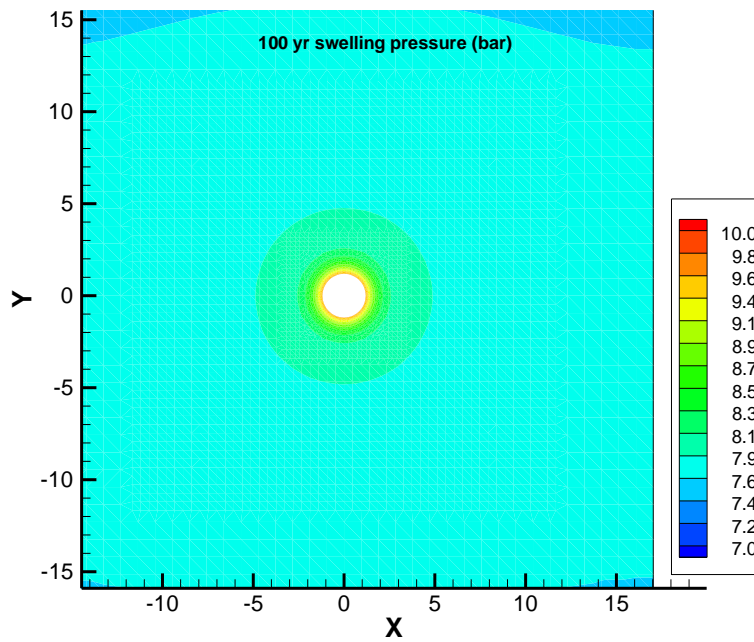
Figure 6.4-24. Spatial distribution of swelling pressure at 100 years.

6.4.3.3 Sensitivity analysis

The key geochemical factors for the swelling pressure change: Three types of geochemical change might affect the swelling pressure of clay rock: the ionic strength (ion concentration of pore water), the volume fraction of the smectite, and the exchangeable cations. Exchangeable cations affect the swelling pressure by changing the weighted average valence of interlayer cations. In the base model, as shown in Figure 6.4-16, the change in weighted average valence is rather minimal and therefore unlikely to affect the swelling pressure. The decrease in ionic strength (Figure 6.4-10) tends to increase the swelling pressure, whereas the decrease in the volume fraction of smectite (Figure 6.4-12) tends to lower the swelling pressure, although the overall effect is that eventually the swelling pressure increases. In order to evaluate how significantly the decrease in the volume fraction of smectite contributes to the final swelling pressure change, we conducted a sensitivity run in which the effect of the decrease in the volume fraction of smectite is not considered (Figure 6.4-25). As expected, the swelling pressure increases about 4% more in the sensitivity run than in the base model, indicating that more significant swelling could be calculated if the loss of smectite due to illitization is not considered.
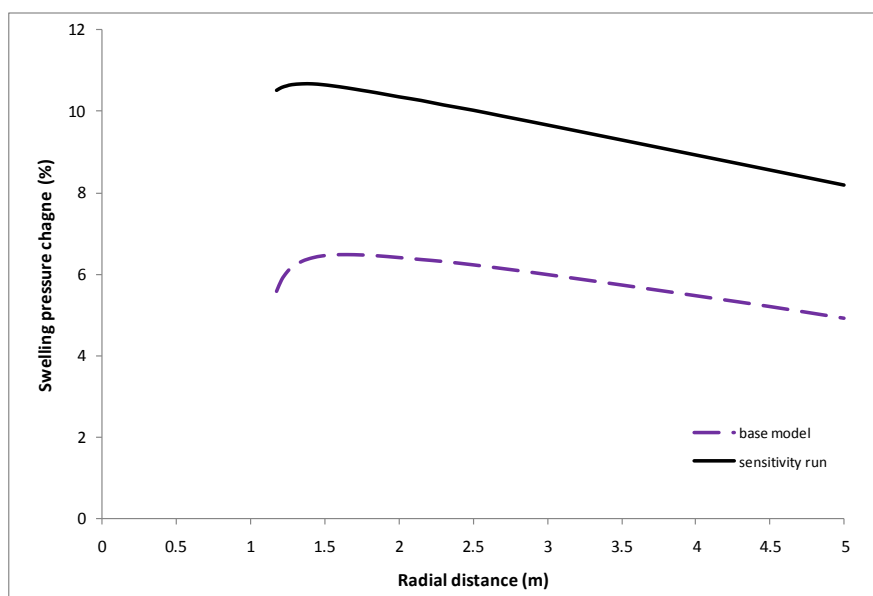
Figure 6.4-25. Comparison of swelling pressure at 100 years computed in the base model and a sensitivity run that does not consider the effect of the decrease of the volume fraction of smectite.

The effect of EBS hydration on swelling pressure change in the host clay rock: As the interaction of the EBS with host clay rock triggers all geochemical changes, the hydration rate of the EBS is expected to play a significant role in the geochemical evolution in the near field, and subsequently the changes in swelling properties. One of the key parameters that determine the hydration rate is the tortuosity of the vapor phase. Liu et al. (2010) shows that the geochemical evolution in EBS and the host clay rock is very sensitive to the tortuosity of the vapor phase in a coupled THC model. In the base model, the tortuosity is a function of the porosity and saturation degree (see Table 6.4-6), which is initially around 0.02 for bentonite and 0.5 for host clay rock. In a sensitivity run, the tortuosity is 0.8 for bentonite and 1.0 for host clay rock. An increase in tortuosity leads to a more rapid hydration of bentonite and therefore fast transport of ions from clay host rock to bentonite. As shown in Figure 6.4-26, at 1 year, the ionic strength

drops sharply in the sensitivity run; after 100 years, the ionic strength in sensitivity runs lower than that in the base run. In the sensitivity run, because bentonite contains more readily-dissolved minerals (mainly carbonate minerals) the dissolution of these minerals increases the ionic strength of the bentonite significantly. As a result, the ionic strength of the bentonite is slightly higher than that in the host clay rock after the bentonite becomes fully saturated, and the back-diffusion leads to an increase in ionic strength near the EBS-NS interface. That is why the spatial trend of ionic strength in the sensitivity run is different from that of base run.
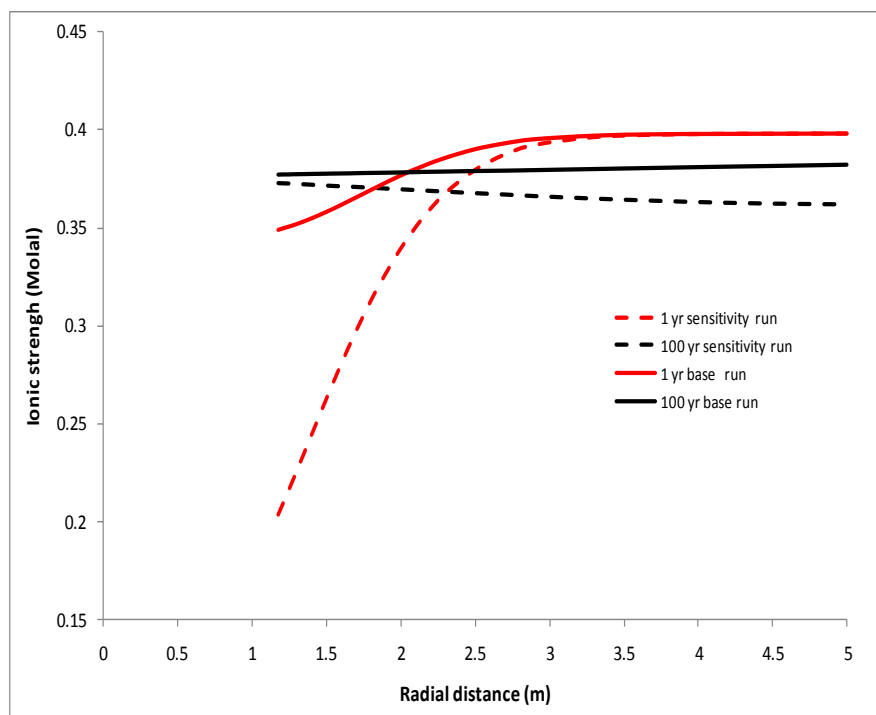
Figure 6.4-26. Computed ionic strength at 1 and 100 years in the base and sensitivity run

As a result of the rapid hydration of the bentonite, the illitization in the host clay rock is enhanced, as illustrated by the more significant dissolution of smectite (Figure 6.4-27) and precipitation of illite (Figure 6.4-28)
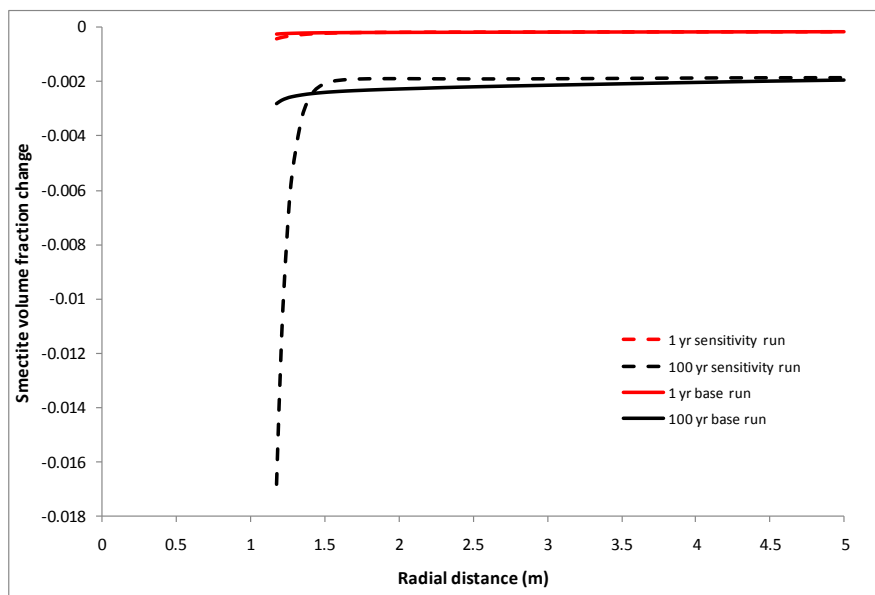
Figure 6.4-27. Computed smectite volume fraction change at 1 and 100 years in the base and sensitivity run.
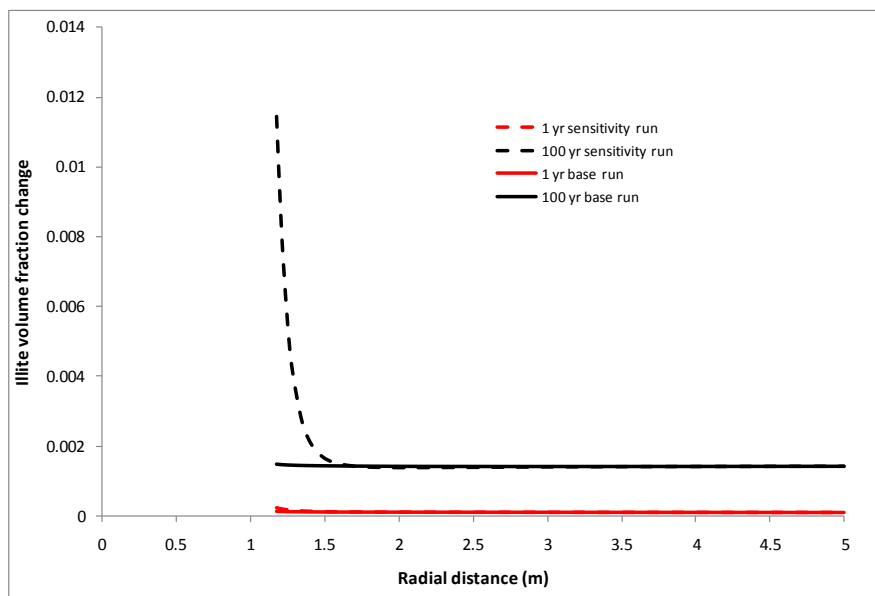
Figure 6.4-28. Computed illite volume fraction change at 1 and 100 years in base and sensitivity run.

Changes in the exchangeable cations are directly tied to the changes in concentration of aqueous cations. Figure 6.4-29 shows the changes in concentration of aqueous sodium and calcium. The concentration of aqueous sodium is mainly controlled by the transport processes, although the dissolution of the smectite affects it to some extent. After 100 years, the concentration of aqueous sodium shows a decreasing trend toward the EBS-HS interface. The concentration of aqueous calcium, on the other hand, is mainly controlled by the dissolution of calcite and shows an increasing trend toward the EBS-HS interface. As a consequence of the changes in concentration of aqueous sodium and calcium, exchangeable sodium and

calcium exhibit a similar trend to their aqueous counterparts (Figure 6.4-30). Compared to the model result in the base run, exchangeable sodium and calcium show more significant change. As a result, the weighted average valence shows remarkable change, rising from 1.28 to as high as 1.46, mainly caused by the increased exchangeable bi-valence cations (Figure 6.4-31).
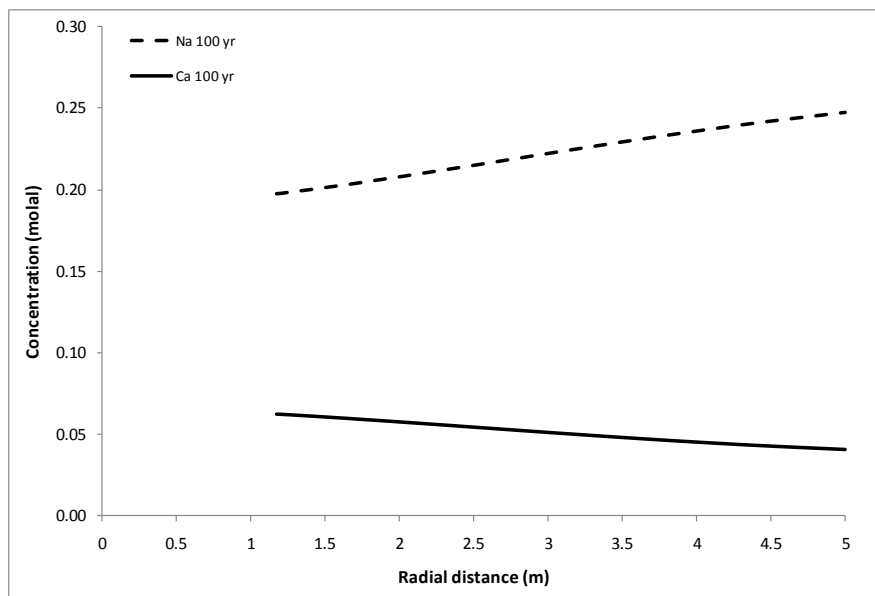
Figure 6.4-29. Computed concentration of aqueous sodium and calcium at 100 year in the sensitivity run.
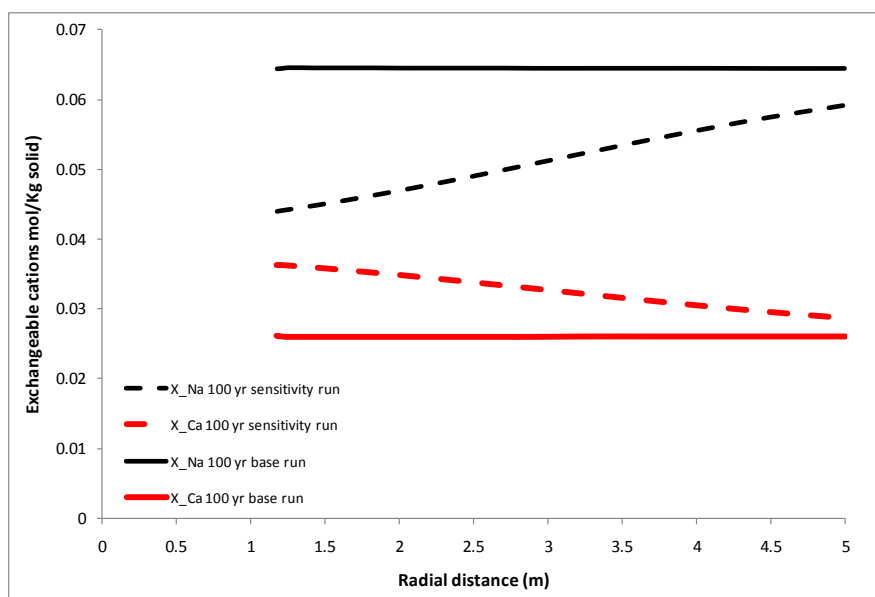
Figure 6.4-30. Computed concentration of exchangeable sodium and calcium at 100 year in the base and sensitivity run.
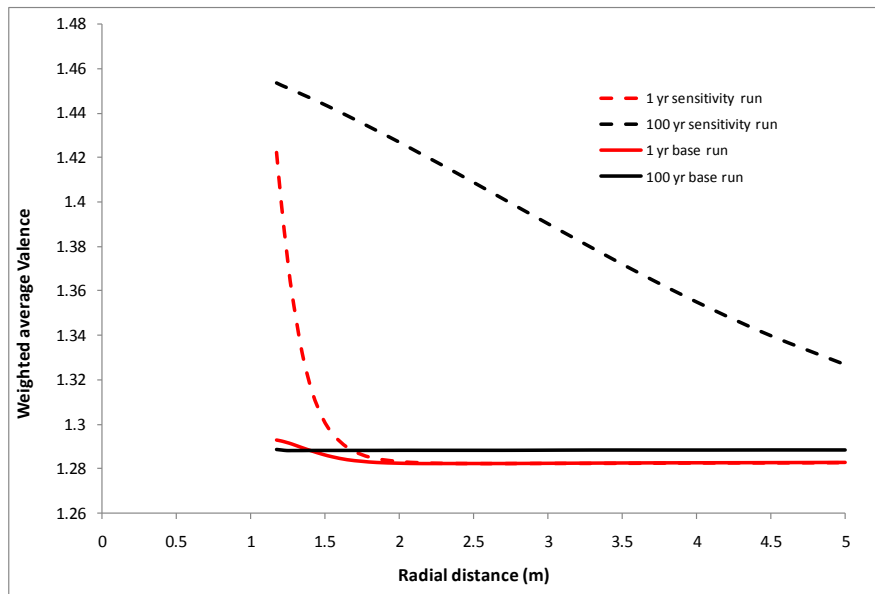
Figure 6.4-31. Computed weighted average valence at 1 and 100 year in the base and sensitivity run

As mentioned above, three types of geochemical change affect the swelling pressure: ionic strength, the volume fraction of smectite and the exchangeable cations (via weighted average valence). In the sensitivity run, the overall decrease in ionic strength tends to increase the swelling pressure, whereas the decrease in the volume fraction of smectite and increase in the weighted average valence of exchangeable cations tends to decrease the swelling pressure. The net effect is, as shown in Figure 6.4-32, a drop in swelling pressure, with a maximum drop of around 60% near the EBS-NS interface. Using Equation (6.4-21), the swelling induced porosity changes are calculated and the sensitivity run leads to a higher swelling-induced porosity, +0.08% in comparison with about -0.01% in the base run. However, the swelling-induced porosity change is still much smaller compared to the porosity change due to mineral precipitation/dissolution (Figure 6.4-33).
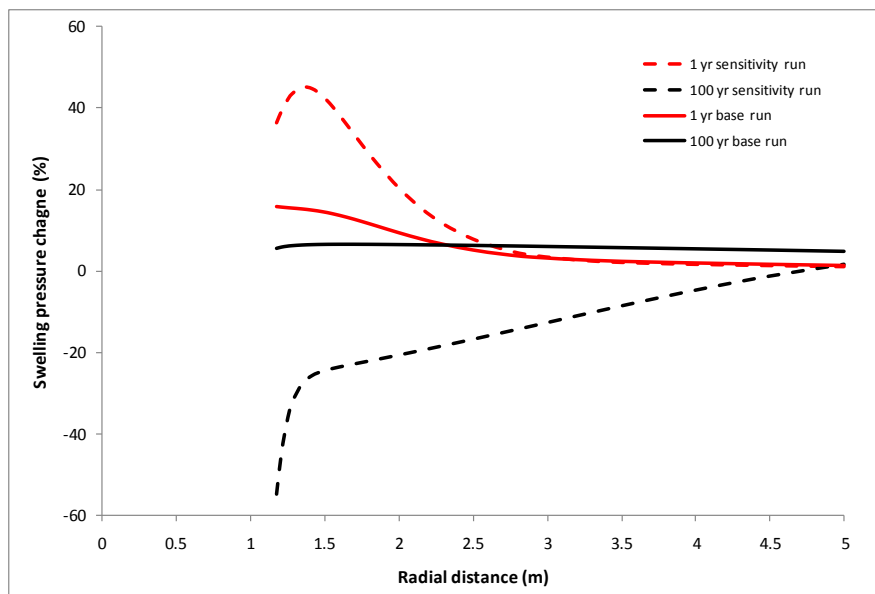
Figure 6.4-32. Computed swelling pressure at 1 and 100 years in the base and sensitivity run
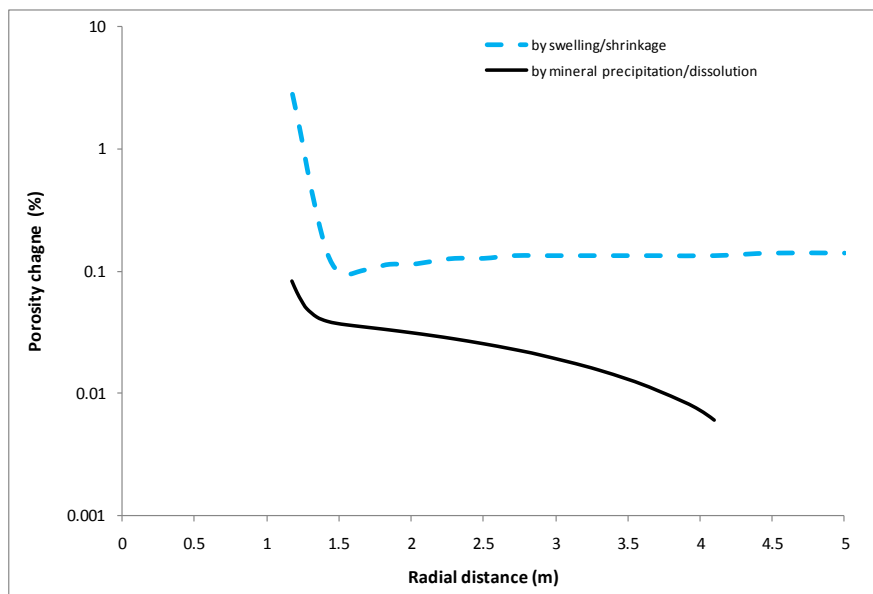
Figure 6.4-33. Porosity change (%) due to mineral precipitation/dissolution and swelling at 100 years in the sensitivity run

As we increase the hydration rate of the EBS in the sensitivity run, the geochemical response in the near-field host clay rock changes remarkably compared to the base run. One significant difference is the composition of exchangeable cations—a significant increase in exchangeable calcium in contrast with just a minor change in exchangeable calcium in the base run. As a result, the change in swelling pressure produced not only different magnitude of change but also a different trend — from a +5% to -60% decrease.

6.4.4 Conclusions

One advantage of emplacing radioactive waste in a clay formation is the potential self-sealing capability of the clay formation, due to its capacity for swelling. The swelling properties of the near-field host clay rock might change due to geochemical reasons (Thury, 2002; Wakim et al., 2009), including a change in ion concentration, exchangeable cations, or the amount of swelling clay minerals. Host clay rock, especially in the near-field area, undergoes geochemical changes due to the interaction between EBS and host clay rock, as demonstrated by THC models for EBS and host rock (Liu et al., 2010). It is therefore necessary to evaluate the geochemically induced changes in swelling properties in near-field host clay rock. In this report, coupled THC models are linked with a swelling model based on DDL theory, and these models are used to evaluate swelling-property changes in the near field of host clay rock.

Major findings based on our current modeling work include:

1) Moderate changes in swelling pressure caused by geochemical effects could be expected, with the possibility that significant change could occur depending on many hydrogeological and geochemical

parameters. Changes in hydration rate of the EBS (via the adjustment of tortuosity) could have a significant effect on the geochemically-induced changes in swelling pressure.

2) Geochemically-induced swelling/shrinkage occurs exclusively in the near-field area, within about 2 to 3 meters of the EBS-NS interface.

3) The swelling/shrinkage-induced porosity change is generally much smaller than that caused by mineral precipitation/dissolution.

4) The geochemically-induced swelling/shrinkage of host clay rock is the combined effect of variation in pore-water ion concentration, changes in exchangeable cations, and changes in the amount of smectite. Neglecting any of these three factors might lead to a miscalculation of geochemically induced swelling pressure.

6.5   Summary and Future Work

6.5.1   Summary

This report has addressed several aspects of hydro-mechanical-chemical coupled processes that are critical for understanding the behavior of an argillaceous host rock for disposal of high-level radioactive waste. By definition, mined geologic disposal involves the excavation of access and waste emplacement openings. Therefore, it is essential to be able to quantitatively predict the behavior of the system that results from the excavation disturbance. Excavation disturbances at a minimum result in changes in mechanical stress near the opening, simply as a result of the removal of rock to create the opening. However, other operational conditions, including tunnel ventilation, emplacement of unsaturated bentonite backfill, and waste heat, result in desaturation of the near-field rock and changes in the chemical composition of the near-field pore water.

Elastic strain-stress relationship under anisotropic stress conditions: The development of a DRZ in argillaceous rock has been well-documented in several studies conducted at underground research laboratories in Switzerland, Belgium, and France. A significant factor defining the DRZ is the development of fractures. Therefore, geomechanical modeling of the DRZ requires the consideration of the effects of fractures on the constitutive relationship between stress and strain. A new constitutive relationship, relating stress and strain for fractured porous rock, that accounts for the different geomechanical behavior of fractures and the general rock mass was documented in the FY10 natural systems report. The model development in the FY10 report was limited to isotropic geomechanical behavior. The new constitutive relationship has been extended here to address anisotropic stress conditions. Furthermore, the model development has also been advanced to describe the functional dependence of porosity and bulk compressibility on stress. Several comparisons with laboratory data on the mechanical response of clay, shale, and other rock types have shown that the nonlinearity introduced by the new constitutive model is needed to reflect the observed behavior.

Unsaturated properties for non-Darcian water flow in clay: Ventilation and the introduction of unsaturated bentonite backfill leads to desaturation of the host rock in the vicinity of the excavation boundary. Desaturation impacts the mechanical and chemical conditions in the rock, and therefore is important in the evolution of the DRZ. In addition, postclosure rehydration of the DRZ and EBS, an essential factor in the swelling of bentonite and sealing of the EBS and DRZ, is dependent on the

behavior of unsaturated flow in the near field. Experimental work on saturated and unsaturated flow through clay shows significant deviations from the traditional Darcy's law relationship between flux and the hydraulic gradient. A new constitutive relationship for unsaturated flow through clay, based on a non-Newtonian flow process, is presented. This leads to a nonlinear relationship between flux and the hydraulic gradient, and a new relationship between hydraulic conductivity and pore size. These results are used to develop a revised relationship between capillary pressure and relative permeability. The new constitutive relationships are fundamentally different from traditional relationships for saturated and unsaturated flow in porous media. Comparisons with data show that the new constitutive relationships are consistent with experimental observations of unsaturated flow through a compacted sand-bentonite mixture.

THM modeling in clay/shale environment: The TOUGH-FLAC thermal-hydrological-mechanical code was updated to include the new stress-strain constitutive model for isotropic conditions presented in Section 6.2.1. The code was used to model rock-mass deformation and pore pressure around an underground excavation, using published hydromechanical parameters and boundary conditions determined for the Opalinus Clay, Switzerland. The modeling considered water evaporation, volume shrinkage/swelling, and different orientations between the tunnel and clay bedding planes during the drying period, in addition to the newly implemented constitutive relationship. Results show that during a 3-year ventilation period: (1) rock dryout is limited to a 40 cm zone around the tunnel; (2) bedding-plane orientation relative to the tunnel has a pronounced effect on development of tensional stress, displacement in the roof and floor zone, and the pattern of extensional failure around the tunnel; and (3) the new constitutive model, as compared with a Hooke's law constitutive model, led to distinct differences in radial elastic deformation at roof and floor of the tunnel, stress distribution, porosity-permeability variation, and DRZ pattern around the tunnel.

THC modeling in a clay/shale environment: A Gouy-Chapman diffuse-double layer model for geochemically induced swelling and shrinkage was implemented in the TOUGHREACT thermal-hydrological-chemical code. Geochemical conditions, such as ion concentration and exchangeable cation compositon, can affect clay swelling. This process is important because fracture self-sealing in the DRZ is affected by swelling behavior. The main findings of the study are: (1) changes in swelling pressure caused by geochemical effects range from moderate to significant, depending on hydrogeologic and geochemical parameters, with particular sensitivity to the tortuosity; (2) geochemically induced swelling/shrinkage is limited to a 2 to 3 m zone at the drift wall; (3) mineral precipitation/dissolution dominates changes in porosity as compared with swelling/shrinkage effects; (4) geochemically-induced swelling/shrinkage depends on ion concentration, cation composition, and smectite content of the rock.

Integration with Other Work Packages: Research and development activities in the natural systems work package are being closely integrated with related activities in other work packages in which LBNL has been involved. For example, a protocol of fully coupled THMC simulators (TOUGHREACT-FLAC3D) is currently under development in the "Repository Science-THCM Near Field" work package. New constitutive models and methodologies developed here will be incorporated into the TOUGHREACT-FLAC3D simulator. This simulator is expected to provide modeling capabilities for THMC processes in the EBS. Constitutive relationships developed here will be incorporated into the TOUGHREACT-FLAC3D simulator employed for studying interactions between natural systems (clay formations) and the EBS. Furthermore, the work reported here supports the ongoing efforts to define FEPs for clay/shale repository host rock environments.

6.5.2 Future Work Activities

This subsection provides recommendations for future work activities on coupled processes related to DRZ evolution and its impact on performance of the natural engineering barrier in clay/shale repositories. While much progress has been made in improving our understand and predictive THM and THC capabilities for near-field behavior of clay/shale repositories, further developments are needed, as described below. It is expected, though, that our work will soon transition to a capability development and application/validation phase, in which international collaborations will be pursued to analyze/model relevant laboratory and particularly field data for clay rock (see Chapter 8 for international opportunities).

Development of constitutive relationship: Constitutive relationships refer to relationships among hydraulic, mechanical, thermal, and mechanical properties. The overall objective of this task is to develop advanced constitutive relationships for coupled processes in clay repository. It is expected that these relationships, with minor modifications, can also be applied to other geological formations. Recommended future work activities include:

- Our current focus has been on the elastic deformation regime for clay rock. The constitutive relationships developed here need to be further extended to plastic regimes. The impact of damage on mechanical and hydraulic properties will be investigated as well.
- While fractures are the key feature within the DRZ, studies on constitutive relationships for fractures are extremely limited for clay rock, especially when swelling/shrinkage processes are involved. In the FY10 report, we provided a preliminary model for a stress-dependence of fracture properties. We will continue the work to improve and validate that model. The fractured DRZ may also be characterized as a dual-continuum system. We will develop a dual-continuum approach for coupled hydro-mechanical processes in clay DRZ.
- As indicated in Section 6.2.2, conventional unsaturated flow relationships may not be able to capture near-field flow behavior (e.g., non-Darcian behavior), although they are still widely used in related simulators because of a lack of alternatives. Building on our study of non-Darcian flow, we are planning to develop new unsaturated flow relationships (among saturation, capillary pressure, relative permeability, and swelling) for clay rock.
- The data are key for developing and validating a variety of constitutive relationships. International collaborations will be perused to access laboratory and field data for clay rock from relevant international groups (Chapter 8).

THM modeling: Coupled THM processes are critical for DRZ formation and evolution in a clay repository. The overall objective of this task is to develop a modeling capability for the THM processes and an improved understanding of how these processes impact DRZ evolution within the context of performance assessment. Recommended work activities include:

- As demonstrated in Section 6.2, constitutive relationships have an important impact on THM simulation results. We will continue to incorporate the new development of constitutive relationships to improve our THM modeling capability.
- Understanding and modeling DRZ formation and evolution is both an important task and a great challenge. Recently, Tang and Hudson (2010) demonstrated that failure processes for brittle rocks could be realistically captured by using fine-grid numerical simulations and taking into account the spatial variability of mechanical properties. Rock failure (or formation of DRZ) is more complex, because it involves unsaturated flow, swelling/shrinkage, and the saturation dependence of mechanical properties. We will explore the feasibility of using the Tang and Hudson's (2010) approach in clay rock. The TOUGH-FLAC3D will be used for this activity.
- Chapter 8 presents international opportunities involving international field tests in clay formations. We will apply our THM modeling capabilities to modeling the relevant field tests,

with a focus on validating our models with experimental observations and improving our understanding of the coupled processes.

THC modeling: An understanding of the geochemical evolution of host clay formations (including the DRZ) is critical to understanding repository performance. With the objective of developing a model capability for the coupled THC processes and improving the understanding of the effect of THC processes on the transport of radionuclides through the clay formation, the following future research is recommended.

- Our current model focuses on changes in aqueous species and mineral precipitation/dissolution. Incorporation of surface complexation in the THC model is clearly needed, because surface complexation provides a useful tool to calculate the adsorption/desorption of behavior of ions (including radionuclides) while considering the competition between ions and changes in pore-water geochemistry
- Radionuclide transport will be coupled to the full THC model, to test the THC modeling tools and improve our understanding of radionuclide transport in coupled systems.
- The coupled THC behavior of clay formations will be greatly boosted by a better understanding of the *in situ* water-rock interaction, which requires a more accurate characterization of the geochemistry of pore water and of the solid phase. Any accomplishment archived under research topic P7, Novel *in situ* technique for groundwater chemistry characterization (Wang, 2011), should therefore be monitored, and any experimental results arising from international collaboration should be considered.
- When international opportunities that involve international field tests in clay formations arise, our THC model will applied to such field tests to validate the model and improve our understanding.

6.6   References

Alonso E. E., Gens A., and Josa A. (1990) A constitutive model for partially saturated soils. Géotechnique, 40(3): 405-430.

Barnichon J.D. and Volckaert G. (2003) Observations and Predictions of Hydromechanical Coupling Effects in the Boom Clay, Mol Underground Research Laboratory, Belgium, *Hydrogeology Journal* 11 (1), 193-202.

Bobet A., Atistorenas G., and Einstein H. (1998) Feasibility Analysis for a Radioactive Waste Repository Tunnel. *Tunneling and Underground Space Technology*, 13(4), 409-426.

Bock, H., Dehandschutter B., and Martin, C. D. (2010) Self-sealing of fractures in argillaceous formations in the context of geological disposal of radioactive waste, Review and Synthesis. *Nuclear Energy Agency*, ISBN 978-92-64-99095-1.

Bolt G. H. (1956) Physico-chemical analysis of the compressibility of pure clays. Géotechnique 6(2), 86–93.

Bossart P., Meier P. M., and Moeri, A. (2002) Geological and hydraulic characterization of the excavation disturbed zone in the Opalinus Clay of the Mont Terri Rock Laboratory. *Engineering Geology*, 66, 19-38.

Brady B. T. (1969) The nonlinear mechanical behavior of brittle rock Part I—Stress-strain behavior during regions I and II, *International Journal of Rock Mechanics and Mining Sciences*, 6,211-225

Brooks R. H. and Corey A. T. (1964) Hydraulic properties for porous media, *Hydro. Rep. No. 3*, Colorado State University, Fort Collins.

Brown E. T., Bray J. W., and Santarelli F.J. (1989) Influence of stress-dependent elastic-modulus on stresses and strains around axisymmetric boreholes, *Rock mechanics and rock engineering* ,22,189-203

Burdine N. T. (1953) Relative permeability calculations from pore size distribution data, *Am. Ins. Min. Metail. Pet. Eng,* 198, 71-77.

Causarano H. (1993) Factors affecting the tensile strength of soil aggregates. *Soil & Tillage Research*, 28, 15-25.

Cazacu O. (1999) On the choice of stress-dependent elastic modulus for transversely isotropic solids, Mechanics *Research Communications*, 26, 45-54

Christopher R. H. and Middleman, S. (1965) Power-law flow through a packed tube, *I and EC Fundamentals*, 4(4), 422-426.

Corkum A. G. and Martin C. D. (2007a) The mechanical behaviour of weak mudstone (Opalinus Clay) at low stresses, *International Journal of Rock Mechanics & Mining Sciences,* 44, 196-209.

Corkum A. G. and Martin C. D. (2007b) Modelling a mine-by test at the Mont Terri rock laboratory, Switzerland. *International Journal of Rock Mechanics & Mining Sciences,* 44, 846-859.

Cuadros J. (2006) Modeling of smectite illitization in burial diagenesis environments. Geochimica et Cosmochimica Acta 70(16), 4181-4195.

Cui Y. J., Tang A. M., Loiseau C., and Delage P. (2008) Determining the unsaturarted hydraulic conductivity of a compacted sand-bentonite mixture under constant-volume and free-swell conditions, Physics and Chemistry of the Earth, 33, S462-S471.

Daniel D. E. (1982) Measurement of hydraulic conductivity of unsaturated soils with thermocouple psychrometers, Soil Science Society of America Journal **20** (6), pp. 1125–1129.

Dixon D. A., Graham J., and Gray M.N. (1999) Hydraulic conductivity of clays in confined tests under low hydraulic gradients, *Can. Geotech. J*., 36, 815-825.

Edlefsen N. E., Anderson A. B. C. (1943) Thermodynamics of soil moisture, *Hilgardia*, 15 (2), 31-298.

El-Swaify S. A. and Henderson D. W. (1967) Water retention by osmotic swelling of certain colloidal clays with varying ionic composition. Journal of Soil Science 18(2), 223-232.

ENRESA (2000) Full-scale engineered barriers experiment for a deep geological repository in crystalline host rock FEBEX Project, European Commission. EUR 19147 EN.

Erdal Ç. and Tilgen H. P. (2010) Shear strength-suction relationship of compacted Ankara clay. *Applied Clay Science* 49, 400-404.

Erguler Z. A., Ulusay R. (2009) Water-induced variations in mechanical properties of clay-bearing rocks. *International Journalof Rock Mechanics & Mining Sciences,* 46, 355-370.

Fernández A. M., Turrero M. J., Sánchez D. M., Yllera A., Melón A. M., Sánchez M., Peña J., Garralón A., Rivas P., Bossart P., and Hernán, P. (2007) On site measurements of the redox and carbonate system parameters in the low-permeability Opalinus Clay formation at the Mont Terri Rock Laboratory. Physics and Chemistry of the Earth, Parts A/B/C 32(1-7), 181-195.

Fouche O., Wright H., Cleach J. L., and Pellenard P. (2004) Fabric Control on Strain and Rupture of Heterogeneous Shale Samples by Using a Non-Conventional Mechanical Test, *Applied Clay Science* 26, 367-387.

Freed A. D. (1995) Natural Strain, *Journal of Engineering Materials and Technology*, 117, 379-385.

Gens A. and Alonso E. E. (1992) A framework for the behaviour of unsaturated expansive clays. Canadian Geotechnical Journal, 29: 1013-1032.

Gercek H. (2007) Poisson's ratio values for rocks, *International Journal of Rock Mechanics and Mining Sciences*, 44, 1-13

Ghassemi A. and Diek A. (2003) Linear chemo-poroelasticity for swelling shales: theory and application. Journal of Petroleum Science and Engineering 38(3-4), 199-212.

Ghorbani A., Zamora M., and Cosenza P. (2009) Effects of desiccation on the elastic wave velocities of clay-rocks. *International Journal of Rock Mechanics & Mining Sciences,* 46, 1267-1272.

Gonzales S. and Johnson K. S. (1984) *Shale and other argillaceous strata in the United States*. Oak Ridge National Laboratory. ORNL/Sub/84-64794/1.

Guimarães L. D., Gens A., and Olivella S. (2007) Coupled thermo-hydro-mechanical and chemical analysis of expansive clay subjected to heating and hydration. Transport in Porous Media, 66 (3): 341-372.

Hansbo S. (2001) Consolidation equation valid for both Darcian and non-Darcian flow, *Geotechnique*, 51(1), 51-54.

Hu Y. and Liu G.T. (2004) Behavior of soft rock under multiaxial compression and its effects on design of arch dam, *Chinese journal of rock mechanics and engineering*, 23, 2494-2498

Itasca Consulting Group Inc. (2001) FLAC-3D Manual: Fast Lagrangian analysis of continua in 3 dimensions–Version 3.1. Itasca Consulting Group Inc., Minnesota, USA.

Jaeger J. C., Cook N. G. W., and Zimmerman R.W. (2007) *Fundamentals of rock mechanics*,4th Edition, Blackwell, Oxford.

Jobmann M., Wilsnack Th., and Voigt H.-D. (2010) Investigation of damage-induced permeability of Opalinus clay. *International Journal of Rock Mechanics & Mining Sciences*, 47, 279-285.

Johnson P. A. and Rasolofosaon P. N. J. (1996) Nonlinear elasticity and stress-induced anisotropy in rock, *Journal of Geophysical Research*, 101, 3113-3124.

Jougnot D., Revil A., Lu N., and Wayllace A. (2010) Transport properties of the Callovo-Oxfordian clay rock under partially saturated conditions. Water Resources Research 46.

Kamei G., Mitsui M. S., Futakuchi K., Hashimoto S., and Sakuramoto Y. (2005) Kinetics of long-term illitization of montmorillonite - a natural analogue of thermal alteration of bentonite in the radioactive waste disposal system. Journal of Physics and Chemistry of Solids 66(2-4), 612-614.

Komine H. and Ogata N. (1996) Prediction for swelling characteristics of compacted bentonite. Canadian Geotechnical Journal 33, 11-22.

Komine H. and Ogata N. (2003) New equations for swelling characteristics of bentonite-based buffer materials. Canadian Geotechnical Journal 40, 460-475.

Kouakou C. H. and Morel J. C. (2009) Strength and elasto-plastic properties of non-industrial building materials manufactured with clay as a natural binder. *Applied Clay Science,* 44, 27-34.

Leverett M. C. (1941) Capillary behavior in porous solids, *Trans. Am. Inst. Min. Metall. Eng.,* 142, 152-169.

Lionço A. and Assis A. (2000) Behavior of deep shafts in rock considering nonlinear elastic models, *Tunnelling and Underground Space Technology*, 15, 445-451.

Liu H. H., Rutqvist J., and Berryman J. G. (2009) On the relationship between stress and elastic strain for porous and fractured rock, *International Journal of Rock Mechanics and Mining Sciences ,*46, 289-296

Liu H. H, Rutqvist J., Zheng L., Sonnenthal E., Houseworth J. and Birkholzer J. (2010) Modeling coupled process in clay formation for radioactive waste disposal. Lawrence Berkeley National Laboratory report, LBNL-3900E.

Lopez X., Valvatne P. H., Blunt M. J. (2003) Predictive network modeling of single-phase non-Newtonian flow in porous media, *Journal of Colloid and Interface Science*, 264, 256-265.

MacBeth C. (2004) A classification for the pressure-sensitivity properties of a sandstone rock frame, *Geophysics*, 69, 497–510

Madsen F. T. and Muller-vonmoss M. (1985) Swelling pressure calculated from mineralogical properties of a jurassic opalinum shale, switzerland. Clays and Clay Min. 33(6), 501-509.

Mavko G. M. and Nur A. (1978) The effect of nonelliptical cracks on the compressibility of rocks, *Journal of Geophysical Research*, 83, 4459-4468

Mayer G., Klubertanz G., and Croise J. (2007) Modelling of an in situ ventilation experiment in the Opalinus Clay. *Physics and Chemistry of the Earth,* 32, 629-638.

Mayor J.-C., Velasco M., and García-Siñeriz, J.-L. (2007) Ventilation experiment in the Mont Terri underground laboratory. Physics and Chemistry of the Earth, 32, 616-628.

Meier P., Trick T., Blumling P., and Volckaert G. (2000) Self-Healing of Fractures within the EDZ at the Mont Terri Rock Laboratory: Results after One Year of Experimental Work. In: *Proceedings of the International Workshop on Geomechanics, hydromechanical and Thermomechanical Behavior of deep argillaceous Rocks: Theory and Experiments*, Paris, October11-12, 2000.

Mitchell J. K. and Soga K. (2005) Fundamentals of Soil Behavior, John Wiley & Sons INC.

Montes-Hernandez G., Duplay J., Martinez L., and Mendoza, C. (2003) Swelling–shrinkage kinetics of MX80 bentonite. *Applied Clay Science,* 22, 279-293.

Montes-Hernandez G., Fritz B., Clement A., and Michau, N. (2005) A simplified method to evaluate the swelling capacity evolution of a bentonite barrier related to geochemical transformations. Appl. Geochem. 20(2), 409-422.

Morgenstern N. R. and Tamuly Phukan A. L. (1969) Non-linear stress-strain relations for a homogeneous sandstone*, International Journal of Rock Mechanics and Mining Sciences*, 6,127-142

Mualem Y. (1976) A new model for predicting the hydraulic conductivity of unsaturated porous media. *Water Resour. Res*, 12, 513-522.

Nur A. (1971) Effects of stress on velocity anisotropy in rocks with cracks, *Journal of Geophysical Research* ,76,2022–2034

Nutt M. (2011) *Used Fuel Disposition Campaign Disposal Research and Development Roadmap* (FCR&D-USED-2011-000065 REV0), U.S. DOE Used Fuel Disposition Campaign.

Olalla C., Martin M., and Sáez J. (1999) *ED-B experiment: geotechnical laboratory test on Opalinus Clay rock samples*,Technical report TN98-57, Mont Terri Project.

Onikata M., Kondo M., Hayashi N., and Yamanaka S. (1999) Complex formation of cation-exchanged montmorillonites with propylene carbonate; osmotic swelling in aqueous electrolyte solutions. Clay Clay Min. 47(5), 672-677.

Ochs M., Lothenbach B., Shibata M., and Yui M. (2004) Thermodynamic modeling and sensitivity analysis of porewater chemistry in compacted bentonite, Physics and Chemistry of the Earth, Parts A/B/C, Volume 29, Issue 1, 129-136.

Panayiotopoulos, K. P. (1996) The effect of matric suction on stress-strain relation and strength of three Alfisols. *Soil & Tillage Research*, 39, 45-59.

Pascal, H. (1983) Rheological behavior effect of non-Newtonian fluids on steady and unsteady flow through a porous medium, *International Journal for Numerical and Analytical Methods in Geomechanics*, 7, 289-303.

Patriarche D., Ledoux E., Simon-Coincon R., Michelot J., and Cabrera J. (2004) Characterization and Modeling of Diffusive Process for Mass Transport through the Tournemire Argillites Aveyron, France, *Applied Clay Science* 26: 109-122, 2004.

Peng S. P. and Zhang J. C. (2007) *Engineering geology for underground rocks*, Spring Berlin Heidelbery, New York

Pham O. T., Vales F., Malinsky L., Nguyen Minh D., and Gharbi H. (2007) Effects of desaturation-resaturation on mudstone. *Physics and Chemistry of the Earth,* 32, 646-655.

Poisson S.D. (1829) Mémoire sur les equations generates de l'équilibre et du nouvement des corps silides élastiques et de fluids, *Journal de l'École Poly technique*, 13,1–174

Popp T., Salzer K., and Minkley W. (2008) Influence of bedding planes to EDZ-evolution and the coupled HM properties of Opalinus Clay. *Physcis and Chemistry of the Earth*, 33, S374-S387.

Pruess K. (2004) The TOUGH codes: A family of simulation tools for multiphase flow and transport processes in permeable media. Vadose Zone Journal, 3, 738-746.

Pruess K., Oldenburg C. M., Moridis G. (1999) TOUGH2 USER'S GUIDE, VERSION 2.0, Earth Sciences Division, Lawrence Berkeley National Laboratory, University of California, Berkeley, California 94720.

Pusch R. and Madsen F. T. (1995) Aspects on the illitization of the kinnekulle bentonites. Clay Clay Min. 43(3), 261-270.

Pusch R., Kasbohm J., and Thao, H. T. M. (2010) Chemical stability of montmorillonite buffer clay under repository-like conditions-A synthesis of relevant experimental data. Appl. Clay Sci. 47(1-2), 113-119.

Rutqvist J. (2011) Status of the TOUGH-FLAC simulator and recent applications related to coupled fluid flow and crustal deformations. *Computers &Geosciences*, doi:10.1016/j.cageo.2010.08.006.

Rutqvist J. and Tsang, C.-F. (2003) TOUGH-FLAC: a numerical simulator for analysis of coupled thermal-hydrologic-mechanical processes in fractured and porous geological media under multi-phase flow conditions. In: Proceedings of the TOUGH Symposium 2003, Lawrence Berkeley National Laboratory, Berkeley, May 12-14.

Rutqvist J., WuY.-S., Tsang C.-F., and Bodvarsson G. (2002) A modeling approach for analysis of coupled multiphase fluid flow, heat transfer, and deformation in fractured porous rock. *International Journal of Rock Mechanics and Mining Sciences*, 39, 429-442.

Rutqvist J., Ijiri Y., and Yamamoto H. (2011) Implementation of the Barcelona Basic Model into TOUGH–FLAC for simulations of the geomechanical behavior of unsaturated soils. *Computers &Geosciences*, doi:10.1016/j.cageo.2010.10.011.

Samper J., Yang Q., Yi S., Garcia-Gutierrez M., Missana T., Mingarro M., Alonso U., and Cormenzana, J. L. (2008) Numerical modeling of large-scale solid-source diffusion experiments in Callovo-Oxfordian clay. Phys. Chem. Earth 33, S208-S215.

Schanz T. and Tripathy S. (2009) Swelling pressure of a divalent-rich bentonite: Diffuse double-layer theory revisited. Water Resour. Res. 45, W00C12.

Shao H., Schuster K., Sönnke J., and Bräuer V. (2008) EDZ development in indurated clay formations – In situ borehole measurements and coupled HM modeling. *Physics and Chemistry of the Earth*, 33, S388–S395.

Shapiro S. A. and Kaselow A. (2005) Porosity and elastic anisotropy of rocks under tectonic stress and pore-pressure changes, *Geophysics*, 70, N27–N38

Sonnenthal E., Ito A., Spycher N., Yui M., Apps J., Sugita Y., Conrad M., and Kawakami S. (2005) Approaches to modeling coupled thermal, hydrological, and chemical processes in the Drift Scale Heater Test at Yucca Mountain. *International Journal of Rock Mechanics and Mining Sciences*, 42, 6987-719.

Spycher N.F., Sonnenthal E.L., Apps J.A. (2003) Fluid flow and reactive transport around potential nuclear waste emplacement tunnels at Yucca Mountain, Nevada. Journal of Contaminant Hydrology, 62–63, 653–673.

Sridharan A. and Jayadeva M. S. (1982) Double layer theory and compressibility of clays. Geotechnique 32(2), 133-144.

Tang C. A. and Hudson J.A. (2010) *Rock Failure Mechanisms*, Taylor & Francis, London, UK.

Thomas H. R. and He Y. (1998) Modelling the behaviour of unsaturated soil using an elastoplastic constitutive model. Géotechnique, 48(5): 589-603.

Thury M. (2002) The characteristics of the Opalinus Clay investigated in the Mont Terri underground rock laboratory in Switzerland. Comptes Rendus Physique 3(7-8), 923-933.

241

Tien Y. M., Lee D. H., and Juang C. H. (1990) Strain, pore pressure and fatigue characteristics of sandstone under various load conditions, *International Journal of Rock Mechanics and Mining Sciences*, 27, 283-289.

Towner G. D. (1987) The Tensile Stress Generated in Clay through Drying. *J. agric. Engng Res*. 37, 279-289.

Tripathy S., Sridharan A., and Schanz T. (2004) Swelling pressures of compacted bentonites from diffuse double layer theory. Canadian Geotechnical Journal 41, 437-450.

Tsang C.-F., Bernier F., and Davies C. (2005) Geohydromechanical processes in the Excavation Damaged Zone in crystalline rock, rock salt, and indurated and plastic clays—in the context of radioactive waste disposal. *International Journal of Rock Mechanics & Mining Sciences*, 42, 109-125.

Van Genuchten M. (1980) A closed-form equation for predicting the hydraulic conductivity of unsaturated soil, *Soil. Sci. Soc. Am. J.*, 44(5), 892-898.

van Olphen H. (1977) An Introduction to Clay Colloid Chemistry: For Clay Technologists, Geologists and Soil Scientists, Wiley-Interscience, New York.

Wakim J., Hadj-Hassen F., and DeWindt L. (2009) Effect of aqueous solution chemistry on the swelling and shrinkage of the Tournemire shale. International Journal of Rock Mechanics & Mining Sciences 46, 1378-1382.

Walsh J. B. (1965) The effect of cracks on the uniaxial elastic compression of rocks, *Journal of Geophysical Research*,70, 399–411

Wang Y. (2011) Research & Development (R&D) *Plan for Used Fuel Disposition Campain (UFDC) Natural System Evaluation and Tool Development*, U.S. DOE Used Fuel Disposition Campaign.

Wayllace, A., 2008. Volume change and swelling pressure of expansive clay in the crystalline swelling regime, University of Missouri. Ph.D.

Wu Y.S. and Pruess K. (1998) A numerical method for simulating non-Newtonian fluid flow and displacement in porous media, *Advances in Water Resources*, 2, 351-362.

Xu G. M., Liu Q. S., Peng W. W., and Chang X. (2006a) Experimental study on basic mechanical behaviors of rocks under low temperatures*, Chinese Journal of Rock Mechanics and Engineering*, 25, 2502-2508

Xu T., Sonnenthal E., Spycher N., and Pruess K. (2006b) TOUGHREACT: A Simulation Program for Non-isothermal Multiphase Reactive Geochemical Transport in Variably Saturated Geologic Media. Computers and Geosciences, 32, 145-165.

Xu T., and Pruess K. (2001) Modeling multiphase non-isothermal fluid flow and reactive geochemical transport in variably saturated fractured rocks: 1. Methodology. American Journal of Science, 301, 16-33.

Xu T., Spycher N., Sonnenthal E., Zhang G., Zheng L., and Pruess K. (2011) TOUGHREACT Version 2.0: A simulator for subsurface reactive transport under non-isothermal multiphase flow conditions. Computers & Geosciences 37(6), 763-774.

Yang Y. L. and Aplin A. C. (2010) A permeability-porosity relationship for mudstones. *Marine and Petroleum Geology*, 27, 1692-1697.

Zhang C.-L. and Rothfuchs T. (2008a) Damage and sealing of clay rocks detected by measurements of gas permeability. *Phys. & Chem. Of the Earth*, 33, 363-373.

Zhang C.-L., Rothfuchs T., Dittrich J., and Muller J. (2008b) Investigations on self-sealing of indurated clay. –GRS Report, GRS-230: 1-67, ISBN 978-3-939355-04-5.

Zhang C.-L., Rothfuchs T., Su K., and Hoteit N. (2007) Experimental study of the thermo-hydro-mechanical behaviour of indurated clays. *Physics and Chemistry of the Earth,* 32, 957-965.

Zhang G., Spycher N., Sonnenthal E., Steefel C., and Xu T. (2008c) Modeling reactive multiphase flow and transport of concentrated aqueous solutions. Nuclear Technology, 164, 180-195.

Zheng L., Apps J. A., Zhang Y., Xu T., and Birkholzer J. (2009) On mobilization of lead and arsenic in groundwater in response to CO_2 leakage from deep geological storage. Chemical Geology, 268, 281-297.

Zou Y. (1996) A non-linear permeability relation depending on the activation energy of pore liquid, *Geotechnique*, 46(4), 769-774.

Chapter 7: Evaluation of the Concept of Direct Disposal of Electrorefiner Salt in a Salt Repository

7.1   Introduction

The United States is now reconsidering its nuclear waste disposal policy and re-evaluating the option of moving away from the current once-through open fuel cycle to a closed fuel cycle. This policy shift creates a unique opportunity for exploring new concepts and ideas that can potentially lead to the development of transformational technologies for an efficient and clean nuclear fuel cycle. In FY10, the concept of combining electrorefining (ER) fuel reprocessing with direct disposal of ER salt waste in a salt geologic repository was explored (Wang et al., 2011). It has been shown that this new concept may be able to significantly simplify key steps of a fuel cycle including fuel reprocessing, waste form development, and waste disposal. This chapter documents the results of further testing of this new concept. This work directly addresses research topics S1 and S9; and it provides a good example of how the choice of nuclear waste disposal option may have significant impacts on the development of overall fuel cycle.

The direct disposal concept was proposed baased on the consideration of the roles of salt in key steps of a nuclear fuel cycle. In a closed fuel cycle, used fuels will be reprocessed and useful components such as uranium or transuranics will be recovered for reuse (e.g., Bodansky, 2006). Two general fuel reprocessing technologies are currently under consideration: the aqueous process and the electrorefining (ER) process (e.g., Simpson and Law, 2010). For the case of aqueous reprocessing, used fuel is dissolved in nitric acid; the uranium (and also plutonium if needed) is then extracted through a complex set of aqueous chemical processes; and the fission products and minor actinides remain as wastes for permanent disposal. In the ER process, metallic used fuel (or reduced oxide fuel) is loaded into anode baskets and lowered into a vessel containing molten chloride salt. When electric current is passed through the salt, the uranium, transuranics, and active metal fission products become oxidized and dissolved in the molten salt. Pure uranium is simultaneously recovered at the primary cathode where it deposits as a metal. A mixture of uranium and transuranics can be periodically recovered from the molten salt using a secondary cathode (e.g., Simpson and Law, 2010; Inoue and Koch, 2008).   The ER process has certain advantages over the aqueous process (Chang and Till, 1991; Chang, 2007). First of all, compared to the aqueous process, ER is relatively compacted and does not involve complex aqueous chemistry. Furthermore, since plutonium is always co-deposited with other actinides, the ER does not produce a pure plutonium product, which is a proliferation-resistant feature. Also, the ER process is highly compatible with metallic fuel fast reactors, because the fuel components extracted from the ER will already be in a metal alloy form. Due to its compactness, the ER facility can be co-located with the fast reactor, thus eliminating the need for off-site shipments. In addition, for electrorefining all reagents, such as electrolyte salts can be recycled, thus minimizing process waste streams. Based on all these considerations, the ER may have a significant financial benefit over the aqueous process.

As potential high-level waste disposal media, salt formations have several unique characteristics. First of all, salt formations are relatively widely spread. They are generally located in stable geologic settings and have existed underground for millions of years (Lowenstein et al., 2005; Satterfild et al., 2005). Salt is essentially impermeable, with typical porosity of 1% and permeability less than 10^{-21} m^2 (Beauheim and Roberts, 2002). It has been found in Salado Formation at the Waste Isolation Pilot Plant (WIPP) site that closely spaced brine weeps in the excavation display distinct chemical compositions (Krumhansl et al., 1991), indicating lack of fluid communication over geological time scales. The pore diffusivity is

estimated to be on the order of 10^{-16} m^2/s (Beauheim and Roberts, 2002). A salt disposal environment also provides favorable chemical conditions for waste isolation, with relatively low Eh (~ -150 mV) and near-neutral pH (Brush, 1990). Also due to the high ionic strength, any colloidal suspension will be unstable in that environment. All these conditions result in overall low radionuclide solubility and mobility in a salt repository (Wang et al., 2011). In addition, salt is plastic and fractures in salt are self-healing. Both experimental and modeling studies show that damaged WIPP rock salt heals within 25 hours under hydrostatic stress of 14.48 MPa (Chan et al., 2001). Waste packages emplaced in a salt repository are expected to be quickly encapsulated by impermeable salt through salt creep.

Futhermore, the ER waste salt itself can be an ideal waste form for disposal in a salt repository. A thermodynamic calculation has shown that WIPP brines are at or close to equilibrium with both major and minor minerals in the formation, including halite (NaCl), sylvite (KCl), glaserite [NaK$_3$(SO$_4$)$_2$], anhydrite (CaSO$_4$), and calcite (CaCO$_3$). Note that typical ER salt waste contains more than 50% of NaCl and KCl in mass fractions (Wang et al., 2011). If it is assumed that the rest of salt components are embedded as inclusions in the matrix of NaCl and KCl, the ER salt waste will be highly durable and potentially thermodynamically stable, in a salt environment. The direct disposal concept would simplify the ER process with respect to the currently proposed waste stream treatment. Basically, it would eliminate all process steps related to waste treatment and waste form development. The benefit of this is obvious, both financially and technologically. Besides the advantages of the ER process over the aqueous process mentioned above, the direct disposal concept would add an additional incentive to the ER process in terms of waste treatment and disposal. The baseline waste processing plan is to combine the salt with zeolite-4A and glass frit to form a ceramic waste form. This ceramic waste form would be considered high level waste (HLW) and would eventually be shipped to a permanent geologic repository. The problems with this approach include high cost and duration for processing the salt into the ceramic waste form. The other problem is that this increases the mass of the waste by about a factor of 10. The direct disposal concept may provide an alternative to the existing baseline approach, resulting in significfant waste volume reduction for disposal.

Electrorefining is currently being performed on spent fuel from the Experimental Breeder Reactor-II (EBR-II) using two systems. One is called the Mark-IV electrorefiner (ER) and is used to process driver fuel containing high-enriched U. The other is the Mark-V ER and is used to process blanket fuel containing depleted U and a relatively high concentration of Pu-239. There is approximately 1 metric ton (MT) of salt contained in these electrorefiners. That amount will increase with further processing of spent fuel over the next 5 to 15 years. The salt is primarily LiCl-KCl in eutectic ratio but also contains NaCl, UCl$_3$, and numerous fission product and transuranic chlorides. Active metal species from the spent fuel are converted to chlorides and partition into the salt phase during each and every electrorefining run. The baseline processing plan is to combine the salt with zeolite-4A and glass frit to form a ceramic waste form. This ceramic waste form would be considered high level waste (HLW) and would eventually be shipped to a permanent geologic repository. The problems with this approach include high cost and duration for processing the salt into the ceramic waste form. The other problem is that this increases the mass of the waste by about a factor of 10. The direct disposal concept may provide an alternative to the existing baseline approach, resulting in significfant waste volume reduction for disposal.

To further advance the direct disposal concept requires better understanding of both the ER process and the near-field evolution of a salt repository. For the ER process, a better understanding of the phase changes during molten salt cooling is needed. This could reveal the importance of striving for tighter process control with respect to cooling rate and salt composition to ensure effective encapsulation of radionuclide inclusions by the NaCl and KCl matrix. With respect to disposal, there is a need to predict ER salt behavior in a salt repository environment. FY11 work was focused on the development of experimental techniques for characterizing microstructure of ER salt and testing the stability of ER salt in simulated repository environments.

7.2   Microstructural Characterization of ER Salt

To better understand fundamental mechanisms of electrorefiner salt dissolution in a salt-based repository environment, an evaluation was performed of the phases in a solidified surrogate salt. A salt mixture was prepared that consisted of a full suite of non-radioactive fission product chlorides (commercially available). The composition for these mixtures is given in Table 7-1.

Table 7-1. Composition of Surrogate Electrorefiner Salt used for Microstructural Evaluation of Solid Phases

Salt	mass fraction
LiCl-KCl	0.60
NaCl	0.20
CsCl	0.04
RbCl	0.01
$SrCl_2$	0.02
$LaCl_3$	0.02
$CeCl_3$	0.03
$NdCl_3$	0.06
YCl_3	0.01
NaI	0.01

The mixture was prepared by adding the individual salts to pre-baked out alumina crucibles and mixing the dry powders by hand in an inert atmosphere glove box (<1 ppm H_2O, O_2). A total of 30 grams of salt was loaded into the crucible. The crucible was then separately heated to melting and slowly cooled in a zone-freezing furnace under vacuum (Figure 7-1). The zone freezing furnace consists of a retort that moves the salt sample from a hot zone ($500^{o}C$) to a cold zone ($300^{o}C$) at a user-specified translation rate. In this experiment, the translation rate was set at 5 mm/hr (20 hrs cooling time).   At $500^{o}C$, the LiCl-KCl will melt and dissolve the rest of the surrogate salt components. Then as the temperature approaches $300^{o}C$, the salt mixture will slowly solidify.

Figure 7-1. Photograph of the Zone Freezing Furnace used for Preparing Surrogate Electrorefiner Salt Samples for Microscopic Evaluation

Solid salt samples were examined using both X-ray fluorescence (XRF) and scanning electron microscopy (SEM). The SEM was manufactured by JEOL (Model JSM-6610LV). It was run in secondary electron imaging mode at 20 kV. SEM samples were coated Au/Pd prior to insertion into the instrument. The XRF analyzer was manufactured by Horiba (Model XGT-7200 equipped with rhodium X-ray generator). Operating parameters for the XRF included 30 kV accelerating voltage with 1.0 mA current, 50 μm beam size. Five accumulations were used for each elemental mapping.

Figure 7-2. Photographs of Surrogate Electrorefiner Salt After Melting and Freezing in the Zone Freezing Furnace.

Photographs of the surrogate salt after melting and freezing (see Table 7-1 for composition) in the zone freezing furnace are shown in Figure 7-2. The right image shows a cross section after the ingot was cut in the axial direction. Elemental maps of the same salt ingot obtained using XRF are shown in Figure 7-3. The light intensity correlates with concentration in this type of mapping. The lighter the pixels, the higher the concentration is of that particular element. The scale of the images is such that the map includes the entire axial length of the salt ingots (shown in Figure 7-2). For the most of the elements, there appears to be a uniform distribution across the ingot. The three exceptions are Nd, Cs, and I. In each of these cases, there is at least one region in the center of the ingot with higher than average concentration. Interestingly, the Cs and I maps appear to be identical in shape of the high intensity regions. The obvious conclusion is that CsI forms in the salt from ion exchange between CsCl and NaI. This is potentially a very important finding for the field of pyroprocessing that iodine in the salt is likely to be bonded with cesium. Understanding the fate of iodine in the process has been identified as an important issue that must be understood for optimizing waste management strategy associated with pyroprocessing.
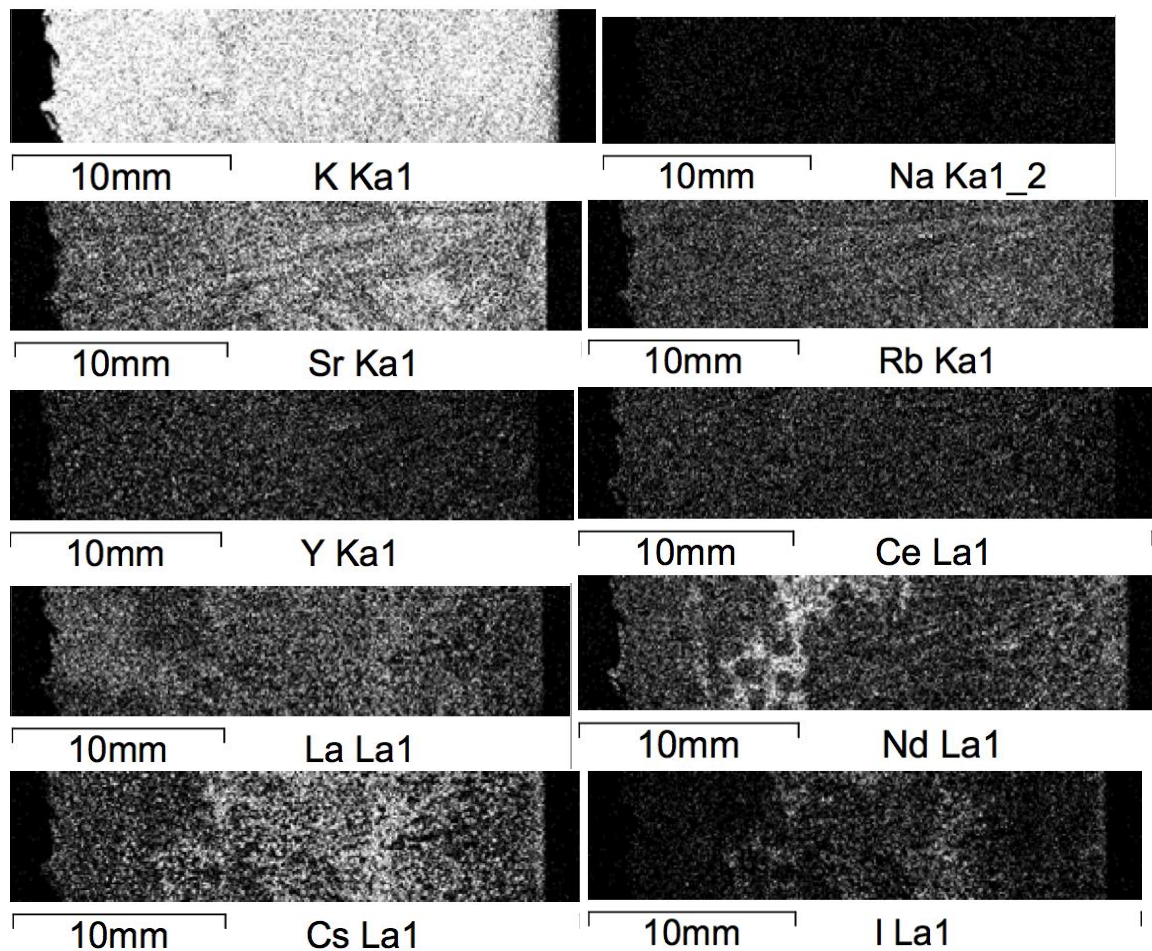
Figure 7-3. XRF Maps for Surrogate Salt Ingot.

The surrogate salt sample was also examined using scanning electron microscopy (SEM). Figure 7-4 shows a relatively low magnification image of the salt. From this image, there appears to be two regions based on light intensity, and the salt in general has a porous texture to it.
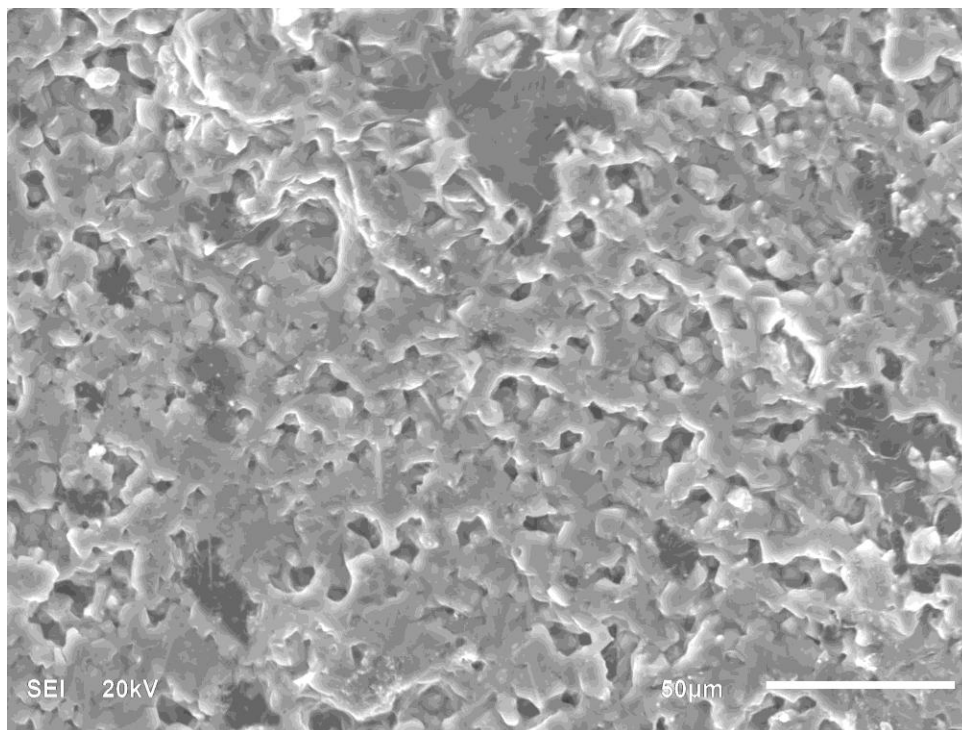
Figure 7-4. Secondary Emission Scanning Electron Microscope Image of Surrogate Salt Sample

Using EDXS, points within the two types of regions were analyzed for elemental composition. Two spots in the dark region were selected and one in the lighter region was selected. The locations of these spots are shown in Figure 7-5. As seen in Table 7-2, there are some differences in the compositions of the various spots. Strangely, the two dark regions exhibit markedly different compositions. Iodine was only observed in Spot 3. Neodymium was in Spot 1 but not in Spots 2 or 3. Lanthanum was not seen in Spot 1 but was in Spots 2 and 3, albeit with significantly different concentrations between the two spots. It is not possible to draw definitive conclusions from this analysis other than that some phase segregation appears to occur during solidification of the salt. The element distributions were found to be non-uniform based on spot analysis. Identification and characterization of specific phases would require extensive continued examination of salt samples using SEM/EDXS.
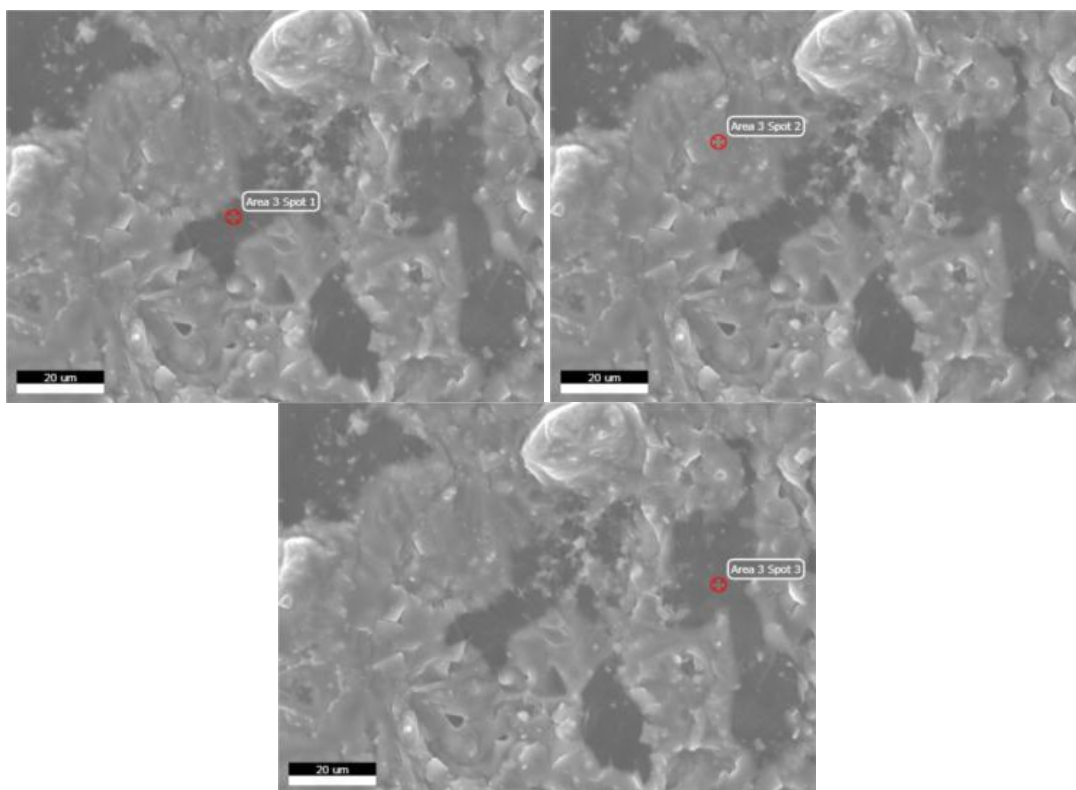
Figure 7-5. Location of Spots Selected for EDXS Analysis Reported in Table 7-2

Table 7-2. Elemental Distributions in Surrogate Electrorefiner Salt Sample. Location of spots shown in Figure 6.

Element	Spot 1 (dark)		Spot 2 (light)		Spot 3 (dark)	
	Wt%	**At %**	**Wt%**	**At %**	**Wt%**	**At %**
Sr	0.68	0.23	0.42	0.15	2.4	0.95
Cl	56.8	48.1	70.3	61.2	49.9	48.6
K	1.3	1.0	5.4	4.3	5.1	4.5
Cs	4.0	0.91	3.2	0.74	3.0	0.78
Nd	5.9	1.2				
La			0.98	0.22	2	0.5
Ce					2.6	0.63
I					2.3	0.62

7.3   Dissolution Tests for ER Salt (Fine Particles)

Preliminary tests were run in FY10 to evaluate the stability of LiCl-KCl based salts in water and representative brine solutions. Samples of pure eutectic LiCl-KCl were subjected to solubility and dissolution rate tests. Brine solutions were prepared that attempted to mimic the Waste Isolation Pilot Plant (WIPP) brines, G-Seep and ERDA-6. The compositions and properties of these brines are given in Table 7-3. For the FY10 tests performed, the pH and electrical properties of the brine solutions were not maintained.

Table 7-3. WIPP brine compositions

	G-Seep	ERDA-6
B^{3+} (mM)	20	63
Br^{-} (mM)	10	11
Ca^{2+} (mM)	20	12
Cl^{-} (M)	5.35	4.8
K^{+} (mM)	770	97
Mg^{2+} (M)	1.44	0.019
Na+ (M)	1.83	4.87
SO_4^{2-} (mM)	40	170
TIC (mM)	10	16
pH	6.5	6.17
Eh (mV)		-152

For the solubility experiments, LiCl-KCl was incrementally added to known volumes of each of the three liquids (water, simulated G-Seep, and simulated ERDA-6) at room temperature. Solubility limits were established at the point where some residual salt remained undissolved. For the dissolution rate tests, eutectic LiCl-KCl beads with a uniform 1.3 mm diameter were added in small amounts to the liquids. The liquids were continuously stirred, and the time required to dissolve all of the beads was recorded. It was found that the LiCl-KCl solubility in the brine solutions was a factor of 5 to 7 lower than that in water. Dissolution rates were also lower for the salt in the brine solutions than water—by about a factor of 10.

For FY11, the objective of the project was to probe further into the subject of salt dissolution. It was desired to use more representative salt compositions instead of pure eutectic LiCl-KCl. Ideally, testing should be performed with actual electrorefiner salt. But the highly radioactive nature of this salt currently makes such an approach cost prohibitive. However, it is practical to create a surrogate salt containing a number of elements present in the actual electrorefiner salt—non-radioactive isotopes that are found in commercially-produced chemicals.

It has been hypothesized that reducing the LiCl concentration in waste electrorefiner salt might make the salt more stable in the presence of water and brine solutions. This is because LiCl is considered to be more hygroscopic than KCl. To test this hypothesis, four simple surrogate salts were prepared that consisted of only LiCl, KCl, and NaCl. The compositions of these mixtures are given in Table 7-3.

Table 7-3. Compositions of Salt Mixtures Used for Salt Dissolution Tests Given in Weight Fraction

Sample	weight fraction		
	LiCl	**KCl**	**NaCl**
S1	0.400	0.509	0.091
S2	0.292	0.617	0.091
S3	0.174	0.735	0.091
S4	0.000	0.909	0.091

For preparing each sample, the salt components were mixed in an inert atmosphere glove box and heated in magnesia or alumina crucibles. The furnace was also located in the glove box. The salts were heated to 800 °C for approximately 2.5 hours. This temperature is above the pure component melting points of both LiCl and KCl, almost identical to that of pure NaCl. Once cool, the salts were crushed and manually sieved using 3-inch Gilson sieve trays. Three ranges of salt particle size were retrieved: >425 μm, 250-425 μm, and 45-250 μm.

Three different liquids were used for dissolution tests involving the samples S1 through S4--distilled, de-ionized water (nanopure), simulated G-Seep brine, and simulated ERDA-6 brine. The formulations for the simulated brines are the same as used in FY10 testing under this project and are given in Table 7-5.

Table 7-4. Salt Mixtures for Simulating the WIPP brine formulations

	Simulated G-Seep	Simulated ERDA-6
NaCl (M)	1.83	4.714
$MgCl_2$ (M)	1.42	
$CaSO_4$ (mM)	20	12
KCl (mM)	760	86
$MgSO_4$ (mM)	20	19
KBr (mM)	10	11
Na_2SO_4 (mM)		139

Dissolution of $MgCl_2$ in water is strongly exothermic. A cool water bath was utilized to prevent boiling of the brine water. Also, dark insoluble particulate was observed upon dissolving the $MgCl_2$ in the nanopure water. This particulate is reported by the manufacturer to be zirconium. The particles were removed from the water using a vacuum flask and a funnel containing filter paper.

Solubility limit tests were performed at room temperature. Solvents (20 mL) were placed into 25 mL Pyrex beakers. Salts were then added in increments over a period of approximately 24 hours. After this time period, the saturated solutions were transferred to screw-top glass jars to be archived. The wet salt that remained in the beakers was placed on a hot plate (115 °C) for approximately 1 hour to vaporize the residual water. Once dry, the remaining mass of salt for each experiment was weighed. This weight value was subtracted from the amount added, and the result was assumed to be the solubility limit. A residue of brine salt appeared in the jars upon evaporation of the water. Although this small amount of salt was

included in the mass that was subtracted from the total amount of salt added, it was an insignificant fraction.

Dissolution rate tests were performed at room temperature by timing the disappearance of salt particles in the solvents. These tests were performed using 25-ml Pyrex beakers containing 25 mL of solvent. Salt particles in the range of 250 to 425 μm were added to the solvent for each measurement. The time required for the largest particles to dissolve was recorded with each addition of particles to the solvent. A photograph of one of the beakers during a dissolution rate test is shown in Figure 7-6. Observation of the particles was aided by using a magnifying glass. Dissolution time was tested ten times for each salt in all three solvents (a total of 120 measurements). Each of the ten tests for a given salt and solvent was performed in the same volume of solution. It was assumed that the small amount of salt added for each test did not affect the dissolution rate by changing the concentration of the solvent.
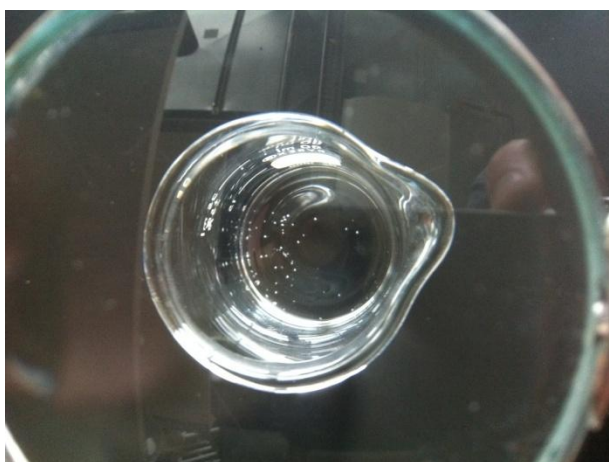
Figure 7-6. View of Salt Particles in a Dissolution Rate Test through a Magnifying Glass

Data from the solubility limit tests are given in Table 7-5. Results of tests performed with LiCl-KCl in FY10 are included in the first row of the table to demonstrate the consistency of the results between the two separate studies. The two sets of experiments do appear to be relatively consistent despite a year in between and different researchers performing the work. . There is a clear decrease of solubility, as would be expected, in going from water to brine solutions. Solubility levels are quite similar between the two brine formulations. Most important for this study, there was no trend observed with respect to varying LiCl concentration in the salt, or any of the salt components for that matter. The results given in Table 7-5 are plotted in Figure 7-7 where this can be more clearly seen. Going from left to right in this plot, the LiCl concentration is decreasing. But for each set of samples in a particular liquid, there is no significant variation in the solubility limit.

Table 7-5. Solubility limits of the salt mixtures in water, G-Seep, and ERDA-6. LiCl-KCl data was obtained in FY10 and may be subject to slightly different conditions than the other samples.

sample	x(LiCl)	Solubility limit (grams/liter)		
		water	**G-Seep**	**ERDA-6**
LiCl-KCl	0.440	297*	69*	40*
S1	0.400	230	42	48
S2	0.292	232	42	56
S3	0.174	244	45	69
S4	0.000	261	38	62

*FY10 experiment results
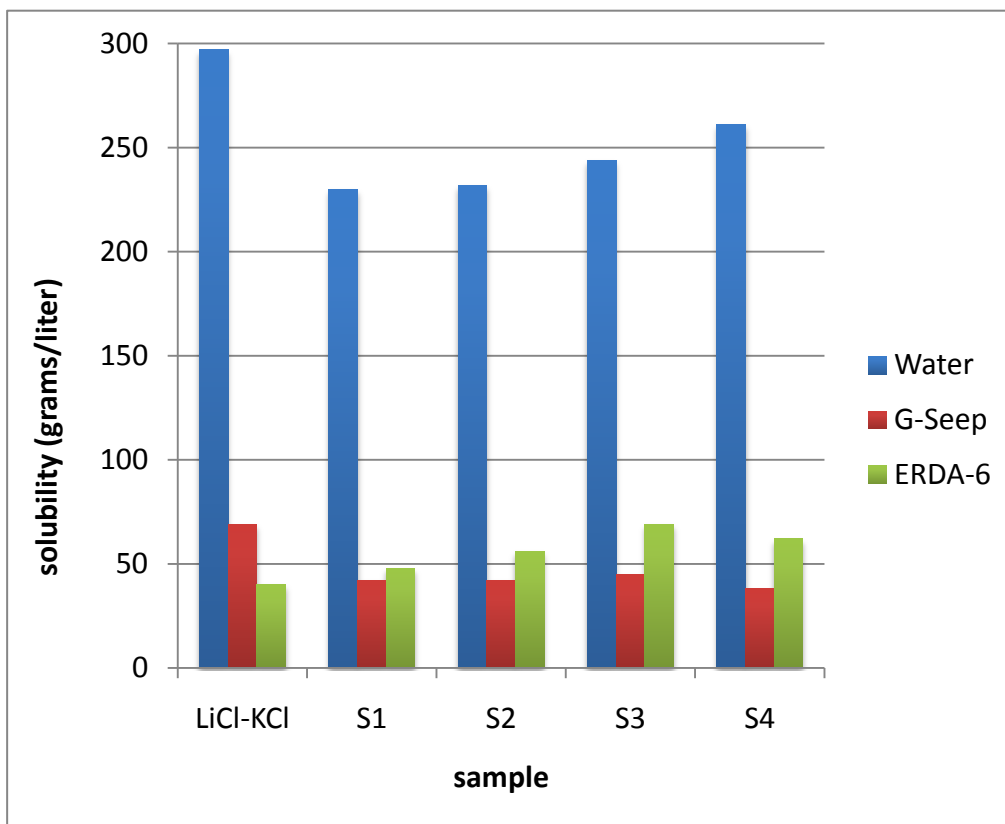
Figure 7-7. Plot of Solubility Limit for Various Salt Samples in Water and Brine Solutions (data given in Table 7-5).

In the dissolution rate experiments, for each of the salt/solvent combinations, average time to complete dissolution with standard deviations was calculated based on ten measurements. The results are given in Table 7-6. With the exception of the tests involving G-Seep, there appears to be a trend that reducing the LiCl content in the salt increases the rate of dissolution.

Table 7-6. Average dissolution rates and standard deviations (in seconds) of salt particles in water, G-Seep, and ERDA-6. Particles observed were the largest of the 250 μm to 425 μm range.

Salt	x(LiCl)	Time to complete dissolution (sec)		
		Water	**G-Seep**	**ERDA-6**
S1	0.400	(46 ± 13) s	(278 ± 30) s	(155 ± 23) s
S2	0.292	(45 ± 13) s	(251 ± 30) s	(144 ± 27) s
S3	0.174	(40 ± 8) s	(279 ± 30) s	(140 ± 20) s
S4	0.000	(29 ± 4) s	(319 ± 31) s	(131 ± 17) s

In FY10, similar experiments were run with eutectic LiCl-KCl but with larger salt particle diameters (1180 **µ**m versus 425 **µ**m). In an attempt to include those results with the new measurements in an overall assessment, dissolution rate in grams per second was estimated. Two key assumptions were required to convert from time to grams per second. First, the diameter of the particles used in the current study was set at the upper limit (425 **µ**m). Second, the density of each salt sample (S1 through S4) was assumed to be constant at 2.0 g/cm^3. This is the known density of solid eutectic LiCl-KCl. Effect on density of adding NaCl and removing LiCl from the salt is not known, but is not likely to be a strong function of composition for the given samples. Still, the rates given in Table 7-7 should be considered to be approximations. For this reason, only two significant figures are reported for the samples S1 through S4.

Table7- 7. Approximate dissolution rates of the salt mixtures in water, simulated G-Seep, and simulated ERDA-6. LiCl-KCl data was obtained in FY-10 and involved larger salt particles than the tests with S1 through S4.

salt	x(LiCl)	Dissolution rate (10^{-6} grams/sec)		
		water	**G-Seep**	**ERDA-6**
LiCl-KCl	0.44	14.2*	1.34*	1.10*
S1	0.4	14	2.3	4.2
S2	0.292	14	2.6	4.5
S3	0.174	16	2.3	4.6
S4	0	22	2.0	4.9

*FY10 experiment results

The rates of dissolution given in Table 7-7 indicate that the FY10 and FY11 experiments were run in a consistent manner. The experiments involving water as the solvent indicated very similar rates of dissolution. In all experiments, dissolution rate decreased significantly in going from water to the brine solutions. ERDA-6 was found to dissolve the salts twice as fast in the FY11 tests, while the two brines performed similarly in FY10 tests. To better view the trends as a function of LiCl concentration, see Figure 7-8. The only solvent for which LiCl concentration has a significant affect is water. Dissolution rate in the brine solutions is relatively unaffected by LiCl.
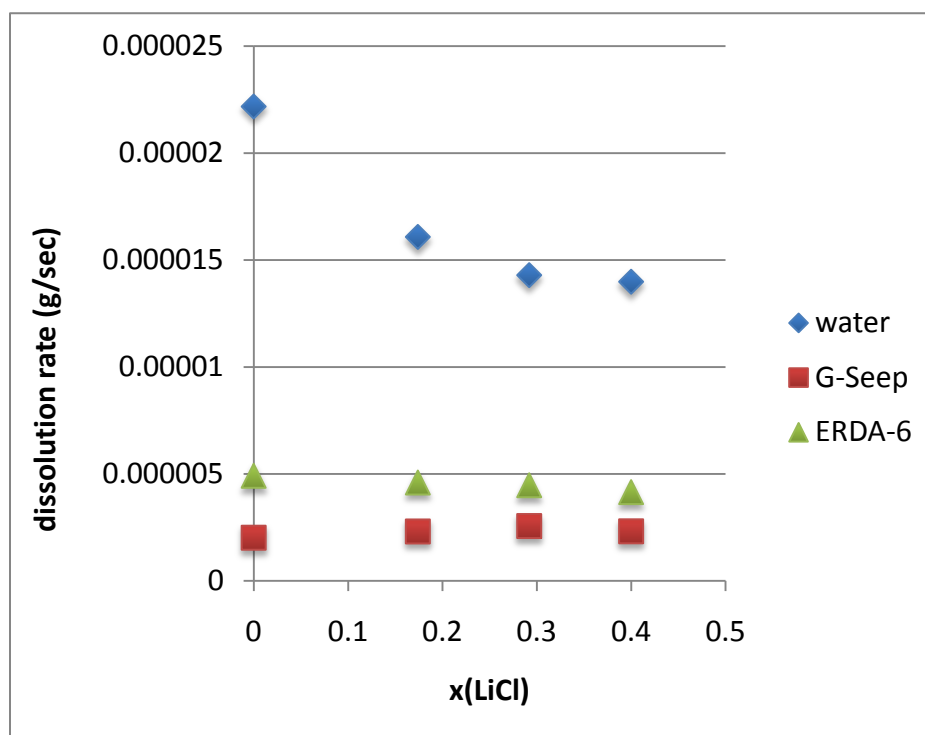
Figure 7-8. Effect of LiCl Concentration on Rate of Salt Dissolution

It should be pointed out that the rates tabulated in Table 7-7 are for the initial salt dissolution.   The duration of this initial dissolution apparently depends on the corresponding water/solid ratios in the system. By no means could these rates be used for the long-term assessment of ER salt stability in a salt repository.   Nevertheless, our dissolution experiments suggest that the contacted solutions in the dissolution experiments reach equilibrium with the corresponding salt samples and that the dissolution rate appears much slower in a concentrated brine than in dilute water even for the initial dissolution.

7.4   Dissolution Test for ER Salt (Pellets)

This section documents the work performed in FY11 on salt pellets to study the effect of salt encapsulation on radionuclide release. As shown in Figure 7-9, the hypothesis to be tested here is that there exists a critical value where the dissolution rate of the waste switches from being determined by the

matrix surrounding the waste and instead is controlled by the embedded waste itself. In order to determine the risk associated with such a disposal scheme, the dissolution rate of the source term must be known. Also, to mitigate the risk associated with disposal, it would be ideal to create waste forms below the critical value.

The experiments that we have designed are aimed to test this critical value hypothesis, and will lead to a quantification of that critical value. WIPP salt samples were procured from the WIPP site. This WIPP salt was mixed with varying amounts of sodium iodide in two different manners. One method was simply a physical mixing of the two different salts; the other method involved the dissolution of both the WIPP and sodium iodide salts and co-precipitation via evaporation. These mixtures were compressed into pellets, and the pellets are currently reacting with a WIPP brine solution.
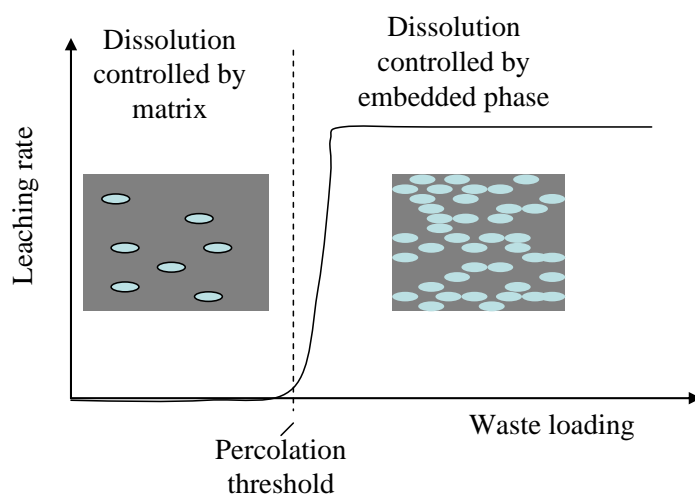
Figure 7-9- Schematic representation of leaching rate of electrorefining salt waste form as a function of waste loading

Sample procurement: WIPP salt was obtained from a field trip to the WIPP repository. While down hole, approximately 50kg of material was collected to bring back to the lab. The large amount allowed for a broad selection of materials of varying compositions. For the first round of experiments visually pure samples were chosen as pellet material. These pure samples were visually clear, and only slightly rosy, meaning that they had a higher proportion of NaCl and lower proportions of KCl and other impurities such as clays and iron oxides. The hand-picked samples were crushed by hand using a mortar and pestle and were sieved to <1mm. The >1mm fraction was reserved for future experiments.

Brine Preparation: Instead of using a synthetic brine, a saturated brine solution was created through dissolution of the WIPP salts. To create the brine, an excess of WIPP salt was added to a known volume of DI water. The solution and solid were allowed to mix from several hours to overnight. The remaining salt was removed by decantation and vacuum filtration. The solid material was allowed to air dry and massed. Working in batches, a total of 2.85L of brine were created with an overall solids concentration of 360.36g/L. Three separate batches were mixed prior to the dissolution experiments. However, for the

evaporative pellet formation, described below, a single batch with a solids concentration of 358.18 g/L was used. There is no detectable amount of iodide in the WIPP brine.

Pellet Formation: Two methods of pellet formation were used: encapsulation and evaporation. For the encapsulation pellets the crushed WIPP salt was physically mixed with different weight percents of sodium iodide (NaI). Once the two salts were well mixed, a hydraulic press and cylinder form was used to make the pellet. Three grams of mixed salt was added to the form with several drops of water; the small amount of added water allowed for a more coherent pellet. The press was put under a load of 20,000psi for two minutes. The pellet was ejected, and placed in a plastic container where the dissolution experiment is taking place. Pellet diameter was fixed at 1.3cm by the form used in the press. However, the height was variable depending on the amount of NaI used; the general trend is decreasing height with increasing NaI content (See Figure 7-10). The total masses used, calculated weight percent of I^- in each pellet, and pellet dimensions are shown in Table 7-8.

For the evaporative pellet formation, the target was to create about five grams total evaporite. A known amount of sodium iodide was dissolved in 14mL of the brine described above. A small amount of water (~1-2mL) had to be added to the higher NaI weight percents (>20%) to foster dissolution. The solution was allowed to evaporate for several days at room temperature, but due to slow evaporation the samples were subsequently moved to a 45°C oven overnight. No visual segregation of the two different salts took place. The total masses and weight percent of I^- are summarized in Table 7-9. From the approximately 5g of produced evaporite, 3g were used to make the pellet, as described above. A similar, but slightly subdued, trend was also observed between pellet height and % I^- in the pellet (Figure 7-10).

Table 7-8. Masses used and dimensions for the encapsulation pellet formation method

Sample ID	Mass Pellet (g)	Actual wt% I^-	Pellet Height (cm)	Pellet Surface Area (cm^2)
Control		0	1.12	7.252
Encap-1%	3.0016	0.85	1.09	7.148
Encap-5%			1.06	6.984
Encap- 10%			0.98	6.673
Encap- 20%	3.0009	16.95	0.91	6.446
Encap- 30%	3.0018	25.41	1.00	6.753
Encap- 40%	3.0024	33.87	0.70	5.537
Encap- 50%	3.0007	42.33	0.63	5.302
Encap- 75%	3.0008	63.47	0.57	5.021
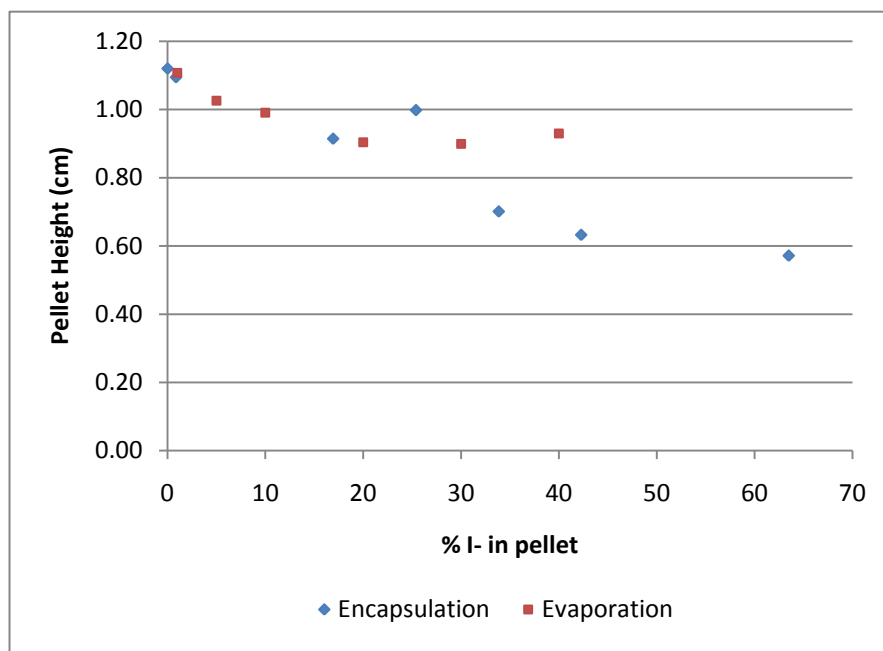
Figure 7-10. Pellet height vs. percent I⁻ in the pellets

Table 7-9. Masses used and dimensions for the evaporation method

Sample ID	Mass Pellet (g)	Actual wt% I⁻	Pellet Height (cm)	Pellet Surface Area (cm²)
Evap-1%	3.0011	1.00	1.11	7.200
Evap-5%	3.0002	5.00	1.03	6.868
Evap-10%	2.9998	10.01	0.99	6.759
Evap-20%	3.0010	20.00	0.90	6.404
Evap-30%	3.0014	30.00	0.90	6.401
Evap-40%	3.0015	39.99	0.93	6.526

Iodide Analysis: Iodide will be quantified using ion chromatography (IC). Specifically, a Dionex ICS-1100 with an ASRS 300 4mm suppressor and an AS23 column will be used. The eluent is a mixture of 4.5mM Na_2CO_3 and 0.8mM $NaHCO_3$. The concentrated brine solution represents a potentially challenging solution matrix to work with. Preliminary method development has shown that many of the potential interferents elute within the first 25 minutes, while iodide does not elute until 33 minutes. However, the concentrated brine must be diluted 1:10 in order to avoid a prolonged chloride tail which

does interfere with the iodide determination. Matrix matched standards do not appear to be necessary. The results from this method development are shown in Table 7-10 with a calibration curve shown in Figure Figure 7-11. Table 7-10 shows the instrument response for several concentrations and two dilution factors for iodide spiked into a WIPP brine matrix. Generally the measured amount is within 5% of the actual value. The exception to this is the 5mg/L diluted 1:10. The measured amount is 13% higher than actual. This may be a deviation from calibration curve consistent with being near the detection limit for this matrix and dilution. The 5mg/L diluted 1:100 contained no detectable iodide. From the amounts of iodide added to the pellets, the maximum amount potentially released from the pellets with the smallest amount of added iodide is 510mg/L. Thus detection of the iodide should not be problematic.

Table 7-10. Measured concentration of iodide spiked into a WIPP brine matrix and diluted either 1:10 or 1:100

Sample ID	Measured Concentration (mg/L)
WIPP 5mg/L 1:100	ND
WIPP 50mg/L 1:100	50.6
WIPP 100mg/L 1:100	97.0
WIPP 5mg/L 1:10	5.7
WIPP 50mg/L 1:10	47.9
WIPP 100mg/L 1:10	97.8
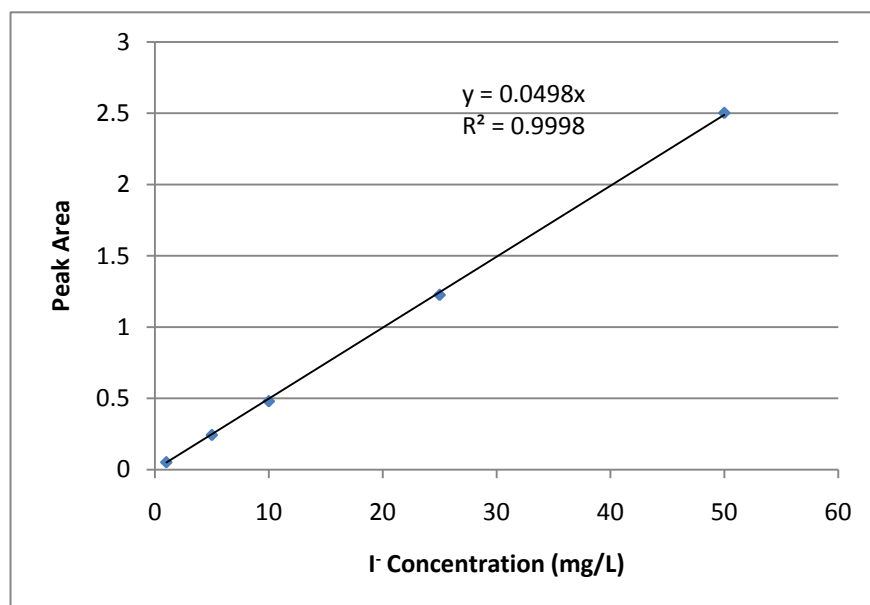
Figure 7-11. Example of an iodide calibration curve

Experimental Process: Once made, the pellets were immersed in 50ml of the combined brine solution. For the majority of the time the samples are left quiescent at room temperature in the dark. The only time that the samples are actively mixed is during sampling. Prior to sampling, a transfer pipette is used to thoroughly mix the solution. For each sampling event, 0.5ml of solution are removed, and placed in a 15ml centrifuge tube for storage. The sample is diluted with 5.0 ml of water giving a final dilution factor of 1:11. The samples are tightly capped and stored in a refrigerator for analysis. Samples are taken periodically, approximately every two days, and sampling will continue until a maximum I⁻ release is observed.

Figure 7-12. Two views of the pellet after 6days of reaction time. A) Barely visible on the top edge are the small amount of precipitates which have formed. In the picture it is slightly fuzzy. B) Small amounts of the pellet fragments can be seen along the bottom of the beaker.

Due to instrumental complications, I⁻ measurements on the experimental pellets have yet to be made. However, an initial experimental pellet (40% I⁻ evaporation method) was placed in a beaker to allow for

visual observations (Figures 7-12a and b). After six days of reaction time, the pellet is largely intact with only a minor amount of chipping/sloughing occurring from the cylinder edges. After about 5 days of reaction time, small precipitates started to form on the cylinder wall growing out into solution. The precipitates are large enough that the pellet can no longer roll along the bottom of the beaker when slanted. They also appear cubic in nature, suggesting halite precipitation. The formation of these precipitates may be due to dissolution of the NaI and a concomitant precipitation of NaCl, or it may be due to a slight evaporative loss caused by an incomplete parafilm seal on the top of the beaker. IC analysis will allow for differentiation; if it is the latter, this same behavior will not occur in the tightly capped plastic bottles being used for the actual experimental pellets.

7.5   Concluding Remark

FY11 work was focused on the development of experimental techniques for characterizing microstructure of ER salt and testing the stability of ER salt in simulated repository environments.   We have developed a process for making surrogate ER salts of various compositions. The surrogate salts have been characterized for their microstructures with XRF and SEM. The microstructural analysis reveals that phase separation appears to occur in the ER salt – a good indicator for microphase encapsulation of radionuclide by a salt matrix. Specifically, it is indicated that iodine tends to bond cesium in the salt. Dissolution experiments for fine surrogate ER salt particles have been performed, which showed that the contacted solution quickly reached the solubility of salt. Removing LiCl from the salt did not reduce its solubility limit or dissolution rate. In some cases it actually increased the solubility and dissolution rate of the salt, indicating a complex behavior of LiCl in concentrated brine solutions. Overall, the results of this study fail to support the notion that electrorefiner salt waste stability in a salt repository can be optimized via separation and recycle of the LiCl. We have also developed a technique for making surrogate ER salt pellets through room temperature mechanical pressing. The pellets with various ratios of NaI to NaCl were made for studying the efficacy of radionuclide encapsulation by salt. A preliminary test indicates that the obtained pellets seem to remain structurally intact during the dissolution experiment with WIPP brines. Due to its effectiveness, the developed pressing technique can potentially be used for densification of ER salt if needed.

The future work will include: (1) systematical evaluation of microstructural evolution of surrogate ER salt as a function of salt composition and melting/colling processes; (2) continuing study of the efficacy of radionuclide encapsulation by salt matrix based on the percolation theory and experimental testing; (3) performing a long-term performance assessment for the viability of the direct disposal concept; and (4) evaluating the potential implications of ER salt as a waste form to waste transportation.

7.6   References

Beauheim R. L. and Roberts R. M. (2002) Hydrology and hydraulic properties of a bedded evaporite Formation, *Journal of Hydrology*, 259, 66-88.

Bodansky D. (2010) Reprocessing spent nuclear fuel, *Physics Today*, December, 2006, 80-81.

Brush L. H. (1990) *Test Plan for Laboratory and Modeling Studies of Repository and Radionuclide Chemistry for the Waste Isolation Pilot Plant*, SAND90-0266, Sandia National Laboratories, Albuquerque, NM.

Chan K. S., Bodner S. R. and Munson D. E. (2001) Permeability of WIPP salt during damage evolution and healing, *International Journal of Damage Mechanics*, 10, 347-374.

Chang Y. I. and Till C. E. (1991) Advanced breeder cycle uses metallic fuel, *Modern Power Systems*, 11(4), 59-63.

Chang Y. I. (2007) Pyroprocessing (Electro-refining), *Workshop on the Security Implications of Increased Global Reliance on Nuclear Power*, CISAC, Stanford University, Sept. 19-21, 2007.

Inoue T. and Koch L. (2008) Development of pyroprocessing and its future direction, *Nuclear Engineering and Technology*, 40(3), 183-190.

Krumhansl J. L., Kimball K. M., and Stein C. L. (1991) *Intergranular Fluid Compositions from the Waste Isolation Pilot Plant (WIPP), Southeastern New Mexico*, SAND90-0584, Sandia National Laboratories, Albuquerque, NM.

Lowenstein T. K., Timofeeff M. N., Kovalevych V. M., and Horita J. (2005) The major-ion composition of Permian seawater, *Geochemica et Cosmochimica Acta*, 69(7), 1701-1719.

Satterfield C. L., Lowenstein T. K., Vreeland R. H., Rosenzweig W. D., and Powers D. W. (2005) New evidence for 250 Ma age of halotolerant bacterium from a permain salt crystal, *Geology*, 33(4), 265-268.

Simpson M. F. and Law J. D. (2010) *Nuclear Fuel Reprocessing*, INL/EXT-10-17753, Idaho National Laboratory, Idaho Falls, ID.

Wang Y., Simpson M., Rath J., Hansen F., Lee J. H., Jove-Colon C., McMahon K., and Swift P. (2011) Closing the fuel cycle with salt, 13th International High Level Radioactive Waste Management Conference, April 10-14, Albuquerque, NM.

Chapter 8: Potential Areas for International Collaboration

8.1   Introduction

For the Used Fuel Disposition Campaign (UFDC), international collaboration is a beneficial and cost-effective strategy for advancing disposal science in multiple disposal options and different geologic environments. While the United States disposal program had focused solely on Yucca Mountain tuff as host rock, several international programs have made significant progress over the past decades in the characterization and performance evaluation of other geologic repository options, most of which are very different from the Yucca Mountain site in design and host rock characteristics. Because Yucca Mountain was so unique (e.g., no backfill, unsaturated densely fractured tuff), areas of direct collaboration with international disposal programs were quite limited during that time. The decision by the U.S. Department of Energy to no longer pursue the disposal of high-level radioactive waste and spent fuel at Yucca Mountain has shifted UFDC's interest to disposal options and geologic environments more in line with many international disposal programs. Much can be gained by close collaboration with these programs, including access to valuable experience and data collected over recent decades.

International geologic disposal programs are at different maturation states, ranging from essentially "no progress" to selected sites and pending license applications to regulators. Table 8-1 summarizes the status of UNF and HLW management programs in several countries. The opportunity certainly exists to collaborate at different levels, ranging from providing expertise to those countries "behind" the U.S. to obtaining access to information and expertise from those countries with mature programs (*Used Fuel Disposition Campaign International Activities Implementation Plan, FCR&D-USED-2011-000016 REV 0, November 2010 [Nutt, 2010]*).

As to the possible types of international involvement, one may distinguish between two broad categories. The first category comprises participation in multinational or bilateral organizations, working groups, or committees, and typically involves high-level information exchanges, expert panels, review functions, training and education, etc. Recent or ongoing UFDC (or NE-53) activities in this area have been summarized in *Used Fuel Disposition Campaign International Activities Implementation Plan (FCR&D-USED-2011-000016 REV 0, November 2010 [Nutt, 2010]*). A few selected examples include multinational activities such as under IAEA (e.g., review activities, conference participation, education within the International training Center, ITC, …), OECD/NEA (e.g., participation in annual meetings, Integration Group for the Safety Case membership, R&D on NEA Thermodynamic Database,…), EDRAM (International Association for Environmentally Safe Disposal of Radioactive Waste), or bilateral agreements such as PUNT (U.S.–China Peaceful Uses of Nuclear Energy) and NEAP (U.S.–Japan Nuclear Energy Action Plan). UFDC will continue participation and/or support of many of the international activities discussed above, and may need to expand on certain activities, but will also need to be selective in its choices, to further those opportunities that are of most benefit to the campaign.

Table 8-1. Summary of UNF and HLW Management Programs in Other Countries

Country	Material to be Disposed	Centralized Storage	Geologic Environments	URL	Site-Selection	Anticipated Start of Repository Operations
Finland	SNF		Granite, Gneiss, Grandiorite, Migmatite	ONKALO (Granite)	Site at Olkiluoto Selected	2020
Sweden	SNF	CLAB - Oskarshamn	Granite	Aspo (Granite)	Site at Osthammar Selected	2023
France	HLW and ILW		Argillite and Granite	Bure (Argillite)	Site near Bure Selected	2025
Belgium	HLW		Clay/Shale	Mol (clay)	Not Initiated	~2040
China	HLW		Granite		Preliminary Investigations Underway - Beishan in Gobi Desert	~2050
Switzerland	HLW	Wulenlingen (ZWILAG)	Clay and Granite	Mont Terri (Clay) Grimsel (Clay)	Initiated	No sooner than 2040
Japan	HLW		Granite and Sedimentary	Mizunami (Granite) Hornonobe (Sedimentary)	Initiated	No Decision Made
Canada	SNF		Granite and Sedimentary	Pinawa (Granite) - being decommissioned	Initiated	No Decision Made
United Kingdom	HLW and ILW		Undecided		Initiated	No Decision Made
Germany	HLW, SNF, heat generating ILW	Gorleben and Ahaus	Salt	Gorleben (Salt)	On Hold	No Decision Made
Republic of Korea	SNF	Envisioned	Granite	Korea Underground Research Tunnel (Granite, Shallow)	Not Initiated	No Decision Made
Spain	No Decision Made	Siting Process Initiated	Granite, Clay, Salt		Not Initiated	No Decision Made

Source: Nuclear Waste Technical Review Board, 2009. Survey of National Programs for Managing High-Level Radioactive Waste and Spent Nuclear Fuel

The second category involves *active* R&D collaboration of UFDC researchers within international projects or programs in close collaboration with multinational scientists. By *active R&D*, we mean here that UFDC scientists work together closely with international scientists on concrete research projects relevant to both sides. Such active collaboration would provide direct access to information, data, and expertise on various disposal options and geologic environments that have been collected over the past decades. Many international programs have operating underground research laboratories (URLs) in clay/shale, granite, and salt environments, in which relevant field experiments have been and are being conducted. Depending on the type of collaboration, UFDC researchers may be able to participate in planning, conducting, and interpreting these experiments, and thereby get early access to field studies without having *in situ* research facilities in the U.S. We consider such active R&D activities to be most beneficial to UFDC, to help efficiently achieve its long-term goals of conducting "experiments to fill data needs and confirm advanced modeling approaches" (by 2015) and of having a "robust modeling and experimental basis for evaluation of multiple disposal system options" (by 2020). Advancing such opportunities will be the primary focus of UFDC's international activities in the next few years. (Obviously, the first category of international involvement discussed above is important in helping identify and facilitate avenues of active R&D collaboration; it is thus important that UFDC or NE-53 continue participation in multinational or bilateral organizations such as IAEA, or OECD/NEA).

Active collaboration can be achieved under different working models. One straightforward option is informal peer-to-peer interaction with international R&D organizations. Several UFDC scientists, most of which are associated with DOE's national laboratories, have close relationships with their international counterparts, resulting from workshops and symposia meetings, or from active R&D collaboration outside of UFDC's scope. Continued UFDC support for participation of UFDC researchers in relevant international meetings will help to foster and expand such relationships.

Other working models for active collaboration may require formal agreement and sometimes long-term (financial) commitment before R&D collaboration can take place. It is advisable that such agreements with international organizations/partners should be exercised by DOE, rather than by the UFDC or individual DOE national laboratories. Examples of valuable multinational and multi-partner initiatives

that promote active R&D in nuclear waste disposal science and that require DOE "membership" are the DECOVALEX Project, the Mont Terri Project, and the Colloid Formation and Migration Project, all of which are further discussed below. Instead of multi-partner initiatives, DOE national laboratories may also directly participate in specific projects run by individual international disposal programs. The latter may or may not require formal bilateral agreements.

As explicitly identified in the R&D Plan for the UFDC Natural Systems Evaluation and Tool Development (Wang, 2011; Chapter 1), many research topics related to natural system evaluation would greatly benefit from international collaboration. This chapter is focused on idenfiying potential areas for such collaboration. The following sections describe in more detail opportunities for active research with international disposal programs. The focus here is on such opportunities that provide access to field data (and respective interpretation/modeling) and/or may allow participation in ongoing and planned field experiments. Of these opportunities, we describe in this report near-term options related to the natural barrier system (NBS) and the engineered barrier system (EBS) work package of the UFDC. The main reason for including both NBS and EBS aspects in this section is that most field experiments provide data on the natural *and* the engineered system. As to the NBS aspects, we focus on clay/shale and crystalline rock collaboration opportunities; as to the EBS, we look mostly into buffer/backfill and seal behavior, and the interaction of these materials with other EBS components and the surrounding host rock. Some of the discussion presented in this report has also been included in a recent EBS status report. Much more detail on any of the experimental efforts and initiatives mentioned below can be provided upon request; the point of contact is Jens Birkholzer at Lawrence Berkeley National Laboratory, UFDC's Technical Lead for International Activities.

The benefit of international collaboration needs to be evaluated in the context of the open R&D issues that can be addressed through collaborative science activities. Open R&D issues with respect to NBS behavior are summarized in the R&D Plan for the UFDC Natural Systems Evaluation and Tool Development (Wang, 2011; Chapter 1) and the previous progress reports (e.g., *Natural System Evaluation and Tool Development – FY10 Progress Report, August 2010* (Wang, 2010)); specific R&D issues related to clay/shale host rock are discussed, for example, in Tsang et al. (2011). EBS-related R&D items have also been considered in previous progress reports (e.g., Steefel et al., 2010). All R&D gaps identified in these reports have been evaluated in consideration of their importance to the safety case in a recently conducted roadmap exercise (*Used Fuel Disposition Campaign Disposal Research and Development Roadmap, FCRD-USED-2011-000065 Rev 0, March 2011; Tables 7 and 8; [Nutt, 2011]*).

8.2   DECOVALEX Project

The DECOVALEX Project is a unique international research collaboration, initiated in 1992, for advancing the understanding and mathematical modeling of coupled thermo-hydro-mechanical (THM) and thermo-hydro-mechanical-chemical (THMC) processes in geological systems—subjects of importance for performance assessment of radioactive waste repositories in geological formations. DECOVALEX is an acronym for "Development of Coupled Models and their Validation against Experiments". Starting in 1992, the project has made important progress and played a key role in the development of numerical modeling of coupled processes in fractured rocks and buffer/backfill materials. The project has been conducted by research teams supported by a large number of radioactive-waste-management organizations and regulatory authorities, including those of Canada, China, Finland, France, Japan, Germany, Spain, Sweden, UK, South Korea, Czech Republic, and the USA. Through this project, in-depth knowledge has been gained of coupled THM and THMC processes associated with nuclear waste repositories, as well as numerical simulation models for their quantitative analysis. The knowledge accumulated from this project, in the form of a large number of research reports and international journal

and conference papers in the open literature, has been applied effectively in the implementation and review of national radioactive-waste-management programs in the participating countries. A good overview of the project is given in Tsang et al. (2009).

The DECOVALEX Project is typically conducted in separate 3-4 year project phases. Each phase features a small number (typically three to five) modeling test cases of importance to radioactive waste disposal. Many test cases are laboratory and field experiments that have been conducted by one of the project partners and are then collectively studied and modeled by DECOVALEX participants. Numerical modeling of these test cases can assist both to interpret the test results and to test the models used. Over the years, a number of large-scale, multiyear field experiments have been studied within the project (e.g., the Kamaishi THM Experiment, FEBEX, and the Yucca Mountain drift-scale heater test). Thus, the project provides access to valuable technical data and expertise to DECOVALEX partner organizations; this is particularly useful in disposal programs that are starting their research on certain disposal or repository environments and have no URLs. DECOVALEX has a modeling focus, but with tight connection to experimental data.

To participate in a given DECOVALEX phase, interested parties—such as waste management organizations or regulatory authorities—need to formally join the project and pay a small annual fee that covers the cost of administrative and technical matters. In addition to this fee, participating organizations provide funding to their own research teams to work on some or all of the problems defined in the project phase. Representatives from the funding organizations form a Steering Committee that collectively directs all project activities.

DOE was a DECOVALEX partner for several project phases, but decided to drop out in 2007 with the increasing focus on the license application for Yucca Mountain. Now that the U.S. has shifted to other disposal options and geologic environments, a renewed DOE engagement with DECOVALEX would provide UFDC researchers access to relevant field data from international programs and allow them to work collaboratively with international scientists on analyzing and modeling these data. The next DECOVALEX phase, referred to as DECOVALEX–2015, will start in early 2012. A planning session for this next DECOVALEX phase was held in a recent workshop in Helsinki, and several modeling test cases involving field data were proposed by prospective funding organizations.

- HE-E Heater Test: Studies of bentonite/rock interaction to evaluate sealing and clay barrier performance, in a micro-tunnel at the Mont Terri URL, proposed by ENRESA (Spain)
- SEALEX Experiment: A long term test of the hydraulic (sealing) performance of a swelling bentonite core (5 m long) in a mini tunnel (60 cm diameter) at the Tournemire URL in France, proposed by ISRN (France)
- MB Test: Mine-by test studying pore pressure and stress evolution during excavation, at the Mont Terri URL, proposed by NAGRA (Switzerland)
- Bedrichov Tunnel Experiment: Interpretation of inflow patterns and tracer transport behavior in a fractured granite, proposed by NAWRA (Czech Republic)
- THMC Processes in Single Fractures: Modeling of laboratory experiments on mechano-chemical impacts on fracture flow, tentatively proposed by KAERI/LBNL (South Korea/USA)
- Possible revisits of past DECOVALEX phases for the purpose of identifying potential tasks containing unsolved but important issues, tentatively proposed by CEA (France)

Of the six modeling test cases, the first two are mostly relevant to the EBS work package of UFDC; both target the behavior of backfill and sealing materials in interaction with clay host rock. The MB Test, the Bedrichov Tunnel Experiment, and the Single Fracture THMC Study are mostly relevant to the Natural System evaluation work package of UFDC. The last bulleted item, revisiting previous DECOVALEX

tasks, could be relevant to both work packages, but it is not clear at this point whether this proposal will be pursued in DECOVALEX–2015. More details on the first five proposed modeling test cases are given below. The DECOVALEX secretariat will soon distribute short summaries of each suggested test case.

One issue to resolve soon is the question of how to handle the cost of international commitments such as the DECOVALEX project. A possible solution is that the "membership fee" for DOE participation would come out of some centralized international fund, while the staff support for active R&D would be covered out of the relevant UFDC work packages (e.g., EBS, NBS). The expected "membership fee" for DECOVALEX–2015 is about \$42,000, somewhat dependent on the final number of participating organizations as well as the currency exchange rate. In the case of the DECOVALEX project, DOE membership ensures that any national laboratory associated with DOE would be allowed to participate.

HE-E Heater Test at Mont Terri URL, Switzerland (Focus: mostly EBS, some NBS)

The HE-E Heater Test at the Mont Terri URL, shown in Figure 8.2-1, focuses on the THM behavior of bentonite barriers in the early nonisothermal resaturation stage and their THM interaction with Opalinus Clay (see Section 8.3 for more information on the Mont Terri URL). The objective is to better understand the evolution of a disposal system of high-level waste in the early postclosure period, with emphasis on the thermal evolution, buffer resaturation (*in-situ* determination of the thermal conductivity of bentonite and its dependency on saturation), pore water pressure in the near field, and the evolution of swelling pressures in the buffer. Because the test is conducted in a micro-tunnel (at 1:2 scale), it is considered a validation, not a demonstration experiment. The heating test involves two types of bentonite buffer materials. The heater-buffer interface will be heated to a maximum of 135°C, and a temperature of 60–70°C is expected at the buffer-rock interface. A dense instrumentation network is already in place in the host rock surrounding the micro-tunnel (from a previous experiment testing the impact of ventilation on the clay host rock) and will be improved (up to 40 piezometers in total); various sensors will also be placed in the buffer material. Heating is expected to start in late summer of 2011 and will be continued for at least three years.
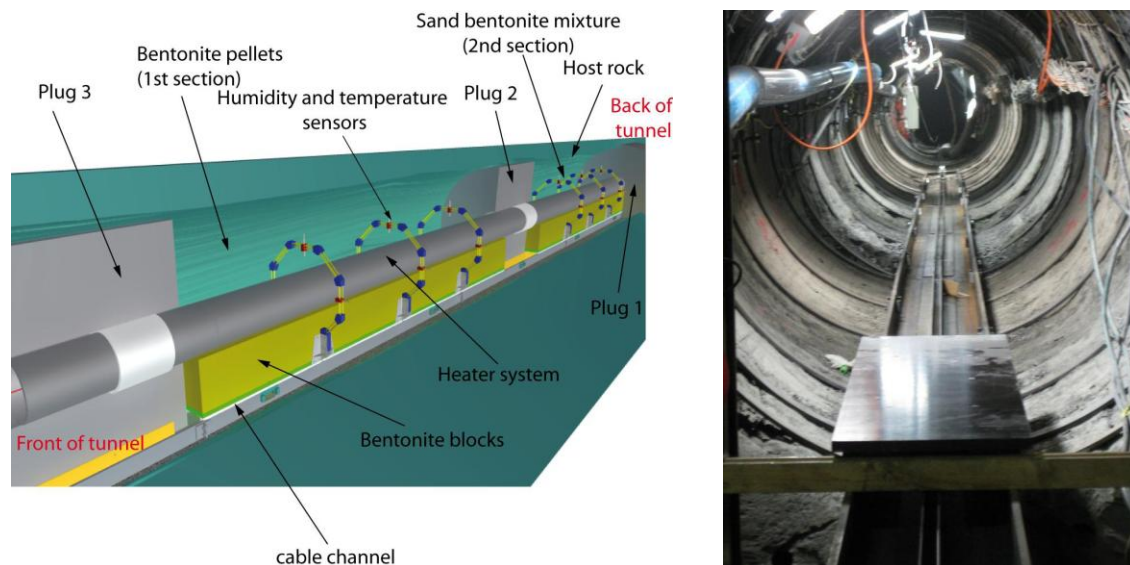
Figure 8.2-1. Schematic setup of HE-E heater test at Mont Terri and photo of micro-tunnel (from Garitte et al., 2011)

SEALEX Experiment at the Tournemire URL,France (Focus EBS)

The SEALEX experiment aims at investigating the long-term HM behavior and hydraulic performance of swelling clay-based seals (Figure 8.2-2). A suite of experiments will be conducted in several 60 cm diameter mini-tunnels (5 m long) that are exposed to nominal conditions, different technological choices for seal mixtures and emplacement, and altered situations (e.g., forced resaturation or not; loss of mechanical confinement or not) (Figure 8.2-3). Forced resaturation can lead to heterogeneous saturation and porosity/permeability fields within the bentonite core, and hence the possibility of clay-core erosion due to flow channeling. The experiments will test these hydraulic parameters and their spatial distribution via state-of-the-art measurement technology (e.g., wireless sensors installed within the core to limit preferential flow along cables). Hydraulic tests (pulse tests + constant load tests) will eventually be conducted to determine the overall hydraulic properties (permeability, leaks) of the seals, for different representative conditions. While not decided yet, IRSN, the French Institute for Radiological Protection and Nuclear Safety, considers adding one particular test to the experimental plan that would evaluate HMC behavior with concrete/steel and concrete/bentonite interaction.
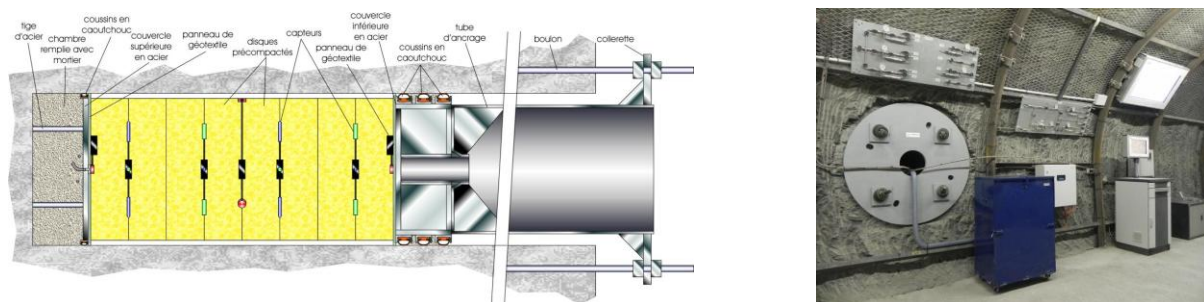
Figure 8.2-2. Schematic setup of mini-tunnel with seal core and instrumentation (left); view from gallery after core emplacement (right) (from Barnichon, 2011)

	Reference Tests	Performance Tests	Intra-core geometry Core conditioning Composition (MX80/sand)	Core view	Altered conditions	Emplacement date
Base case	RT-1	PT-N1	Monolithic disks Precompacted (70/30)		No	12/2010 06/2011
Variations / Base case	-	PT-A1	Monolithic disks Precompacted (70/30)		Confinement loss	06/2012
	-	PT-N2	Disks + internal joints (4/4) Precompacted (70/30)		No	12/2011
	RT-2	PT-N3	Pellets/powder In situ compacted (100/0)		No	12/2012 06/2013
	-	PT-N4	Monolithic disks Precompacted (20/80)		No	12/2013

Figure 8.2-3. Planned experiments and schedule (from Barnichon, 2011)

The SEALEX experiments are conducted at the Tournemire URL in the south of France. This site is characterized by a subhorizontal indurated argillaceous claystone layer 250 m thick. A railway tunnel, constructed in 1881 through the argillaceous formation, is 2 km long, 6 m high, and 4.7 m wide, and was excavated using a pneumatic tool. In 1996 and 2003, additional research tunnels were excavated off the main railway tunnel. Thus, this facility allows study of near-field rock behavior in indurated clay with different time periods of exposure to the atmosphere, namely 130, 15 and 8 years, respectively (Rejeb and Cabrera, 2006) (Figure 8.2-4).
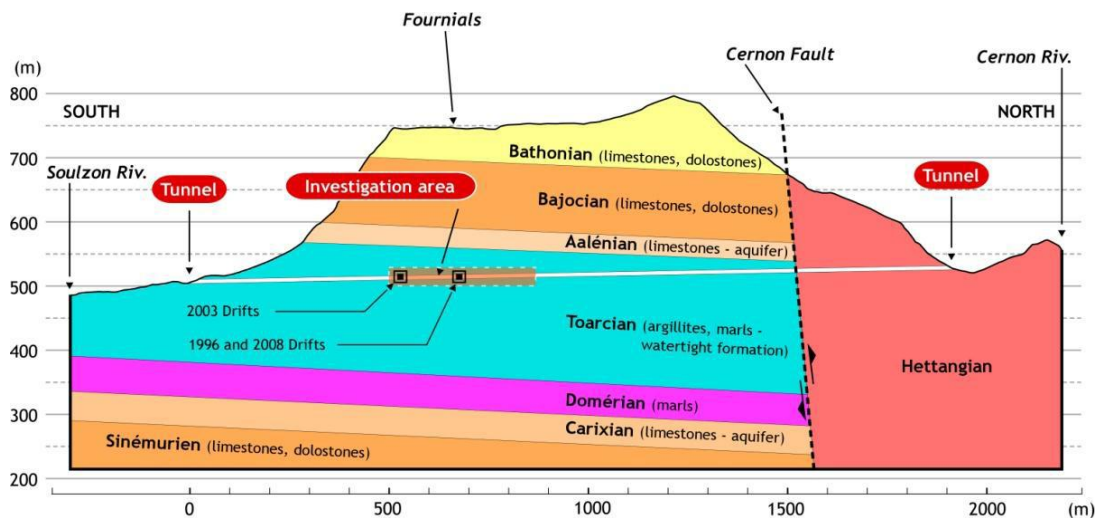
Figure 8.2-4. Geological cross section of the Tournemire site, South France (from Barnichon, 2011)

MB Test at Mont Terri URL, Switzerland (Focus: NBS)

The MB Mine-By Test at the Mont Terri URL, shown in Figure 8.2-5, involved tunneling through a pre-instrumented region of Opalinus Clay (see Section 8.3 for more information on the Mont Terri URL). The test, which was conducted at full tunnel scale, has been completed recently, and several years of data on damage-zone (DZ) behavior are available for modeling and interpretation. The test allows evaluating the excavation-generated pressure, stress, displacement, and rock damage response in the argillaceous clay host rock near a mined tunnel, and also provides measurements of related changes in the near-field hydrologic properties. Data available for analysis include stress and convergence measurements, pore-pressure results, and hydrotest results before and after mining. Some of the most interesting observations are related to the fact that pore pressure and deformation signals can be observed several meters before the advancing tunnel face, a response that cannot be easily explained with existing constitutive relationships. New fractures created in the DZ show interaction with bedding planes and crosscutting joints. Mine-by leads to a significant increase of hydraulic conductivity by up to 4 orders of magnitude. Note that the MB Test niche functions as the access gallery to the tunnel sections that hosts the soon-to-be-conducted FE Heater Test (see Section 8.3).
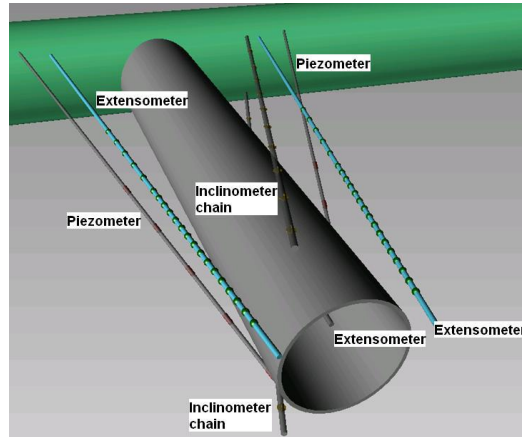
Figure 8.2-5. Schematic setup of MB Mine-by test at Mont Terri showing location of selected boreholes for piezometer, extensometer, and inclinometer data (from Vietor et al., 2011)

Bedrichov Tunnel Experiment (Focus: NBS)

The Bedrichov tunnel is an existing tunnel of 2,600 m length located in the Northern Czech Republic. The tunnel hosts a water pipe, but was recently made available for geologic studies. NAWRA (the Radioactive Waste Management Authority of the Czech Republic) and associated university researchers use the tunnel as an underground laboratory to study the suitability of the Bohemian granitic massif as a host rock for a radioactive waste repository (Figure 8.2-6). The modeling test case proposed for DECOVALEX–2015 aims at better understanding and predicting flow patterns and tracer transport behavior within the fractured rock, between the ground surface (about 120 m above the tunnel axis) and the tunnel. Measured data include tunnel water inflow patterns and rates (vs. infiltration at ground surface), water temperature, and water chemistry, the latter including chemical composition of major elements, pH, and several natural isotopes as tracers. Discrete fracture representations of the fractured granite surrounding the tunnel have been built based on fracture mapping in the tunnel and electrical resistivity profiles.
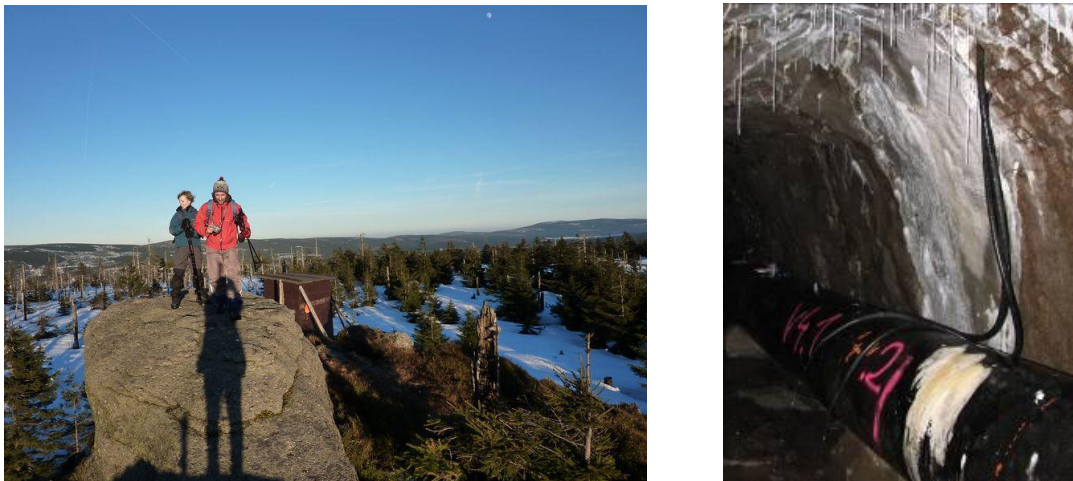
Figure 8.2-6. Bohemian granitic massif in Czech Republic and Water Inflow Evidence in the Bedrichov Tunnel (from Hokr and Slovak, 2011)

THMC Processes in Single Fractures (Focus: NBS)

This modeling task proposes to use data from single-fracture-flow laboratory experiments to evaluate the linkage of thermal stresses mediating chemical effects, and conversely of chemical potentials mediating mechanical behavior (e.g., pressure solution), and how any of these processes affects flow behavior. This task requires fully coupled THMC model capabilities, which only recently have become available and still require thorough validation. Early laboratory experiments available to target such THMC behavior have been conducted on single rock fractures in novaculite (a form of microcrystalline or cryptocrystalline quartz) (Figure 8.2-7) (Polak et al., 2003; Yasuhara et al., 2004). These experiments involved reactive flow-through compression and shear tests conducted on single natural-fracture specimens at different temperature, stress, and chemical conditions. The experiments were constrained by concurrent monitoring of stress/strain, influent and effluent flows/chemical reactants, and by intermittent nondestructive imaging by x-ray CT. More recently, similar experiments have been conducted on granite and tuff fractures (Rutqvist and Min, 2011). The data sets from these experiments will be used for the validation of THMC models with direct CM coupling between chemical reaction and strain.
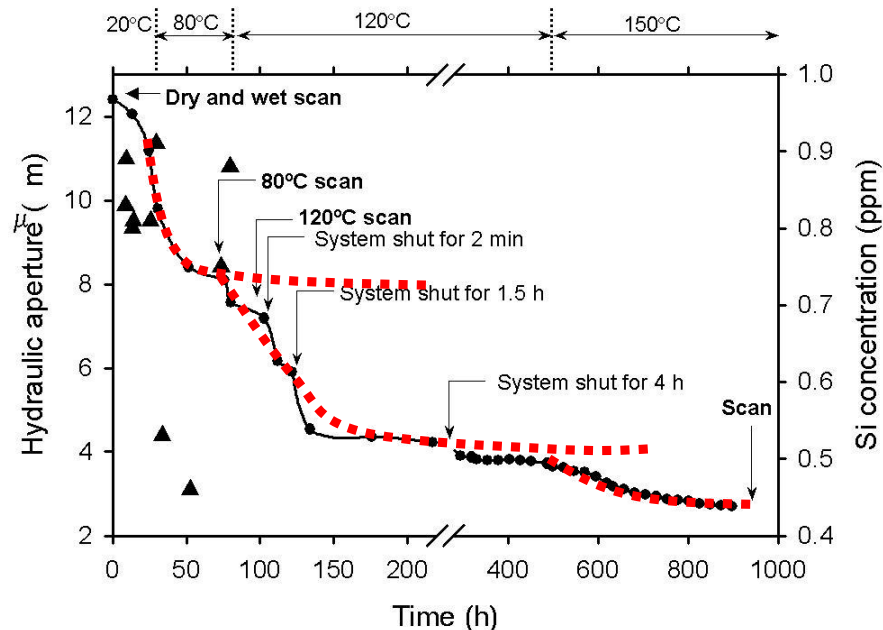
Figure 8.2-7. Results showing THMC behavior effects in a single fracture exposed to different external temperatures and varying stress conditions (from Polak et al., 2003)

8.3　Mont Terri Project

The Mont Terri Project is an international research project for the hydrogeological, geochemical and geotechnical characterization of a clay/shale formation suitable for geologic disposal of radioactive waste (Zuidema, 2007). The project utilizes an underground rock laboratory, which lies north of the town of St-Ursanne in Northeastern Switzerland and is located at a depth of ~300 m below the surface in argillaceous claystone (Opalinus Clay). Construction of the facility in conjunction with a motorway tunnel started in 1987, and the Mont Terri Project was officially initiated in 1996 (Figure 8.3-1). (http://www.mont-terri.ch/ids/default.asp?TopicID=72).

Often using co-sponsorship from European Community funds, the project essentially operates as a collaborative program providing open access to an existing URL. Mont Terri partner organizations may select and conduct experiments, and they have access to all project results from past and ongoing efforts. Larger field experiments are often conducted by more than one organization. Current project partners are from Switzerland (swisstopo/SGS, ENSI, NAGRA), Belgium (SCK/CEN), France (ANDRA, IRSN), Germany (BGR, GRS), Japan (OBAYASHI, JAEA, CRIEPI), Spain (ENRESA, Empresa), Canada (NWMO), and USA (Chevron).

Participation of DOE as a partner in the Mont Terri Project would provide UFDC researchers access to relevant field data and project results from past efforts. Mont Terri has been in operation for a long time, and a wide range of experimental studies on clay/shale behavior (including backfill/buffer behavior) have already been conducted. More importantly, UFDC researchers could work collaboratively with international scientists on *ongoing and future* experimental studies, which would include all design, characterization, modeling, and interpretation aspects related to field experiments. In the long term,

UFDC researchers would also be able to propose and eventually conduct their own experiments at the Mont Terri URL. This type of international collaboration goes beyond the mostly modeling focus of DECOVALEX, and may arguably be the most fruitful approach to active international R&D. Three prominent experiments are currently being conducted or are in preparation stages, two of which are also proposed as DECOVALEX modeling test cases (e.g., the HE-E Heater Test with focus mostly on EBS and the MB Mine-By Test with focus on NBS, as introduced in Section 8.2 above). The third one, referred to as the FE Heater Test (described below in more detail), is a long-term (>10 years), full-scale test that will serve as an ultimate validation and demonstration test for emplacement of heat-producing waste in Opalinus Clay, at realistic temporal and spatial scales. Validation will include THM coupling effects with focus on both the EBS components and the NBS host rock behavior.

In order for DOE to become a formal Mont Terri partner, there are two main requirements: (1) the present Mont Terri Project partners have to unanimously accept new partner organizations, and (2) as a buy-in, new partners have to invest about 500K Swiss Francs (about $500K), which can be spread over a period of 3 years. The buy-in fee can partially be provided in kind (i.e., by having UFDC researchers conduct work). The fraction of in-kind contributions can be negotiated with the Mont Terri partners, but is expected to be somewhere between 30 to 50% of the total. In addition to the "membership fee" for DOE participation, staff support for active R&D would have to be covered out of the relevant UFDC work packages (e.g., NBS, EBS).
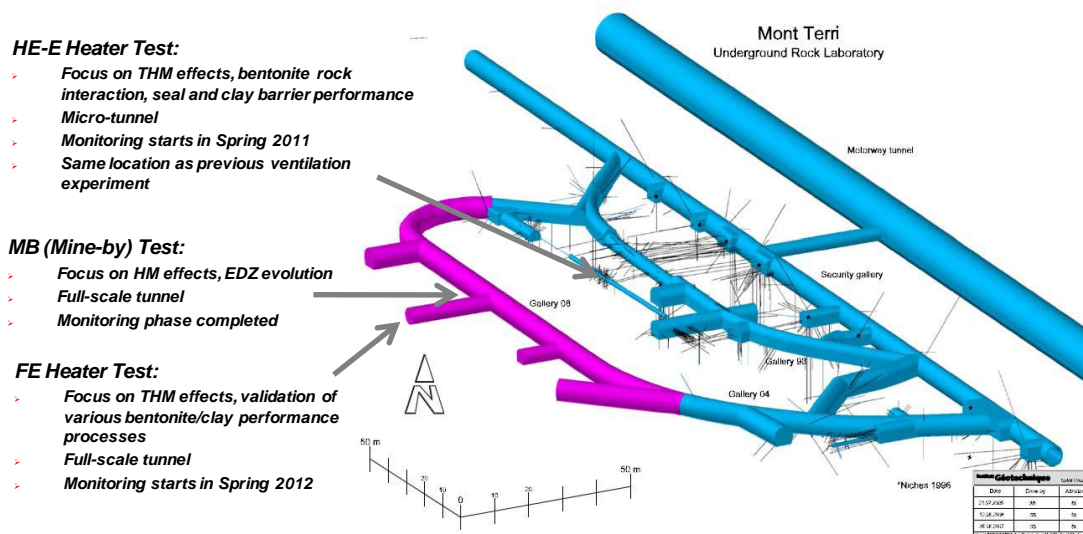
Figure 8.3-1. Summary schematic of the Mont Terri URL with side galleries and drifts for testing (based on Garitte, 2010)

FE Heater Test at Mont Terri URL, Switzerland (Focus: both NBS and EBS)

Because of its potential relevance to UFDC's NBS and EBS areas, we provide here some further detail on the FE Heater Test, one of the largest and longest-duration heater tests worldwide. As mentioned before, this heater experiment is undertaken by NAGRA and other European partners as an ultimate test for the performance of geologic disposal in Opalinus Clay, with focus on both the EBS components and the host-rock behavior. The experiment will provide data useful for the validation of THM coupling effects

regarding the processes in the host rock while correctly accounting for (and examining) the conditions in the emplacement tunnel (temperature, saturation, and swelling pressure). Due to the 1:1 scale of the experiment, it will be possible to achieve realistic temperature, saturation, and stress gradients. It will also be possible to test backfilling technology with granular bentonite as well as lining technology with shotcrete, anchors, and steel rips. Processes examined in the test cover many aspects of repository evolution, such as DZ creation and desaturation of the DZ during tunnel excavation and operation (including ventilation for about one year), as well as reconsolidation of the DZ, resaturation, thermal effects, thermal stresses, and thermal pore pressure increase after backfilling and heating (heating and monitoring period > 10 years).

As shown in Figure 8.3-2, the FE Heater Test will be conducted in a side tunnel at Mont Terri, excavated along the claystone bedding plane for this purpose, with 50 m length and about 2.8 m diameter. Heating from emplaced waste will be simulated by three heat-producing canisters of 1500 W maximum power. A sophisticated monitoring program is planned, including dense pre-instrumentation of the site for *in situ* characterization, dense instrumentation of bentonite buffer and host rock, and extensive geophysical monitoring (seismic and electric "tomography"). A THM modeling program will be conducted in parallel with the testing and monitoring activities.
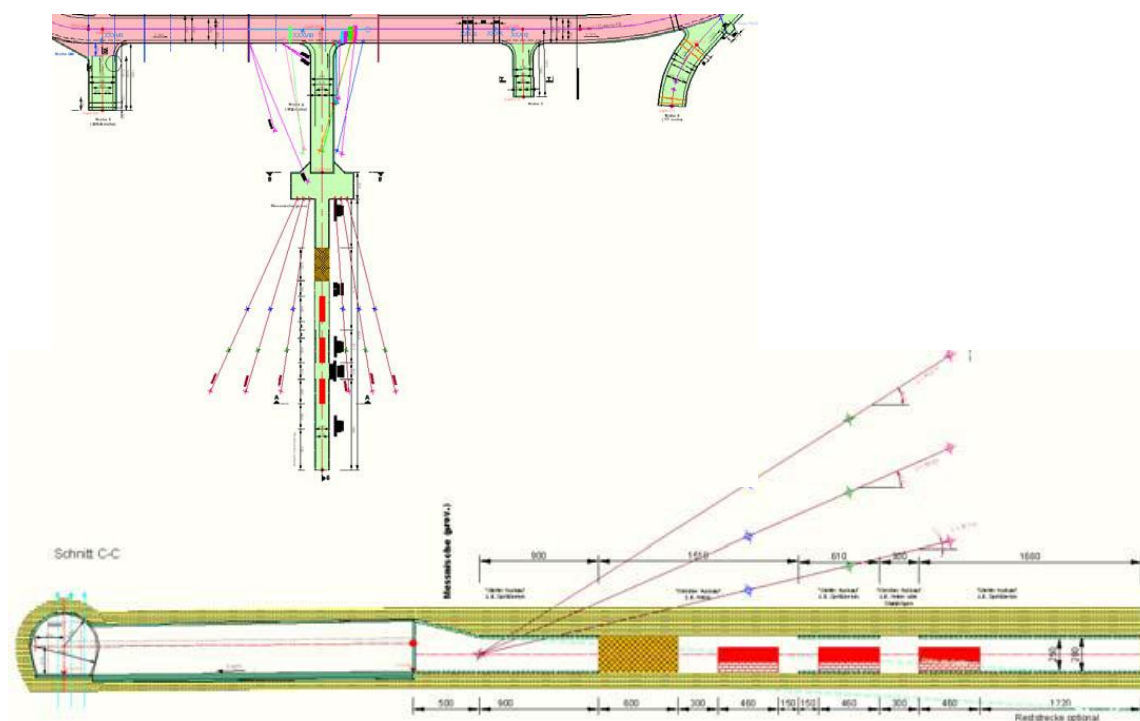

Figure 8.3-2. Plan (top) and side view (bottom) of experiment setup and observation borehole layout (from Garitte, 2010)

8.4   Colloid Formation and Migration (CFM) Project

The Colloid Formation and Migration Project is an international research project for the investigation of colloid formation/bentonite erosion, colloid migration, and colloid-associated radionuclide transport, relevant to both NBS and EBS areas of UFDC. This collaborative project is associated with the Grimsel Test Site (GTS) in the Swiss Alps, a URL situated in sparsely fractured crystalline host rock (http://www.grimsel.com/). Colloid-related R&D comprises *in situ* field work, but also laboratory and modeling studies. Current CFM project partners are from Germany (KIT and GRS), Japan (JAEA, CRIEPI), Sweden (SKB), Spain (CIEMAT), South Korea (KAERI), Finland (POSIVA), and Switzerland (NAGRA).

The main R&D objectives, relevant to both NBS and EBS issues, are as follows:

- To examine colloid generation rates and mechanisms at the Engineered Barrier System (EBS)– host rock boundary under *in situ* conditions,
- To study the long-term geochemical behavior (mobility, mineralization, colloid formation, etc) of radionuclides at the EBS–host rock boundary,
- To evaluate the long-distance migration behavior of radionuclides and colloids in water-conducting features in a repository-relevant flow system (i.e., with a very low flow rate/water flux),
- To examine reversibility of radionuclide uptake onto colloids,
- To gain experience in long-term monitoring of radionuclide/colloid propagation near a repository.

A series of colloid-facilitated radionuclide field transport experiments have been conducted at the Grimsel Test Site. More CFM field tests will start soon, as described below (from Reimus, 2011). These *in situ* experiments are complemented by many other activities conducted in parallel, such as laboratory experiments, interpretive modeling, etc.

Colloid-Facilitated RN Tracer Test (Focus: NBS)

A colloid-facilitated radionuclide tracer test will be conducted in a fracture shear zone at Grimsel in late summer or fall of 2011. This test will involve the injection of a tracer/radionuclide "cocktail" that includes conservative tracers, weakly sorbing solutes, strongly sorbing solutes and bentonite colloids (generated from a bentonite obtained from a Spanish mine that is being considered for use in the Spanish nuclear waste disposal program). The radionuclides will be presorbed onto the colloids to varying degrees, dictated by their sorption to the colloids (probably ~100% sorbed for Pu and Am, ~50% sorbed for U and Np, somewhere in between for fission products Cs and Sr). As in all the recent CFM tracer tests, the test configuration will be a passive dipole with water being withdrawn from the tunnel wall at a fixed rate (probably 25 ml/min) while the cocktail is continuously circulated through the injection interval (from the tunnel) with no net injection or withdrawal, with provisions to monitor the tracers in the circulation loop as the test progresses. The cocktail will bleed into the fracture shear zone, and concentrations in the circulation loop will decrease at a rate dictated by the flow rate through the injection interval induced by the withdrawal of water from the tunnel wall (i.e., very similar to a borehole point-dilution test).

Two previous colloid-facilitated transport tests were conducted in this configuration, but they involved nonradioactive homologues, not radionuclides. Prior to the above test, there will be at least one tracer test involving nonradioactive tracers to evaluate the ability to sample the fracture zone very close to the main injection borehole using three new small-diameter boreholes drilled within a few cm of the injection

borehole. The test(s) will also evaluate the influence that these new boreholes have on the flow field through the injection interval and to the tunnel wall.

Radionuclide-Doped Bentonite Plug Transport Experiment (Focus: NBS and EBS)

Late in 2011 or in early 2012, a bentonite plug (FEBEX backfill material) will be doped with a suite of radionuclides and emplaced into the CFM 06.002 injection interval used in previous tracer tests. The test configuration is schematically depicted in Figure 8.4-1. The exact method for doping the bentonite is still being worked out, but it will probably involve generating doped "pills" that are inserted into small holes drilled into the main bentonite plug at the depth of the fracture zone. Emplacement of the bentonite plug will be followed by long-term monitoring (over several years) of both colloids and radionuclides. Many of the same radionuclides will be used as in the test described above, but different isotopes will allow the observations from the two tests to be distinguished. The bentonite will be allowed to swell into the fracture zone and erode under the influence of the flow field, while samples are collected at the tunnel wall. The new small boreholes will be instrumented for sampling at very low rates to provide an early indication of swelling and radionuclide release. At the conclusion of the test, these boreholes will be filled with a resin to stabilize the rock mass, and a large-diameter overcore of the entire injection interval. While the primary purpose of this overcoring procedure is to recover the majority of the radionuclide inventory remaining at the source location at the conclusion of the test, this procedure will also afford the opportunity to do detailed post-mortem characterizations of bentonite swelling into the fracture shear zone and determination of radionuclide dispositions in the emplacement borehole and shear zone at the end of the test.

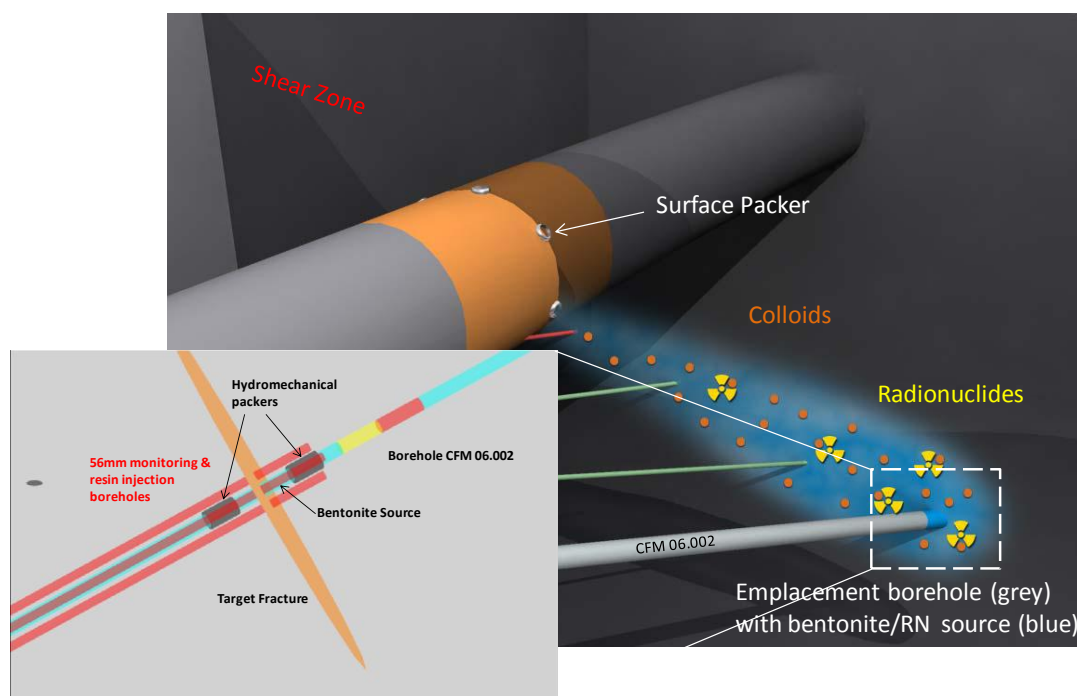

Figure 8.4-1. Schematic setup drawing of bentonite plug emplacement and bentonite swelling/erosion and colloid transport experiment. Note that the boreholes between CFM 06.002 and the main tunnel (green and red) will likely not be drilled.

Similar to the Mont Terri Project discussed above, DOE may consider becoming a formal partner of the Colloid Formation and Migration Project (CFM). Formal partnership would give DOE and affiliated national laboratories easier access to CFM data from past and ongoing experiments and encourage DOE interpretations of these experiments, which have only been qualitatively interpreted to date. More importantly, it would allow for UFDC researchers to work collaboratively with international scientists in *ongoing* experimental and modeling studies, and it would involve them in the planning of new experimental studies to be conducted in the future. DOE partnership would require a "membership contribution" of approximately 85K Swiss Francs per year, or ~$95K per year based on recent currency exchange rates. It is likely that a commitment of at least three years is required, but this has yet to be confirmed. In addition to the "membership fee" for DOE participation, staff support for active R&D would be covered out of the relevant UFDC work packages (e.g., NBS, EBS).

8.5   Other Active Collaboration Opportunities

In some cases, access to data on international field experiments and participation of UFDC researchers in collaborative field studies may also be facilitated via direct informal or semi-formal agreements between national laboratories and international partners. Several UFDC scientists already have close relationships with their international counterparts, resulting from workshops and symposia meetings, or from collaboration outside of UFDC's scope. International disposal programs are aware of the technical capabilities of UFDC scientists and are generally quite open to include them in their ongoing research teams. This may or may not require bilateral MoUs or other types of agreements. Below is a short list of selected major (soon-to-start or planned) field experiments conducted by international disposal programs that may be open to national laboratory participation, without "membership fees" or other long-term commitments on behalf of DOE. This list is being amended as needed.

PRACLAY Test at HADES URL, Belgium (Focus: mostly NBS, some EBS)

The PRACLAY Heater Test is a full-scale validation and confirmation experiment to be conducted at the HADES (High Activity Disposal Experimental Site) URL, excavated at 223 m depth in Boom Clay, a tertiary clay formation in Mol, Belgium. The heater test, which will begin in early 2012, will involve heating a 30 m gallery section for 10 years with many monitoring sensors (Figures 8.5-1, 8.5-2, and 8.5-3), for the purpose of investigating the thermo-hydro-mechanical (THM) behavior of near-field plastic clay under the most "mechanically critical" conditions that may occur around a repository (Van Marcke and Bastiaens, 2010) For plastic clay under the influence of temperature change, these are undrained conditions, which then generate a higher pore pressure increase and a higher possibility of near-field damage. For this objective, a hydraulic seal has been installed at the intersection between the planned heated and unheated sections of the gallery. This installation makes up the Seal Test, which was initiated in 2010, and allows testing the functionality of the hydraulic seal under heated repository conditions. The Belgium organizations involved in conducting and interpreting these experiments (EIG Euridice, SCK CEN, ONDRAF/NIRAS) have long-standing relationships with scientists at Lawrence Berkeley National Laboratory (LBNL); they have already invited LBNL researchers to provide THM modeling expertise to the project team.
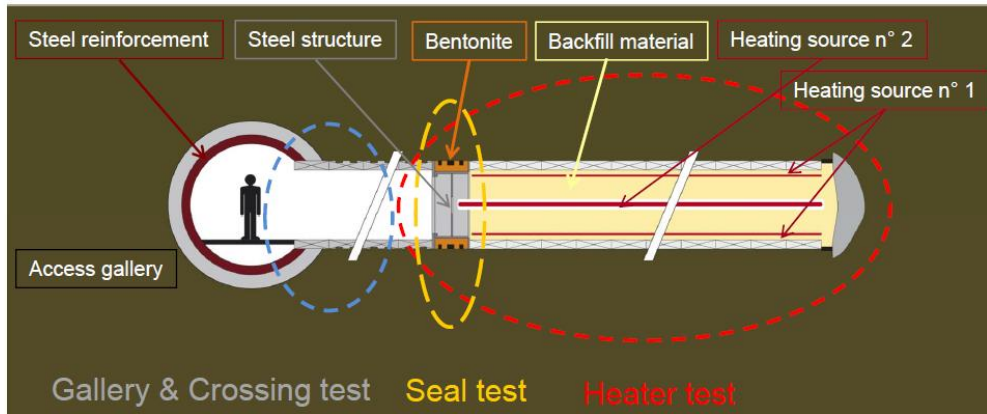
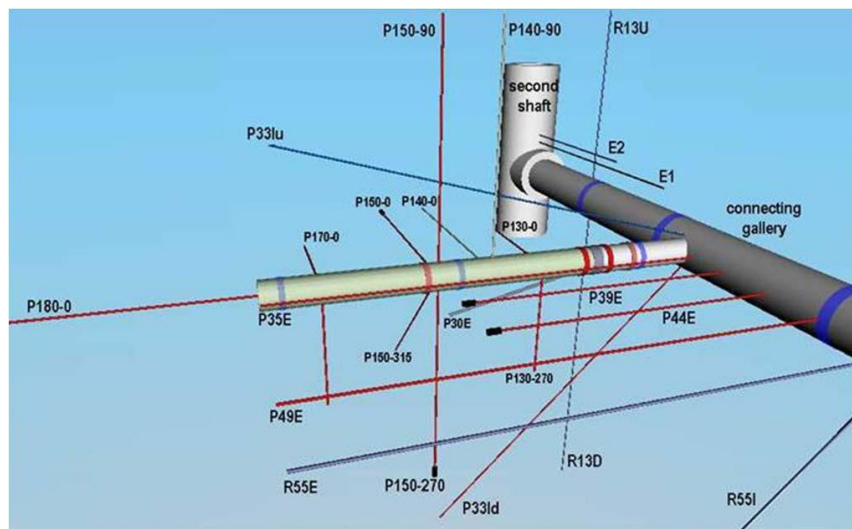**Figure 8.5-1**. Layout of the PRACLAY In-Situ Experiment (from Li, 2011)

Figure 8.5-2. Configuration of boreholes for pressure, stress, displacement, and water chemistry measurements (from Li, 2011)
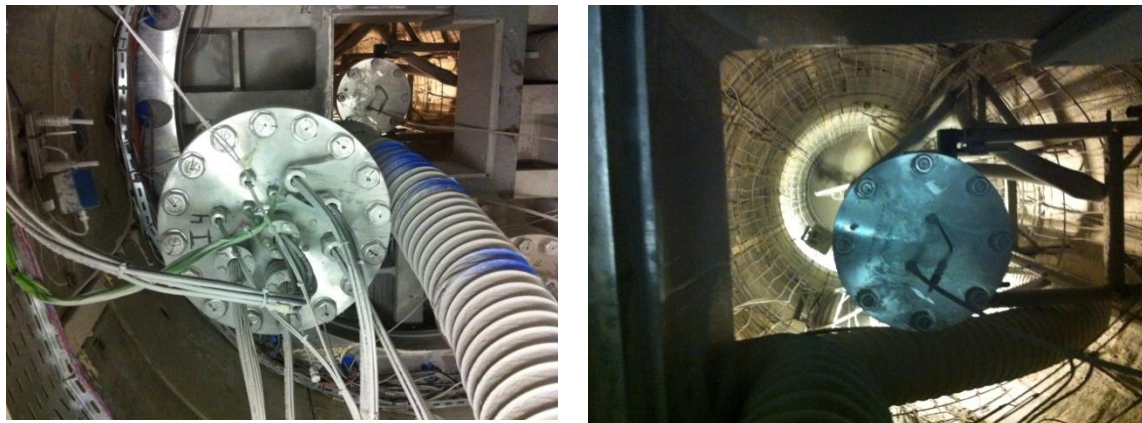
Figure 8.5-3. Photo on left shows hydraulic seal from the outside, with an access hole to the right which soon will be closed. Phot on right was taken from access hole into the heater gallery section, which is currently being backfilled starting in the back (from Birkholzer, 2011)

Radionuclide Migration Experiments at HADES URL, Belgium (Focus: NBS)

The Belgium waste management program has been conducting a suite of long-term radionuclide migration *in situ* experiments in dense clays at their HADES URL near Mol. Two of these experiments, named CP1 (Figure 8.5-4) and Tribicarb-3D, have been ongoing for 23 and 16 years, respectively, and offer valuable data on the slow diffusion-controlled migration of radionuclides in clay rocks. Because of their duration, they offer unique test cases for model and process validation. Recently, two other ongoing large-scale migration experiments were initiated at HADES. The TRANCOM test involves colloid transport with C-14 labeled humic substances. The RESEAL shaft seal experiment investigates transport of iodine-125 through the disturbed zone and the interface between Boom Clay and bentonite. As mentioned above, the Belgium organizations involved in conducting and interpreting these experiments are open to participation of DOE research groups.
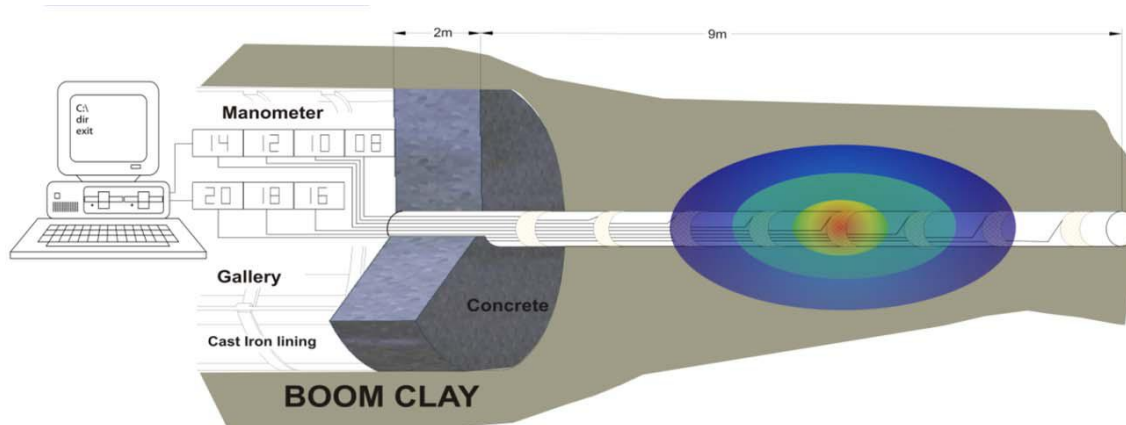
Figure 8.5-4. Schematic of CP1 diffusion experiment (from Maes et al., 2011)

Gas-Permeable Seal Test (GAST) at Grimsel Test Site, Switzerland (Focus: EBS)

The objective of the soon-to-start GAST experiments is to demonstrate the construction and performance of repository seals and plugs and to improve the understanding and the base datasets for reliably predicting water and gas transport through these sealing systems. The experiment will test a specific design option called "engineered gas transport system (EGTS)" (Figure 8.5-5), which involves specially designed backfill and sealing materials such as high porosity mortars or sand/bentonite (S/B) mixtures. The reason to develop these special designs is to allow for increased gas transport capacity (to mitigate pressure buildup from gas generation) of the backfilled underground structures without compromising the radionuclide retention capacity of the engineered barrier system. The managing organization for this experiment is NAGRA (Switzerland); a few other European partners are also involved. NAGRA has expressed that it would possibly be open for UFDC scientists to participate in aspects of the experiment.
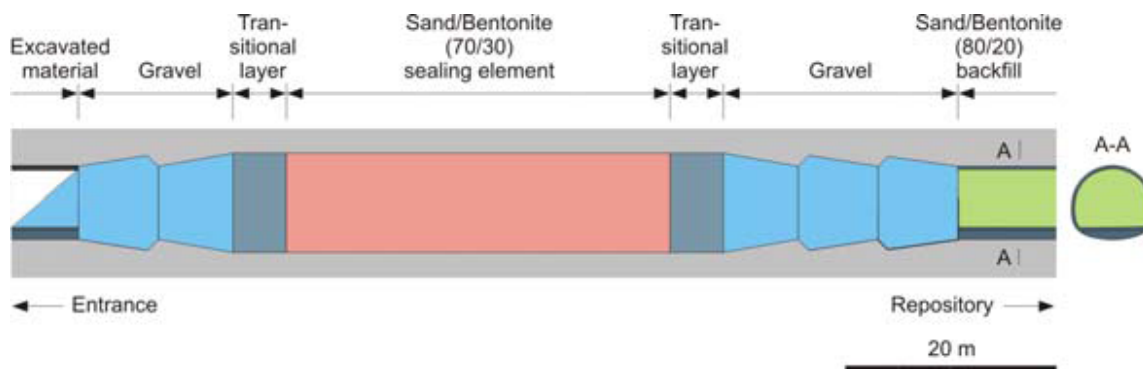

Figure 8.5-5. Schematic picture of repository seal design for GAST experiment (from Vomvoris, 2011)

Large-Scale Gas Injection Test (LASGIT) at Äspö URL, Sweden (Focus: Mostly EBS)

This ongoing field experiment, which has been in operation for over five years, evaluates gas flow processes (related to the potential for gas generation from canister corrosion) in an unsaturated bentonite embedded in fractured crystalline rock. Current knowledge pertaining to gas flow in a compact saturated bentonite is based on small-scale laboratory studies; the LASGIT tests are designed to address specific issues relating to gas migration and its long-term effect on the hydro-mechanical performance of the buffer clay, the question of heterogeneity and tortuosity of flow paths and the possible generation of new flow paths, and the complex coupling between gas, stress, and pore-water pressure at different scales (Figure 8.5-6). The main organization conducting the experiment is SKB (Sweden), together with the British Geological Survey (BGS). The LASGIT experiment was initially proposed as a modeling test case for DECOVALEX-2015, but is not under consideration anymore. However, SKB and BGS may be open to collaboration or participation of UFDC scientists.
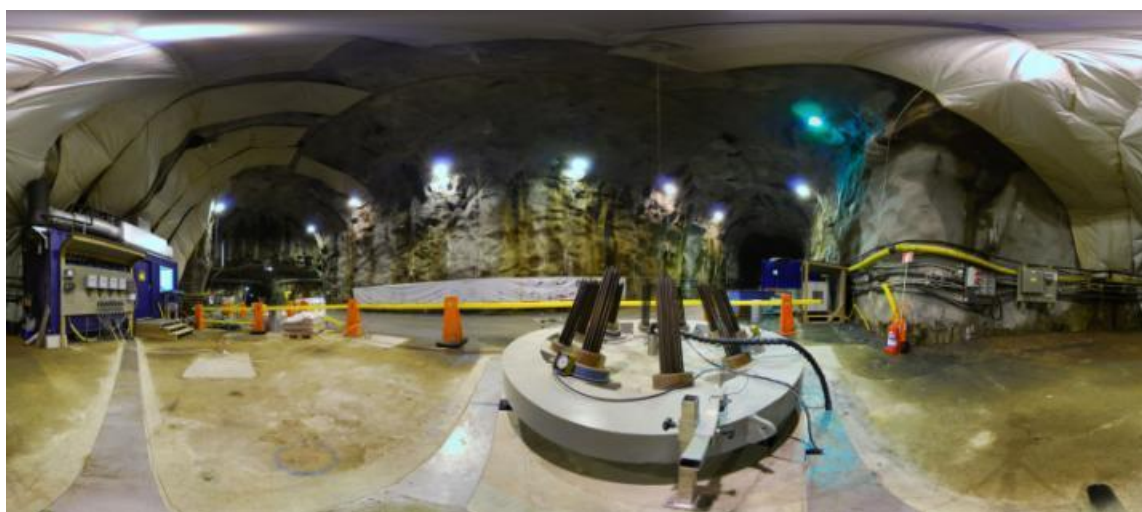
Figure 8.5-6. LASGIT experiment at Äspö (from Cuss, 2010)

Bentonite Rock Interaction Experiment (BRIE) at Äspö URL, Sweden (Focus: Both EBS and NBS)

Another option for UFDC engagement may be the upcoming BRIE test to be conducted at the Äspö URL in Sweden. The main objective of this experiment is to enhance the understanding of the hydraulic interaction between the fractured crystalline rock at Äspö and unsaturated bentonite used as backfill. The setup is aligned with the Swedish concept of emplacing canisters into vertical deposition holes that are subsequently backfilled. The main organization conducting the experiment is SKB (Sweden).

Other Participation Options for Mont Terri Project and CFM Experiments

Note that some benefits that the above-mentioned multinational and multi-partner initiatives (such as the Mont Terri Project or the Colloid Formation and Migration Project) can provide to UFDC may also be achievable via less formal partnerships. For example, LBNL has been offered the opportunity to become one of NAGRA's modeling and analysis partners for the full-scale FE Heater experiment at Mont Terri. Similarly, scientists at Los Alamos National Laboratory (LANL) have been engaged in the Colloid Formation and Migration Project without DOE being a full partner, and could presumably continue to do so. However, in both cases, without formal agreement, LBNL's and LANL's role would be limited to ad-hoc contributors. Full partnership, on the other hand, would give *all* DOE national laboratories full access to *all* of the many experiments that have been or will be conducted within the Mont Terri Project and CFM, respectively. Full partnership would also allow for DOE to be in a position to propose or conduct its own suite of experiments.

8.6   Summary and Future Work

Active collaboration with international programs, initiatives, or projects is considered very beneficial to UFDC, providing access to the decades of experience that some international programs have in various disposal options and geologic environments. We postulate that increasing international engagement will help efficiently achieve UFDC's long-term goals of conducting "experiments to fill data needs and confirm advanced modeling approaches" (by 2015) and of having a "robust modeling and experimental basis for evaluation of multiple disposal system options" (by 2020). The report section above discusses different opportunities of active international collaboration, with focus on both NBS and EBS aspects and those opportunities that provide access to field data (and respective interpretation/modeling) or allow participation in ongoing field experiments.

The next step will be to develop a concise list of promising international opportunities, which documents their cost and benefits, the mode of participation, and the key research gaps addressed (with tight link to roadmap and FEPs importance ranking; using the *Used Fuel Disposition Campaign Disposal Research and Development Roadmap, FCRD-USED-2011-000065 Rev 0, March 2011 [Nutt, 2011]*) and the *R&D Plan for the UFDC Natural Systems Evaluation and Tool Development* (Wang, 2011; Chapter 1). Based on this, potential activities will be ranked and recommendations will be made in time for the DOE/NE-53 and UFD planning process for FY12 and beyond. An early decision point is about DOE's possible participation in international agreements such as the DECOVALEX Project, the Mont Terri Project, and the Colloid Formations and Migration Project.

8.7 References

Barnichon J. D. (2011) *IRSN proposal - the SEALEX In Situ Tests*, Presentation given at 7th DECOVALEX 2011 workshop, April 2011, Helsinki.

Birkholzer J. T. (2011) Personal Communication.

Cuss, R. (2010) *Large scale gas injection test (Lasgit): Progress to May 2010*, Presentation given at 6th DECOVALEX 2011 workshop, October 2010, Wuhan.

Garitte B. and others (2011) *HE-E experiment - In situ Heater Test*, Presentation given at 7th DECOVALEX 2011 workshop, April 2011, Helsinki.

Garitte B. (2010) *New In Situ Experiments at Mont Terri*, Presentation given at 6th DECOVALEX 2011 workshop, October 2010, Wuhan.

Hokr M. and Slovak J. (2011) *Bedrichov Tunnel test case proposal for DECOVALEX 2015*, Presentation given at 7th DECOVALEX 2011, April 2011, Helsinki.

Li X. (2011) *Design and Status of the PRACLAY Seal and Heater Test*, Presentation given at HADES Workshop, May 2011, Antwerp.

Maes N., Weetjens E., Aertsen M., Govaerts J., and Van Ravestyn L. (2011) *Added Value and Lessons Learned from In-Situ Experiments – Radionuclide Migration*, Presentation given at HADES Workshop, May 2011, Antwerp.

Nutt M. (2010) *Used Fuel Disposition Campaign International Activities Implementation Plan*, (FCR&D-USED-2011-000016 REV 0), U.S. DOE Used Fuel Disposition Campaign.

Nutt M. (2011) *Used Fuel Disposition Campaign Disposal Research and Development Roadmap,* (FCR&D-USED-2011-000065 REV0), U.S. DOE Used Fuel Disposition Campaign.

Polak A., Elsworth D., Yasuhara H., Grader A. S., and Halleck P. M. (2003) Permeability reduction of a natural fracture under net dissolution by hydrothermal fluids, *Geophys. Res. Lett.*, 30(20), 2020.

Reimus P. (2011) Personal Communication.

Rejeb A. and Cabrera J. (2006) *Time-dependent evolution of the excavation damaged zone in the argillaceous Tournemire Site (France)*, Proceedings "GeoProc 2006," Invited lecture in the 2nd International Conference on Coupled THMC Processes in Geosystems and Engineering, May 22-25 2006, Nanjing, China, pp. 65-74.

Rutqvist J. and Min, K.-B. (2011) *THMC Modeling of Rock Fractures*, Presentation given at 7th DECOVALEX 2011 workshop, April 2011, Helsinki.

Steefel C., Rutqvist J., Tsang C.-F., Liu H. H., Sonnenthal E., Houseworth J., and Birkholzer J. T. (2010) *Reactive Transport and Coupled THM Processes in Engineering Barrier Systems (EBS)*, Lawrence Berkeley National Laboratory (LBNL), Final Report of FY2010 Activities, Berkeley, August 2010.

Tsang C.-F., Stephansson O., Jing L., and Kautsky F. (2009) DECOVALEX Project: from 1992 to 2007, *Environmental Geology*, 57, 1221–1237, 2009.

Tsang C.-F., Barnichon J. D., Birkholzer J. T., Li X. L., Liu H. H., Sillen X., and Vietor T. (2011) A Review of Coupled Thermo-Hydro-Mechanical Processes in the Near-field of a High-Level Radioactive Waste Repository in a Clay Formation, submitted to *International Journal of Rock Mechanics and Mining Sciences*, in review.

Van Marcke P. and Bastiaens W. (2010) *Construction of the PRACLAY Experimental Gallery at the Hades URF*, Clay in Natural and Engineered Barriers for Radioactive Waste Confinement, 4th International Meeting, March, 2010, Nantes, France.

Vietor T., Polster M., Garitte B., and Martin, D. (2011) *Mine-by test in the Mont Terri rock laboratory – MB Experiment*, Presentation given at 7th DECOVALEX 2011 workshop, April 2011, Helsinki.

Vomvoris S. (2011) Personal Communication.

Wang Y. (editor) (2010) *Natural System Evaluation and Tool Development – FY10 Progress Report*, U.S. DOE Used Fuel Disposition Campaign, August 2010.

Wang Y. (2011) *Research & Development Plan for Used Fuel Disposition Campaign (UFDC) Natural Systems Evaluation and Tool Development*, U.S. DOE Used Fuel Disposition Campaign, May 25, 2011.

Yasuhara H., Elsworth D., and Polak A. (2004) The evolution of permeability in a natural fracture: significant role of pressure solution, *J. Geophys. Res*., Vol. 109.

Zuidema P. (2007) *Advancements in Deep Geological Disposal of Radioactive Waste through International Cooperation: The Role of Underground Laboratories – Mont Terri Project*, Proceedings of the 10 Year Anniversary Workshop, pp 69-71, Rep. Swiss Geol. Surv. 2.

Chapter 9: Summary

The major accomplishments are summarized as follows:

- Based on international experience, discrete fracture network simulation is likely to play an important role in any future investigation of a hard-rock site for a nuclear waste repository, either alone or as part of a hybrid continuum/DFN computational strategy. Initial scoping investigations suggest that LaGriT, FEHM, and the unstructured grid particle tracking method could be used in combination to build a prototype simulation capability. In order to model more complex systems with large numbers of fractures, automated workflows need to be developed that interfaces software that generate fracture network realizations, either stochastic or deterministic, with automated mesh generation tools.

- Spatial heterogeneity in K_d has a significant effect on radionuclide breakthough in a natural system. The appropriate treatment of K_d in a performance assessment context depends on the spatial correlation length relative to the length of the transport path. If the correlation length is short relative to the length of the transport path, then the effective upscaled K_d approximates the mean K_d. In this situation, a constant K_d equal to the mean K_d gives good results. Conversely, if the correlation length is long compared to the travel distance, then K_d is essentially an uncertain parameter. Substituting parametric uncertainty for spatial variability could lead to significant overestimation of peak of the mean radionuclide discharge into the biosphere.

- A comprehensive review was conducted on radionuclide interactions with clay minerals and clay formations. The review considers how chemical reactions couple with the geomechanical compaction under conditions relevant to nuclear waste disposal. From a geochemical perspective, the degree of compaction ranges from the single clay particle or dilute suspensions up to heavily compacted clay columns. This range of systems allows for a broad range of chemical variability based on the degree of particle-particle interaction even though the chemistry of the solid phase may be consistent throughout. The review discusses the interfacial chemistry in physically restrictive environments and its implications radionuclide sorption to clays. A comprehensive list of K_d values and diffusion coeeficients of radionuclides and heavy metals in various clay formations is complied.

- Research has been performed on the behavior of aqueous Pu(IV) and intrinsic Pu(IV) nano-colloids in the presence of goethite at 25 and 80°C and over a range of concentrations from undersaturated to oversaturated with respect to PuO_2(am, hyd). The strong affinity of aqueous Pu(IV) for the goethite surface is explained by the epitaxial growth of bcc Pu_4O_7 nano-colloids on goethite. The behavior is affected minimally by temperature. This strong affinity cannot be achieved when intrinsic Pu(IV) nano-colloids are reacted with goethite over 103 days. The results indicate that the fate of Pu is dependent on its initial form and its subsequent stability under changing geochemical conditions. Both intrinsic colloids and those sorbed to goethite have the potential to be transported with groundwater. This work has been extended to examine the behavior of aqueous Pu(IV) and intrinsic Pu(IV) nano-colloids and interaction with clay mineral montmorillonite.

- Geomechanical modeling of the DRZ requires the consideration of the effects of fractures on the constitutive relationship between stress and strain. A new constitutive relationship, relating stress and strain for fractured porous rock, that accounts for the different geomechanical behavior of fractures and the general rock mass was developed in FY10. The new constitutive relationship has been extended here to address anisotropic stress conditions. Furthermore, the model development has also been advanced to describe the functional dependence of porosity and bulk compressibility on stress. Several comparisons with laboratory data on the mechanical response of clay, shale, and other rock types have shown that the nonlinearity introduced by the new constitutive model is needed to reflect the observed behavior.

- Experimental work on saturated and unsaturated flow through clay shows significant deviations from the traditional Darcy's law relationship between flux and the hydraulic gradient. A new constitutive relationship for unsaturated flow through clay, based on a non-Newtonian flow process, was developed. This leads to a nonlinear relationship between flux and the hydraulic gradient, and a new relationship between hydraulic conductivity and pore size. These results were used to develop a revised relationship between capillary pressure and relative permeability. The new constitutive relationships are fundamentally different from traditional relationships for saturated and unsaturated flow in porous media. Comparisons with data show that the new constitutive relationships are consistent with experimental observations of unsaturated flow through a compacted sand-bentonite mixture.

- The TOUGH-FLAC thermal-hydrological-mechanical code was updated to include the new stress-strain constitutive model. The code was used to model rock-mass deformation and pore pressure around an underground excavation, using published hydromechanical parameters and boundary conditions determined for the Opalinus Clay, Switzerland. A Gouy-Chapman diffuse-double layer model for geochemically-induced swelling and shrinkage was implemented in the TOUGHREACT thermal-hydrological-chemical code. The model simulation shows that geochemical conditions, such as ion concentration and exchangeable cation compositon, can affect clay swelling.

- To further test the concept of direct disposal of ER salt in a salt repository, experimental techniques were developed for characterizing microstructure of ER salt and testing the stability of ER salt in a repository environment. A process for making surrogate ER salts of various compositions was developed. The surrogate salts have been characterized for their microstructures with XRF and SEM. The microstructural analysis reveals that phase separation appears to occur in the ER salt – a good indicator for microphase encapsulation of radionuclide by a salt matrix. Iodine tends to bond cesium in the salt. Dissolution experiments for fine surrogate ER salt particles have been performed, which showed that the contacted solution quickly reached the solubility of salt. Removing LiCl from the salt may not reduce its solubility limit or dissolution rate. A technique for making surrogate ER salt pellets was developed using room temperature mechanical pressing. The pellets with various ratios of NaI to NaCl were made for studying the efficacy of radionuclide encapsulation by salt. A preliminary test indicates that the obtained pellets seem to remain structurally intact during the dissolution experiment with WIPP brines. Due to its effectiveness, the developed pressing technique can potentially be used for densification of ER salt if needed.

- International collaboration has been considered to be essential for many research topics. Potential areas and approaches for such collaboration were identified.

All the FY11 work will be continued in FY12. The FY12 will be expanded to include the following three research topics, which have been identified to be in high priority in the R&D plan:

- **Topic S2:** Disposal concept development for natural systems. The work will define a generic set of key parameters (e.g., lithology, water chemistry) for natural system studies.
- **Topic S3:** Disposal system modeling. The work will develop a comprehensive subsystem model for natural system performance evaluation. This subsystem model will be used for integration and prioritization of relevant natural system evaluation activities.
- **Topic S4:** Development of a centralized technical database for natural system evaluation.